SAPIENZA
UNIVERSITÀ DI ROMA

Dipartimento di Ingegneria Meccanica e Aerospaziale

DOTTORATO DI RICERCA IN TECNOLOGIA AERONAUTICA E SPAZIALE
CICLO XXVII

Gravity and geodesy of the Jovian system bodies with the Juno and JUICE missions

Candidate:

Marzia Parisi

Advisor:

Prof. **Luciano Iess**

Tutor:

Prof. **Paolo Gaudenzi**

Anno Accademico 2013-2014

Acknowledgements

I want to thank my advisor Professor Luciano Iess and all my colleagues from the Radio Science Laboratory for guiding me during the last four years.

Dr. Yohai Kaspi, Dr. Eli Galanti and Dr. Ravit Helled for their support during my visit in Israel.

My parents Francesco and Rosetta, my sister Maria Alessandra, my grandmother Maria and my whole family, Gabriele, my best friends Marta and Marzia, for loving me and for putting up with me.

Contents

List of Figures

List of Tables

Abstract

The key to the understanding of our Solar System, how it originated and evolved, lies with the exploration of the miniature system of its largest planet, Jupiter. To this end, a number of space missions have been dedicated to probing the planet itself and its satellites, aiming at studying and comprehending the physical phenomena taking place within the system. In this context, a fundamental role is played by the determination of the gravity field of the bodies forming the system, by means of onboard radio science experiments. The main purpose of my research is to assess the accuracies attainable with the gravity measurements performed by NASA's Juno and ESA's JUICE missions, that will influence the comprehension of the interior structure and dynamics of the Jovian system bodies. In the frame of this dissertation I show how the precise reconstruction of the gravitational potential of Jupiter and its largest moons have the potential of improving our knowledge of the geodesy of the whole system.

Introduction

Jupiter had been known to humanity since ancient times, while the Galilean moons, the largest in the system, were first observed by Galileo Galilei in 1610, using a telescope. Half a century later, Giovanni Domenico Cassini discovered that Jupiter appeared oblate and noticed the differential rotation of its atmosphere bands. As the technological innovation advanced, more questions arose that needed to be answered.

The first spacecraft to ever fly by Jupiter were Pioneer 10 and 11, the encounters occurred over a two-year period (1973-1974), capturing the first close images of the planet and the Galilean moons. Furthermore, the mission provided the first *in-situ* measurements of the planet's main features: the complex atmosphere, the huge magnetosphere and radiation environment, and even attempted to get a grasp of the interior. After the end of the Pioneer program, the exploration of the Jovian system was took over by Voyager 1 and Voyager 2 missions (1979). Among the extremely important scientific breakthroughs, made by means of Voyager observations, there were the discovery of Jupiter's ring (Smith *et al.*, 1979) and the observation of active volcanism on Io (Morabito *et al.*, 1979).

A turning point in the exploration of Jupiter system was the orbit insertion of the Galileo spacecraft around the planet, in 1995. During its tour of the system, not only did the probe complete 35 orbits around Jupiter (NASA/JPL, 2009), but also carried out multiple encounters with its major satellites (*i.e.* Galilean moons). Despite the failure of the onboard high-gain antenna, the mission managed to gather crucial information about the complex environment, regarding both the planet and the satellites. The most striking discoveries made by this mission concern the collection of the first observations of ammonia clouds in a planet's atmosphere other than Earth's and the identification of Jupiter's magnetosphere global structure.

In July 1995, a probe detached from the main spacecraft and entered the atmosphere, collecting data for almost an hour before being destroyed by pressure and temperature. It managed to detect and measure atmospheric elements, giving indication on how the planet formed from the primary solar nebula (NASA, 2003).

The Galileo mission also provided the first evidence for the presence of subsurface oceans on icy satellites. The spacecraft collected enough magnetometer data to verify the presence of induced magnetic fields surrounding Europa, Callisto (Khurana *et al.*, 1998; Zimmer *et al.*, 2000) and Ganymede (Kivelson *et al.*, 2002). For the first two satellites, the absence of an intrinsic magnetic field, made the identification of induced magnetic dipoles much easier. For Ganymede, which possesses an intrinsic magnetic field generated within the satellite's core, the decoupling between the induced field and the satellite's own magnetosphere was harder. The most reasonable explanation for the existence of these induced magnetic dipoles remains the presence of global oceans underneath the satellites' surfaces. Europa's and Ganymede's topographies show evidence for geological differentiation, where the presence of a liquid water layers between two high-pressure ice layers is very likely. On the other hand, Callisto appears to be an undifferentiated body of ice and rock. Nevertheless, a global or partial subsurface liquid ocean still represents a possibility.

For all the above reasons, the gravity investigation of these bodies needs to move further. Only with the newest missions to Jupiter, Juno and JUICE, dedicated to the exploration of the planet and its satellites, will we be able to answer the key questions about the interior configuration and composition of some bodies among the most interesting and active of the Solar System.

This task can be accomplished by using highly accurate Doppler tracking of the spacecraft. Precise gravity measurements are enabled by an onboard Ka-transponder capable of establishing a radio link between the spacecraft and Earth stations, characterized by high phase stability. The real innovation with respect to previous missions is the exploitation of Ka-band links in both uplink and downlink (34 GHz and 32.5 GHz respectively). The expected accuracies on range-rate measurements are around 0.012 mm/s at 60 s integration time. Furthermore, a complete cancellation

of the plasma noise will be possible, if the Ka/Ka link is operated together with X/X and X/Ka links (enabled by the onboard DST).

Both missions envisage an onboard radio science experiment, though they are, at present, in two very different phases. Juno has been launched in August 2011 and is now on its way to Jupiter (arrival due in July 2016). The spacecraft will complete 33 highly-eccentric polar orbits around Jupiter, of which 25 will be dedicated to gravity measurements aimed at determining and resolving the open issues about the interior structure and dynamics of Jupiter. The determination of the planet's low-degree gravity field is related to the mass and size of the core, while the high-frequency anomalies of the surface gravity indicate localized variations in the density distribution. Recently, the opportunity of determining the scale height of Jupiter's thermal winds by using gravity measurements has been explored (Galanti *et al.*, 2013). Indeed, compared to a fast-rotating solid body, Jupiter's odd-zonal and tesseral harmonics, related to zonal and meridional winds, are much larger (Kaspi *et al.*, 2009).

JUICE is advancing through phase A/B1 of early definition and planning of its scientific goals and requirements. The current mission profile envisages three different science cases dedicated to as many Galilean moons: Ganymede, Callisto and Europa. The spacecraft will perform an orbital phase around Ganymede, the main target of the mission, part of which will be spent in a circular polar orbit. The low altitudes ensure the determination of the satellite's gravity field up to degree and order 20 (at least), with very high accuracy. Furthermore, the wide range of mean anomalies at which Ganymede will be observed, allows the determination of the degree-2 Love number k_2, a crucial parameter in the detection of subsurface oceans. JUICE will also perform 20 flybys of Callisto, the main gravity science objective for this phase is the determination of the octupole gravity field. Since Callisto will be observed close enough to its perijove and apojove, the determination of k_2 will be attempted for this body as well. Europa is perhaps the most interesting of the Galilean satellites, though a severe radiation environment makes its exploration very difficult. For this reason, the number of JUICE Europa flybys will be limited to 2, even so, the determination of its quadrupole gravity field may be possible.

This work focuses on crucial aspects of the numerical simulations of Juno and JUICE radio science experiments and is organized as follows: Chapter 1 is dedicated to an overview of the two space missions, a description of the nominal gravity experiments and a report on the current knowledge of the involved celestial bodies; Chapter 2 contains theoretical principles of planetary geodesy; Chapter 3 introduces the problem of orbit determination in terms of mathematical formulation and adopted techniques; Chapter 4 is dedicated to the description of the adopted dynamical models and numerical simulation setup; Chapter 5 contains analysis results concerning the influence of Jupiter's thermal winds on Juno gravity experiment performance; Chapter 6 contains analysis results concerning the attainable accuracies in the determination of the Galilean satellites' gravity fields with the JUICE mission; Chapter 7 is dedicated to conclusions and discussion.

Chapter 1

Juno and JUICE disclose Jovian system's mysteries

Despite being two separate missions, Juno and JUICE are destined to be synergic and interconnected, for they will share a similar severe environment and mission conditions throughout their exploration of the Jovian system. However, the main scientific objectives deeply differ from one another. While Juno will have as its major target the gas giant itself, JUICE's interests in the planet will be limited to an initial high-latitude phase, and will focus instead on probing three Galilean moons.

This chapter will give an overview of the two missions, their scientific objectives and trajectories, with particular focus on the description of the onboard radio science experiments.

1.1 The Juno mission

NASA's Juno mission was named after the Roman-Greek goddess, wife of Jupiter, who was able to discover her husband's true nature by removing the cloudbank surrounding him. Likewise, the Juno spacecraft will figuratively unveil all the mysteries and secrets of the planet Jupiter, and will forever change our understanding of the whole system.

Juno was approved in 2005 as the second mission of NASA's New Frontiers program (Grammier, 2009) and was launched in 2011. After a 5-year cruise, the spacecraft will arrive at Jupiter and perform several complete orbits around the planet, collecting a great amount of science data.

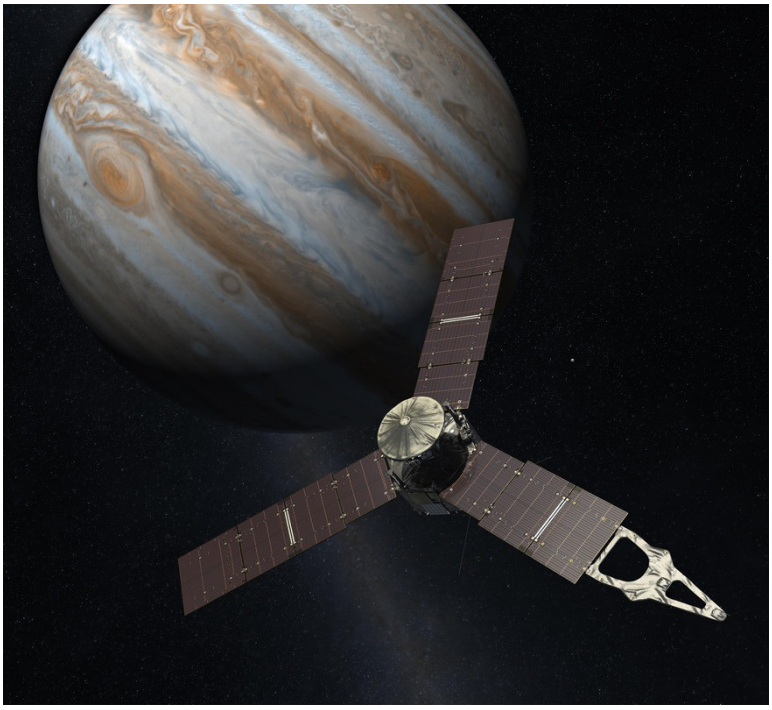

Figure 1.1: Artist concept of Juno and Jupiter. Image credit: NASA/JPL-Caltech.

1.1.1 Scientific objectives

Juno is the natural step further in the exploration of Jupiter after the Galileo mission, and will be the second spacecraft to ever orbit the planet.

The gas giant presents three different fundamental realities: the magnetosphere, the atmosphere and the interior. The main scientific objectives regarding these main features can be summarized as follows (Grammier, 2009):

- Magnetosphere:
  - determination and characterization of the 3D structure of Jupiter's magnetosphere;
  - observations of Jupiter's auroras;
- Atmosphere:
  - determination of the atmospheric composition, including the measure of oxygen abundance and variations in water and ammonia concentrations;

- characterization of the temperature profile;
- study of the winds at great depth;
- investigation of convection phenomena;
- study of the clouds dynamics and characteristics;

- Interior:

  - determination of Jupiter's gravitational and magnetic fields;
  - set constraints on the core mass;
  - assess the depth of the winds and their influence on high-degree gravity field.

Since Juno orbit will be polar, the mission will achieve completely innovative and un-addressed scientific goals, aiming at answering crucial questions about the formation and evolution of the system.

1.1.2 Launch, trajectory and orbit around Jupiter

Juno lifted off on August 5, 2011 from Cape Canaveral Air Force Station in Florida, on an Atlas V 551. During launch, telecommunications with ground stations were provided by the Deep Space Network Station (DSS) at Canberra (Nybakken, 2011). Right after the separation (SEP), the solar arrays deployed and the spacecraft was inserted in a EGA (Earth Gravity Assist) trajectory. In preparation for the Earth flyby, two deep space maneuvers were scheduled after 13 months from launch, to adjust Juno trajectory. The encounter with our planet took place in October 2013 and represented the first critical event of the mission (Nybakken, 2011).

Upon its arrival at Jupiter, the spacecraft will perform a Jupiter Orbit Insertion maneuver (JOI), 59 months after launch (Nybakken, 2011). The maneuver will be followed by a long-duration capture trajectory of 107 days, before entering the science phase. The chosen orbit is characterized by high eccentricity (e=0.947) and high inclination ($90° \pm 10°$). Each passage will take about 11 days to be completed, for a total duration of at least 1 year (and 33 pericenters). Juno cruise phase is sketched in Figure 1.2.

The first two orbits will be dedicated to further checkouts and verification before the beginning of the science observation phase. In order

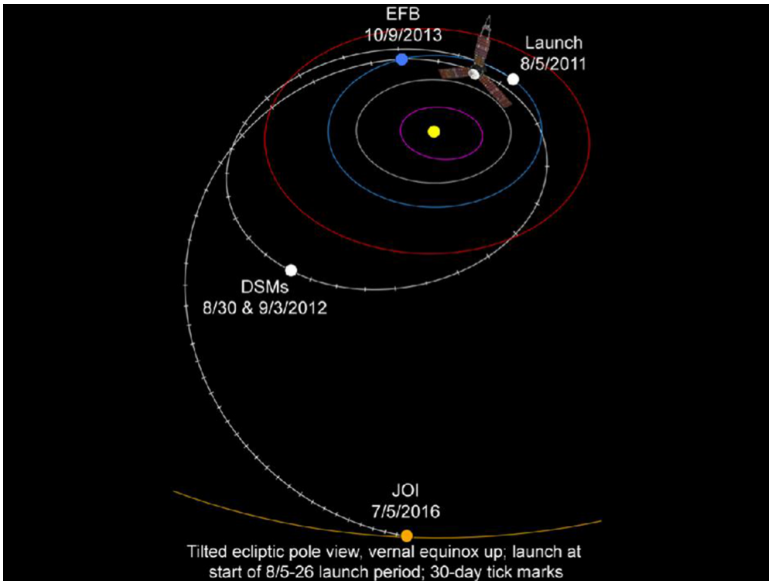

Figure 1.2: Juno trajectory during cruise (2011-2016). Image credit: NASA/JPL-Caltech.

to collect highly significant data, Juno will fly within 4600 km of Jupiter's surface (Grammier, 2009). Due to the fast rotation of the planet under the spacecraft, Juno will span the planet in longitude (span of $12°$), while the pericenters are confined at latitude between $5°$ and $+35°$ (see Figure 1.3a).

Of these 33 science orbits, 25 will be dedicated to the gravity experiment (4 and 9 to 32), while the remainder will be used for MicroWave Radiometric (MWR) measurements. Other instruments do not require a particular attitude of the spacecraft and therefore can operate simultaneously with one another (see Figure 1.3b).

Orbit 34 will mark the end of the mission through a de-orbiting phase: the spacecraft will fly through Jupiter's atmosphere and be destroyed.

1.1.3 The spacecraft

Juno will be the first solar powered spacecraft to go as far from the Sun as Jupiter's orbit. This condition of extreme distance from our star is one of the key drivers of the craft design. In fact, the solar arrays mounted on Juno will be the largest panels to ever fly, since their size must guarantee enough power to operate the instruments and the onboard equipment. The

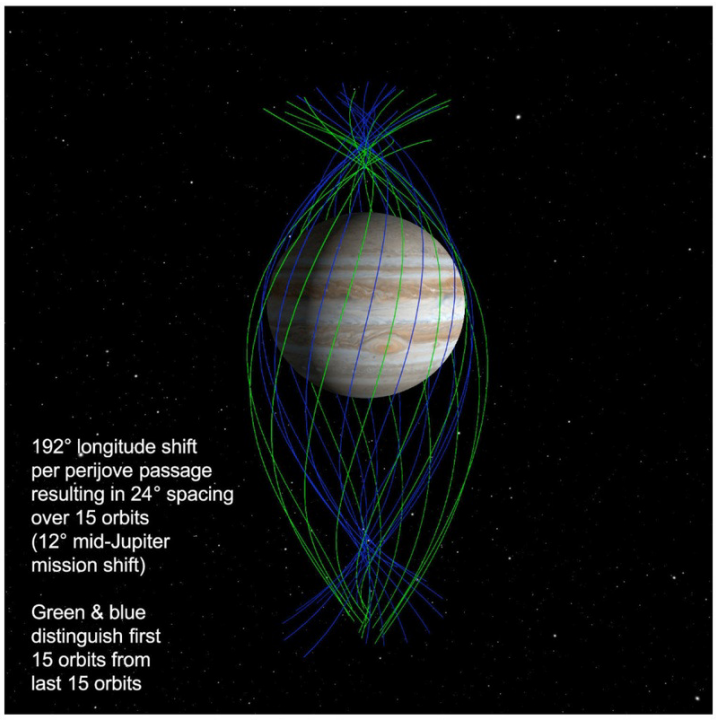

(a)

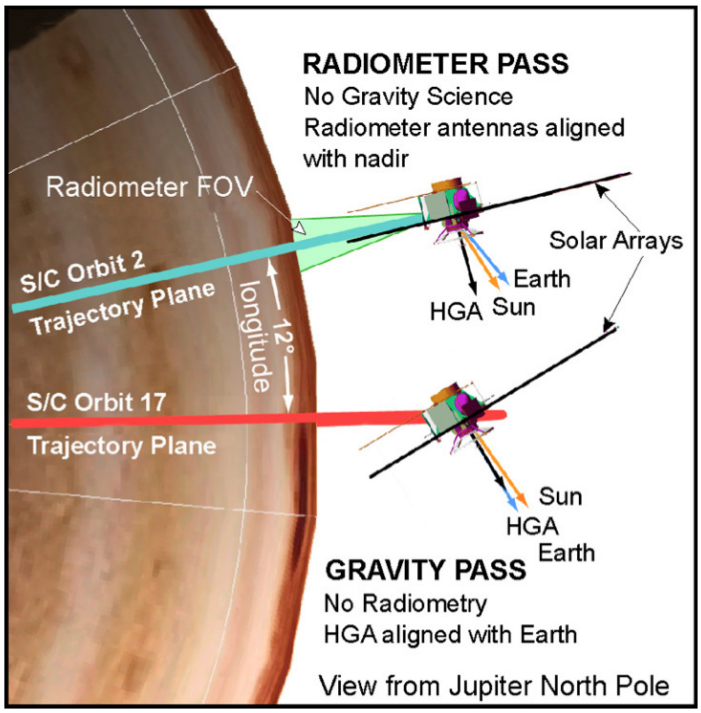

(b)

Figure 1.3: a) Juno science orbits around Jupiter. Image credit: NASA/JPL-Caltech. **b)** Juno attitude during science observations through orbits 3-33 (Grammier, 2009). Image credit: NASA/JPL-Caltech.

spacecraft design envisages three solar arrays symmetrical about the bus (forming a 120° angle with each other) for an overall area of 60 m^2 (of which 45 m^2 are active, Grammier, 2009). One of the arrays also hosts a boom for magnetometer observations (Grammier, 2009, see Figure 1.1).

The need for such large solar panels influenced the choice of a spin-stabilized spacecraft over a stabilization based on reaction wheels, much more expensive in terms of energy consumption. Also, this decision allowed avoiding the complications related to the use of instrument scan platforms, associated with complex spacecraft maneuvers and pointing requirements (Grammier, 2009). The instruments will be placed on the edges of the main hexagonal structure, ensuring the required field of view needed for the scheduled observations and measurements.

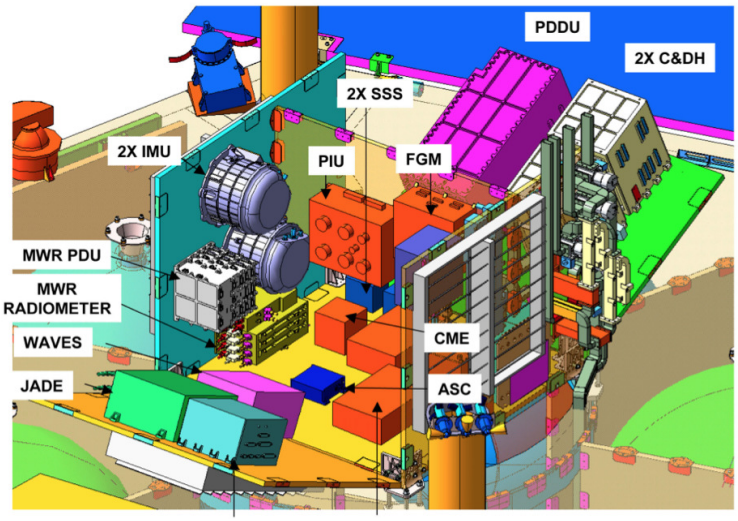

Figure 1.4: Juno view inside the vault (Grammier, 2009). Image credit: NASA/JPL-Caltech.

The radiation environment at Jupiter is one of the harshest in the Solar system, for this reason, Juno electronics and instruments are located under a radiation vault, in order to prevent them from degradation (see Figure 1.4). The vault covers the main structure of the spacecraft and has a mass of about 160 kg. This safety measure reduces the total radiation dose absorbed by internal equipment throughout the mission from 100 Mrads to a maximum of 25 krad (Nybakken, 2011). Also, the geometry of the science orbits allows the collection of $\pm$ 3h of science data below Jupiter's radia-

tion belt, maximizing the science return and minimizing the radiation dose absorbed during observations.

The spacecraft is provided with a high gain antenna as main asset for the transmission of science data. In addition to the HGA, the spacecraft is also endowed with a medium gain antenna (MGA) and two low gain antennas (LGAs).

The main engine will be used for the two deep space maneuvers, while four thrusters will be used to perform minor maneuvers, including the de-orbiting (Grammier, 2009).

1.1.4 Payload

Juno payload is composed of 8 scientific instruments plus a visible camera (JunoCam) whose purpose is to capture images of Jupiter for education and public outreach. The onboard experiments can be divided into two main categories (Grammier, 2009):

- Instrument payload:
  - Microwave Radiometer;
  - Magnetometer;
  - Radio Science Package;
- Fields and particles instruments:
  - Jovian Auroral Distribution Experiment;
  - Jupiter Energetic-particle Detector Instrument;
  - Waves instrument;
  - Ultraviolet Spectrometer;
  - Juno Infra-Red Auroral Mapper;

Table 1.1 contains a list of the instruments with a brief description of their scientific objectives and characteristics.

Instrument	Classification	Scientific Objectives and characteristics
Juno Gravity Experiment	Radio Science Experiment	Investigation of the interior structure through the determination of Jupiter's gravity field. X- and Ka- band uplink and downlink.
MAG	Magnetometer	Investigation of the interior structure and magnetic dynamo of Jupiter. Dual flux-gate magnetometers and two advanced stellar compasses.
MWR	Microwave Radiometer	Deep atmospheric sounding and measure of water and ammonia abundance. Six peripherally mounted antennas; radiometers; control/calibration electronics for 6 wavelengths (1.3 - 50 cm).
JEDI	Juno Energetic particle Detector Instrument	Auroral distributions and measure of electrons and ions in the Jovian polar region. TOF vs. energy, ion and electron sensors.
JADE	Jovian Auroral Distributions Experiment	Auroral distributions and measure of the time variable pitch angle and energy distributions of electrons and ions over both polar regions. 1 ion mass spectrometer and 3 electron analyzers.
Waves	Radio and Plasma Wave Detector	Measure of the radio and plasma wave emissions associated with the auroral phenomena in Jupiter's polar magnetosphere to reveal the processes responsible for particle acceleration. 4-m. electric dipole and search coil.
UVS	Ultraviolet Spectrometer	Characterize the spatial and temporal structure of ultraviolet auroral emissions. FUV spectral imager; 1024 256 micro channel plate (MCP).
JIRAM	Juno Infra-Red Auroral Mapper	Investigation of auroral structure and upper troposphere structure, atmospheric sounding. IR imager and IR spectrometer (λ = 2 - 5 μm).

Table 1.1: Juno payload (Grammier, 2009 and Bolton, 2010).

1.2 The JUICE mission

The European Space Agency officially selected the JUICE mission in May 2012, as the first European large-class science mission in ESA's *Cosmic Vision* 2015-2025 program. The launch is scheduled for 2022 and, after a 8-year cruise, the spacecraft will reach the Jovian system in 2030. The current mission timeline entails two Europa flybys (2030), twenty Callisto flybys (2031) and an orbital phase around Ganymede (2033) (Parisi *et al.*, 2012). The latter represents the main target of the mission, being the largest natural satellite of the Solar System and the only moon known to possess an intrinsic magnetic field. JUICE's exploration of the Jovian system will allow the scientific community to address two key science themes: the conditions for planet formation and the emergence of life (ESA, 2011). All these bodies could host sub-surface oceans, so the spacecraft will, very ambitiously, assess the possibility for the moons to be potential habitats for human life (ESA, 2012).

The current mission is heir to a joint ESA/NASA mission to Ganymede (JGO) and Europa (JEO), respectively, known as EJSM/Laplace. After NASA withdrawal in 2011, ESA took over part of the scientific objectives expected from the exploration of Europa, and reformulated a new European-led mission, called, indeed, JUICE. The acronym stays for Jupiter Icy moons Explorer.

1.2.1 Scientific objectives

JUICE is part of a space program devoted to the exploration of the outer solar system. Its main, ambitious goal is the research of possible environments in the Jovian system that would (or already have) allow the emergence and/or establishment of life. To this day, many extra-solar planets orbiting around nearby stars are known to be very similar to our gas giant Jupiter, thus the study and exploration of the latter will provide several pieces of information about the evolution and formation of these outer bodies. The tag line of the mission could be the study of the physical properties, interior structure, composition and geology of Ganymede and the research for subsurface oceans on three Galilean satellites. More specifically, the main scientific goals of the mission can be summarized as follows

(ESA, 2011):

- search for favorable environments for the emergence of life, among which stands out the presence of liquid water oceans and/or thick ice layers underneath the surface;
- study of the interaction between high-pressure ice and underlying layers on icy satellites;
- identification of the chemical composition of the satellites;
- characterization of Ganymede's intrinsic magnetic field;
- study of the satellites' geology and topography, identification of their surface activity, past and present;
- study of the thermal structure and dynamics of Jupiter's atmosphere;
- characterization of Jupiter's magnetosphere, affected by the fast rotation of the planet;
- observation of Jupiter's polar auroras.

Some of these goals are very innovative, since JUICE will be the first spacecraft to ever orbit a moon other than ours.

1.2.2 Launch, trajectory and tour of the satellite system

The JUICE mission will be launched in 2022, using an Ariane 5 ECA launcher from ESA's spaceport in Kourou, with a backup opportunity in 2023. The spacecraft will be inserted in a direct escape trajectory from Earth with an injected mass of 4800 kg and a hyperbolic escape velocity of 3.15 km/s. JUICE will perform a Venus-Earth-Earth gravity assist sequence, allowing to save a great amount of chemical propellant (ESA, 2011).

After a cruise lasting 7.6 years, the probe will arrive in the Jovian system in January 2030 and a JOI (Jupiter Insertion Orbit) will be performed (Figure 1.5). This maneuver is the most critical of the mission, and will be preceded by a Ganymede gravity assist, to gain the required ΔV. The spacecraft will be inserted in a highly eccentric orbit (13x243 RJ) around the planet, outside Ganymede's orbit. Its geometry has been defined not

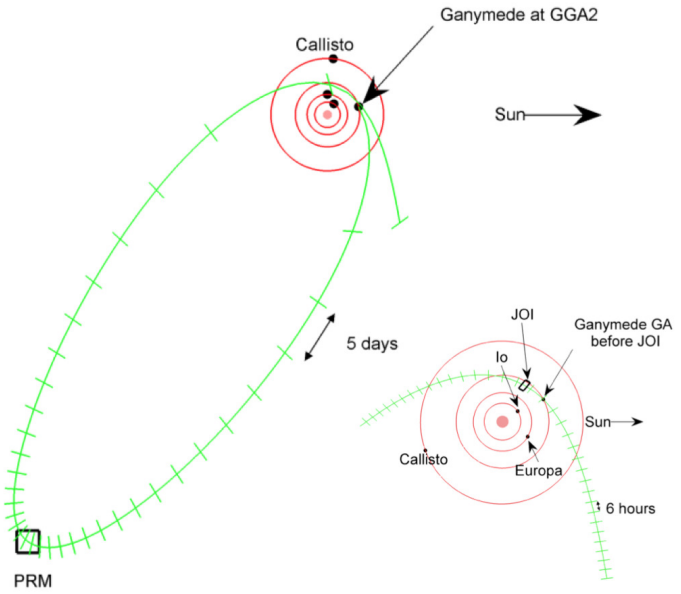

Figure 1.5: JUICE orbit insertion around Jupiter (JOI). The image also shows the orbits of the Galilean satellites (ESA, 2011). Image credit: ESA.

only optimizing the propellant consumption, but also trying not to force the spacecraft to undergo extreme radiation exposure.

The next step in the exploration of the system will consist of two Europa flybys, added after the reformulation of the mission. Europa is the innermost of the satellites designated as scientific objectives of the mission. Being so close to Jupiter, the radiation conditions which the spacecraft is exposed to reach almost unbearable levels. For this reason, the flybys are designed so that the integrated radiation dose is as low as possible. The flybys are scheduled to take place within 14 days from one another, probing the satellite in a region centered at 180° longitude, while the range of explored latitudes will be wider, about $\pm\ 45^\circ$ (see Figure 1.6).

Callisto science phase will be used to increase the inclination of the Jovi-centric orbit up to 30° over Jupiter's equator. This maneuver will allow the sampling and the probing of the planet's magnetosphere as well as exploring and studying the satellite, almost the same size as Ganymede. The orbit will be Callisto-resonant and the total duration of this phase will be about 200 days. The mission profile envisages 20 flybys of Callisto, of which 10 will take place at very low altitudes (200 - 400 km). The coverage

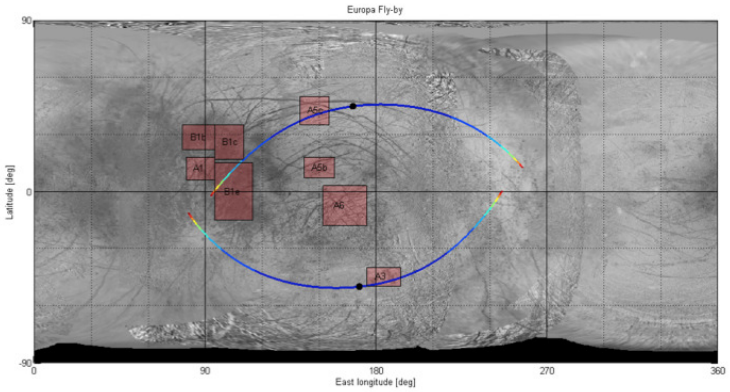

Figure 1.6: Ground tracks of the Europa flybys (ESA, 2011). Image credit: ESA.

of the satellite's surface, obtained through these encounters, is constrained by the geometry of the spacecraft trajectory (see Figure 1.7).

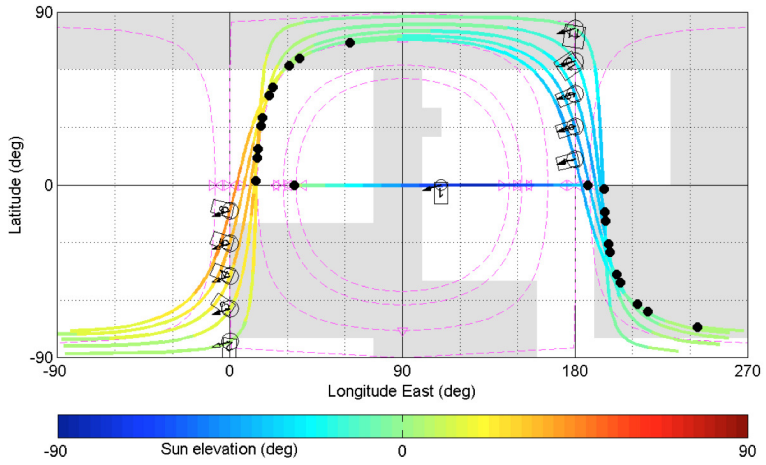

Figure 1.7: Coverage of Callisto surface after 20 flybys. The closest approaches are divided into two groups around two different longitudes. Conventionally, for Galilean moons, $0°$ longitude indicates the side facing Jupiter. Different colors indicate different Sun elevation of the sub-nadir point (ESA, 2011). Image credit: ESA.

Being the orbit in resonance with Callisto, JUICE will encounter the satellite always at the same mean anomalies. For this reason, since Callisto is tidally locked to Jupiter, the closest approaches will all occur in a certain range of longitudes, except the spacecraft will skip a number of gravity assists around the moon that will allow a change of quadrant (Figure 1.7).

Also, Jupiter's northern polar region will be visible during this phase, allowing the observation of polar auroras (ESA, 2011).

After the numerous flybys of Callisto, the orbiter will finally be transferred to Ganymede, through a number of CGC gravity assists. As anticipated, the scientific phase at Ganymede will be the most important and extensive, composed of several sub-phases, each of which will be dedicated to achieving different scientific objectives. The sub-phases are summarized in Table 1.2.

Phase	**Altitude (km)**	**Duration (d)**
Elliptical	200x10,000	30
Circular 5000	50,000	90
Elliptical	200x10,000	30
Circular 500	500	102
Circular 200	200	30

Table 1.2: Ganymede science phase: sub-phases.

Of course, from a scientific point of view, the circular polar orbit phases at low altitudes will be the most interesting. The spacecraft will be able to complete several orbits around the satellite, gathering a great deal of science data.

The end of the mission, as scheduled, will be in 2033: the spacecraft will crash onto Ganymede surface at the end of the last science phase. Since the probe equipment does not include radioactive sources, the thermal condition would not compromise the environment of the satellite.

1.2.3 The spacecraft

Being the mission in its A/B1 phase, the spacecraft design is still only a concept. So far, three independent studies have been conducted by different industrial possible contractors. For the sake of this particular work, I chose to briefly describe one of these configurations, since the impact on the numerical simulations of the radio science experiment is limited, although a good model of the spacecraft would help assessing the effect of non-gravitational forces on the trajectory of the probe. In general, the main drivers of the spacecraft development can be summarized as (ESA, 2011):

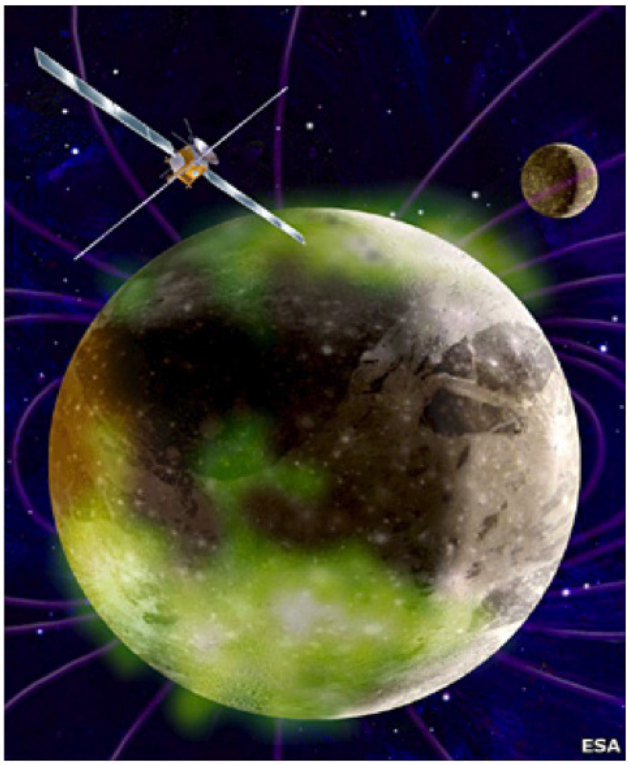

Figure 1.8: Artistic view of Ganymede and the spacecraft (ESA, 2011). Image credit: ESA.

- great distance from the Sun and the Earth;
- use of solar power generation;
- Jupiter's severe radiation environment;

The most strict constrains are then (ESA, 2011):

- high ΔV requirement that leads to a high wet/dry mass ration;
- maximization of the diameter of the high gain antenna (HGA) for maximum science return;
- use of large solar arrays (60-75m^2);
- maximization of the shielding efficiency;

The main structure is built around the propulsion sub-system. One main MON tank will be mounted inside a central cylinder, with the four

MMH tanks around it, providing a total thrust of 400 N. Two auxiliary helium tanks will also be included for pressurization, for an overall propellant mass around 2400 kg. The payload will be located in a separate box, so that the compactness of the allocation will work as additional shielding of the onboard instruments. The 3.2m high-gain antenna will be mounted on top of the spacecraft, with the axis along +X direction (Figure 1.9).

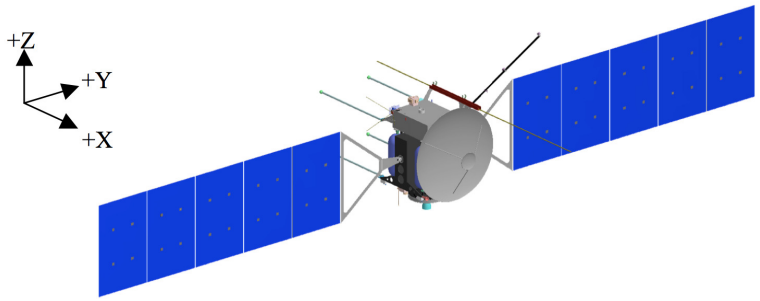

Figure 1.9: Spacecraft configuration as seen in solution 3. The +Z direction represents the nadir direction. (ESA, 2011). Image credit: ESA

The solar arrays will be aligned with the Y direction, providing an overall exposed area of 64 m^2. The box containing all instruments will be allocated at the +Z panel, with the remote sensing instruments aligned with the nadir direction and the *in situ* instruments mounted on the -X panel. Using this disposition there is no need to change the spacecraft orientation with respect to the flight direction in between remote and *in situ* observations (ESA, 2011).

In this configuration, the overall size of the spacecraft will be 3.52 m x 2.76 m x 3.47 m, with a wing span, after the solar arrays deployment of 27.5 m (ESA, 2011). The maximum dry and wet mass at launch would be 1255.1 kg and 4078.9 kg, respectively, with a w/d ratio of 3.25 (ESA, 2011).

JUICE will be three-axis stabilized, the AOCS subsystem allows the orientation of the spacecraft in the desired direction, during communications and observation phases. The subsystem comprises four reaction wheels (maximum capacity of 68 Nm), two star trackers and two Sun trackers. A navigation camera will be used in the most critical passages. Correction maneuvers and de-saturation of the wheels will be operated by the thrusters (10 N each, ESA, 2011).

The inclusion of Europa science case, has overloaded the already difficult prospect on the radiation environment, to which JUICE will be subjected. The total radiation dose absorbed by the spacecraft depends mostly on the total electron fluence over the different mission phases (Figure 1.10).

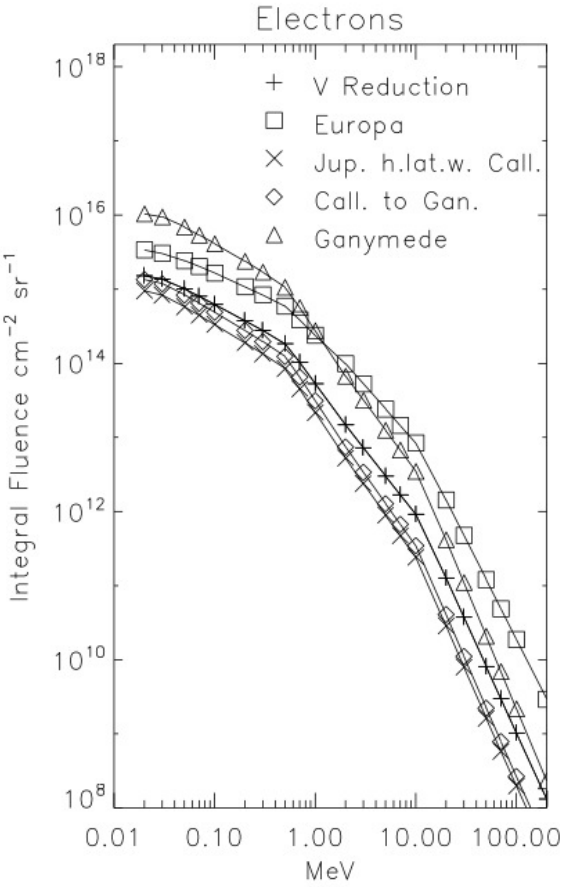

Figure 1.10: Fluence spectrum of electrons, divided by mission phases. (ESA, 2011). Image credit: ESA.

The most severe conditions are found during the phases that bring the spacecraft close to Jupiter. The energy spectrum of such electrons span between 0.01 and 10,000 MeV. Higher energy means higher frequency, thus deeper penetration into the structure. Consequently, a thick shielding (10-15mm Al) of the instruments and electronic components will be needed. The total radiation dose, absorbed over the entire duration of the mission, inside a 10 mm solid Al sphere would be around 240 krad. Furthermore, possible employment of high Z materials such as tantalum or tungsten is

being considered, implying a remarkable reduction of the shielding mass (ESA, 2011).

1.2.4 Payload

In February 2013 the European Space Agency selected the instruments to carry onboard the JUICE mission. The payload comprises 11 scientific experiments, involving many European countries and also contributions from the US and Japan. The onboard experiments can be divided into two main categories: the remote sensing package and the *in situ* package. Actually, the classification is a bit more complicated than that, in particular we can differentiate between:

- remote sensing package:
  - spectro-imaging instruments, from UV to NIR;
  - camera package;
  - sub-millimeter wave instrument;
  - radio science instruments;
- geophysical package:
  - laser altimeter;
  - ice penetrating radar;
  - radio science instruments;
- *in situ* package:
  - magnetometer;
  - radio and plasma wave instrument;
  - particle package;

The choice of the payload has been made by ESA Science Study Team (SST) so that the mission scientific return is maximized. Table 1.3 contains a list of the instruments with a brief description of their scientific objectives and characteristics, while Figure 1.11 shows the allocation of the instruments for the chosen configuration.

Instrument	Classification	Scientific Objectives and characteristics
JANUS	Camera system	Global, regional and local imaging of Ganymede, Callisto and Europa. Mapping of the clouds on Jupiter. Use of 13 filters; FoV = $1.3°$; Spatial resolution up to 2.4 m on Ganymede and about 10 km at Jupiter.
GALA	Laser Altimeter	Measure of the satellites' topographies. Measure of Ganymede's tidal deformations. 20 m spot size; 0.1 m vertical resolution at 200 km.
RIME	Ice Penetrating Radar	Identification of the satellites' strati-graphic and structural subsurface patterns. Resolution down to 9 km depth with vertical resolution of up to 30 m in ice.
3GM	Radio Science Experiment	Investigation of the interior structure of Ganymede, Callisto and Europa through the determination of their gravity fields. Verify the presence of subsurface oceans by measuring their tidal response. 2-way Doppler and ranging with Ka-band transponder; 1-way Doppler at X-and Ka-band with Ultra-stable Oscillator.
MAJIS	Imaging Spectrometer	Characterization of ices and minerals on the surfaces of icy moons. Observations of tropospheric clouds features and minor species on Jupiter. λ = 0.4 $\div$ 5.7 μm; Spectral resolution of 3-7 nm; Spatial resolution up to 25 m on Ganymede and about 100 km on Jupiter.
UVS	UV imaging Spectrograph	Characterization of the composition and dynamics of the exospheres of the icy moons. Study of the Jovian auroras. Investigation of the composition and structure of Jupiter's upper atmosphere. Nadir observations and solar and stellar occultation sounding; λ = 55 $\div$ 210 nm; Spectral resolution ¡0.6 nm; Spatial resolution up to 0.5 km at Ganymede and up to 250 km at Jupiter.

SWI	Sub-millimeter Wave Instrument	Direct measure of Jupiter's atmospheric vertical profile (velocity, composition and temperature). Heterodyne spectrometer using a 30 cm antenna and working in two spectral ranges 1080-1275 GHz and 530-601 GHz with spectral resolving power of 10^7.
J-MAG	Magnetometer	Characterization of the Jovian magnetic field, Study of its interaction with the intrinsic magnetic field of Ganymede. Study of possible induced magnetic field signatures due to subsurface oceans on the icy moons. Use of fluxgates (inbound and outbound) sensors mounted on a boom.
PEP	Particle Environment Package	Characterization of the plasma environment in the Jovian system. Measure of the density and fluxes of positive and negative ions, electrons, exospheric neutral gas, thermal plasma and energetic neutral atoms in the energy range from < 0.001 eV to > 1 MeV with full angular coverage. The composition of the moons' exospheres will be measured with a resolving power of more than 1000.
RPWI	Radio & Plasma Wave Investigation	Characterization of the radio emission and plasma environment of Jupiter and its icy moons. Use of a set of sensors, including two Langmuir probes to measure DC electric field vectors up to a frequency of 1.6 MHz; use of antennas to measure electric and magnetic fields in radio emission in the frequency range 80 kHz- 45 MHz.
PRIDE	Planetary Radio Interferometer & Doppler Experiment	Use of standard telecommunication system of the JUICE spacecraft and VLBI - Very Long Baseline Interferometry - to perform precise measurements of the spacecraft position and velocity.

Table 1.3: JUICE payload (ESA, 2011), (ESA, 2013a).

The radio science package is the core of the gravity experiment, for this reason an additional section will be dedicated to the description of the involved instruments (see Section 1.4).

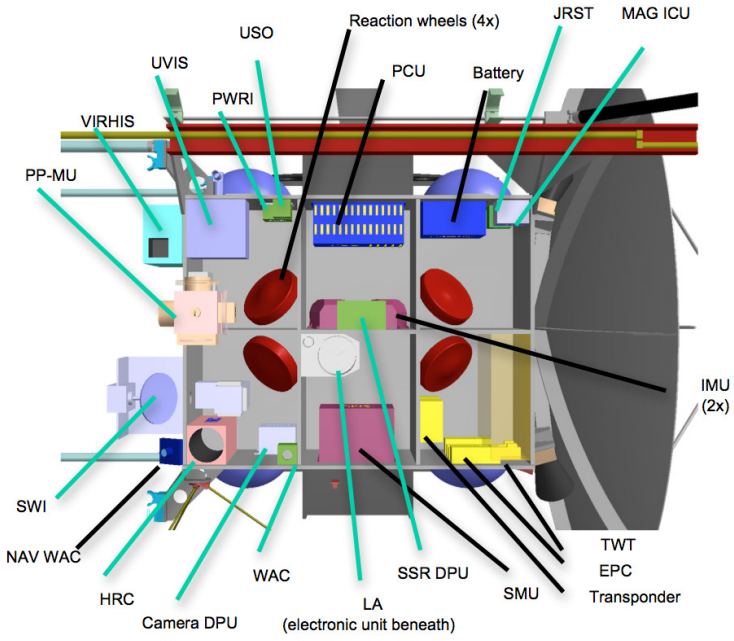

Figure 1.11: JUICE payload configuration (ESA, 2011). Image credit: ESA.

1.3 Planetary targets of the gravity experiments

The reasons why the scientific community has decided to fly so many missions with the intent of exploring Jupiter and its system, are numerous and heterogeneous. Truth is, the gas giant is home to physical conditions and phenomena unique in the solar system, that are not only worth being observed, but also deeply investigated.

The purpose of this subsection is to provide basic information about the planet and its satellites that are relevant to the Juno and JUICE missions and their gravity experiments.

1.3.1 Jupiter

Jupiter is, very likely, the first planet to have formed in the solar system, besides being the largest. As other gas giants, its composition is very rich in light elements such as hydrogen ($>$ 87% of the total mass) and helium, very much like the Sun, although heavy elements (mostly oxygen) are present in greater quantities (Bagenal *et al.*, 2004).

Jupiter is a striped huge spherical body without topography (Bagenal *et al.*, 2004), whose atmosphere is the vastest in the solar system, governed by strong east-west winds (NASA, 2011). The horizontal bands are traditionally divided into zones (white bands) and belts (dark bands) which rotate the opposite way. The winds generate giant long-lasting storms, the greatest is known as the Great Red Spot and spins near Jupiter's equator. The clouds are made mostly of ammonia while water concentrations can be found at depth. The boundaries between atmosphere and deeper layers are not well-defined, conventionally the atmosphere extends down to a pressure of 20 bar (Seiff *et al.*, 1998). The planet is the fastest spinner of the solar system, its day lasting only 9.9 hours on average, in fact the rotation period is 5 minutes longer at the poles than at the equator, making Jupiter a differential rotator.

Figure 1.12: Jupiter with the visible Great Red Spot. Image credit: NASA.

As the depth increases, pressure and temperature rise, allowing the

change of state of the hydrogen, which becomes electrically conductive and behaves like a metal. Considering that Jupiter spins exceptionally fast, this phenomenon generates the impressive magnetic field, characteristic of the planet (NASA, 2011). Auroras take place on Jupiter, very similarly to what happens in some regions of the Earth, yet the phenomenon is much more powerful and amplified. Jupiter's magnetic field traps great quantities of electrons and ions that are accelerated, creating immense electrics current and thus, the auroras (NASA, 2011).

The current knowledge of the interior structure of Jupiter envisages a radial division into three main layers (Bagenal *et al.*, 2004). From top to bottom (Figure 1.13) these are:

- a helium-poor molecular hydrogen envelope which includes the atmosphere;
- deeper, a helium-rich metallic hydrogen envelope;
- a central dense liquid core of uncertain composition.

The upper atmosphere deficiency of helium can be explained by its separation into metallic hydrogen that takes place at depth, though this hypothesis requires the presence of a deeper helium-rich region. The two regions are homogeneous in composition thanks to convective phenomena and are separated by a narrow in-homogeneous region in which helium demixing occurs (Bagenal *et al.*, 2004). The extent and position of this region remains a key question about the planet's interior. The measure of Jupiter's gravitational moments postulates the presence of a dense core, though its compositions and structure is still unknown (Bagenal *et al.*, 2004).

The task of the new missions to Jupiter, regarding the interior of the planet, is to constrain three fundamental parameters:

- the mass of the core;
- the mass mixing ratio of heavy elements in the molecular region;
- the mass mixing ratio of heavy elements in the metallic region.

For centuries Saturn has been, in the collective imagination, the only planet to possess rings. In truth, fainter rings formed also around Jupiter

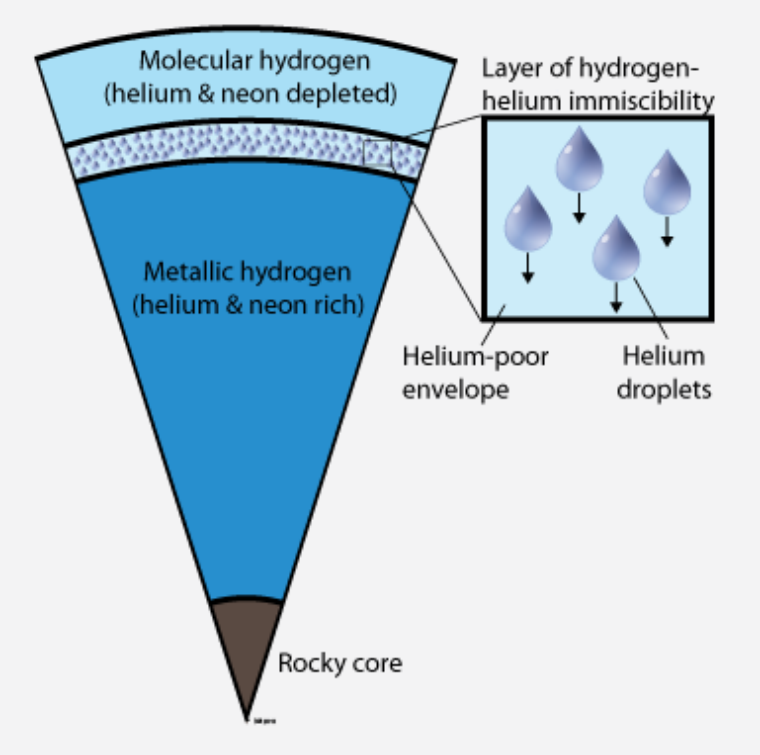

Figure 1.13: View of Jupiter's interior. Image credit: Burkhard Militzer at University of California, Berkeley.

equatorial belt, consisting of thin dusts related to the formation of its biggest moons (NASA, 2011).

1.3.2 Ganymede

Ganymede is the largest natural satellite of the solar system with a mean radius of 2631.2 $\pm$ 1.7 km (Bagenal *et al.*, 2004), is larger than Mercury and its size is about three quarters of that of Mars. This moons is the typical icy satellite composed of mostly water and silicates.

Early gravity measurements indicate a mean density for Ganymede of 1942.0 $\pm$ 4.8 kg/m^3 (Bagenal *et al.*, 2004), pointing to a partial differentiation of the satellite between the icy surface and the rocky core (McKinnon and Parmentier, 1986, Schubert *et al.*, 1986). Moreover, the presence of a self-generated magnetic field suggests that the differentiation process has gone even further, leading to a three-layer model: water-ice shell, a rock mantle and a metallic core (Schubert *et al.*, 1996). Crary and Bagenal (1998)

pointed out that, even rock cores that have high magnetic susceptibility (because rich in magnetite) cannot be sufficiently magnetized by the external Jovian field. Thus they indicate the metallic core as the possible and more plausible cause of Ganymede's intrinsic magnetic field. Also, Schubert *et al*. (1986) concluded that the mentioned magnetic field is generated by dynamo action in a liquid or partially liquid metallic core. In both cases a metallic core for Ganymede is required.

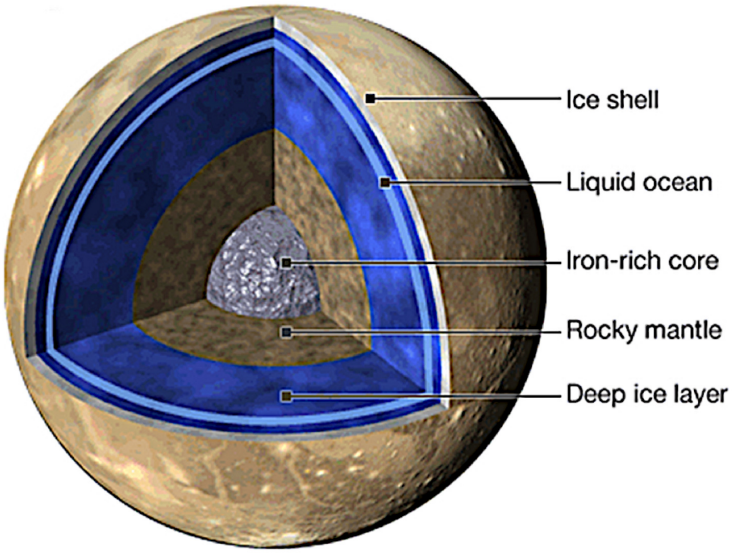

Figure 1.14: View of the interior structure of Ganymede. Image credit: NASA.

The Galileo mission collected several pieces of evidence for a subsurface ocean at Ganymede (Kivelson *et al*., 2002). The spacecraft detected an induced magnetic field at shallow depths (100-200 km underneath Ganymede's surface) in response to the huge Jovian magnetosphere, usually associated to the presence of salty, conductive liquid water (Kivelson *et al*., 2002). However the interpretation of the magnetometer data proved quite challenging, due to interference from Ganymede's intrinsic magnetic field. Still, the evolution model of Ganymede based on its topography is compatible with a subsurface, salty, conductive ocean amidst two high-pressure ice layers. Nonetheless, its composition, location and extension are still unknown. A solid detection of a global ocean requires the measure of its tidal deformation, whose entity would be much larger in case of presence of liquid layers. Only gravitational measurements collected by a dedicated

space mission to Jupiter's moon will confirm the existence of liquid water reservoirs, local or global, within Ganymede's surface layer.

Ganymede possesses sufficient mass to attract and retain a thin atmosphere. The Hubble telescope has detected the presence of atomic oxygen by means of Far Ultra Violet (FUV) observations (λ = 130.4 - 135.6 nm). The atomic oxygen results from the dissociation of molecular oxygen, which is the dominant species of the atmosphere, due to incident collisions with free electrons. The column density of Ganymede's atmosphere probably ranges between $1 \div 10 \cdot 10^{14}$ cm^{-2} (Hall *et al.*, 1998). In turn, the molecular oxygen might come from the dissociation of water molecules on Ganymede's surface, as a result of incident radiation. The hydrogen is, on the other hand, scattered because of its small density.

1.3.3 Callisto

Callisto is the outermost of the Galilean moons, its mean radius is about 200 km smaller than Ganymede's, and its density is very similar to that of the bigger moon, being 1834.4 ± 3.4 kg/m^3 (Bagenal *et al.*, 2004).

Callisto formation occurred after Jupiter's cooling, allowing the consolidation of water masses into ice and preventing the vaporization of volatile elements. Callisto surface is ancient, dark, heavily cratered and, unlike Ganymede, shows no evidence for geological internal activity. This kind of information led to the conclusion that Callisto was undifferentiated (Schubert *et al.*, 1981, 1986). However, gravity measurements from the Galileo mission indicated that Callisto interior was, at least partially, differentiated (Anderson *et al.*, 1998, 2001). Even more surprisingly, magnetometer observations detected signatures characteristic of an induced magnetic field, evidence for a subsurface ocean at Callisto (Zimmer *et al.*, 2000). Despite the apparent lack of internal activity, the high-resolution camera onboard Galileo, revealed the presence of erosion and degradation processes on the surface of Callisto. These phenomena are caused by the exposition to the severe and highly-corrosive Jovian environment, giving Callisto the characteristic lumpy look.

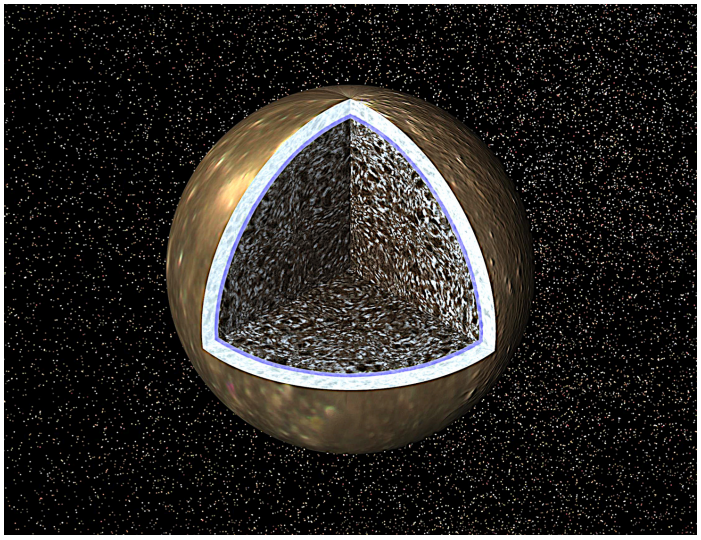

Figure 1.15: View of the interior structure of Callisto. Image credit: NASA/JPL-Caltech.

A simple layered model has been proposed for Callisto, consisting of (Bagenal *et al.*, 2004):

- a denser (more rock and dense-ice-phase rich) interior;

- a less rock-rich and more low-density ice-polymorph-rich shell;

The depth at which the layers differentiate obviously depends on the mean densities. The upper limit of the interior density is that of a cool, undifferentiated and dehydrated rock+metal (3850 kg/m^3). This condition would set the extension of the outer shell to 1250 km, while the lower limit is represented by the case of a clean-ice shell with or without a water ocean, for an extension of 300 km (Bagenal *et al.*, 2004).

The existence of this two-layer model is legitimated by the fact that ice and rock can separate either by melting of the ice or by sinking of the rocks through ice. Considering the latter phenomenon, a rocky core could form, surrounded by a rock+ice layer and an outer shell, leading to a three-layer model (Mueller and McKinnon, 1988). In this model, the core of Callisto is composed of (18$\pm$ 4) % of its total rock and extends up to 900 km in radius (Bagenal *et al.*, 2004). The ocean would lay between the rock+ice layer and the pure ice shell, where thermal conditions leading to the melting of ice operate at the ice minimum-melting temperature.

1.3.4 Europa

The size of this satellite makes it the smallest among the Galilean satellites, despite that, Europa is, perhaps, the most interesting body in the Jovian system. Unfortunately the harsh radiation environment makes its exploration very challenging. The estimated mean radius is 1565.0 ± 8.0 km, for a mean density of 2989 ± 46 kg/m^3 (Bagenal *et al.*, 2004).

Gravity measurements collected by the Galileo spacecraft show that the satellite is likely to be differentiated and a three-layer model has been proposed, consisting of (Anderson *et al.*, 1997):

- a metallic core (mostly iron);

- a silicate mantle;

- a water ice-liquid outer shell.

As always, gravity interpretations are not unique and there still is uncertainty on the state of the core and the outer shell, that could be either solid or fluid. For instance the interior could be composed of a mixture of silicates and metal, surrounded by an ice-water shell (Bagenal *et al.*, 2004). For the latter, a mean density of 1050 kg/m^3 is assumed, while for the core two different options exist (Bagenal *et al.*, 2004):

a) a *Fe* core of density 8000 kg/m^3, in this case the radius of the core could be only as large as 13% of Europa radius if the ice shell is 170 km thick;

b) a *Fe-FeS* core of density 5150 kg/m^3, corresponding to a core radius as large as 45% of Europa radius, with 100 km thickness of ice.

Given the uncertainty on the composition of the mantle, it is not possible to set a lower bound on the radius of the core, however, the density of this mid layer must be at least 3800 kg/m^3, implying that the mixture must be rich in metal and cannot be purely rock (Bagenal *et al.*, 2004). Furthermore, supposing the mantle density is at least 3000 kg/m^3, the outer shell must be at least as thick as 80 km, in order to fulfill the constraint on the mean density.

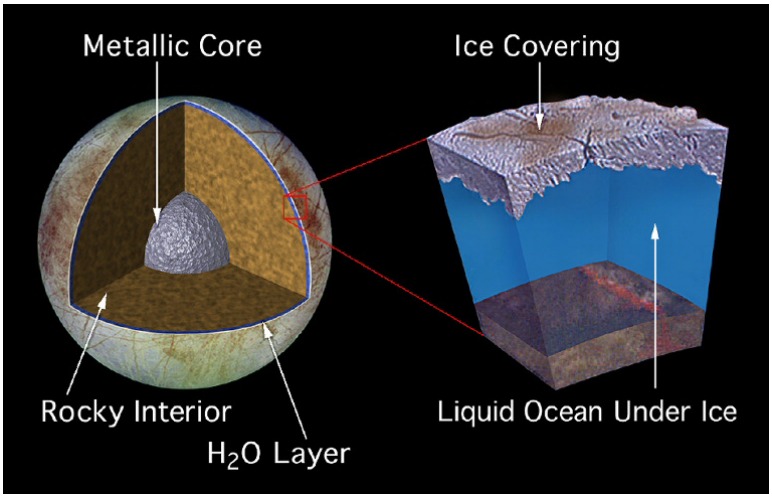

Figure 1.16: View of the interior structure of Europa. Image credit: NASA/JPL-Caltech.

Galileo magnetometer observations have not detected an intrinsic magnetic field at Europa (Schilling *et al.*, 2004), thus they do not provide information about the state of the core (Bagenal *et al.*, 2004). The generation of an internal magnetic field requires the core to be at least partially molten, however, the lack of dynamo action does not exclude a liquid core, in fact this could still be fluid but non convective (Bagenal *et al.*, 2004).

Different conclusions can be drawn regarding the state of the outer shell, in fact observations have demonstrated that Europa responds to the time-variant magnetic field of Jupiter producing internal electric currents (Bagenal *et al.*, 2004). In turn, these currents produce an induced magnetic field, providing information on the electrical conductivity, depth and thickness of the conductive region within Europa. Zimmer *et al.* (2000) located this region within 200 km of the surface, with an electrical conductivity compatible with that of sea water, postulating the presence of a subsurface ocean at Europa (see Figure 1.16).

1.4 Radio science experiments

Radio science experiments (RSE) exploit the radio-frequency link between a spacecraft and ground stations, in order to determine crucial parameters related to physical properties of a celestial body. In general, the

main scientific goals pursued by this kind of experiments can be summarized as:

- determination of a planetary gravity field;

- study of a planetary surface;

- study of a planetary atmosphere.

In the frame of this work, this section will be dedicated to the implementation of gravity experiments onboard recent missions to the Jupiter system. By means of radiometric observations, one can determine several parameters characterizing planetary gravity fields and providing information on the interior models and structures of celestial bodies. To this end, changes in phase, frequency and polarization of a microwave signal are analyzed and interpreted.

The success of gravity experiments strongly depends on technical characteristics of the onboard and ground equipment, but also on optimal mission conditions. In the following subsections, a detailed description of the instruments composing the radio science system will be provided.

1.4.1 Space segment

The key onboard instrument of a state-of-the-art radio science experiment is the Ka-band transponder, which is able to establish radio links with ground characterized by high phase stability. The crucial innovative aspect of the newest experiments is the exploitation of the Ka-band of the electromagnetic spectrum (26.5 - 40.0 GHz), both in up-link and down-link. The transponder can also operate in a multi-frequency configuration (with X-band links, 7.0 to 11.2 GHz), so as to make possible the total cancellation of plasma noise in critical conditions, such as solar conjunctions (see Section 3.3.2).

In the triple-link configuration, two uplink and three downlink carrier signals are employed at the same time:

- X-band (8.4 GHz) downlink and X-band (7.2 GHz) uplink;

- Ka-band (32.5 GHz) downlink and X-band (7.2 GHz) uplink;

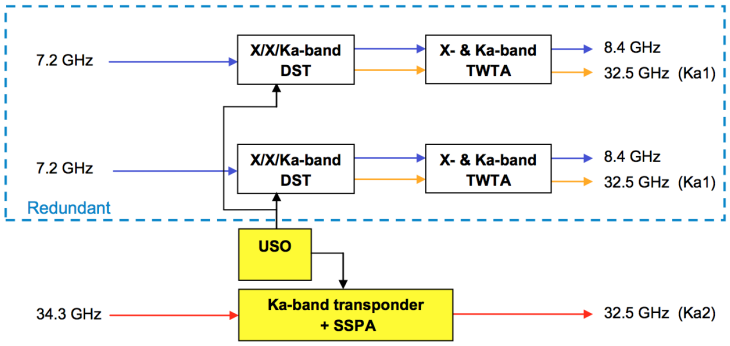

Figure 1.17: Triple-link configuration of the Ka-band transponder (ESA, 2011).

- Ka-band (32.5 GHz) downlink and Ka-band (34.0 GHz) uplink.

The main link used for gravity science investigation is the Ka-Ka link. Radiometric measurements are characterized by high accuracies, in particular range-rate measurements (radial velocity of the spacecraft) can be as well resolved as 3μm/s @ 1000 s integration time, while the average accuracy of a range measurement (radial distance of the spacecraft) is about 20 cm for a two-way link.

All measurements must be carried out in a coherent way, using frequency standard characterized by high stability (hydrogen masers) for the generation and conversion of the carrier. The Ka-band transponder supports an innovative wide-band Pseudo Noise (PN) ranging modulation scheme for the carriers (Thales, 2012).

A very important parameter characterizing the Ka-band transponder is the phase stability and the group delay, which is, currently, better than 0.1 ns pk-pk over a time of 36 hours (Thales, 2012). Aging effects on the KaT could degrade the group delay stability, jeopardizing the accuracies on range measurement. The KaT Allan deviation is also indicative of the frequency stability of the instrument. At this stage of development, the Allan deviation is assured to be better than 10^{-15}.

For further information, the technical performance of the KaT can be found in Table 1.4, where information about the mass and power consumption are reported as well (Thales, 2012).

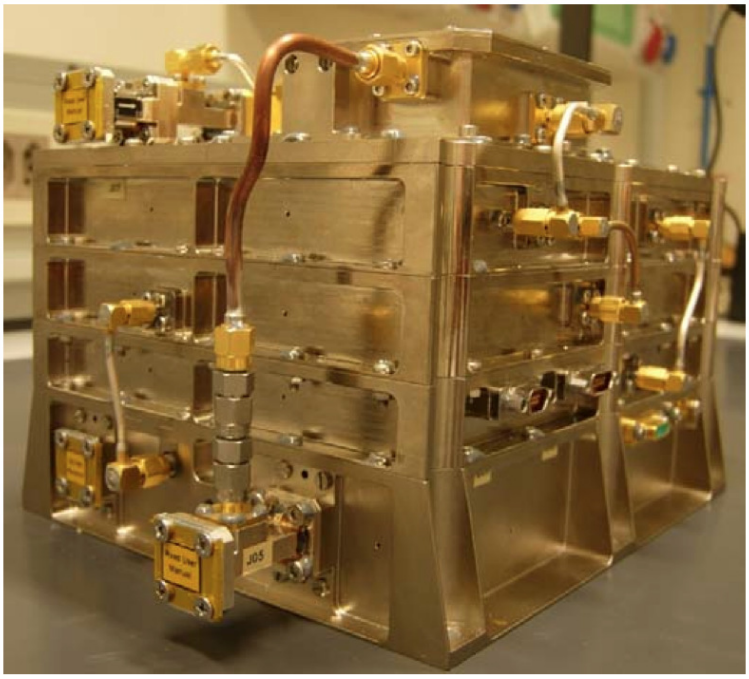

Figure 1.18: The Ka-band transponder (Thales, 2012). Image credit: Thales Alenia Space.

Mass	3 kg
Power consumption	$<$ 40 W (for 32 dBm output power)
Dimension (LxWxH)	215x140x175 mm
Qualification temperature range	20/+65°C (operative)
Design life	>15 Years
Acquisition threshold	-131 dBm @ 4 kHz/s
Tracking threshold	-135 dBm @ 1.2kHz/s (-138 dBm @ 400 Hz/s)
Turn-around ratio	3360/3599
Output power	Up to 35 dBm @ 32GHz
Allan Deviation	$\leq$4x10^{-16} @ 1000s
Doppler shift	$\pm$6 MHz
Noise figure	<4 dB
PN Ranging Chip rate	up to 25 Mcps
Transparent Ranging BW	27 MHz
Mixed Ranging low-frequency BW	4 MHz
KaT Group-delay stability	¡0.1ns pk-pk

Table 1.4: KaT Technical Typical Performance (Thales, 2012).

1.4.2 Ground segment

An equally important role in the radio science experiments is played by ground stations with which the spacecraft establishes deep space radio links. In this frame the ground segment is composed of NASA's Deep Space Network (DSN) and ESA's Estrack tracking stations.

NASA's DSN is composed of three complexes (DSCC): one in Goldstone (California), one in Robledo (Spain) and one near Camberra (Australia). Each complex has one 70-m diameter station, one 34-m high-efficiency (HEF) station, and at least one 34-m beam-wave-guide (BWG) station (Kliore *et al.*, 2004). Each DSN station comprises several subsystems (see Figure 1.19, all important to the acquisition of radio science data (Kliore *et al.*, 2004):

- monitor and control subsystem: receives and archives information sent to the complex from the control center, handles and displays responses to directives for configuration or information;
- antenna mechanical subsystem: the primary surface is a paraboloid that collects and forms a narrow microwave beam from and to the spacecraft;
- microwave subsystem: accepts the S-, X-, and/or Ka-bands and directs them to low-noise amplifiers, then the amplified signals are down-converted by local oscillators and routed to the receivers;
- receiver-exciter subsystem: the closed-loop receiver is the primary receiver for telemetry and tracking data, it phase-locks to the signal carrier and demodulates science data, engineering data, and ranging signals transmitted by the spacecraft;
- transmitter subsystem: utilizes a frequency reference to synthesize the uplink frequency channel assigned to a specific spacecraft, can transmit at S-, X- or Ka-bands;
- tracking subsystem: measures Doppler shifts and ranging information based on the closed-loop receiver output;
- spectrum processing subsystem;

- frequency and timing subsystem: provides a reference that drives the local oscillator devices throughout the complex.

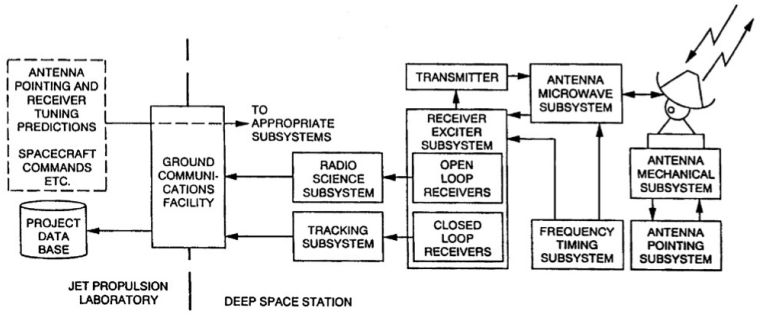

Figure 1.19: DSN subsystems (Kliore *et al.*, 2004).

The 70-m diameter stations are currently equipped for transmission at the S-band frequencies and reception at S- and X-band frequencies. Only one 34-m diameter BWG station in the Californian (DSS 25) complex is instrumented for transmission and reception at Ka-band frequencies, developed to meet stringent Radio Science requirements. It is expected that Ka-band downlink will be available at 34-m BWG stations DSS-54 and DSS-34 in Spain and Australia, respectively (Kliore *et al.*, 2004).

ESA's deep space tracking stations are located in Cebreros (Spain), New Norcia (Australia) and Malargue (Argentina). All complexes are equipped with 35-m diameter antennas which communicate using mostly X-band, while data rates typically range from 256 Kbit/s to 8 Mbit/s, depending on the mission and other factors (ESA, 2013b). ESA had also added Ka-band signal reception capabiliteis at both Cebreros (DSA 2) and Malargue (DSA 3), unblocking larger data rate for future deep space missions (ESA, 2013b).

The antenna design is based on waves guided by multiple mirrors (M1 to M5, see Figure 1.20), reflecting all frequency bands. The M6 and M7 mirrors pass specific ranges of frequencies while reflecting others (ESA, 2013b). The pointing accuracy has been increased to 0.0035° by increasing the mechanical rigidity and installing sensors to compensate for the deformation of the structure due to changes in temperature (ESA, 2013b).

Table 1.5 reports the technical profile of a typical ESA X-band ground station (ESA, 2013b).

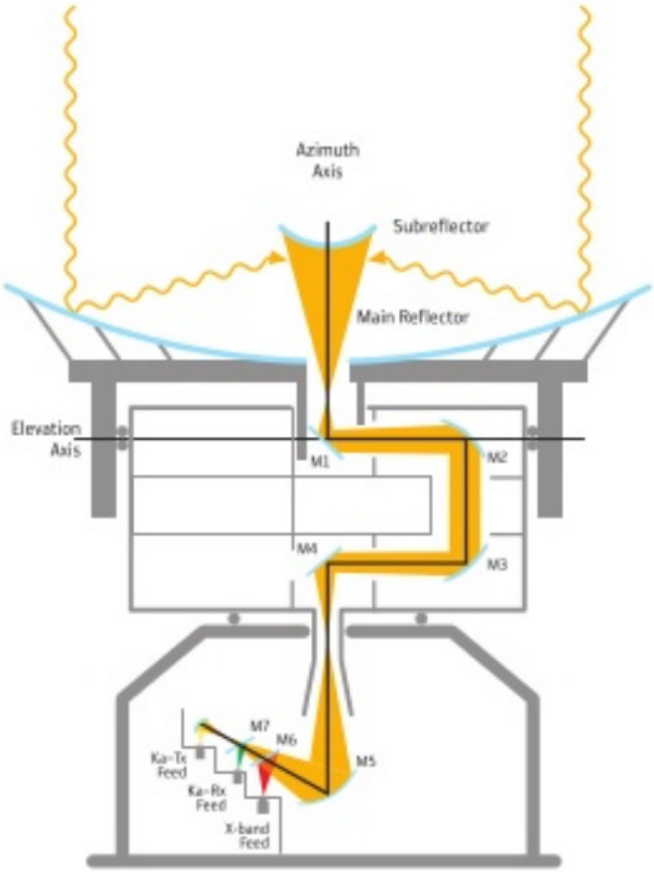

Figure 1.20: DSA diagram (ESA, 2013b).

Antenna dish diameter	35m
Transmit frequency	X-band 7.145-7.235 GHz
Receive frequency	X-band 8.400-8.500 GHz
Telemetry (downlink)	Maximum data rate up to 105 Mbps
Telecommand (up-link)	Normal data rate 2 Kbps
Tracking	Range accuracy 1 m; Range rate accuracy 0.1 mm/s

Table 1.5: DSA technical profile (ESA, 2013b).

In this work it is assumed that Ka-band transmitting capabilities will be available at all DSAs within the next few decades.

1.4.3 Media Calibration system

One of the main sources of phase and amplitude noise for a spacecraft radio signal is the Earth's atmosphere. In particular, Doppler signal are affected by tropospheric noise due to the presence of water vapor in the troposphere, especially at low station elevations, when the signal path increases significantly. For each deep space complex, dual frequency GPS measurements and weather data can be combined to obtain good calibration of the tropospheric delay, at least for the dry component, known as Tracking System Analytical Calibration (TSAC). On the other hand, the wet component of the troposphere is much smaller but much more variable, and unlike plasma noise, propagation in the troposphere is effectively non-dispersive at microwave frequencies (Armstrong, 2008). The experience with the Cassini mission at Saturn, has demonstrated how water vapor radiometer measurements could calibrate and remove much of the tropospheric noise in precision spacecraft Doppler tracking observations (Armstrong, 2008). For this reason, a water-vapor-radiometer-based Advanced Media Calibration (AMC) system was installed near DSS 25 (Armstrong, 2008). In an AMC system, two identical radiometer units are placed close enough to each other and to DSS 25 that the coherence of the tropospheric signal on the time scales of interest was high in all three time series (Armstrong, 2008). The AMC calibrations were used successfully in both the Cassini gravitational wave observations and in relativity and plasma experiments taken near solar conjunction (Armstrong, 2008).

Chapter 2

Basic principles of geophysics

Gravitational and non-gravitational forces influence, sometimes ever so slightly, the spacecraft trajectory as it flies by or orbits a planetary body. Thus, the detection of possible deflections allows the determination of parameters of interest such as those characterizing gravitational fields (Bagenal *et al.*, 2004). The main goal of an onboard gravity experiment is to exploit radiometric measurements, such as Doppler data, to derive the body's mass and gravitational coefficients. To this end, it's most important to define a solid mathematical model able to describe very accurately gravitational actions. This chapter is dedicated to the description of the models used to express a body's gravity field and density distribution.

2.1 Harmonic representation of the gravity field

The real mass distribution of a celestial body generally deviates from the ideal case of spherical symmetry (Bertotti *et al.*, 2003). This status is actually fortunate since the interior structure of a body affects its gravitational potential only if the condition of spherical symmetry is not fulfilled (as in the totality of the cases). The main deviation from sphericity is axisymmetrical and is due to the oblateness of the body (degree 2 gravity field). On the other hand, gravity anomalies corresponding to high-frequency variations of the gravity field, give information about local mass concentrations or deficiencies and are much more sensitive to the decrease of the distance from the body center (Bertotti *et al.*, 2003). One of the main objectives of this chapter is to introduce the spherical harmonic basis, used to represent

the gravitational potential of a body.

2.1.1 Gravitational potential and spherical harmonics

In a generic geometrical point P, external to the body, where no mass is present, the gravitational potential U, satisfies Laplace equation (Bertotti *et al.*, 2003):

$$\nabla^2 U = \frac{\partial^2 U}{\partial x^2} + \frac{\partial^2 U}{\partial y^2} + \frac{\partial^2 U}{\partial z^2} = 0 \tag{2.1}$$

where x, y, z are Cartesian coordinates of a body-fixed reference frame, whose origin is typically chosen in correspondence to the center of mass of the body.

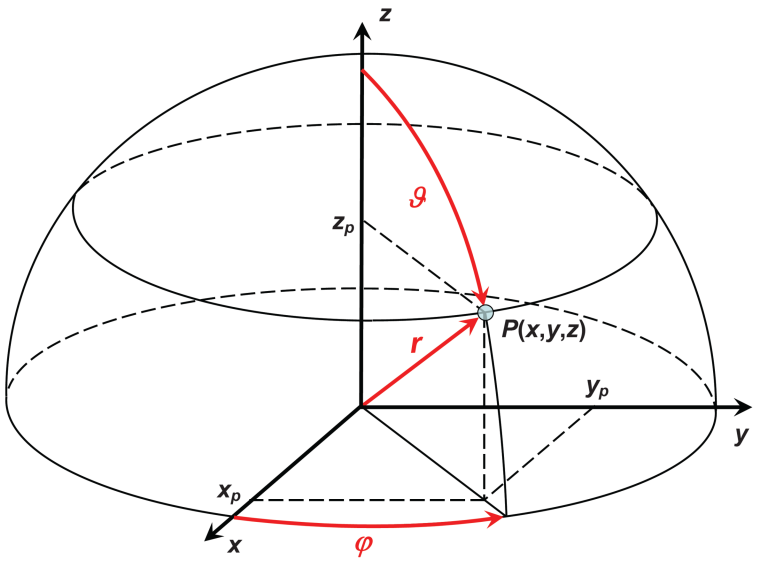

Figure 2.1: Spherical coordinates. Image credit: SEOS Project.

A homogeneous polynomial $p_l(\boldsymbol{r})$ of degree l, fulfills Laplace equation, provided that the coefficients of the polynomial are chosen appropriately. Also, it can be shown that the function:

$$U_l(\boldsymbol{r}) = \frac{p_l(\boldsymbol{r})}{r^{2l+1}} \tag{2.2}$$

satisfies Laplace equation as well (Bertotti *et al.*, 2003), depends only on $\boldsymbol{r}/r$ and is called *spherical harmonic*. It is easily demonstrated that there

are only *2l + 1* independent spherical harmonics of degree *l*, solutions of Laplace equation (Bertotti *et al.*, 2003).

Evidently, the gravitational potential in *P* can be conveniently expanded in series of spherical harmonic functions $Y_{lm}(\theta, \phi)$ of degree *l* and order *m*:

$$U(r) = -\frac{GM}{r} + \delta U = -\frac{GM}{r}\left[1 + \sum_{l\geq 1}\left(\frac{R}{r}\right)^{l}\sum_{m=0}^{l} U_{lm}Y_{lm}(\theta,\phi)\right] \tag{2.3}$$

where *G* is the gravitational constant, *M* is the mass of the body, *R* is the mean radius of the body, *r* is the distance between *P* and the center of the body, θ is the colatitude and ϕ is the longitude. The predominant monopole term $-\frac{GM}{r}$ represents the degree-*0* harmonic. The constants U_{lm} are the spherical harmonic coefficients and the functions Y_{lm} are the surface spherical harmonics:

$$Y_{lm}(\theta,\phi) = P_{lm}(cos\theta)\, e^{im\phi}, \quad l \geq 1, \quad m = 0, .., l \tag{2.4}$$

with P_{lm} un-normalized Associated Legendre polynomials which depend only on $u = (cos\theta)$:

$$P_{lm}(u) = \left(1-u^2\right)^{m/2}\frac{d^m}{du^m}\left[\frac{1}{2^l l!}\frac{d^l}{du^l}\left(u^2-1\right)^l\right], \quad l \geq 1, \quad m = 0, .., l \tag{2.5}$$

2.1.2 Normalization

Since these functions tend to large values as degree increases, while the harmonic coefficients tend to decrease with *l*, it is convenient to adopt a normalization for both the Associated Legendre functions and the harmonic coefficients:

$$\begin{aligned} \bar{P}_{lm}(u) &= N_{lm}P_{lm}(u), \quad l \geq 1, \quad m = 0, .., l \\ \bar{U}_{lm}(u) &= \tfrac{1}{N_{lm}}U_{lm}(u), \quad l \geq 1, \quad m = 0, .., l \end{aligned} \tag{2.6}$$

where:

$$N_{ml} = \sqrt{2-\delta_{m0}}\sqrt{2l+1}\left[\frac{(l-m)!}{(l+m)!}\right], \quad l \geq 1, \quad m = 0, .., l \tag{2.7}$$

The gravitational potential, expressed as an infinite sum of harmonic functions, still satisfies Laplace equation, being it linear. U_l denotes the contribution of degree *l* to the gravitational potential, which tends to 0 when *r* increases indefinitely. The larger is *l*, the more U_l becomes a high-frequency contribution, and the more it decreases dramatically with the *l+1* power of the distance *r*. Thus we can say that:

$$U_l(r) = O\left(\frac{1}{r^{l+1}}\right), \quad l \geq 1 \tag{2.8}$$

Switching from a dimensionless, complex basis to a real one, the gravitational potential in (2.3) can be divided into cosine and sine contributions (Bertotti *et al.*, 2003):

$$U(r) = -\frac{GM}{r}\left[1 + \sum_{l\geq 1}\left(\frac{R}{r}\right)^l \sum_{m=0}^{l} \bar{C}_{lm}\bar{Y}_{lm}^C(\theta,\phi) + \bar{S}_{lm}\bar{Y}_{lm}^S(\theta,\phi)\right] \tag{2.9}$$

where:

$$\begin{aligned} \bar{Y}_{lm}^C(\theta,\phi) &= N_{lm}P_{lm}(cos\theta)\,cos(m\phi), \quad l \geq 1, \quad m = 0,..,l \\ \bar{Y}_{lm}^S(\theta,\phi) &= N_{lm}P_{lm}(cos\theta)\,sin(m\phi), \quad l \geq 1, \quad m = 0,..,l \end{aligned} \tag{2.10}$$

that is the standard representation in geophysics (Bertotti *et al.*, 2003). The relation between the complex and real bases is:

$$\begin{aligned} &\bar{C}_{l0} = \bar{U}_{l0}, \quad l \geq 1 \\ &\bar{C}_{lm} - i\bar{S}_{lm} = \sqrt{2}\bar{U}_{lm}, \quad l \geq 1, \quad m = 0,..,l \end{aligned} \tag{2.11}$$

The harmonics characterized by degree *l* and order *0* are the so-called zonal harmonics and they do not depend on the longitude ϕ. If the harmonics are un-normalized, then the following expression for the coefficients J_l is valid:

$$\sqrt{2l+1}\bar{C}_{l0} = -J_l, \quad l \geq 1 \tag{2.12}$$

2.1.3 Low-degree harmonics

Suppose the origin of the reference frame does not coincide with the body's barycenter for a translation of modulus *a*, then the distance *r* between a generic point and the origin can be expressed as:

$$\frac{1}{r} = \frac{1}{|\boldsymbol{r'} + \boldsymbol{a}|} = \frac{1}{r'}\left[1 - \frac{\boldsymbol{r'} \cdot \boldsymbol{a}}{r'^2} + O\left(\frac{a}{r'}^2\right)\right] \tag{2.13}$$

where r' is the distance in the old reference frame centered at the barycenter. An additional dipole term appears, along with higher order contributions. This means the reference frame can always be optimally chosen (origin in the barycenter) so that the degree-1 coefficients are identically null (Bertotti *et al.*, 2003).

The harmonic of degree *l* and order *m* divides the globe in *(l-m)+1* latitudinal bands (meaning the harmonics has *l-m* zeros) and *2m* longitudinal ones (with *2m* zeros, see Figure 2.2). Aside from the monopole term (*GM*), the quadruple (*l=2*) contribution is the first non-null term in the spherical harmonic expansion, and it is characterized by five coefficients. In particular, the order-0 coefficient, J_2, represents the body oblateness, and its positive for bodies flattened at the poles and negative otherwise (see Figure 2.2).

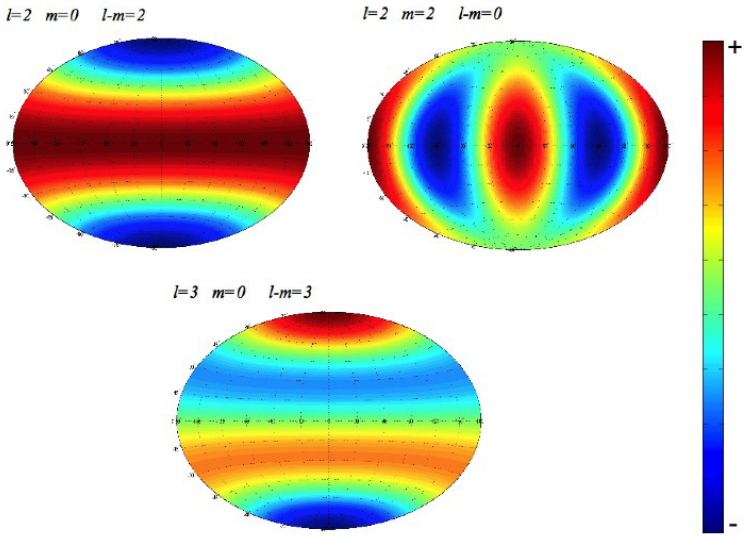

Figure 2.2: Visualization of low-degree spherical harmonics.

The degree and order *2* real coefficient (C_{22}) represents the ellipticity about the equator, it's basically a measure of how much the equator shape deviates form a circumference (Bertotti *et al.*, 2003). Tesseral coefficients C_{21} and S_{21} and sectorial S_{22} are related to the polar motion and in a Cartesian system based on the principal axes of inertia these coefficients vanish

(Bertotti *et al.*, 2003). Also very interesting is the degree 3 and order 0 coefficient J_3, which represents the asymmetry between North and South (Figure 2.2), the so-called superior or inferior *pear* shape.

2.1.4 Kaula's rule

Harmonic coefficients of same degree l tend to be of the same order of magnitude, which generally decreases as l increases (Bertotti *et al.*, 2003). To show this trend, there can be defined coefficients that only depend on l and consists essentially of the sum of the square of the normalized gravity coefficients over the order m:

$$C_l^2 = \frac{1}{2l+1} \sum_m \left(\bar{C}_{lm}^2 + \bar{S}_{lm}^2 \right) \tag{2.14}$$

Kaula (1966) was the first to notice that the decrease in C_l^2 was proportional to the 4^{th} power of l:

$$C_l^2 = A_k \frac{10^{-10}}{l^4}, \qquad l \gg 1 \tag{2.15}$$

this empirical relation has been known as *Kaula's rule* and holds very well for the Earth (with $A_k = 0.7$, Bertotti *et al.*, 2003) and for terrestrial planets in general, provided that $l \gg 1$, although the explanation is not yet known.

2.2 Tides

The gravitational potential of an isolated body is given by (2.9). If an external perturbing body is present, perturbations to this potential can arise: tides, defined as variations in the mass distribution of a non-rigid body due to disturbances exerted by perturbing masses. In the frame of this thesis, I will discuss the case where the distance between two bodies (perturbed and perturbing) is much greater than their mean radii. Hence, the cause of tidal stresses is the differential (tidal) acceleration that exists between two points belonging to the perturbed body.

The study of tidal processes is very important since they are responsible for long-term variations of the body's rotational and orbital elements.

Furthermore, they produce time-variant deformations and energy dissipation within the body.

Let's indicate with subscript *1* the perturbed body and with subscript *2* the perturbing mass. For each object, the equation of motion must hold:

$$\begin{aligned} \ddot{\boldsymbol{r}}_1 &= -\boldsymbol{\nabla} U\left(\boldsymbol{r}_1\right) \\ \ddot{\boldsymbol{r}}_2 &= -\boldsymbol{\nabla} U\left(\boldsymbol{r}_2\right) \end{aligned} \tag{2.16}$$

here $\boldsymbol{r}_1$ ($\boldsymbol{r}_2$) is the distance between the origin of the chosen reference frame and the center of the perturbed (perturbing) body. By subtracting the two equations in 2.16 one gets:

$$\ddot{\boldsymbol{r}}_2 - \ddot{\boldsymbol{r}}_1 = \ddot{\boldsymbol{r}} = -\boldsymbol{\nabla} U\left(\boldsymbol{r}_2\right) + \boldsymbol{\nabla} U\left(\boldsymbol{r}_1\right) \tag{2.17}$$

where **r** is the relative distance between bodies *1* and *2*. One can expand the gravitational potential of the perturbing body at the first order around the potential of the perturbed body (Bertotti *et al.*, 2003):

$$\ddot{\boldsymbol{r}} = -\boldsymbol{r} \cdot \boldsymbol{\nabla} \boldsymbol{\nabla} U\left(\boldsymbol{r}_1\right) + O\left(r^2\right) \tag{2.18}$$

The relative motion between the two bodies depends only on the initial position and velocity and not on their masses. Figure 2.3 shows that tides are caused by the differential force per unit mass existing between a generic point which belongs to the body and its barycenter. The maximum tidal stress within a body can be found on two points of its surface, along the conjunction line between the bodies' barycenters. Intuitively, tidal deformations are also maximum in correspondence to this points and are axisimmetrically distributed about this direction (Bertotti *et al.*, 2003).

Each point is subjected to two opposite actions: on one hand there's the tidal stress exerted by the external body, on the other hand there's the body's own gravitational acceleration.

If the body of mass M_p is not completely rigid, one can approximately estimate the entity of the tidal effect by computing the ratio of the tidal displacement h_T of the perturbed body to its mean radius R_p (Bertotti *et al.*, 2003):

$$\frac{h_T}{R_p} \approx \frac{m}{M_p} \left(\frac{R_p}{R}\right)^3 \tag{2.19}$$

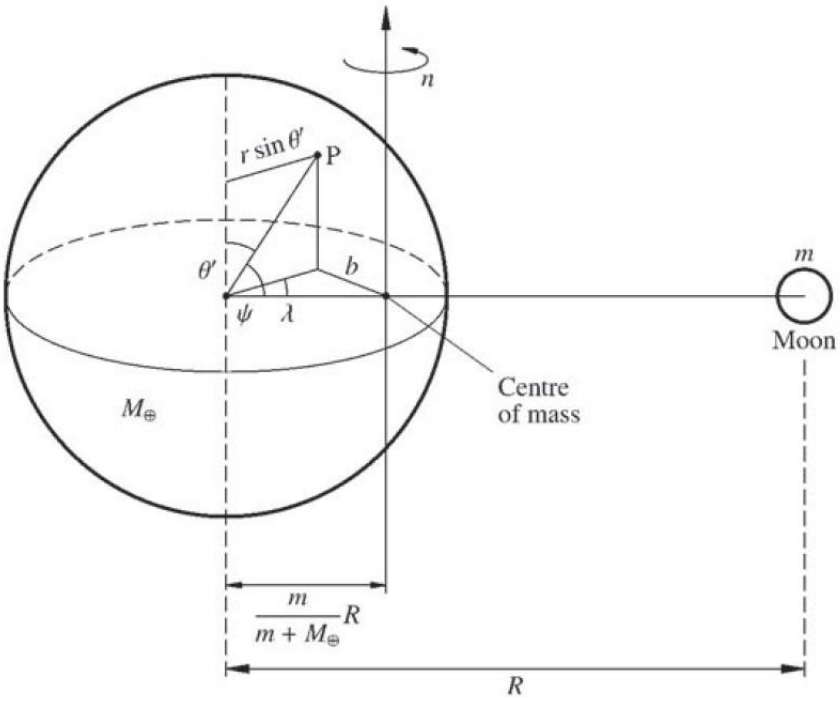

Figure 2.3: Tidal effects on the perturbed body. (Bertotti *et al.*, 2003).

known as the tidal parameter (m is the mass of the perturbing body). If the body is made of fluid, the work done by the two actions are of the same order of magnitude.

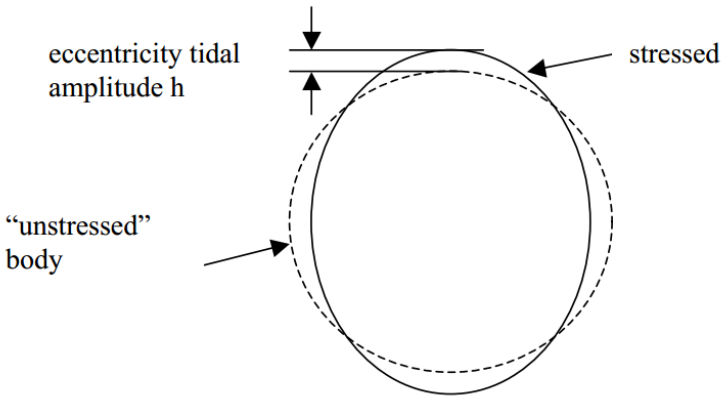

Figure 2.4: Tidal displacement. Image credit: David J. Stevenson, Notes of Planetary Structure and Evolution, California Institute of Technology.

2.2.1 Tidal potential

Suppose the perturbing body is characterized by a mean motion n and that the rotational axis passes through its center of mass and is also perpendicular to its orbital plane. Then the external potential U at a point P located on the surface of the perturbed body and caused by the external mass is (Bertotti *et al.*, 2003):

$$U = -\frac{Gm}{\mid \boldsymbol{R} - \boldsymbol{r} \mid} - \frac{1}{2} n^2 b^2 \tag{2.20}$$

where b is the distance between P and the rotation axis. The potential is the sum of two contributions: the gravitational attraction and the rotational energy.

Before it has been assumed that $r \ll R$, then it is possible to use the expansion for the term $\mid \boldsymbol{R} - \boldsymbol{r} \mid$:

$$\frac{1}{\mid \boldsymbol{R} - \boldsymbol{r} \mid} = \frac{1}{R} \sum_{l \leq 0} \left(\frac{r}{R} \right)^l P_l \left(cos\psi \right) \tag{2.21}$$

where ψ is the angle between **r** and **R** (Figure 2.3). It's very easy to show that:

$$cos\psi = cos\theta' cos\lambda \tag{2.22}$$

where θ' is the colatitude of P with respect to the perturbing body orbital plane and λ is its longitude from the point where **R** pierces the perturbed body surface. Using Carnot theorem (Bertotti *et al.*, 2003):

$$b^2 = \left(\frac{mR}{m + M_p} \right)^2 + \left(rsin\theta' \right)^2 - 2 \left(\frac{mR}{m + M_p} \right) rcos\psi \tag{2.23}$$

By applying Kepler's third law to the system (perturbing + perturbed) one gets:

$$n^3 R^3 = G \left(M_p + m \right) \tag{2.24}$$

Putting equations (2.23) and (2.24) into equation (2.20) one gets (Bertotti *et al.*, 2003):

$$U = -\frac{Gm}{R}\left(1 + \frac{1}{2}\frac{m}{m+M_p}\right) - \frac{1}{2}n^2r^2sin^2\theta' - \frac{Gm}{R}\sum_{l\leq 2}\left(\frac{r}{R}\right)^l P_l\left(cos\psi\right) \tag{2.25}$$

The second term represents the rotational potential about the axis through the perturbed body barycenter and normal to its orbital plane. The effect of this term is to produce a permanent equatorial bulge and perturbing the quadrupole field.

The last term is the most important for the analysis carried out in this work, it represents the *tidal potential*. Since $r/R \ll 1$, the largest term of the perturbing gravitational potential is the quadrupole term (Bertotti *et al.*, 2003):

$$U_2 = -\frac{Gm}{R}\left(\frac{r}{R}\right)^2 P_2\left(cos\psi\right) = -\frac{Gm}{2R}\left(\frac{r}{R}\right)^2\left(3cos^2\psi - 1\right) \tag{2.26}$$

Due to this perturbation, the body's equipotential surfaces are deformed in prolate ellipsoids, axisymmetric around the line connecting the centers of the two bodies.

It is useful to get an idea of the order of magnitude of the phenomenon of tides. If the planetary body is rigid, then it doesn't respond to the perturbation of an external body by deforming or changing its mass distribution. However, a variation of the surface gravity due to tidal phenomena exists and is of order (Bertotti *et al.*, 2003):

$$\frac{\delta g_R}{g} = \left(\frac{R_p^2}{GM_p}\right)\left(-\frac{\partial U_2}{\partial r}\right)_{r=R_p} = -\frac{m}{M_p}\left(\frac{R_p}{R}\right)^3\left(3cos^2\psi - 1\right) \tag{2.27}$$

As an example, for the Earth-Moon tidal system, this number is approximately 10^{-7}. In addition, the equipotential surfaces are subject to a variation in their height of about (Bertotti *et al.*, 2003):

$$\delta h_R = \frac{U_2}{g} = \frac{1}{2}\frac{m}{M_p}\left(\frac{R_p}{R}\right)^3 R_p\left(3cos^2\psi - 1\right) \tag{2.28}$$

of order 1 m for the Earth-Moon system.

2.2.2 Love numbers

If the body is non perfectly rigid, then the presence of tidal stresses will result in the deformation of the body itself. The perturbing external potential on the surface of the body is denoted with $U_2\left(R_p\right)$, and causes variations in the shape of the perturbed body. This deformation will cause, in turn, variation in the gravitational potential of the body, denoted with $U_T\left(R_p\right)$ (Bertotti *et al.*, 2003).

In the case where $R \gg R_p$, we can assume that U_2 and U_T are linearly related:

$$U_T\left(R_p\right) = k_2 U_2\left(R_p\right) \tag{2.29}$$

by the coefficient k_2. Analogously, the ratio of total tidal deformation δh_T to δh_R defines:

$$h_2 = \frac{\delta h_T}{\delta h_R} \tag{2.30}$$

These two parameters are referred to as *Love numbers* of degree-2. From equations (2.28) and (2.30) (Bertotti *et al.*, 2003):

$$\delta h_T = h_2 \frac{U_2}{g} \tag{2.31}$$

In principle, the presence of a perturbing tidal potential gives rise to variations in the body's potential U_T at all degrees and orders, although in this work higher-degree contributions are neglected, since the changes in the degree-2 coefficients are the most relevant. If the resulting potential U_T is proportional to U_2, then it must be a degree-2 term as well, thus being proportional to $\frac{1}{r^3}$ (Bertotti *et al.*, 2003):

$$U_T\left(r\right) = \left(\frac{R_p}{r}\right)^3 U_T\left(R_p\right) = \left(\frac{R_p}{r}\right)^3 k_2 U_2\left(R_p\right) = -k_2 \frac{Gm}{R_p}\left(\frac{R_p}{r}\right)^3 P_2\left(cos\psi\right) \tag{2.32}$$

In turn, the variation in the gravitational acceleration δg_T of the deformed perturbed body can be expressed as the sum of two contributions: the variation of the potential (perturbed + perturbing) with the radial distance r and the presence of a tidal deformation δh_T (Bertotti *et al.*, 2003):

$$\delta g_T = -\frac{\partial \left(U_2 + U_T\right)}{\partial r} + \frac{\partial g}{\partial r}\delta h_T \tag{2.33}$$

Substituting equations (2.27), (2.31) and (2.32) into (2.33) we obtain:

$$\delta g_T = -\left(1 - \frac{3}{2}k_2 + h_2\right)\left(\frac{\partial U_2}{\partial r}\right) = \left(1 - \frac{3}{2}k_2 + h_2\right)\delta g_R \tag{2.34}$$

which represents the relation between the variation in the gravitational acceleration for a rigid body (g_R) and for a tidally deformed body (g_T).

Analogously, we can compare the variations in the height of equipotential surfaces in the two different cases:

$$\delta z = \left(1 + k_2 - h_2\right)\frac{U_2}{g} = \left(1 + k_2 - h_2\right)\delta h_R \tag{2.35}$$

where $\Delta = 1 + k_2 - h_2$ is a very important parameter related to the thickness of the body's icy crust.

2.2.3 Eccentricity tides

The tidal potential U_2 and the entity of the body's tidal deformation depend on time because of two fundamental effects: variations in the angle ψ (Figure 2.3) with time, basically variations in the angular position of the perturbing body with respect to the perturbed one; and changes in the value of **R**, not constant because of the eccentricity of some orbits.

For many natural satellites such as Ganymede and the Moon, the rotation period around their axes is equal to their orbital period around the central body (1:1 resonance). This condition is referred to as being tidally locked. In this case the relative motion is locked and the central body always faces the same side of the satellite. The result is that for tidally locked satellites, the variations due to changes in ψ are negligible.

Intuitively, satellites that rotate slowly and distant from the central body are less affected by tidal and rotational perturbations and their shape tends to be closer to a sphere. On the other hand, when satellites orbit fast and close to the planet, as for Ganymede, the body is subject to perturbations that are stronger, the lower its mean density.

In either case, it's logical to expect variations in the degree-2 coefficients with respect to the gravitational potential of an isolated body. Therefore we

can express coefficients C_{2m} as the sum of a static component and a tidal variation:

$$\begin{aligned} J_2 &= J_{2s} + \Delta J_2 \\ C_{21} = C_{21s} + \Delta C_{21}, &\quad S_{21} = S_{21s} + \Delta S_{21} \\ C_{22} = C_{22s} + \Delta C_{22}, &\quad S_{22} = S_{22s} + \Delta S_{22} \end{aligned} \tag{2.36}$$

It is also consistent to expect that these alterations are proportional to the perturbation through the *Love number* k_{2m} (Jacobson, 2011):

$$\begin{aligned} \Delta J_2 &= \tfrac{1}{2} k_{20} \left(\tfrac{m}{M_p}\right) \left(\tfrac{R_p}{R}\right)^3 \left(1 - 3cos^2\theta'\right) \\ \Delta C_{21} - i\Delta S_{21} &= k_{21} \left(\tfrac{m}{M_p}\right) \left(\tfrac{R_p}{R}\right)^3 cos\theta' sin\theta' e^{-i(\lambda+\xi)} \\ \Delta C_{22} - i\Delta S_{22} &= \tfrac{1}{4} k_{22} \left(\tfrac{m}{M_p}\right) \left(\tfrac{R_p}{R}\right)^3 \left(1 - cos^2\theta'\right) e^{-2i(\lambda+\xi)} \end{aligned} \tag{2.37}$$

In this notation λ is the longitude of the planet with respect to the satellite orbital plane and ξ is the longitude offset angle, due to the fact that the satellite is not moving along a circle but rather along an ellipse, thus its Prime Meridian is not always aligned with the elliptical radial direction pointing towards the central body.

Through some mathematical manipulation one can express the changes in the quadrupole field coefficients in terms of orbital elements of the satellite with respect to the planet and then switch to a real representation (for details see Jacobson, 2011). Also, considering that for satellites in synchronous rotation the relation: $\lambda \approx e \sin M$ holds, then:

$$\begin{aligned} \Delta J_2 &= \tfrac{1}{2} k_{20} \left(\tfrac{m}{M_p}\right) \left(\tfrac{R_p}{a}\right)^3 (1 + 3e\cos M) \\ \Delta C_{21} &= k_{21} \left(\tfrac{m}{M_p}\right) \left(\tfrac{R_p}{a}\right)^3 \sin I \sin(M+\omega) \cos\xi \\ \Delta S_{21} &= k_{21} \left(\tfrac{m}{M_p}\right) \left(\tfrac{R_p}{a}\right)^3 \sin I \sin(M+\omega) \sin\xi \\ \Delta C_{22} &= \tfrac{1}{4} k_{22} \left(\tfrac{m}{M_p}\right) \left(\tfrac{R_p}{a}\right)^3 [\cos 2\xi + e\cos 2\xi \cos M + 2e\cos(M+2\xi)] \\ \Delta S_{22} &= \tfrac{1}{4} k_{22} \left(\tfrac{m}{M_p}\right) \left(\tfrac{R_p}{a}\right)^3 [\sin 2\xi + e\sin 2\xi \cos M + 2e\sin(M+2\xi)] \end{aligned} \tag{2.38}$$

where *a* is the semi-major axis of the satellite orbit around the planet, *e* is the eccentricity, M is the mean anomaly, I is the inclination and ω is the argument of periapsis.

Satellite	**Inclination (°)**	**Eccentricity**
Io	0.036	0.0041
Europa	0.466	0.0094
Ganymede	0.177	0.0013
Callisto	0.192	0.0074

Table 2.1: Inclination and eccentricity of the orbits of the Galilean satellites with respect to Jupiter's equator ("Planetary Satellite Mean Orbital Parameters". Jet Propulsion Laboratory, California Institute of Technology).

At this point, there are a number of considerations that I wish to make. Firstly, the orbits of the four Galilean satellites are characterized by very small inclinations, as reported in Table 2.1. If $I \approx 0$, from equation (2.39) it is evident that we can neglect the variations of C_{21} and S_{21} due to tides:

$$\begin{aligned} \Delta C_{21} &\approx 0 \\ \Delta S_{21} &\approx 0 \end{aligned} \tag{2.39}$$

Also, given the small eccentricity characterizing the orbits of the Galilean satellites (Table 2.1), we can assume that the variations in the qudrupole coefficient due to the longitude offset angle ξ are much smaller than the variations depending on the quickly varying mean anomaly:

$$\begin{gathered} \cos 2\xi \approx 1 \\ \cos\left(M + 2\xi\right) \approx \cos M, \quad \sin\left(M + 2\xi\right) \approx \sin M \\ \sin 2\xi + e \sin 2\xi \cos M \ll 2e \sin M \end{gathered} \tag{2.40}$$

The new form of equations (2.38) is then:

$$\begin{aligned} \Delta J_2 &= \tfrac{1}{2} k_{20} \left(\tfrac{m}{M_p}\right) \left(\tfrac{R_p}{a}\right)^3 + \tfrac{1}{2} k_{20} \left(\tfrac{m}{M_p}\right) \left(\tfrac{R_p}{a}\right)^3 3e \cos M \\ \Delta C_{22} &= \tfrac{1}{4} k_{22} \left(\tfrac{m}{M_p}\right) \left(\tfrac{R_p}{a}\right)^3 + \tfrac{1}{4} k_{22} \left(\tfrac{m}{M_p}\right) \left(\tfrac{R_p}{a}\right)^3 3e \cos M \\ \Delta S_{22} &= \tfrac{1}{4} k_{22} \left(\tfrac{m}{M_p}\right) \left(\tfrac{R_p}{a}\right)^3 2e \sin M \end{aligned} \tag{2.41}$$

The first terms in equations (2.41a) and (2.41b) represent the permanent tidal deformation of the body, independent of the mean motion of the satellite around the planet. Since the estimate of these contributions can't be decoupled from that of static components (J_{2s} and C_{22s}) of the degree-2

coefficients, we can simply ignore those terms when speaking of variations in the harmonics due to periodic effects.

Lastly, we have to take into account another important phenomenon that affects the changes in the coefficients, namely the angle δ due to the misalignment between the maximum tide height and the line through the centers of the perturbing and perturbed bodies (Figure 2.5).

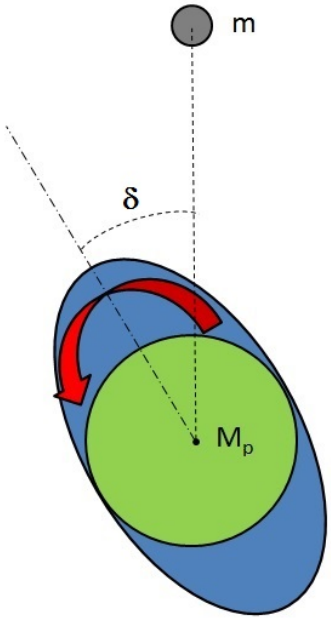

Figure 2.5: Offset angle between the tidal bulge of the satellite and the line through the centers of the perturbing and perturbed bodies.

This angle exists because the elastic response of the satellite lags behind (in time) the tidal potential. This effect is also responsible for the presence of a tidal torque between the two bodies. If the satellite's spin rate is greater than its orbital motion, then the bulge will lead the planet, otherwise the bulge lags the planet and the torque changes sign (ref: *Cornell Education*).

In this scenario, the maximum deformation is not reached at periapsis ($M = 0$) but rather when $M = \delta$. Thus, in order to obtain the correct formulation, we have to substitute M with the angle $M - \delta$ in equations (2.41):

$$\begin{aligned}\Delta J_2 &= \tfrac{1}{2}k_{20}\left(\tfrac{m}{M_p}\right)\left(\tfrac{R_p}{a}\right)^3 3e\cos\left(M-\delta\right)\\ \Delta C_{22} &= \tfrac{1}{4}k_{22}\left(\tfrac{m}{M_p}\right)\left(\tfrac{R_p}{a}\right)^3 3e\cos\left(M-\delta\right)\\ \Delta S_{22} &= \tfrac{1}{4}k_{22}\left(\tfrac{m}{M_p}\right)\left(\tfrac{R_p}{a}\right)^3 2e\sin\left(M-\delta\right)\end{aligned} \tag{2.42}$$

If the body is characterized by two distinct degree-2 Love numbers k_{20} and k_{22} it means that it responds differently depending on the direction of the deformation. On the other hand we can safely assume, to the first order, that the body behaves isotropically, therefore being described by one global degree-2 Love number, namely: $k_2 = k_{20} = k_{22}$. Furthermore, for clarity we can indicate with:

$$q_t = -3\left(\frac{m}{M_p}\right)\left(\frac{R_p}{a}\right)^3, \quad k_{2_\Re} = k_2\cos\delta, \quad k_{2_\Im} = -k_2\sin\delta \tag{2.43}$$

where $k_{2_\Re}$ and $k_{2_\Im}$ are the real and imaginary components of k_2, respectively. Then using some mathematical manipulation:

$$\begin{aligned}\Delta J_2 &= -\tfrac{1}{2}k_{2_\Re}q_t e\cos M + \tfrac{1}{2}k_{2_\Im}q_t e\sin M\\ \Delta C_{22} &= -\tfrac{1}{4}k_{2_\Re}q_t e\cos M + \tfrac{1}{4}k_{2_\Im}q_t e\sin M\\ \Delta S_{22} &= -\tfrac{1}{6}k_{2_\Re}q_t e\sin M - \tfrac{1}{6}k_{2_\Im}q_t e\cos M\end{aligned} \tag{2.44}$$

valid for eccentricity tides of satellites characterized by very small inclinations with respect to the central body and in presence of a phase lag.

2.3 Introduction to thermal wind balance

A planetary atmosphere is defined as a layer of fluid on a sphere characterized by a thickness much less than its horizontal extent. Fluids are different from solid bodies in many regards but mainly because they form a continuum and are able to flow and deform. As a consequence, the equations describing the behavior of fluids are different from those governing solid body mechanics, although both respond to the same basic principles such as Newton's laws (Vallis, 2006).

In this section it is my intent to introduce some basics of fluid dynamics in order to quantify the effects that zonal and meridional winds, involving a great deal of fluid mass on gas giants such as Jupiter, have on the gravity field of the planet itself.

2.3.1 Eulerian and Lagrangian viewpoints

When describing the motion of a solid body, it is sufficient to report on the evolution of the position and velocity of the center of mass of the object and its attitude with respect to a body-fixed reference frame. The state of every other mass element belonging to the body can be then simply inferred assuming that the body is undeformable. Clearly, in fluid dynamics this is not the case, therefore there exist two different approaches to studying the motion of a fluid, both capable of describing its evolution in space and time but with different characteristics, defined as follows.

We refer to a *fluid element* or *parcel* as an infinitesimal, indivisible, piece of fluid of fixed mass. The *Lagrangian* or *material* point of view consists in following independently every single fluid parcel in its motion, as if each of them were marked with a specific label. In this view, the equations of motion are solved for every element, also considering the internal forces between different parcels. The *material derivative* $\frac{D}{Dt}$ is the operator associated to the variations in time of a scalar property ϕ of a specific fluid parcel (*e.g.* density of a single element). Although this approach provides an extremely detailed description of the motion of a fluid, it is often redundant and difficult to implement (Vallis, 2006).

Another option is to look at the temporal variability of properties of the fluid that we are interested in (velocity, density, temperature) at fixed points in space. This viewpoint is known as *Eulerian* or *field*, where we observe the evolution in time of a fluid field from an anchored reference frame. The *Eulerian derivative* $\frac{\partial}{\partial t}$ is then the rate of change of a certain property at a fixed point in space. The two derivatives are related through the expression:

$$\frac{D\phi}{Dt} = \frac{\partial \phi}{\partial t} + (\boldsymbol{v} \cdot \nabla)\, \phi \tag{2.45}$$

where on the right side we find an additional term that depends on the velocity field $\boldsymbol{v}(\boldsymbol{x}, t)$ (which gives the fluid speed at every fixed point and instant of time). Hence the two operators differ from one another by a term that depends on the spatial variation of ϕ, due to the parcel moving in the continuum (Vallis, 2006).

We might as well be interested in the material derivative of a vector field $\boldsymbol{b}$, the expression is all in all analogous to that for a scalar field:

$$\frac{D\boldsymbol{b}}{Dt} = \frac{\partial \boldsymbol{b}}{\partial t} + (\boldsymbol{v} \cdot \nabla)\, \boldsymbol{b} \tag{2.46}$$

with the term in parenthesis being a operator to apply to the vector field. For a formal derivation of equation (2.45)-(2.46) see the reference (Vallis, 2006, section 1.1.2)

2.3.2 Equations of motion for fluids

The purpose of this subsection is to introduce a set of equations capable of describing the behavior of a fluid as a continuum.

The *mass continuity equation* states that the mass of a fluid system is conserved as it flows into and away from regions and as its density changes, provided there are no sources or sinks of mass (Vallis, 2006). The differential, Eulerian form of the equation is the following:

$$\frac{\partial \rho}{\partial t} + \nabla \cdot (\rho \boldsymbol{v}) = 0 \tag{2.47}$$

The equation asserts that possible changes in the fluid density must be matched by inflow or outflow of mass and this must be true for every point of the continuum. On the other hand, from a Lagrangian point of view the mass continuity equation simply states that the mass of every single parcel is constant:

$$\frac{D\left(\rho \Delta V\right)}{Dt} = 0 \tag{2.48}$$

whit ΔV being the infinitesimal volume of the fluid element. By manipulating the expression (for detail see Vallis, 2006, section 1.2.2), equation (2.48) can be written in the form:

$$\frac{D\rho}{Dt} + \rho \nabla \cdot \boldsymbol{v} = 0 \tag{2.49}$$

In addition to the mass balance, the *momentum equation* is needed to account for changes in the momentum of the fluid, due to the action of internal and external forces. From Newton's second law:

$$\rho \frac{D\boldsymbol{v}}{Dt} = \boldsymbol{F} \tag{2.50}$$

or, in term of field derivative of the velocity (Vallis, 2006):

$$\frac{\partial \boldsymbol{v}}{\partial t} + (\boldsymbol{v} \cdot \nabla)\, \boldsymbol{v} = \frac{\boldsymbol{F}}{\rho} \tag{2.51}$$

thus the acceleration of the fluid is proportional to the applied forces (not all external) and inversely proportional to the mass of the fluid (density if the equation is written per volume unit).

Now we need to specify the right hand of equation (2.51), characterizing the different contributions. In the balance we must take into account the effects of the direct contact between two fluid elements. One of these contact forces is the so-called *pressure force* F_p. Intuitively, the pressure term of the momentum equation would be proportional to the pressure gradient with a changed sign since fluid tends to flow from high-pressure regions to low-pressure ones (for a complete formulation see Vallis, 2006, sect. 1.3.2). Then, equation (2.51) becomes:

$$\frac{\partial \boldsymbol{v}}{\partial t} + (\boldsymbol{v} \cdot \nabla)\, \boldsymbol{v} = -\frac{\nabla p}{\rho} + \boldsymbol{F}' \tag{2.52}$$

where $\boldsymbol{F}' = (\boldsymbol{F} - \boldsymbol{F}_p)/\rho$. Another contribution is due to the *viscosity* of the fluid. For most Newtonian fluids, a very good approximation of the viscous force per unit volume is (Vallis, 2006):

$$\hat{\boldsymbol{F}}_v = \mu \nabla^2 \boldsymbol{v} \tag{2.53}$$

where μ is the viscosity. Since all equations have been written per unit volume, it is convenient to introduce the *kinetic viscosity* as $\nu \equiv \frac{\mu}{\rho}$. For a gas, the kinetic viscosity is roughly equal to the product of the mean free path and the mean molecular velocity. That being so, equation (2.53) takes now the form:

$$\frac{\partial \boldsymbol{v}}{\partial t} + (\boldsymbol{v} \cdot \nabla)\, \boldsymbol{v} = -\frac{1}{\rho}\nabla p + \nu \nabla^2 \boldsymbol{v} + \boldsymbol{F}_b \tag{2.54}$$

where it has been chosen to represent the combination of all external (body) forces, such as gravity, with the notation $\boldsymbol{F}_b$.

2.3.3 Hydrostatic balance

When talking about planetary atmosphere, it is useful to introduce in this context a set of spherical coordinates as done in section 2.1. The velocity of the fluid can then be expressed in terms of longitudinal, latitudinal and radial components (u, v, w) respectively (see Figure 2.6).

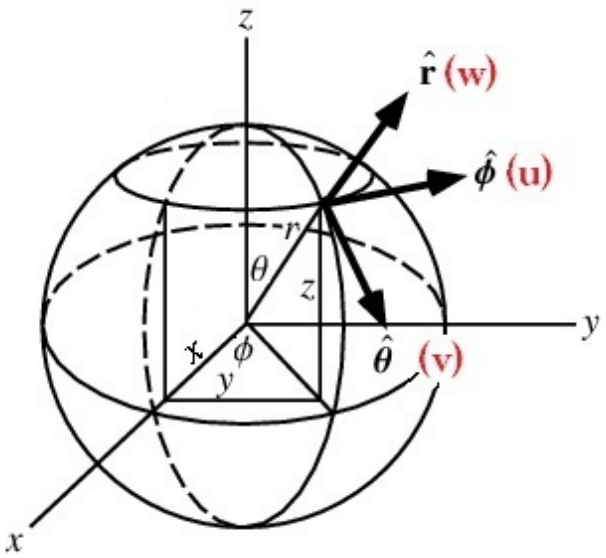

Figure 2.6: Components of the fluid velocity in spherical coordinates (Weisstein, Eric W. *Spherical coordinates*. From MathWorld, A Wolfram Web Resource).

The projection of the momentum equation in the radial direction $\hat{r}$ is:

$$\frac{Dw}{Dt} = -\frac{1}{\rho}\frac{\partial p}{\partial z} - g \tag{2.55}$$

where g is the gravitational acceleration.

If the fluid has no motion in the radial direction, namely $w \equiv 0$, then the pressure and gravitational terms balance each other out:

$$\frac{\partial p}{\partial z} = -\rho g \tag{2.56}$$

This condition is known as *hydrostatic equilibrium* and states that at every fixed point the pressure is due to the weight of the fluid column above (Vallis, 2006).

2.3.4 Incompressible flows

A fluid is referred to as *incompressible* when its density is constant from a Lagrangian point of view:

$$\frac{D\rho}{Dt} = 0 \tag{2.57}$$

then the mass conservation equation in (2.49) can be written as:

$$\nabla \cdot \boldsymbol{v} = 0 \tag{2.58}$$

In this case, equation (2.48) can be manipulated to prove that the volume of each fluid parcel is constant in time and thus it doesn't deform (Vallis, 2006).

Although in the context of planetary atmospheres there are basically no real flows that can be considered strictly incompressible, sometimes the temporal variations in the density can be neglected if compared to the divergence term in equation (2.49), explicitly:

$$\left|\frac{D\rho}{Dt}\right| \ll \rho \nabla \cdot \boldsymbol{v} \tag{2.59}$$

It is worth noting that for not strictly incompressible flows, although the changes in the fluid density can be neglected in the mass conservation equation, and thus equation (2.58) stands, this doesn't imply that these variations can be neglected when standing alone, namely it can't be subsequently assumed that $\frac{D\rho}{Dt} = 0$ (Vallis, 2006).

2.3.5 Equations of motion in a rotating reference frames

The rotation of a celestial body about one of its axis influences greatly the dynamics of a planetary atmosphere. For this reason it is very convenient to write the equations of motion for a fluid with respect to a rotating reference frame.

Switching from an inertial reference frame (indicated by the subscript *I*) to a rotating one (indicated by the subscript *R*) the relation between the acceleration of an arbitrary point in space as seen by the two frames is (for details on the mathematical derivation see Section 2.1.2 of Vallis, 2006):

$$\left(\frac{d\boldsymbol{v}_R}{dt}\right)_R = \left(\frac{d\boldsymbol{v}_I}{dt}\right)_I - 2\boldsymbol{\Omega} \times \boldsymbol{v}_R - \boldsymbol{\Omega} \times (\boldsymbol{\Omega} \times \boldsymbol{r}) \tag{2.60}$$

where $\boldsymbol{v}_R$ is the relative velocity as seen in the rotating reference frame, $\boldsymbol{v}_I$ is the inertial velocity and $\boldsymbol{\Omega}$ is the body's rotation rate.

In this context we introduce the *Coriolis acceleration* ($-2\boldsymbol{\Omega} \times \boldsymbol{v}_R$) and the *centrifugal acceleration* ($-\boldsymbol{\Omega} \times (\boldsymbol{\Omega} \times \boldsymbol{r})$). These forces for unit mass are the so-called apparent forces, affecting the motion of a body only when this is described in a non-inertial reference frame.

From (2.60) it follows that the Coriolis acceleration affects the motion of a body in a rotating frame only when the body is provided with a non-null relative velocity. If this is the case, this apparent force tends to deflect the motion of the body to right angles with respect to their direction of motion (Vallis, 2006).

A useful vectorial identity is:

$$\boldsymbol{\Omega} \times (\boldsymbol{\Omega} \times \boldsymbol{r}) = (\boldsymbol{\Omega} \cdot \boldsymbol{r}_\perp)\, \boldsymbol{\Omega} - (\boldsymbol{\Omega} \cdot \boldsymbol{\Omega})\, \boldsymbol{r}_\perp \tag{2.61}$$

here $\boldsymbol{r}_\perp$ is the component of the position vector perpendicular to the rotation rate $\boldsymbol{\Omega}$. Noting that the first term on the right side of equation (2.61) is zero because of the dot product, the centrifugal acceleration can be expressed as:

$$-\boldsymbol{\Omega} \times (\boldsymbol{\Omega} \times \boldsymbol{r}) = \Omega^2 \boldsymbol{r}_\perp \tag{2.62}$$

In principle, this force can be expressed in term of a scalar potential Φ_{ce} (Vallis, 2006) so that:

$$\boldsymbol{F_{ce}} = -\nabla \Phi_{ce} \tag{2.63}$$

then for equations (2.62) and (2.63) to be equivalent it must be:

$$\Phi_{ce} = -\frac{\Omega^2 \boldsymbol{r}_\perp^2}{2} \tag{2.64}$$

Applying these considerations to the equations of motion, it is intuitive that the rate of change of a scalar quantity such as the density of a fluid, is invariant of the reference frame. this means that the mass conservation equation maintains the same formulation in both inertial and rotating reference frames (Vallis, 2006, Section 2.1.4).

On the other hand, when coming to the momentum equation, it is necessary to take into account the presence of the centrifugal and Coriolis accelerations when switching to a rotating reference frame. In particular, equation (2.54) becomes:

$$\frac{D\boldsymbol{v}}{Dt} + 2\boldsymbol{\Omega} \times \boldsymbol{v} = -\frac{1}{\rho}\nabla p - \nabla\Phi \tag{2.65}$$

where $\boldsymbol{v}$ is now the relative velocity and the potential function Φ comprises both the gravitational and centrifugal terms.

2.3.6 Geostrophic and thermal wind balance

The presence of a centrifugal term in the effective gravity ($-\nabla\Phi$) results in the equipotential surfaces not being spherical because of Φ dependence on latitude through $\boldsymbol{r}_\perp$. Given this, by keeping the traditional formulation of spherical coordinates, the horizontal component of the momentum equation would be dominated by the centrifugal and pressure gradient terms, as well as the vertical balance, whereas it is important to emphasize the role of the Coriolis acceleration in the horizontal flow.

For this reason, it is common practice to redefine the vertical direction in spherical coordinates as the normal to the new equipotential surfaces, this way the component of the effective gravity in the vertical direction is again null. By carrying on with the formulation of the equations of motion as if the equipotential surfaces were spherical, a small geometric error is accepted and traded with bigger dynamical errors introduced by the appearance of centrifugal and gravitational accelerations in the horizontal momentum balance (I refer the reader willing to go into more detail of this discussion to Section 2.2.1 of Vallis, 2006).

In the approximation discussed above the terms depending on the vertical component w of the velocity can be neglected in the horizontal momentum equation, thus the projection of equation (2.65) on the plane defined by $\hat{\boldsymbol{\theta}}$ and $\hat{\boldsymbol{\phi}}$ is:

$$\frac{D\boldsymbol{u}}{Dt} + \boldsymbol{f} \times \boldsymbol{u} = -\frac{1}{\rho}\nabla_z p \tag{2.66}$$

where $\boldsymbol{u} = u\hat{\boldsymbol{\phi}} + v\hat{\boldsymbol{\theta}}$ is the horizontal velocity, $\boldsymbol{f} = 2\Omega\cos\theta\boldsymbol{k}$ is the Coriolis parameter and ∇_z is the gradient operator at constant z (Vallis, 2006). The relation can be expressed in terms of stationary variations as well, obtaining:

$$\frac{\partial \boldsymbol{u}}{\partial t} + (\boldsymbol{v}\cdot\nabla)\,\boldsymbol{u} + \boldsymbol{f} \times \boldsymbol{u} = -\frac{1}{\rho}\nabla_z p \tag{2.67}$$

The order of magnitude of the advective term (second term on the left hand) is given by U^2/L where U is the magnitude of the horizontal velocity and L is the characterizing length scale. This quantity can be compared to the magnitude of the Coriolis acceleration (about fU) by defining the *Rossby number*:

$$Ro = \frac{U}{fL} \tag{2.68}$$

that characterizes the importance of rotation in a fluid. If the celestial body is a fast rotator (like Jupiter), than the Rossby number is very small and the advective term in the horizontal momentum equation can be neglected (Vallis, 2006), leading to:

$$\boldsymbol{f} \times \boldsymbol{u} \approx -\frac{1}{\rho}\nabla_z p \tag{2.69}$$

basically, when $Ro \ll 1$, the horizontal pressure gradient is balanced by the Coriolis force only. This balance is known as *geostrophic*. In Cartesian coordinates (Vallis, 2006):

$$\begin{aligned} fu &\approx -\ \tfrac{1}{\rho}\tfrac{\partial p}{\partial y} \\ fv &\approx \quad \tfrac{1}{\rho}\tfrac{\partial p}{\partial x} \end{aligned} \tag{2.70}$$

whence the flow is parallel to isobaric lines. Also note that for $f > 0$ (i.e. in the northern hemisphere) the flow has an anticlockwise motion around regions of low pressure and clockwise motion around high-pressure areas (see Figure 2.7). Viceversa is true for the southern hemisphere.

Leaving this 2D formulation (that holds for every equipotential surface) for a 3-D model, the *thermal wind balance* is then the combination of the geostrophic and hydrostatic approximation (Vallis, 2006). This union

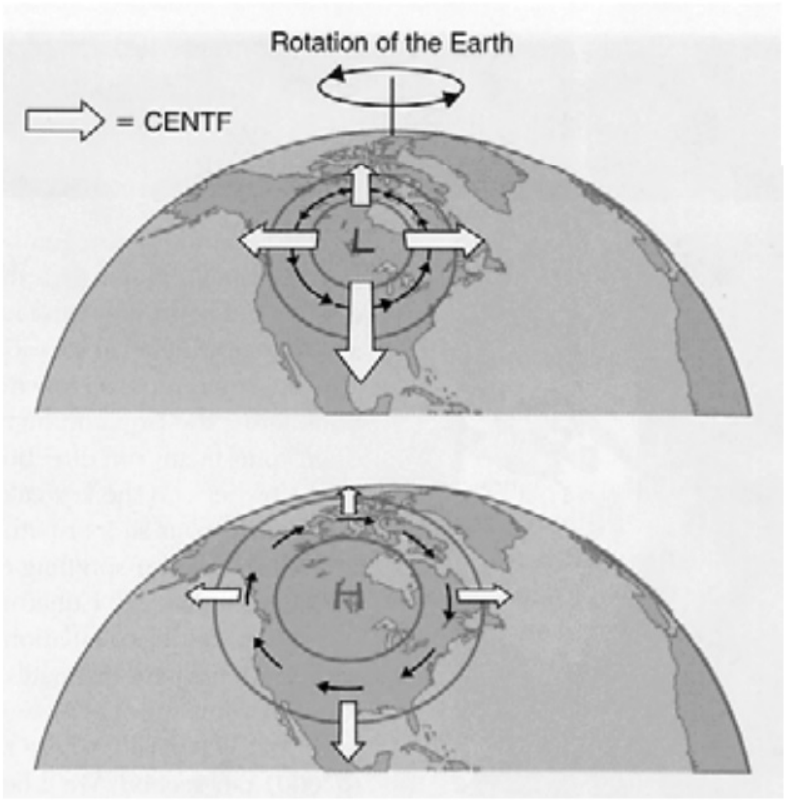

Figure 2.7: Geostrophic (anti) clockwise flow around (low) high pressure regions. Explanatory image for the Earth rotation. Image credit: *UCI Edu ESS124*.

introduces vertical derivatives of the geostrophic winds (u and v) in the vertical direction. In order to show that, it is convenient to express the 3-D inviscid momentum equation (2.65) in terms of the vorticity $\nabla \times \boldsymbol{v}$:

$$\frac{\partial \boldsymbol{v}}{\partial t} + (2\boldsymbol{\Omega} + \nabla \times \boldsymbol{v}) \times \boldsymbol{v} = -\frac{1}{\rho}\nabla p - \nabla \Phi \tag{2.71}$$

By taking the curl of the equation above, one gets (for a detailed mathematical formulation see Kaspi *et al.*, 2009):

$$2\Omega\nabla\cdot(\rho\boldsymbol{v})-2\boldsymbol{\Omega}\cdot\nabla(\rho\boldsymbol{v})=-\nabla\rho\times\boldsymbol{g} \tag{2.72}$$

Before proceeding further, there are a few considerations to be made. Since the system is in hydrostatic equilibrium, the following relation holds:

$$\nabla\tilde{p}=-\tilde{\rho}\nabla\Phi \tag{2.73}$$

where $\tilde{p}$ and $\tilde{\rho}$ are the reference hydrostatic pressure and density, respectively, that depend only on the radial direction ($\hat{\boldsymbol{r}}$). The deviations of the total pressure and density p' and ρ' from this reference stationary values are very small and functions not only of the depth but also of colatitude θ and longitude ϕ:

$$\begin{aligned}p&=\tilde{p}(r)+p'(r,\theta,\phi)\\ \rho&=\tilde{\rho}(r)+\rho'(r,\theta,\phi)\end{aligned} \tag{2.74}$$

Supposing that the temporal variations of the total density are negligible if compared to the divergence term in equation (2.49) (and they are, if the Rossby number is small), then the mass conservation equation becomes:

$$\rho\nabla\cdot\boldsymbol{v}=0 \tag{2.75}$$

then it's clear that the first term on the left hand of equation (2.72) is null, thus:

$$2\boldsymbol{\Omega}\cdot\nabla(\rho\boldsymbol{v})=\nabla\rho\times\boldsymbol{g} \tag{2.76}$$

Now, given that:

$$\tilde{\rho}\boldsymbol{v}\gg\rho'\boldsymbol{v} \tag{2.77}$$

and $\nabla\tilde{\rho}$ is parallel to $\boldsymbol{g}$, equation (2.76) can be reduced to:

$$2\boldsymbol{\Omega}\cdot\nabla(\tilde{\rho}\boldsymbol{v})=\nabla\rho'\times\boldsymbol{g} \tag{2.78}$$

known as the standard thermal wind relation (Kaspi *et al.*, 2009). If the temperature decreases going from the equator to the poles, as it happens on Earth, then equation (2.78) states that eastward winds increase with height, a phenomenon that has been observed on our planet (Vallis, 2006). In a

continuum, regions where the fluid is colder are characterized by larger densities, thus, for the hydrostasy equation (2.73), these regions are also characterized by greater vertical pressure gradients, giving rise to the vertical shear, representative of thermal winds.

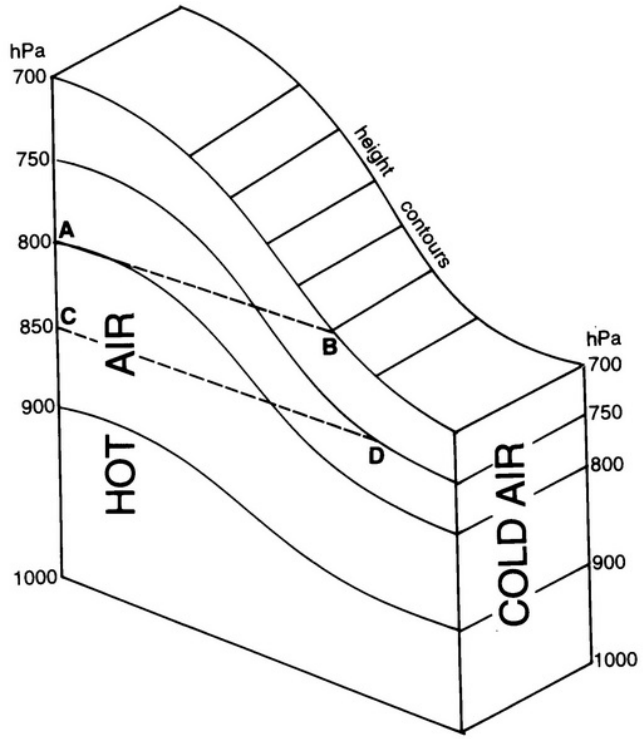

Figure 2.8: Mechanism of thermal wind for an atmospheric layer between 700 and 1000 hPa. Image credit: B. Geerts, University of Wyoming, Dep. of Atmospheric Science.

To get a grasp of this phenomenon, let's take a look at Figure 2.8. The presence of a horizontal temperature gradient results in the deformation of isobaric lines. As a consequence, the horizontal pressure gradient is larger between points A and B than between C and D, meaning that thermal winds increase with height (B. Geerts, University of Wyoming, Dep. of Atmospheric Science).

Chapter 3

Orbit determination

The discipline of orbit determination is a very powerful tool used to determine the trajectory of a body (celestial or not) in space, with respect to an observational reference frame (*e.g* Earth-centered). In this chapter I will focus on the description of the orbit determination problem for an artificial satellite (*i.e* spacecraft or probe). I will introduce the mathematical formulation of the problem, as well as the optimization method used in order to attain the optimal reconstruction of the satellite trajectory and the best estimate of physical parameters affecting the motion of the body.

In Sections 3.1, 3.2 and 3.3, I will use the same mathematical terminology as in Tapley (2004), although the argumentations will be reformulated.

3.1 Introduction

The orbit determination of non-celestial bodies consists of obtaining the best estimate, yet undefined, of a complete set of initial conditions that represents the state of the body $\boldsymbol{X}(t_0)$ at some reference epoch t_0. Intuitively, the minimal collection of parameters necessary to describe the state of a satellite is the composition of the position and velocity vectors. Nevertheless, this set can be further expanded including parameters characterizing the dynamical model in which the spacecraft is immersed, in order to obtain a better description of the surroundings.

For the fundamental theorem of calculus, the knowledge of the initial state represents enough information to define the future evolution of a dynamical system, provided that the set of differential equations that governs

its motion is known and can be integrated. Once the initial conditions are made available, the state of the system $\boldsymbol{X}(t)$ at every future instant of time t can be derived by simply propagating the initial state forward.

In practice, the initial state of a spacecraft (*e.g* components of position and velocity in Cartesian coordinates at t_0) is never known with the desired accuracy, as well as the constants characteristic of the dynamical model or the mathematical formulation itself. All these effects make the prediction of the body trajectory very difficult from a deterministic point of view, hence the necessity of tracking the spacecraft from Earth stations of well-known position in order to provide a better estimate of the orbit. However, the state of a satellite is never directly observed, the actual observable quantities are usually of the kind of *range* and *range-rate* measurements that represent the relative distance and velocity between the spacecraft and the Earth along the line of sight, respectively. One could even exploit angular observations, measuring the angle between the probe-station direction and the local horizon (Figure 3.1).

These observations are, of course, subject to both random and systematic errors, creating the necessity of defining and then finding the *best* estimate of the body state in a statistical sense. Yet, even after the optimization process (to be described in the next sections), the *estimated trajectory* $\hat{X}$ will be different from the *true trajectory* X actually outlined by the spacecraft, for several reasons:

- Errors in the estimate of the initial state due to:
  - inaccuracies in the formulation of the dynamical model or in the updating procedure;
  - observation errors;
  - computational errors;
- Integration errors due to error in the dynamical model (*e.g* linearization) or truncation and round-off errors.

All the effects listed above contribute to create the necessity of constantly updating the trajectory of the spacecraft by solving the orbit determination problem for the body at different epochs. In fact, after a certain

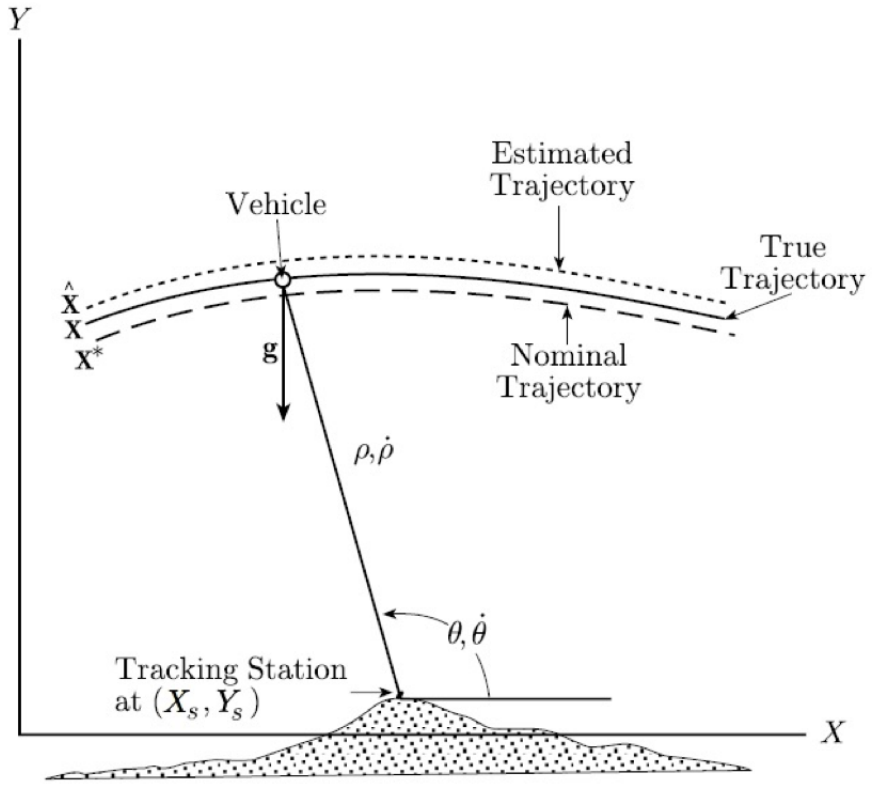

Figure 3.1: Differences between estimated, true and nominal trajectories. ρ, $\dot{\rho}$ and θ represent range, range-rate and angular observations, respectively. Image credit: Tapley, 2004.

amount of time, the approximations used and the errors involved make the prediction of the orbit not good enough.

The *nominal trajectory* X^* is, instead, the best realization of the trajectory before the orbit determination process; in a way, the desired trajectory as designed by the project of a space mission. Needless to say, this reference trajectory also differs from both the estimated and the true trajectories.

From Figure 3.1 it is clear that the values of the actual *observed observables* are functions of both the state of the spacecraft $\boldsymbol{X}$ and the position of the station $\boldsymbol{X}_S$ at the epoch of the observation, a dependence on time that one must take into account when formulating the orbit determination problem. On the other hand, it is possible to produce another set of observables, calculated starting from a reference dynamical model, nominal trajectory of the spacecraft, position of the tracking station and some relations capable

of linking the observables with the state of the spacecraft. These quantities are the so-called *computed observables* that will be discussed in more detail in the following sections. The difference between observed and computed observables at any instant of time can provide information on the goodness of the real-time knowledge of the spacecraft motion and a tool to improve the satellite estimated trajectory as well as the dynamical model.

3.2 Observables

Nowadays, several set of observables are made available by onboard tracking systems, capable of measuring scalar quantities related to the state of the spacecraft. In the frame of this dissertation, I will focus on the description of two of the most common radiometric measurements: *two-way range* and *two-way range-rate*, as these will be the observations carried out by the radio science instrument of the Juno and the JUICE missions.

3.2.1 Two-way range

Range measurements are related to the linear distance between the spacecraft and the Earth. If $\boldsymbol{r}_I$ is the position vector of the ground station and $\boldsymbol{r}$ is the position vector of the spacecraft with respect to the origin of a reference coordinate system (*e.g* Earth-centered), then the idealized linear distance between the two bodies is:

$$\rho = \sqrt{[(\boldsymbol{r} - \boldsymbol{r}_I) \cdot (\boldsymbol{r} - \boldsymbol{r}_I)]} \tag{3.1}$$

which is a function of the specific instant of time at which the measurement is performed, namely $\boldsymbol{r}_I = \boldsymbol{r}_I(t)$, $\boldsymbol{r} = \boldsymbol{r}(t)$. Obviously, the distance between two points is invariant of the reference frame, for example in a Earth-centered inertial frame it would be:

$$\rho = \sqrt{(X - X_I)^2 + (Y - Y_I)^2 + (Z - Z_I)^2} \tag{3.2}$$

In the idealized case in which it is possible to measure the true range this will not differ from the observed one, while in fact, due to medium propagation and instrumental limitations, the observed range never coincides with the actual radial distance, but rather:

$$\rho_{obs} = \rho + \epsilon \tag{3.3}$$

where ϵ is the error term, the nature of these alterations will be specified later in the dissertation.

Now that the geometric nature of ρ has been specified, it is important to understand how this kind of observations are carried out, as they are related to the measure of the *time of flight* of a radio signal in the microwave region (section 1.4.1). In the case of two-way range, a signal is originally transmitted from the ground station, received, amplified and coherently re-transmitted back by the spacecraft transponder to the same station. The signal trip from the ground instrumentation to the satellite is known as *uplink*, while the way back is known as *downlink*, whence the label two-way.

Suppose the ground-based hardware transmits a pulse of Gaussian shape at the time t_T. Suppose also that the spacecraft receives the signal and re-transmits it back without any time delay. Then, the station will detect the returning pulse at the time t_R, measured by the same clock as the transmitting time. The back and forth signal path is then:

$$\rho_{rt} = c(t_R - t_T) \tag{3.4}$$

where c is the speed of light. At this point it is essential to make some considerations about the clock model. In fact, there are some differences between the time t as measured by the clock and the true time T. A suitable relation between these two quantities is:

$$t = T + a + b\,(T - T_0) + \epsilon_{clock} \tag{3.5}$$

where a is the clock constant offset, b is the linear drift, ϵ_{clock} is a term comprising other possible errors (non-linear and stochastic) and T_0 is the reference time. Applying this definition to equation (3.4) one gets:

$$\rho_{rt} = c(T_R - T_T) + b(T_R - T_T) + \epsilon_{clock} \tag{3.6}$$

here the constant offset disappears as the time measurements are based on the same clock, indeed this property represents the biggest advantage in adopting two-way range measurements.

In reality, atmospheric delays must be taken into account as well, then equation (3.6) becomes:

$$\rho_{rt} = c(T_R - T_T) + b(T_R - T_T) + \epsilon_{clock} + \delta\rho_{atm} \tag{3.7}$$

the last term will be discussed in much more detail in Chapter 4.

In this ideal formulation the round-trip distance is twice the distance between the spacecraft and the Earth station:

$$\rho_{avg} = \frac{\rho_{rt}}{2} \tag{3.8}$$

although for several reasons, such as the finite propagation speed of light, this is true only up to the sub-millimeter level (Tapley, 2004).

3.2.2 Two-way range-rate

Range-rate measurements correspond to the rate of change, in time, of the radial distance between the ground station and the spacecraft. The mathematical expression for these observations can be determined by differentiating equation (3.2) in time:

$$\dot{\rho} = \frac{(X - X_I)\left(\dot{X} - \dot{X}_I\right) + (Y - Y_I)\left(\dot{Y} - \dot{Y}_I\right) + (Z - Z_I)\left(\dot{Z} - \dot{Z}_I\right)}{\left[(X - X_I)^2 + (Y - Y_I)^2 + (Z - Z_I)^2\right]^{1/2}} \tag{3.9}$$

in which temporal variations of the station location, due to Earth rotation (if the adopted reference frame is inertial), tectonics and so on, are accounted for. As expected, also in this case systematic and randomic effects must be considered, giving rise to an error term ϵ:

$$\dot{\rho_{obs}} = \dot{\rho} + \epsilon \tag{3.10}$$

In the next few paragraphs I will show how range-rate observations are related to recordings of the Doppler shift of a radio signal.

In most Doppler tracking systems, the ground station transmits a periodic radio signal of frequency f_T, between two instants of time t_{T_1} and t_{T_2}. Suppose that this signal is received back by the station instrumentation between times t_{R_1} and t_{R_2}, after being coherently re-transmitted back by the spacecraft. Then:

$$\begin{aligned} t_{R_1} &= t_{T_1} + \Delta t_1 = t_{T_1} + \tfrac{2\rho_1}{c} \\ t_{R_2} &= t_{T_2} + \Delta t_2 = t_{T_2} + \tfrac{2\rho_2}{c} \end{aligned} \tag{3.11}$$

where $2\rho_1$ is the round-trip distance between the station and the satellite at the time t_{R_1}, the same applies for $2\rho_2$. Here I used the same approximation as in expression (3.8).

The process of extracting the received frequency f_R includes the multiplication with the reference frequency standard f_G, representative of the transmitted frequency. The outcome of the beating is a pair of periodic signals of frequencies $f_G + f_R$ (which is filtered out) and $f_G - f_R$, containing the desired information content. The next step is counting the number of cycles between t_{R_1} and t_{R_2} by integrating the differential frequency:

$$N_{1,2} = \int_{t_{R_1}}^{t_{R_2}} (f_G - f_R)\, dt \tag{3.12}$$

Developing the integral:

$$N_{1,2} = f_G \left[t_{T_2} - t_{T_1} + \frac{2\,(\rho_2 - \rho_1)}{c} \right] - \int_{t_{R_1}}^{t_{R_2}} f_R dt \tag{3.13}$$

The numbers of recorded oscillations of the transmitted and received signals are the same, thus:

$$\int_{t_{R_1}}^{t_{R_2}} f_R dt = \int_{t_{T_1}}^{t_{T_2}} f_T dt = f_T\,(t_{T_2} - t_{T_1}) \tag{3.14}$$

Equation (3.13) becomes:

$$N_{1,2} = (f_G - f_T)\,(t_{T_2} - t_{T_1}) + f_G \frac{2\,(\rho_2 - \rho_1)}{c} \tag{3.15}$$

If $\delta\rho = \rho_2 - \rho_1$, then:

$$N_{1,2} = f_T \frac{2\delta\rho}{c} \tag{3.16}$$

because, in principle $f_G = f_T$. Dividing by $\delta t = t_{R_2} - t_{R_1}$ and treating these finite differences as proper derivatives (this is the least rigorous assumption), comparing with equation (3.12) one gets:

$$\frac{N_{1,2}}{\delta t} = f_T - f_R = f_T \frac{2}{c} \frac{\delta\rho}{\delta t} \tag{3.17}$$

whence the Doppler shift is:

$$f_T - f_R = \Delta f = f_T \frac{2\dot{\rho}}{c} \tag{3.18}$$

in relation to the range-rate of the spacecraft.

3.3 Mathematical formulation

In section 3.1 it has been discussed how the n-component state vector of a body $\boldsymbol{X}$ can be univocally determined for every instant of time $t > t_k$ if the differential equations that govern its motion are perfectly known along with a set of initial conditions $\boldsymbol{X}_k$ at the reference epoch t_k:

$$\begin{cases} \dot{\boldsymbol{X}} = F(\boldsymbol{X}, t) \\ \boldsymbol{X}(t_k) \equiv \boldsymbol{X}_k \end{cases} \tag{3.19}$$

However, since the state of a satellite is never directly observed, in section 3.2 it's been specified what are the classes of observations used in space navigation and gravity science to get the best estimate of the initial state vector $\boldsymbol{X}_k$ and other physical parameters. These observables are connected to the state of the body through the *observation equations* (*e.g.* equation (3.2) and (3.9)) that can be written in a compact form as:

$$\boldsymbol{Y}_i = G(\boldsymbol{X}_i, t_i) + \boldsymbol{\epsilon}_i \qquad i = 1, ..., l \tag{3.20}$$

where $\boldsymbol{Y}_i$ is the p-dimension observation vector at the time t_i and $\boldsymbol{\epsilon}_i$ is the vector of observation errors as defined in section 3.1. In the case of both range and range-rate measurements it would be $p = 2$. Usually, $p < n$ but, in order to overcome this under-parametrization of the problem a great number of observations is used so that: $m = p \cdot l \gg n$.

3.3.1 Linearization

There is one fundamental thing to be noted: there is no reason not to assume that the equations of motion and the observation equations are, in general, non-linear. It is not my intent in the frame of this dissertation to convince the reader how the linearization of these equations would be beneficial to the solution of the orbit determination problem. Let just say that if a sufficiently reliable nominal trajectory $\boldsymbol{X}^*$ is available, then it is possible

to expand the true trajectory $\boldsymbol{X}$ around the nominal state, provided that the interval of time in which this approximation is used is small enough that the two trajectories are close enough. Applying the linearization to equations (3.19) and (3.20) one gets:

$$\dot{\boldsymbol{X}} = F\left(\boldsymbol{X}^*, t\right) + \left[\frac{\partial F\left(t\right)}{\partial \boldsymbol{X}\left(t\right)}\right]^* \left[\boldsymbol{X}\left(t\right) - \boldsymbol{X}^*\left(t\right)\right] + O\left[\boldsymbol{X}\left(t\right) - \boldsymbol{X}^*\left(t\right)\right] \quad (3.21)$$

$$\begin{aligned} &\boldsymbol{Y}_i = G\left(\boldsymbol{X}_i^*, t_i\right) + \left[\tfrac{\partial G}{\partial \boldsymbol{X}}\right]_i^* \left[\boldsymbol{X}_i\left(t_i\right) - \boldsymbol{X}_i^*\left(t_i\right)\right] + O\left[\boldsymbol{X}_i\left(t_i\right) - \boldsymbol{X}_i^*\left(t\right)\right] + \boldsymbol{\epsilon}_i \\ &i = 1, ..., l \end{aligned} \quad (3.22)$$

where the partial derivatives are computed on the nominal trajectory. But $F\left(\boldsymbol{X}^*, t\right) = \dot{\boldsymbol{X}}^*$ and $G\left(\boldsymbol{X}_i^*, t_i\right) = \boldsymbol{Y}_i^*$, also one could introduce the quantities $\boldsymbol{x}\left(t\right) = \dot{\boldsymbol{X}} - \dot{\boldsymbol{X}}^*$ and $\boldsymbol{y}\left(t_i\right) = \boldsymbol{Y}_i - \boldsymbol{Y}_i^*$ as the deviations of the state and observation vectors with respect to the nominal state, then expression (3.21) and (3.22) become:

$$\dot{\boldsymbol{x}}\left(t\right) = A\left(t\right)\boldsymbol{x}\left(t\right) \quad (3.23)$$

$$\boldsymbol{y}_i = \tilde{H}_i \boldsymbol{x}_i + \boldsymbol{\epsilon}_i \qquad i = 1, ..., l \quad (3.24)$$

defining $A\left(t\right) = \left[\frac{\partial F(t)}{\partial \boldsymbol{X}(t)}\right]^*$ as the time-dependent coefficient matrix of the system of linear differential equations of motion, $\tilde{H}_i = \left[\frac{\partial G}{\partial \boldsymbol{X}}\right]_i^*$ as the partial derivatives matrix of the observations with respect to the components of the state and $\boldsymbol{y}_i$ as the difference between the observed observables $\boldsymbol{Y}_i$ and the computed observables $\boldsymbol{Y}_i^*$ calculated starting from the nominal state at the time t_i.

Provided that the coefficient matrix is not singular, the solution to system (3.23) of n unknowns is:

$$\boldsymbol{x}\left(t\right) = \Phi\left(t, t_k\right)\boldsymbol{x}_k \quad (3.25)$$

where $\Phi\left(t, t_k\right)$ is the *state transition matrix* that links the state vector $\boldsymbol{x}\left(t\right)$ at the generic instant of time t to the state vector $\boldsymbol{x}_k = \boldsymbol{x}\left(t_k\right)$ calculated at the reference epoch t_k.

Introducing expression (3.25) in system (3.23) one gets:

$$\dot{\Phi}\left(t, t_k\right) \boldsymbol{x}_k = A\left(t\right) \Phi\left(t, t_k\right) \boldsymbol{x}_k \tag{3.26}$$

reducing to:

$$\dot{\Phi}\left(t, t_k\right) = A\left(t\right) \Phi\left(t, t_k\right) \tag{3.27}$$

One of the properties of the state transition matrix is:

$$\boldsymbol{x}_k = \Phi\left(t_k, t_k\right) \boldsymbol{x}_k \quad \longrightarrow \quad \Phi\left(t_k, t_k\right) = I \tag{3.28}$$

that can be used as the initial condition for system (3.27), to get a solution for Φ, which is unique if $A\left(t\right)$ is composed of continuous functions of time (Tapley, 2004).

The reason why it is more convenient to formulate the problem in terms of the state transition matrix is that, using this approach, instead of solving system (3.23) for each epoch t, it is possible to refer every observation to a reference epoch t_k.

The system of equations (3.24) is now to be dealt with. In principle, for each epoch t_i, there is an algebraic equation to be solved for $\boldsymbol{x}_i$. Instead, thanks to the introduction of the transition matrix, we can express all equations in terms of $\boldsymbol{x}_k$, going from $l \cdot n$ unknowns to n:

$$\begin{aligned} \boldsymbol{y}_1 &= \tilde{H}_1 \Phi\left(t_1, t_k\right) \boldsymbol{x}_k + \boldsymbol{\epsilon}_1 \\ \boldsymbol{y}_2 &= \tilde{H}_2 \Phi\left(t_2, t_k\right) \boldsymbol{x}_k + \boldsymbol{\epsilon}_2 \\ &\vdots \\ \boldsymbol{y}_l &= \tilde{H}_l \Phi\left(t_l, t_k\right) \boldsymbol{x}_k + \boldsymbol{\epsilon}_l \end{aligned} \tag{3.29}$$

In a compact form:

$$\boldsymbol{y} = H \boldsymbol{x}_k + \boldsymbol{\epsilon} \tag{3.30}$$

It would appear that the system has been reduced to m equation and n unknowns, representing an over-parameterized problem that would lead, in principle, to a unique solution if some of the equations were linear combinations of others. However, also the vector of observation errors $\boldsymbol{\epsilon}$ is to be considered not known, turning the problem into a $m \times (m + n)$ system.

Since the problem is characterized by an infinite set of solutions from a deterministic point of view, the best estimate of the state vector must be found using optimization considerations.

3.3.2 Weighted Least Square solution with *a priori* information

The least square method (Gauss, 1809) consists of choosing, among the infinite solutions for $\boldsymbol{x}_k$ of system (3.30), the one that minimizes the following *cost function*:

$$J\left(\boldsymbol{x}_k\right) = \frac{1}{2}\boldsymbol{\epsilon}^T\boldsymbol{\epsilon} \tag{3.31}$$

defined as the sum of the squares of the observation residuals (Tapley, 2004). Extracting vector $\boldsymbol{\epsilon}$ from (3.30), an alternate expression for $J\left(\boldsymbol{x}_k\right)$ is:

$$J\left(\boldsymbol{x}_k\right) = \frac{1}{2}\left(\boldsymbol{y} - H\boldsymbol{x}_k\right)^T\left(\boldsymbol{y} - H\boldsymbol{x}_k\right) \tag{3.32}$$

This function has a minimum if both conditions:

$$\frac{\partial J}{\partial \boldsymbol{x}_k} = 0 \tag{3.33}$$

$$\delta\boldsymbol{x}_k^T\frac{\partial^2 J}{\partial \boldsymbol{x}_k^2}\delta\boldsymbol{x}_k > 0 \qquad \forall\delta\boldsymbol{x}_k \neq 0 \tag{3.34}$$

are fulfilled, in particular expression (3.34) requires that the matrix $\frac{\partial^2 J}{\partial \boldsymbol{x}_k^2}$ is *positive definite*. Applying condition (3.33) to expression (3.32) one gets:

$$-\left(\boldsymbol{y} - H\hat{\boldsymbol{x}_k}\right)^T = -H^T\left(\boldsymbol{y} - H\hat{\boldsymbol{x}_k}\right) = 0 \tag{3.35}$$

leading to the best estimate $\hat{\boldsymbol{x}_k}$ of the state defined as:

$$\hat{\boldsymbol{x}_k} = \left(H^TH\right)^{-1}H^T\boldsymbol{y} \tag{3.36}$$

where the *n x n* symmetric matrix H^TH is the *normal matrix*, which can be also defined by calculating the (*Hessian*) matrix of second derivatives:

$$\frac{\partial^2 J}{\partial \boldsymbol{x}_k^2} = H^TH \tag{3.37}$$

positive definite if H is full (n) rank (Tapley, 2004).

One of the main limitations of the simple least square method, is that all observations are uniformly weighted, regardless of the observation conditions. Suppose instead to assign to each observation $\boldsymbol{y}_i$ a different diagonal weighting matrix w_i, with its elements ranging from 0 to 1. The cost function is now:

$$J(\boldsymbol{x}_k) = \frac{1}{2}\boldsymbol{\epsilon}^T W \boldsymbol{\epsilon} \tag{3.38}$$

where $W = diag(w_1, w_2, ..., w_l)$. Repeating all the calculations done from (3.32) to (3.36), the weighted least square solution is:

$$\hat{\boldsymbol{x}_k} = \left(H^T W H\right)^{-1} H^T W \boldsymbol{y} \tag{3.39}$$

with $H^T W H$ positive definite.

If an *a priori* estimate $\bar{\boldsymbol{x}}_k$ of the state is available, together with an *a priori* weighting matrix $\bar{W}_k$, the definition of the cost function can be further modified:

$$J(\boldsymbol{x}_k) = \frac{1}{2}\boldsymbol{\epsilon}^T W \boldsymbol{\epsilon} + \frac{1}{2}\left(\bar{\boldsymbol{x}}_k - \hat{\boldsymbol{x}_k}\right)^T \bar{W}_k \left(\bar{\boldsymbol{x}}_k - \hat{\boldsymbol{x}_k}\right) \tag{3.40}$$

and the associated solution is:

$$\hat{\boldsymbol{x}_k} = \left(H^T W H + \bar{W}_k\right)^{-1} \left(H^T W \boldsymbol{y} + \bar{W}_k \bar{\boldsymbol{x}}_k\right) \tag{3.41}$$

The *a priori* solution functions as a "spring", keeping the estimate of the state not far from its previous realization. The rigidity of the spring is characterized by its *a priori* weighting matrix $\bar{W}_k$.

The *n x n* matrix:

$$P_k = H^T W H + \bar{W}_k \tag{3.42}$$

is known as the *covariance matrix* and is the inverse of the normal matrix. It is to be noted that P_k is related to two fundamental conditions: the observability of the parameters, if all the physical parameters in the solve-for vector are observable, then the covariance matrix will be full rank and have an inverse; the accuracy of the estimate, associated to the inverse of the elements of the covariance matrix.

To demonstrate the latter point, one can write equation (3.41) explicitly for each component j of the estimated state vector:

$$\hat{x_j} = \sum_{k=1}^{n} P_{jk} \left(\sum_{i=1}^{m} H_{ki} w_i y_i \right) \tag{3.43}$$

where m is the total number of observations. The weights on the measurements can be expressed as the inverse of the *variance* of the expected errors:

$$w_i = \frac{1}{\sigma_i^2} \qquad i = 1, ..., m \tag{3.44}$$

then:

$$\hat{x_j} = \sum_{k=1}^{n} P_{jk} \left(\sum_{i=1}^{m} \frac{H_{ki} y_i}{\sigma_i^2} \right) \tag{3.45}$$

suppose we want to determine what is the expected variation δx_j in the estimate of the components of the state vector when the observations vary within their *standard deviation* σ_i. Differentiating with respect to the observation vector:

$$\delta x_j = \sum_{i=1}^{m} \frac{\partial x_j}{\partial y_i} \delta y_i \tag{3.46}$$

but also from equation (3.45), the differential of x_j is:

$$\frac{\partial x_j}{\partial y_i} = \frac{\partial}{\partial y_i} \sum_{k=1}^{n} P_{jk} \left(\sum_{r=1}^{m} \frac{H_{kr} y_r}{\sigma_r^2} \right) = \sum_{k=1}^{n} P_{jk} \frac{H_{ki}}{\sigma_i^2} \tag{3.47}$$

The next step is to compute the correlation products between the different components of $\hat{\boldsymbol{x}}$ as:

$$\langle \delta x_k \delta x_l \rangle = \langle \sum_{i=1}^{m} \frac{\partial x_k}{\partial y_i} \delta y_i \sum_{j=1}^{m} \frac{\partial x_l}{\partial y_j} \delta y_j \rangle = \sum_{i=1}^{m} \sum_{j=1}^{m} \frac{\partial x_k}{\partial y_i} \frac{\partial x_l}{\partial y_j} \langle \delta y_i \delta y_j \rangle \tag{3.48}$$

Supposing that the observation errors are un-correlated one gets:

$$\langle \delta y_i \delta y_j \rangle = \sigma_i^2 \delta_{ij} \tag{3.49}$$

where δ_{ij} is the Dirac Delta. Consequently:

$$\langle \delta x_k \delta x_l \rangle = \sum_{i=1}^{m} \frac{\partial x_k}{\partial y_i} \frac{\partial x_l}{\partial y_i} \sigma_i^2 \tag{3.50}$$

We can substitute expression (3.47) for the partial derivatives into (3.50):

$$\begin{aligned}\langle \delta x_k \delta x_l \rangle &= \sum_{i=1}^{m} \left(\sum_{a=1}^{n} P_{ka} \frac{H_{ia}}{\sigma_i^2} \right) \left(\sum_{b=1}^{n} P_{lb} \frac{H_{ib}}{\sigma_i^2} \right) \sigma_i^2 \\ &= \sum_{a=1}^{n} \sum_{b=1}^{n} P_{ka} P_{lb} \sum_{i=1}^{m} \frac{H_{ia} H_{ib}}{\sigma_i^2}\end{aligned} \tag{3.51}$$

the last term represents the (a, b) component of the normal matrix, which is the inverse of the covariance matrix, thus:

$$\langle \delta x_k \delta x_l \rangle = \sum_{a=1}^{n} \sum_{b=1}^{n} P_{ka} P_{lb} P_{ab}^{-1} \tag{3.52}$$

the product between the two latter matrices represents the matrix multiplication between the covariance matrix and its inverse, hence:

$$P_{lb} P_{ab}^{-1} = \delta_{kb} \tag{3.53}$$

expression (3.52) becomes:

$$\langle \delta x_k \delta x_l \rangle = \sum_{b=1}^{n} P_{lb} \delta_{kb} = P_{lk} \tag{3.54}$$

meaning that the covariance matrix is related to the correlation product of two components of the state vector due to errors on the observables within the expected *standard deviation*.

A shortcoming of the least square method is that this criterion does not consider the statistical nature of the observation errors and makes no attempt on characterizing them as random processes (Tapley, 2004), as highlighted in expression (3.49).

In real applications, it is most unlikely that the optimal solution, as the one that minimizes the sum of the squares of the residuals, is reached after one iteration. In fact, it is highly recommended to iterate the process so that the best estimate $\hat{\boldsymbol{x}}_k^j$ at iteration j is the reference state for iteration $j + 1$.

The convergence criterion is arbitrary and can be chosen so as the difference between two consecutive estimates of the state is sufficiently small:

$$||\hat{\boldsymbol{x}}_k^j - \hat{\boldsymbol{x}}_k^{j+1}|| < \epsilon \tag{3.55}$$

The least square filter is part of a larger group of methods known as batch processors in which all the observations are referenced to the same reference epoch and a unique estimate of the state at that reference time is obtained. In the frame of this dissertation, this will be the only family of filters used and analyzed.

3.3.3 Estimate propagation

Suppose that an estimate $\hat{\boldsymbol{x}}_k$ of the state and its associated covariance matrix P_k are available at the time t_k. One could be interested in propagating the state and the covariance matrix forward in time to get a forecast of the position of the satellite at different epochs. Given the state transition matrix, the state at the time t_l is:

$$\bar{\boldsymbol{x}}_l = \Phi\left(t_l, t_k\right) \hat{\boldsymbol{x}}_k \qquad t_l > t_k \tag{3.56}$$

while the propagated covariance matrix is defined as:

$$\begin{aligned} \bar{P}_l &= E\left[\left(\bar{\boldsymbol{x}}_l - \boldsymbol{x}_l\right)\left(\bar{\boldsymbol{x}}_l - \boldsymbol{x}_l\right)^T\right] \\ &= E\left[\Phi\left(t_l, t_k\right)\left(\hat{\boldsymbol{x}}_k - \boldsymbol{x}_k\right)\left(\hat{\boldsymbol{x}}_k - \boldsymbol{x}_k\right)^T \Phi^T\left(t_l, t_k\right)\right] \end{aligned} \tag{3.57}$$

where E is the operator of the *expected value* or *mean*. In expression (3.57), $\Phi\left(t_l, t_k\right)$ is deterministic, thus:

$$\begin{aligned} \bar{P}_l &= \Phi\left(t_l, t_k\right) E\left[\left(\hat{\boldsymbol{x}}_k - \boldsymbol{x}_k\right)\left(\hat{\boldsymbol{x}}_k - \boldsymbol{x}_k\right)^T\right] \Phi^T\left(t_l, t_k\right) \\ &= \Phi\left(t_l, t_k\right) P_k \Phi^T\left(t_l, t_k\right) \end{aligned} \tag{3.58}$$

The covariance matrix at the time t_l is built by pre- and post-multiplying the covariance matrix at t_k for the transition matrix between the two epochs.

3.4 Multiarc method

Gravity experiments onboard planetary missions may last several months as in the case of Juno pericenters about Jupiter and the Ganymede phase of the JUICE mission. Therefore, instead of analyzing a huge amount of data as a single batch, sometimes it is convenient to divide the duration of the mission into many non-overlapping arcs of short duration (*e.g.* 1 day).

In section 3.1 it has been mentioned as the vector of solve-for parameters in orbit determination problems is often composed not only of the

position and velocity vectors of the spacecraft but also of other physical parameters of interest. Among these quantities, the spacecraft state vector at the initial epoch of each arc and every other parameter characteristic of the specific interval, are labeled as *local parameters*. On the other hand, there are some constants such as the coefficients of the spherical harmonic expansion of the gravity field of a planet or satellite, Love numbers and so on, that are shared by all trajectory segments and do not change arc by arc, thus they are called *global parameters*.

A single-arc estimate of the solve-for vector as described in subsection 3.3.2 is an independent solution for all local and global parameters using uniquely radiometric data collected within the single arc, not considering any correlations between adjacent arcs are not considered. The main issue with this approach is that the number of local (and therefore total) parameters to be estimated increases dramatically with the number of arcs. Also, possible mis-modelings of non-gravitational forces tend to produce errors that accumulate with time and can bias the estimate of the parameters, making single-arc estimates often inadequate for long-duration gravity experiment.

These complications can be overcome by using a multi-arc filter that includes an independent estimate of the local parameter vector $\boldsymbol{l}_i$ relative to each single arc (i) and a combined estimate of the global parameter vector $\boldsymbol{g}$, shared by all arcs. This method provides the required and necessary over-parameterization of the problem.

Going into more detail, suppose the tracking phase is divided into n arcs: the duration of the single arc must be neither too long, in order to avoid accumulation of dynamical errors, nor too short, for in this case the solution could be driven to instability.

The solve-for vector is the combination of the local and global parameters:

$$\boldsymbol{x} = [\boldsymbol{g}; \boldsymbol{l}]\,, \qquad \boldsymbol{l} = [\boldsymbol{l}_1; \boldsymbol{l}_2; ...; \boldsymbol{l}_n] \tag{3.59}$$

Analogously, the vector of observations $\boldsymbol{y}$ is an ensemble of all single observation vectors $\boldsymbol{y}_i$ ($i = 1, ..., n$) collected within the i^{th} single arc:

$$\boldsymbol{y} = [\boldsymbol{y}_1; \boldsymbol{y}_2; ...; \boldsymbol{y}_n] \tag{3.60}$$

In the multiarc solution, the matrix of the partial derivatives H is composed of two different parts:

- Partial derivatives of the observables with respect to each local-parameter vector $H^j_{\boldsymbol{l}_i} = \frac{\partial \boldsymbol{y}_j}{\partial \boldsymbol{l}_i}$
- Partial derivatives of the observables with respect to the vector of the global parameters $H^j_{\boldsymbol{g}} = \frac{\partial \boldsymbol{y}_j}{\partial \boldsymbol{g}}$

The overall matrix is then:

$$H = \begin{bmatrix} \frac{\partial \boldsymbol{y}_1}{\partial \boldsymbol{l}_1} & 0 & \dots & 0 & \frac{\partial \boldsymbol{y}_1}{\partial \boldsymbol{g}} \\ 0 & \frac{\partial \boldsymbol{y}_2}{\partial \boldsymbol{l}_2} & \dots & 0 & \frac{\partial \boldsymbol{y}_2}{\partial \boldsymbol{g}} \\ \dots & \dots & \dots & \dots & \dots \\ 0 & 0 & 0 & \frac{\partial \boldsymbol{y}_n}{\partial \boldsymbol{l}_n} & \frac{\partial \boldsymbol{y}_n}{\partial \boldsymbol{g}} \end{bmatrix} \tag{3.61}$$

At this point, to build the normal matrix C, the contribution from each single arc must be taken into account (Milani and Gronchi, 2010):

$$C = \begin{bmatrix} \left(C_{gg} + \Gamma_g^{-1}\right) & C_{gl_1} & \dots & C_{gl_{n-1}} & C_{gl_n} \\ C_{l_1 g} & \left(C_{l_1 l_1} + \Gamma_{l_1}^{-1}\right) & \dots & 0 & 0 \\ \vdots & \vdots & \vdots & \vdots & \vdots \\ C_{l_{n-1} g} & 0 & \dots & \left(C_{l_{n-1} l_{n-1}} + \Gamma_{l_{n-1}}^{-1}\right) & 0 \\ C_{l_n g} & 0 & \dots & 0 & \left(C_{l_n l_n} + \Gamma_{l_n}^{-1}\right) \end{bmatrix} \tag{3.62}$$

where:

$$C_{l_i l_j} = \left(H^j_{l_i}\right)^T H^j_{l_j} \qquad C_{gl_i} = C^T_{l_i g} = \left(H^i_g\right)^T H^i_{l_i} \qquad C_{gg} = \sum_{i=1}^{n} \left(H^i_g\right)^T H^i_g \tag{3.63}$$

the first matrix is different from the zero matrix only when $i = j$. Other matrices are the *a priori* covariance matrices for global and i-arc local parameters Γ_g and Γ_{l_i}, respectively.

The second term of the right side of normal equation (3.36), depends on the observation vector and, in the multiarc method, can be written as:

$$D = [D_g; D_l], \qquad D_g = -\sum_{i=1}^{n} \left(H^i_g\right)^T \boldsymbol{y}_i, \qquad D_{l_i} = -\left(H^i_{l_i}\right)^T \boldsymbol{y}_i \tag{3.64}$$

The normal equations for each section of the normal matrix are (Milani and Gronchi, 2010):

$$\begin{cases} C_{gg}\Delta\boldsymbol{g} + C_{gl}\Delta\boldsymbol{l} = D_g \\ C_{lg}\Delta\boldsymbol{g} + C_{ll}\Delta\boldsymbol{l} = D_l \end{cases} \tag{3.65}$$

where $\Delta\boldsymbol{g}$ and $\Delta\boldsymbol{l}$ are the corrections to the state vector obtained with the multiarc method and represent the solution for local and global parameters to a long-lasting orbit determination problem. Some weighting process for the observations and the presence of an *a priori* solution must be considered as well, I refer the interested reader to Chapter 15 of Milani and Gronchi (2010).

Chapter 4

Dynamical model and simulation setup

Simulations of radio science data acquisition are crucial during the early stage of interplanetary mission planning. By means of this numerical tool, the assessment of the experiment performance, the choice of the optimal spacecraft trajectory and the search for an effective estimation method are possible. The purpose of this chapter is to characterize in detail the dynamical model used in order to reproduce the most realistic scenario in which the spacecraft will operate. The simulation setup includes mainly the description of relevant gravitational and non-gravitational forces acting on the probe (Section 4.2), the characterization of the radio-link noise and the definition of the observation schedule.

4.1 Simulation process

Space missions dedicated to the exploration of the solar system are very long-term projects that take decades from their first concept to the decommission of the spacecraft. Until the date of the orbit insertion about the investigated body, the only available mean to get a grasp of what will be the expected accuracies in the determination of the gravity field of a planet or satellite, is to simulate, in the most realistic way, the prospected trajectory of the spacecraft and the observed observables along with it.

To do so, the necessary steps are:

- Choice of a simulated dynamical model, comprising gravitational and non-gravitational forces, the latter is dependent on both the mass and the shape of the spacecraft, therefore a description of its design model and configuration is required;

- Selection of a reference trajectory in terms of spacecraft position and velocity at defined epochs. Integration of the spacecraft trajectory using an appropriate dynamical model and nominal initial conditions;

- Production of realistic simulated tracking data, provided that the position of the ground stations involved in the experiment and the observation model are known.

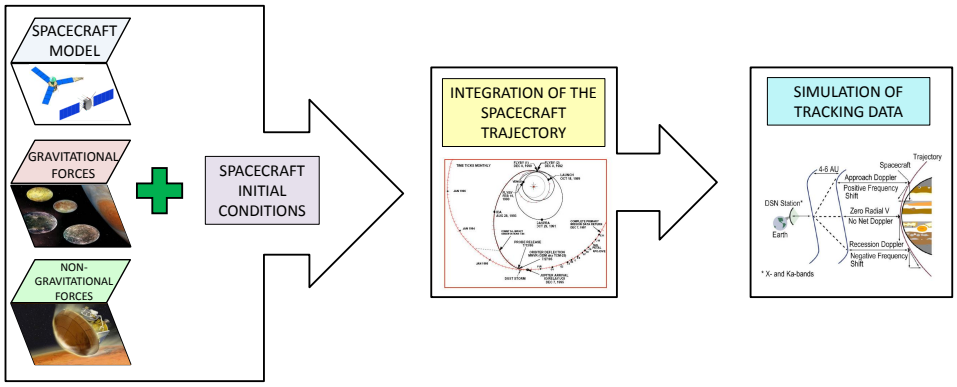

Figure 4.1: Block diagram of the simulation process, from the definition of the dynamical model to the simulation of synthetic tracking data. Image credit: JPL/Caltech for the Juno spacecraft; ESA for the JUICE spacecraft; NASA for the Jupiter system; JPL Robotics for the Aerocapture Systems Definition; NASA/JPL for the Galieleo trajectory; University of Wisconsin for Juno Doppler tracking.

Each point of the process will be thoroughly described in the next few sections.

4.2 Dynamical model

The equation of motion for a spacecraft in orbit about a central body, with respect to an inertial reference frame, can be written as:

$$\ddot{\vec{r}}_s = -\mu_p \frac{\vec{r}_{ps}}{r_{ps}^3} - \sum_k \mu_k \frac{\vec{r}_{ks}}{r_{ks}^3} - \sum_i \mu_i \left(\frac{\vec{r}_{is}}{r_{is}^3} + \frac{\vec{r}_{pi}}{r_{pi}^3} \right) + \sum_j \Delta\ddot{\vec{r}}_j \qquad (4.1)$$

where the term on the left hand represents the inertial acceleration vector of the spacecraft; the first term on the right hand is the gravitational pull due to the monopole term of the central body, the second one is the gravitational pull exerted by the kth satellite, the third one represents the third-body perturbations external to the sphere of influence of the primary body, the last one is the collection of all other gravitational and non-gravitational forces acting on the spacecraft (*e.g.* higher-degree gravity field, atmospheric drag, solar radiation pressure, etc.).

Each term of the equation will be separately discussed in the following subsections, as part of the adopted dynamical model.

4.2.1 Gravitational accelerations

In orbital mechanics gravitational forces represent the bulk of the actions which the spacecraft is subject to. For this reason, when dealing with orbit determination problems, it is crucial to define a consistent model of the gravity fields of the involved bodies.

The gravity field of Jupiter

Jupiter is a very fast rotator with an estimated rotation period of 9 h 55 m 29.71 s. As one would expect, this phenomenon affects greatly the gravity field of the body, which is supposedly, for a fluid body, almost purely zonal and symmetric with respect to the equatorial plane (Bagenal, 2004):

$$U(r,\theta) = \frac{GM}{r} \left[1 - \sum_{l=1}^{\infty} \left(\frac{R_{eq}}{r} \right)^{2l} J_{2l} P_{2l} (\cos\theta) \right] \qquad (4.2)$$

with no dependence on the longitude. Here R_{eq} is the equatorial radius and the other parameters are those introduced in Section 2.1. Equation (4.2) is exactly true when the planet acts as a rigid rotator and the flow

is a function of only the distance from the rotation axis, thus of r and θ. Deviation from the rigid rotation condition are believed to be very small for Jupiter (Hide and Stannard, 1976; Stevenson and Salpeter 1977), therefore a model that envisages the rotation of Jupiter as a solid body is an acceptable approximation.

In 2012 Hubbard proposed a model for the gravity field of a rigid rotating liquid planet based on a numerical approach to the Maclaurin solution for even zonal harmonics J_l of a constant-density body. Starting from the observation of the low-degree gravity field of Jupiter from pre-Juno observations (Jacobson, 2003), the results for the even zonal harmonics of Jupiter up to degree 30, are reported in Table 4.1. I refer the interested reader to Hubbard (2012).

degree (n)	$J_n \times 10^6$ (calculated)	$J_n \times 10^6$ (observed)[a]
2	14696.43	14696.43 ± 0.21
4	-587.14	-587.14 ± 1.68
6	30.82	34.25 ± 5.22
8	-1.862	...
10	0.1227	...
12	-8.573×10^{-3}	...
14	6.253×10^{-4}	...
16	-4.711×10^{-5}	...
18	3.641×10^{-6}	...
20	-2.873×10^{-7}	...
22	2.304×10^{-8}	...
24	-1.873×10^{-9}	...
26	1.534×10^{-10}	...
28	-1.154×10^{-11}	...
30	6.358×10^{-13}	...

Table 4.1: Jupiter's un-normalized even zonal harmonics. [a]Jacobson (2003).

The harmonic coefficients in Table 4.1 are used as the reference gravity field in the simulations of the Juno gravity experiment (Finocchiaro, 2013), while possible asymmetrical deviations from the condition of perfectly zonal flows will be discussed extensively in Chapter 5 as part of this

dissertation.

Regarding Jupiter's tidal deformations due to the perturbing effect of Io, in the frame of these simulations Jupiter's Love numbers of degree 2 and 3 (k_2 and k_3) have been tentatively set to the value of 0.5.

The gravity field of Ganymede and Callisto

The Galileo mission has performed several flybys of Jupiter's main satellites, some of which were dedicated to the determination of their gravity fields, up to different degrees. Table 4.2 shows the current knowledge of the Jovian satellite gravity in terms of estimated spherical harmonic coefficients for three of the Galilean moons, by means of Doppler tracking of the Galileo spacecraft (Bagenal, 2004).

Body	$GM\ (km^3/s^2)$	$J_2\ (10^6)$	$C_{22}\ (10^6)$	μ
Ganymede	9887.83 ± 0.03	127.53 ± 2.9	38.26 ± 0.87	1.000
Callisto	7179.29 ± 0.01	32.7 ± 0.8	10.2 ± 0.3	0.997
Europa	3202.72 ± 0.02	435.5 ± 8.2	10.2 ± 0.3	0.993

Table 4.2: Low-degree un-normalized spherical harmonic coefficients for the gravity fields of Ganymede, Callisto and Europa from Galileo gravity data (Bagenal, 2004). μ is the correlation coefficient.

The estimate of the degree-2 coefficients for the satellites of Jupiter has been carried out applying the condition of hydrostatic equilibrium ($J_2/C_{22} = 10/3$), which explains the high-correlation between the coefficients of the spherical harmonic expansion. For the simulations of the JUICE gravity experiment, these values are considered as the baseline for the simulated gravity field.

Ganymede is the main scientific objective of the JUICE mission, therefore some effort has been put in order to simulate a more realistic gravity field expansion then that in Table 4.2. Specifically, its gravitational potential has been expanded in spherical harmonics up to degree and order 30, in the following way:

- degree-2 coefficients from the hydrostatic solution by Anderson *et al.* (1996, Table 4.2);

- degree-3 coefficients as a mean between Titan SOL1 + 1σ and SOL2 + 1σ in Iess *et al*. (2010);
- degree-4 to 30 coefficients using Kaula's rule (Section 2.1.4) with $A_k = 2$, corresponding to a very weak field.

The reference high-degree gravity field is tabulated in Table 4.3, where, however, only the zonal harmonics are displayed for simplicity.

Coefficient (zonal)	Simulated value
C_{30}	7.6 $\times 10^{-7}$
C_{40}	5.6 $\times 10^{-7}$
C_{50}	-7.0 $\times 10^{-7}$
C_{60}	4.8 $\times 10^{-7}$
C_{70}	-1.8 $\times 10^{-7}$
C_{80}	-2.1 $\times 10^{-7}$
C_{90}	-1.3 $\times 10^{-7}$
$C_{10\,0}$	8.4 $\times 10^{-8}$
$C_{11\,0}$	-5.6 $\times 10^{-7}$
$C_{12\,0}$	4.9 $\times 10^{-7}$
$C_{13\,0}$	-4.3 $\times 10^{-7}$
$C_{14\,0}$	3.9 $\times 10^{-7}$
$C_{15\,0}$	-3.5 $\times 10^{-7}$
$C_{16\,0}$	3.2 $\times 10^{-7}$
$C_{17\,0}$	-2.9 $\times 10^{-7}$
$C_{18\,0}$	2.7 $\times 10^{-7}$
$C_{19\,0}$	-2.4 $\times 10^{-7}$
$C_{20\,0}$	2.3 $\times 10^{-7}$
$C_{21\,0}$	-2.1 $\times 10^{-7}$
$C_{22\,0}$	2.0 $\times 10^{-7}$
$C_{23\,0}$	-1.8 $\times 10^{-7}$
$C_{24\,0}$	1.7 $\times 10^{-7}$
$C_{25\,0}$	-1.6 $\times 10^{-7}$
$C_{26\,0}$	1.5 $\times 10^{-7}$
$C_{27\,0}$	-1.4 $\times 10^{-7}$
$C_{28\,0}$	1.4 $\times 10^{-7}$
$C_{29\,0}$	-1.3 $\times 10^{-7}$
$C_{30\,0}$	1.2 $\times 10^{-7}$
$k_{2_{\Re}}$	0.30
$k_{2_{\Im}}$	0.00

Table 4.3: Normalized simulated full 30×30 zonal gravity field of Ganymede (weak case) plus tidal Love numbers.

Ganymede's degree-2 Love numbers were set to a Earth-like value for the real component ($k_{2_{\Re}} = 0.3$) and to null for the imaginary component ($k_{2_{\Im}} = 0.0$).

The 20 flybys of Callisto will allow the determination of its full degree-3 gravity field plus the real component of its Love number k_2. In addition to the estimated values for the quadrupole field reported in Table 4.2, a full octupole expansion has been considered, with the coefficients randomly chosen among those that satisfy Kaula's rule with A_k computed using the degree-2 coefficients (though the law should be applied for $l \gg 2$).

The following values were used for the integration of the spacecraft trajectory during the Callisto phase:

Coefficient (real)	Simulated value	*Coefficient (imaginary)*	Simulated value
C_{30}	-7.4403 $\times 10^{-6}$		
C_{31}	4.4815 $\times 10^{-6}$	S_{31}	4.2071 $\times 10^{-6}$
C_{32}	1.0356 $\times 10^{-6}$	S_{32}	-1.0708 $\times 10^{-6}$
C_{33}	-1.4090 $\times 10^{-6}$	S_{33}	-2.7244 $\times 10^{-6}$
$k_{2_{\Re}}$	0.30	$k_{2_{\Im}}$	0.00

Table 4.4: Un-normalized simulated 3x3 gravity field for Callisto.

The real component of the tidal Love number was set to $k_{2_{\Re}}$ = 0.3 for Callisto as well.

Other gravitational effects

In addition to the detailed definition of the gravity fields of the bodies directly involved in the Juno and JUICE gravity experiments, one must take into account the point mass acceleration exerted by all other main bodies in the solar system: Sun, Mercury, Venus, Earth, Mars, Saturn, Uranus, Neptune, Pluto, Moon, Jupiter's moons Io and Amalthea. Information about the mass of celestial bodies are provided by NASA/JPL's planetary ephemerides. For Juno and JUICE simulations, ephemeris set DE421 was used.

For Jupiter, Saturn and the Sun, relativistic effects become relevant because of their masses and must be considered in the dynamical model.

4.2.2 Planetary rotation model

The rotational models used in the simulations of the gravity experiments are those filed in the official Report of the IAU Working Group (Archinal *et al.*, 2010), giving the rotation of the pole and the prime meridian of planets and satellites.

4.2.3 Non-gravitational accelerations

Unlike the study of the motion of celestial bodies, the trajectory of an artificial satellite is markedly influenced by non-gravitational effects. In general, the absence of an onboard accelerometer makes the detailed modeling of such perturbations, that depend on both the mass and the geometry of the spacecraft, necessary. For this reason, a brief description of the Juno and the JUICE spacecraft models, in their science phase configurations, will precede the characterization of non-gravitational accelerations.

Juno spacecraft model for orbit determination

The Juno spacecraft will be the first solar-powered mission to ever reach the Jovian system. Consequently, the design of the spacecraft is mainly driven by the necessity of collecting enough solar power.

Figure 4.2: The Juno spacecraft. Image credit: NASA.

The geometry of the spacecraft is, in fact, dominated by three supersized surfaces hosting more than 18,000 solar cells for a span of over 20 m

(Juno Press Kit, Figure 4.2). In addition, the hexagonal bus of the spacecraft and the High Gain Antenna are also identified as main components.

In the orbit determination code, the probe is sketched as a compound of five basic components, synthetically described in Table 4.5.

Element	**Model**	**Pointing**	**Size**
Solar array 1	flat plate	$\vec{n} \parallel \vec{r}_{EP}$	$S = 23.85m^2$
Solar array 2	flat plate	$\vec{n} \parallel \vec{r}_{EP}$	$S = 23.85m^2$
Solar array 3	flat plate	$\vec{n} \parallel \vec{r}_{EP}$	$S = 23.85m^2$
High Gain Antenna	antenna	$\vec{k} \parallel \vec{r}_{EP}$	$r = 1.25m$
			$d = 0.47m$
Bus	cylinder	$\vec{k} \parallel \vec{r}_{EP}$	$r = 1.75m$
			$l = 3.50m$
Overall Mass			1593.0 kg

Table 4.5: Summary of the geometric properties of the Juno spacecraft components. $\vec{n}$ is the normal unit vector, S is the overall surface, $\vec{k}$ specifies the axis direction, r is the radius, d is the depth and l is the length. The information has been retrieved from the Juno Launch Press Kit.

A constant value for the overall mass of the spacecraft has been considered, although changes in this value are expected due to maintenance maneuver fuel consumption.

Some of the non-gravitational accelerations such as solar radiation pressure, albedo and planetary infrared emission depend on the optical properties of the listed components. The incident electromagnetic radiation that hits the surfaces of the spacecraft, is partially (ratio of r) reflected both specularly (ratio of s) and diffusively (ratio of $1-s$). These phenomena are characterized by specular reflection ν_s and diffusive reflection ν_d coefficients, respectively. Table 4.6 lists the adopted value for these properties:

Element	ν_s	ν_d
Solar array 1	0.016	0.123
Solar array 2	0.016	0.123
Solar array 3	0.016	0.123
High Gain Antenna	0.036	0.176
Bus	0.074	0.252

Table 4.6: Optical properties adopted for the Juno spacecraft model. For the solar panels and the other components, SMART-1 like and Cassini-like properties have been adopted, respectively.

JUICE spacecraft model for orbit determination

The current JUICE spacecraft design foresees the exploitation of solar radiation as the main source of power during all the phases of the exploration of Jupiter's satellite system. Therefore the same considerations pointed out before about the geometry of the spacecraft are still valid.

At present, three different spacecraft concepts are being evaluated by ESA and undergoing feasibility studies. Since detailed descriptions of the design are not yet available, in this work, the adopted 2-panel model is the heritage from the joint ESA/NASA EJSM/Laplace mission, withdrew in 2011 and predecessor of JUpiter ICy moon Explorer (Figure 4.3; ESA, 2009). For orbit determination purposes, four main structural elements have been identified: 2 solar arrays, 1 HGA and 1 bus. The properties and characteristics of each element are listed in Table 4.7.

Element	Model	Pointing	Size	ν_s	ν_d
Solar array 1	Flat plate	$\vec{n} \parallel \vec{r}_{EP}$	$S = 32m^2$	0.016	0.123
Solar array 2	Flat plate	$\vec{n} \parallel \vec{r}_{EP}$	$S = 32m^2$	0.016	0.123
High Gain Antenna	Antenna	$\vec{k} \parallel \vec{r}_{EP}$	$r = 1.40m$	0.036	0.176
			$d = 0.52m$		
Bus	Cylinder	$\vec{k} \parallel \vec{r}_{EP}$	$r = 1.0m$	0.074	0.252
			$l = 2.50m$		
Overall Mass			1493.5 kg		
Drag Coefficient			2.05		

Table 4.7: Summary of the geometric properties of the JUICE spacecraft components.

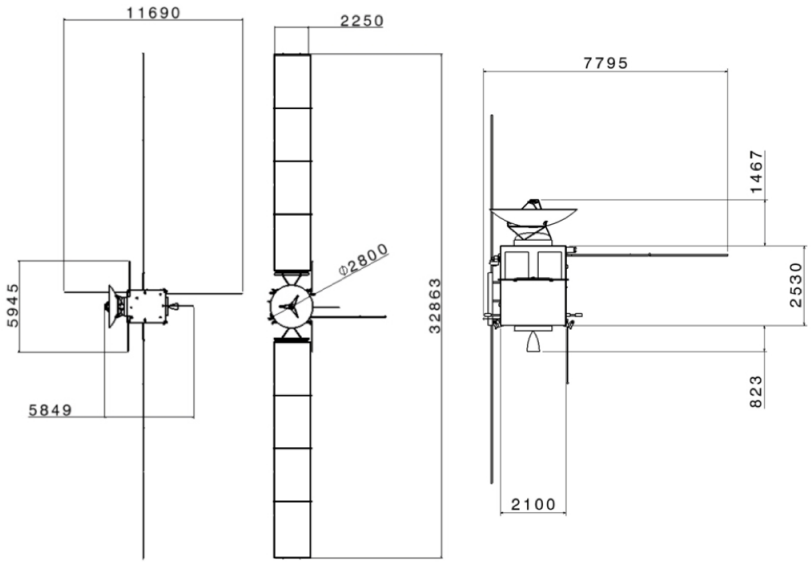

Figure 4.3: Sketched model of the JUICE spacecraft, dimensions are given in mm. Image credit: ESA.

The optical properties have been chosen using the same criteria as for the Juno spacecraft model.

As Ganymede possesses a thin atmosphere (likely rich of H_2, H_2O, O_2, OH, O and H) the JUICE spacecraft will be subject to atmospheric drag during the science phase at this satellite. For this reason, a realistic value of the drag coefficient of the spacecraft must be assigned. For the purpose of this dissertation, a Cassini-like value of $C_D = 2.05$ has been adopted.

Solar Radiation Pressure

It is defined as the force per unit area exerted on the spacecraft surfaces by solar electromagnetic radiation. The presence of large panels oriented towards the Sun in both designs suggests that solar pressure will cause non-negligible perturbations on the trajectory of the probes.

The acceleration sensed by the spacecraft and due to this phenomenon can be expressed as (ODP User's Manual v.1, p.113):

$$\vec{\ddot{r}} = \left(\frac{C_1 P}{m r_{SP}^2} \right) \vec{F_B} \tag{4.3}$$

where $C_1 = \frac{\Phi_{1AU} r_{1AU}^2}{c} = 1.02 \times 10^8 \frac{kgkm^3}{m^2 s^2}$ is the solar flux constant at

one Astronomic Unit; P is the shadow factor ($P = 1$ if the spacecraft is in clear sunlight, $P = 0$ if the spacecraft is in umbra); m is the mass of the spacecraft; r_{SP} is the distance between the Sun and the probe; $\vec{F_B}$ is a vector that depends on the ratio of the effective area to the nominal area of the spacecraft in each direction $\hat{U}_{SP}, \hat{X}_{SP}, \hat{Y}_{SP}$ (where the first direction is along $\vec{r}_{SP}$) and degradation factors;

Albedo and thermal emission

These non-gravitational effects are due to the sunlight reflected by the surface of a planet or satellite and act on the spacecraft causing a non-negligible acceleration (ODP User's Manual v.1, p.128):

$$\vec{\ddot{r}} = \int_S G \left(\sum_i F_{Ti} \hat{N}_i + F_{Ri} \hat{r}_{pS} \right) \frac{cos\psi}{\pi r_{pS}^2} dA \tag{4.4}$$

for albedo:

$$G = \frac{-C_1 K \cos\psi_s}{m r_{cs}^2} \sum_{l=0}^{10} \sum_{m=0}^{l} \left(C_{lm}^A \cos m\lambda + S_{lm}^A \sin m\lambda \right) P_{lm} \left(sin\phi \right) \tag{4.5}$$

for thermal emission:

$$G = \frac{-C_1}{4 m r_{cs}^2} \sum_{l=0}^{10} \sum_{m=0}^{l} \left(C_{lm}^E \cos m\lambda + S_{lm}^E \sin m\lambda \right) P_{lm} \left(sin\phi \right) \tag{4.6}$$

where K is the analogous of the shadow factor; r_{cs} is the planet-Sun distance; ψ_s is the Sun - planet center - point P on the planet (dA) angle; A is the albedo of the planet in spherical harmonics; E is the thermal emission coefficient in spherical harmonics.

For the bodies involved in the Juno and JUICE missions, the following albedo and thermal coefficients have been assumed:

Body	A			E		
Jupiter	C_{00}^{A}	=	0.520^{a}	C_{00}^{E}	=	1.020^{b}
				C_{10}^{E}	=	0.056
				C_{20}^{E}	=	-0.474
				C_{30}^{E}	=	-0.106
				C_{40}^{E}	=	0.007
				C_{50}^{E}	=	0.078
				C_{60}^{E}	=	-0.110
				C_{70}^{E}	=	-0.060
				C_{80}^{E}	=	0.013
				C_{90}^{E}	=	0.009
				C_{100}^{E}	=	-0.011
Ganymede	C_{00}^{A}	=	0.430^{c}	C_{00}^{E}	=	0.950^{d}
Callisto	C_{00}^{A}	=	0.170^{c}	C_{00}^{E}	=	0.800^{e}
Europa	C_{00}^{A}	=	0.670^{c}	C_{00}^{E}	=	0.960^{f}

Table 4.8: Planetary radiation coefficients. [a]Jupiter albedo coefficients for the Juno orbit determination (Finocchiaro, 2013); [b]Jupiter thermal emission coefficients for the Juno orbit determination (Finocchiaro, 2013); [c]Yeomans (2006); [d]Spencer *et al.*, 1983; [e]Burgdorf *et al.*, 2000; [f]Marshall *et al.*, 2011.

Atmospheric drag

The acceleration on the spacecraft caused by the atmospheric drag exerted by a planetary atmosphere is (ODP User's Manual v.1, p.147):

$$\ddot{\vec{r}} = -\frac{1}{2m}\rho C_D S V_b \vec{V}_b \tag{4.7}$$

where ρ is the atmospheric density, C_D is the spacecraft drag coefficients, S is the cross-sectional area and $\vec{V}_b$ is the body-fixed spacecraft velocity. The implementation of a suitable atmosphere-spacecraft interaction is relevant only in the Ganymede science phase of the JUICE mission, at least in this work.

In 2007, Marconi proposed a kinetic, multispecies, 2-D axisymmetric model of Ganymede's neutral atmosphere, using the available observations. The resulting density profiles of different compounds are shown to depend on the altitude and the subsolar latitude, keeping in mind that the subsolar point (subsolar latitude = 0) is the point on the planet or satellite where the Sun is perceived to be at zenith. Figure 4.4 shows the results of

the simulations in terms of species abundance.

From Figure 4.4 it is clear that the natural choice for the atmospheric model to be implemented in the numerical simulation of JUICE Ganymede phase is that of a density profile depending on both the altitude and the angular distance from the subsolar point.

For instance, the Harris-Priester atmospheric model can be adopted, where (ODP User's Manual v.1, p.155):

$$\rho\left(h\right) = \left(1 + \rho_0 \cos^n\left(\psi/2\right)\right)\left(\rho_m\left(h\right) + \left(\rho_M\left(h\right) - \rho_m\left(h\right)\right)\cos^n\left(\psi/2\right)\right) \quad (4.8)$$

here ρ_0 and n are model constants, ψ is the subsolar latitude of the spacecraft, and ρ_m and ρ_M are the minimum and maximum densities at a certain altitude h, respectively.

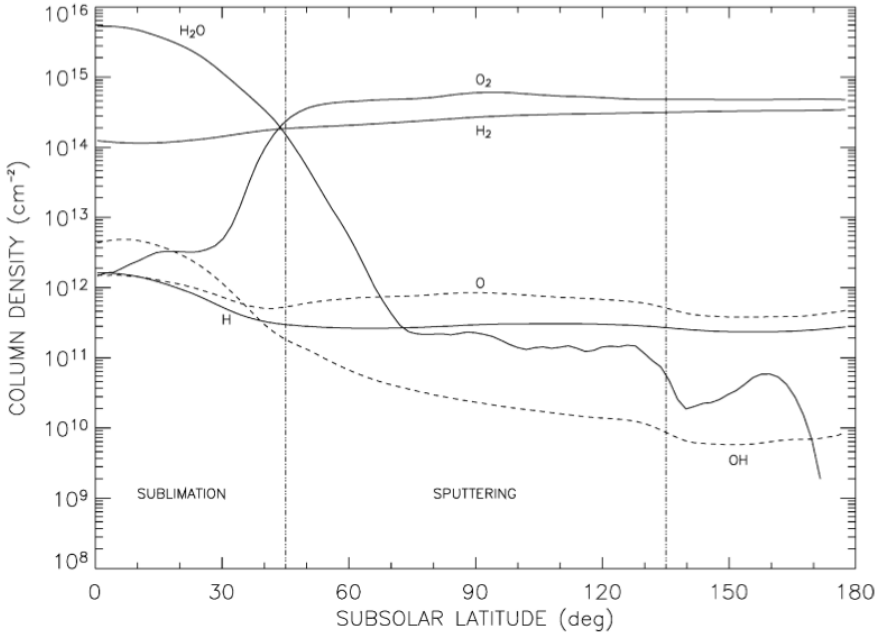

(a)

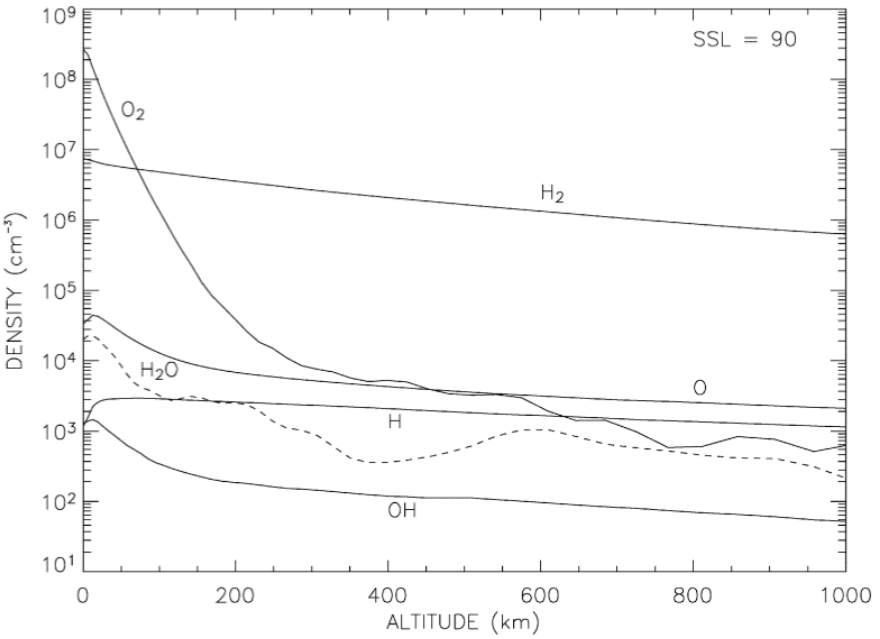

(b)

Figure 4.4: Plots from Marconi (2007). Column density of Ganymede's atmosphere with respect to subsolar latitude (a). Density at 90° subsolar latitude with respect to the altitude over Ganymede's surface (b).

4.2.4 Simulated trajectories

Juno

The nominal trajectory of the Juno mission is stored in a SPICE kernel provided by NASA/JPL. In the simulations of the Juno gravity experiment the science phase has been divided into 25 arcs of duration $24h$ ($\pm 12h$ from perijove), corresponding to the 25 pericenters dedicated to gravity investigations. The state of the Juno spacecraft is re-initialized at every starting epoch of each arc.

The geometry of the science orbits has been briefly introduced in Chapter 1: the orbit is highly eccentric ($e = 0.95$), highly inclined ($i = 90^\circ \pm 10^\circ$) and repetitive in an inertial reference frame (Figure 4.5). The observation period for the gravity experiment goes from November 21, 2016 to September 25, 2017.

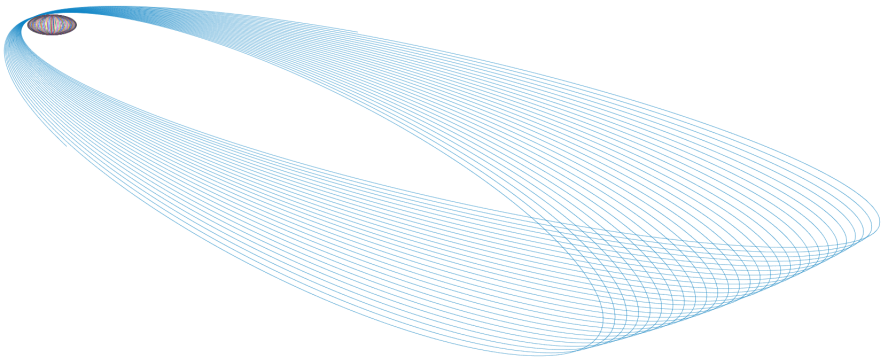

Figure 4.5: Juno science orbits around Jupiter. The size of the orbits and Jupiter is to scale.

Table 4.9 reports all the relevant information about Juno simulated closest approaches to Jupiter.

Since the design of the spacecraft and that of the trajectory is driven by the necessity of pointing the solar panels towards the Sun, as a consequence the angle α between the orbital plane and the line of sight of the spacecraft is always close to 90°, not representing the best scenario for radio science experiments.

Orbit	Day of C/A	Latitude (°)	Longitude (°)	Altitude (km)	α (°)
1	11/21/2016	6.5	156.9	4162.6	73.5
2	01/15/2017	11.3	277.8	3636.6	67.3
3	01/26/2017	12.3	86.2	3722.9	66.2
4	02/06/2017	13.2	254.24	3743.3	65.9
5	02/17/2017	14.2	62.7	3671.6	66.4
6	02/28/2017	15.1	230.9	3988.1	67.5
7	03/11/2017	16.1	39.0	3760.4	68.4
8	03/22/2017	17.0	207.5	3891.8	69.0
9	04/02/2017	18.0	15.6	3940.1	70.8
10	04/13/2017	18.9	183.9	3808.7	71.5
11	04/13/2017	19.9	4.2	3716.1	73.1
12	05/05/2017	20.8	172.4	3937.5	74.4
13	05/16/2017	21.8	340.5	3705.4	75.0
14	05/27/2017	22.8	149.0	3855.5	75.3
15	06/07/2017	23.7	317.1	4000.9	75.9
16	06/18/2017	24.7	125.5	3890.1	76.0
17	06/29/2017	25.6	293.7	4022.8	75.1
18	07/10/2017	26.6	102.0	4130.6	74.3
19	07/21/2017	27.5	270.2	4117.1	74.3
20	08/01/2017	28.5	78.7	4137.4	72.1
21	08/11/2017	29.3	246.8	4380.6	71.2
22	08/22/2017	30.4	55.1	4123.6	68.8
23	09/02/2017	31.2	223.5	4414.2	67.5
24	09/13/2017	32.2	31.6	4397.0	65.3
25	09/24/2017	33.2	200.1	4567.7	63.1

Table 4.9: Information about the geometry of the ground tracks at the epochs of pericenters. The latitude and longitude of the C/As are given with respect to Jupiter body-fixed reference frame. α is the angle between the line of sight and the orbital plane.

JUICE

ESA provided JUICE Science Team with the SPICE kernel of the spacecraft trajectory covering the whole duration of the mission. For the simu-

lations of the gravity experiment the nominal trajectory has been divided into the following phases (in chronological order):

- 20 arcs of 1-day duration representing the 20 gravity flybys of Callisto (from November 16, 2030 to February 1, 2032). The state of the spacecraft is initialized $12h$ prior to each closest approach. Figure 4.6 shows the ground tracks (yellow curves) of the spacecraft over the surface of Callisto during this science phase:

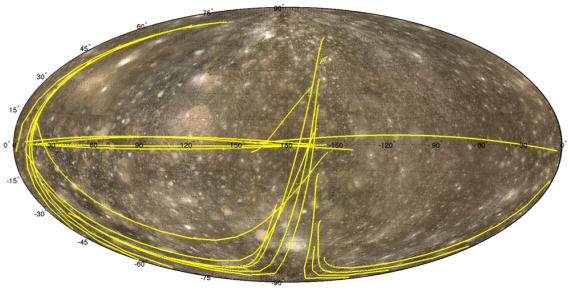

Figure 4.6: JUICE ground tracks over Callisto's surface around closest approach ($\pm 4h$).

- 132 continuing arcs of 1-day duration (from February 22, 2033 to July 3, 2033) representing the polar orbital phase at Ganymede. Figure 4.7 shows the altitude of the spacecraft over the surface of the satellite through the 3-month investigation;

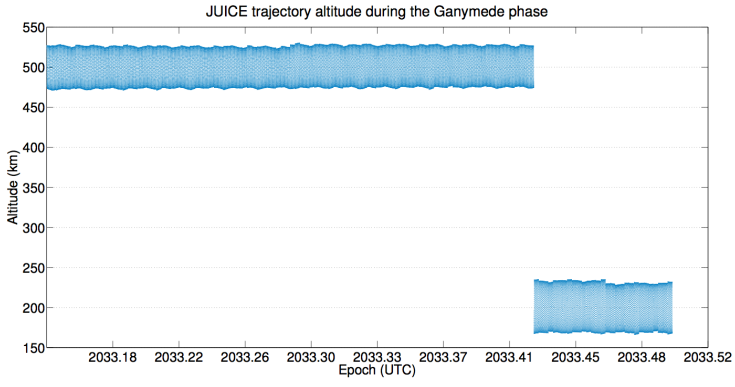

Figure 4.7: Altitude of the JUICE spacecraft over Ganymede during the orbital phase. The separation between the 500-km altitude and 200-km altitude phases is evident.

4.3 Sources of noise on radiometric measurements

For the sake of the simulations of gravity experiments, it is crucial to correctly account for all possible noise sources affecting radiometric observables. Being the Doppler measurement the main mean by which interplanetary probes are tracked by ground stations, in this section I will focus on the description of possible disturbances affecting range-rate observations. The main causes of errors on these measurements are those due to media propagation and instrumentation itself. Here the observations will be noted as $y(t)$, defined as the ratio of the fluctuation in frequency between the received and reference signals and the nominal frequency f_0 (Asmar *et. al.*, 2005):

$$y(t) = \frac{\Delta f(t)}{f_0} \tag{4.9}$$

This quantity includes both the signal and the noise. The Allan deviation represents frequency fluctuation as a function of the averaging time τ (Asmar *et. al*, 2005):

$$\sigma_y^2(\tau) = \frac{1}{2}\langle \mid \bar{y}(t) - \bar{y}(t+\tau) \mid^2 \rangle \tag{4.10}$$

where: $\bar{y}(t) = \int_{t'}^{t'+t} y(t')\, dt'$. This parameter is a measure of the frequency stability.

4.3.1 Instrumental noise

This source of random errors depends upon the characteristics of the onboard and ground instrumentation. This contribution can be divided into several separate effects (Asmar *et. al*, 2005).

Thermal noise

One of the major instrumental effects is that due to the finiteness of the radio link signal to noise ratio (SNR). This phase noise is white and is also regarded as thermal noise, causing the degradation of the radio signal. Every not-idealized system characterized by a temperature above the absolute zero (like the onboard DST and KaT) produces a noise component due to

the thermal agitation of the particles characterized by electric charge, causing fluctuations in the electric tension. The SNR is defined, intuitively, as the ratio of the power associated to the signal and the noise power. In order to quantify the thermal noise, one must consider that the effect is governed by the least favorable leg of the link, in the case of two-way Doppler measurements, the downlink, because of the limited onboard power. The Allan deviation associated with thermal noise can be estimated as:

$$\sigma_y(\tau) = \frac{1}{2\pi f_0 \tau}\sqrt{\frac{3B}{(SNR)_{UL} + (SNR)_{DL}}} \tag{4.11}$$

where f_0 is the downlink frequency and B is the working bandwidth of the phase locked loop.

To quantify the entity of the thermal noise superimposed to two-way Doppler measurements, it is necessary to carry out the link budget between the spacecraft and the ground station. Generally speaking, the power received by the receiving antenna can be expressed, in terms of dBW, as:

$$P_{RX} = EIRP + G_{RX} - L_{ATM} - L_{FS} \tag{4.12}$$

where $EIRP = P_{TX} + G_{TX}$ is the Equivalent Isotropically Radiated Power, P_{TX} is the transmitted power, G_{TX} and G_{RX} are the transmitting and receiving antenna gains, respectively, L_{ATM} is the media propagation attenuation and L_{FS} is the free space attenuation.

In turn, the generic antenna gain can be computed as:

$$G = \eta\left(\frac{\pi D}{\lambda}\right)^2 \tag{4.13}$$

where η is the antenna efficiency, D is the antenna diameter and λ is the wavelength of the electromagnetic signal. The free space losses depend on the radial distance R between the station and the spacecraft:

$$L_{FS} = \left(\frac{4\pi R}{\lambda}\right)^2 \tag{4.14}$$

The power associated to the noise has to be quantified as well. For this quantity, the following simple relation holds:

$$N = KT_{sys}B \tag{4.15}$$

Parameter	**Juno**	**JUICE**
Ground Station antenna diameter (m)	34.0$^{(a)}$	35.0$^{(b)}$
Ground Station antenna efficiency	0.6	0.6
Ground Station system temperature (K)	39.6$^{(a)}$	39.6
Ground Station PLL bandwidth (Hz)	0.1	0.1
Spacecraft antenna diameter (m)	2.5	2.8
Spacecraft antenna efficiency	0.6	0.6
Spacecraft system temperature (K)	300$^{(c)}$	300
Spacecraft PLL bandwidth (Hz)	1.0$^{(c)}$	1.0
Distance from Earth (AU)	4.0-6.5	4.0-6.5
Uplink frequency (GHz)	34.4	34.4
Uplink wavelength (mm)	8.7	8.7
Transmitted power (dBW)	28.8$^{(a)}$	29.0
Transmitting antenna gain (dBi)	79.5	79.8
Transmitting antenna polarization loss (dB)	0.08	0.08
Transmitting antenna pointing loss (dB)	0.12$^{(a)}$	0.12
Free Space loss (dB)	302.2	302.3
Atmospheric attenuation (dB)	0.37$^{(a)}$	0.37
Receiving antenna gain (dBi)	56.9	57.9
Receiving circuit loss (dB)	1.69	1.69
Receiving antenna pointing loss (dB)	0.20	0.20
Received power (dBW)	-139.5	-139.0
Noise power (dBW)	-203.8	-203.8
Uplink SNR	64.3	64.8
Downlink frequency (GHz)	32.0	32.0
Downlink wavelength (mm)	9.4	9.4
Transmitted power (dBW)	4.0$^{(d)}$	7.0
Transmitting antenna gain (dBi)	56.2	57.5
Transmitting antenna circuit loss (dB)	1.69	1.69
Transmitting antenna pointing loss (dB)	0.20	0.20
Free Space loss (dB)	301.6	301.9
Atmospheric attenuation (dB)	0.37	0.37
Receiving antenna gain (dBi)	78.9	79.1
Receiving antenna polarization loss (dB)	0.08	0.08
Receiving antenna pointing loss (dB)	0.12	0.12
Received power (dBW)	-165.9	-160.8
Noise power (dBW)	-212.6	-212.6
Downlink SNR	46.7	51.8

Table 4.10: Summary of the link budget for a space mission at Jupiter. $^{(a)}$ Slobin, 2012; $^{(b)}$ ESA, 2013b; $^{(c)}$ TAS-I; $^{(d)}$ Simone *et al.*, 2009. Values of other parameters, such as the power transmitted by the JUICE spacecraft, have been arbitrarily, yet coherently, selected.

where K is the Boltzmann constant, T_{sys} is the system temperature and B is the bandwidth.

Table 4.10 reports the link budget carried out for both legs of the link, for the missions Juno and JUICE.

Other sources of instrumental noise

The ground and spacecraft electronics also affect the total noise budget. However, at present, the transponder noise and ground instrumental noise do not contribute markedly to the total system noise. As a reference one can use the value of the transponder noise as measured on the ground for the Cassini mission: 10^{-15} for the DST and as small as 2×10^{-16} for the Ka-band translator.

Another source of Doppler noise is represented by un-modeled perturbations of the spacecraft motion, contributing with few parts per 10^{16} (at 1000 seconds integration time) to the total noise, provided that the spectra is measured for $f > 0.1mHz$. The very low frequency contribution is, instead, of a few parts in 10^{15}. Also, one must consider the ground antenna motion noise that can cause significant disturbances of the radio link ($1 - 4 \times 10^{-15}$ at $\tau = 1000s$) depending on the diameter of the antenna.

Noise associated to the frequency and timing system (FTS), is not really an issue for two-way Doppler measurements. In fact, the frequency standard is the same for both the uplink and the downlink, which is ground-based with a stability better than 10^{-15} at 1000 seconds integration time when using, for example, hydrogen masers.

4.3.2 Propagation in the medium

When dealing with the propagation of radio signals, one must take into account that, in order to connect to deep space probes, the electromagnetic wave passes through at least three different media characterized by different refractive indexes: the Earth's troposphere and ionosphere and the solar wind. These diverse contributions will be briefly described in the following subsections.

Tropospheric noise

In the microwave region of the electromagnetic spectrum, the Earth's troposphere behaves as a non-dispersive medium, meaning that the refractive index is not a function of the frequency, but is, indeed, dominated by the water vapor content. The troposphere is that portion of the atmosphere that extends from the sea level up to 17 km at the equator and 9 km at the poles. It is dominated by the motion of large fluid masses due to density and temperature gradients.

The refractive index n of the medium depends on the polarization of the gas molecules, on the fluid density and its absolute temperature. Introducing the *refractivity* as $N = (n-1) \times 10^6$, the fluctuations due to the dry and wet component of the troposphere can be expressed as (Bernardini, 2008):

$$N = \frac{A}{T}\left(p_{tot} + \frac{p_v B}{T}\right) = N_{dry} + N_{wet} \tag{4.16}$$

where $A = 77.6K/mbar$ and $B = 4180K$ are constants, T is the absolute temperature, p_{tot} is the total pressure, p_v is the water vapor partial pressure. This parameter is, evidently, a function of the altitude. The effect of n not being unitary, is that the signal path is not straight but rather bent, the optical path is defined as:

$$L_{opt} = \int_L n\,(s)\,ds \tag{4.17}$$

where L is the trajectory of the signal. The difference between the optical and geometric paths is:

$$\Delta L = \int_L (n-1)\,ds = f\,(E) \tag{4.18}$$

being a function of the station elevation E, which is the angle between the local horizon and the spacecraft as seen by the spacecraft (Figure 4.9). The smaller is the elevation angle, the wider is the portion of the troposphere crossed by the signal and the larger is the tropospheric delay.

Studies of water vapor seasonal fluctuations show that these are higher during summer rather than during winter (Asmar *et. al*, 2005). The disturbances affecting the refractive index are variable depending if considering

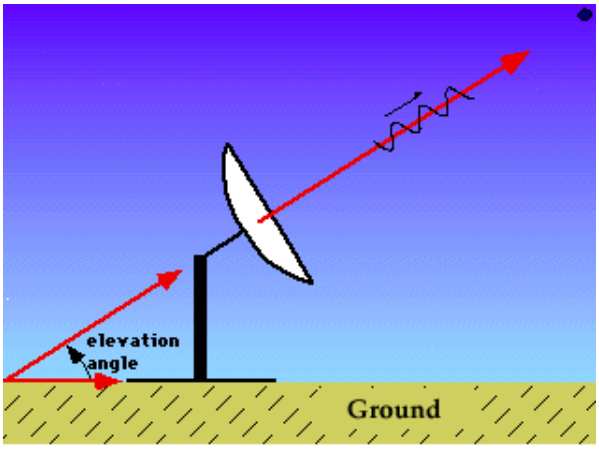

Figure 4.8: Ground station elevation angle (MeteoTrentino.it).

the dry or wet component: usually the latter is the dominant part where the fluctuations can vary in the range $3 - 30 \times 10^{-15}$ at $\tau = 1000s$.

Ionospheric noise

The ionosphere is the region of the Earth's atmosphere that extends from 85 km of altitude to about 600 km. The effect of the direct exposition to solar radiation (UV) is that this layer is ionized and therefore composed of plasma rich in atoms and electrically charged atoms and molecules, deeply affecting radio propagation.

The fluctuations due to the crossing of the terrestrial ionosphere by the signal are proportional to $\frac{1}{f^2}$, where f is the carrier frequency. This relation clearly states that the ionosphere is a dispersive medium, with disturbances the weaker, the higher the frequency. For radio links exploiting the Ka-band ($\sim 32GHz$) these effects are very small compared to those affecting the X and S bands.

Intuitively, the refraction index is not only a function of the carrier frequency, but also of the electron density N_e. To quantify this correlation, a very important property introduced in the study of ionospheres is the *Total Electron Count* (TEC), defined as the integral of N_e along the signal path:

$$TEC = \int_L N_e(s)ds \tag{4.19}$$

It can be shown that, both the range corrections and the phase delay

due to ionospheric noise are proportional to this parameter:

$$\delta\rho, \delta\phi \propto \frac{TEC}{f^2} \tag{4.20}$$

Interplanetary plasma

The hot plasma composing the solar wind is one of the main noise source for radiometric measurements. 95% of the interplanetary medium is composed of protons and electrons and the remainder 5% of α particles (helium nuclei).

The phase delay due to the signal passing through interplanetary plasma, is inversely proportional to the square of the carrier frequency in this case as well, but it is also a function of the angle between the Sun, The Earth and the probe (SEP). When the SEP is small, The Sun is between the Earth and the spacecraft and the contribution of plasma noise is very high (solar conjunction) due to the high temperatures and high electron concentration of the solar corona. On the contrary, when the SEP angle is around 180° the plasma noise affecting Doppler measurements is irrelevant (solar opposition).

The power spectral density of one-way plasma fluctuations is plotted in Figure 4.10 (Asmar *et. al*, 2005) versus the SEP angle.

The plot reports phase differential observations of the Viking spacecraft in S and X bands (circles) and of the Cassini spacecraft in X and Ka bands. The solid curves for the X and Ka bands are scaled for the one obtained for the S band. The axis on the right represents the Allan deviation of the disturbances at 1000 seconds integration time.

4.3.3 Calibration of the propagation noise

The fluctuations due to the wet component of the Earth's troposphere can be vey well calibrated at a 90 % level under favorable conditions (Asmar *et. al*, 2005) by using Advanced Media Calibration (AMC) based on the use of water vapor radiometers located in deep space communication complexes. The smaller contributions due to the dry component are instead calibrated using surface meteorology and a model for its elevation dependence (Asmar *et. al*, 2005). Figure 4.11 shows Cassini Doppler residual in

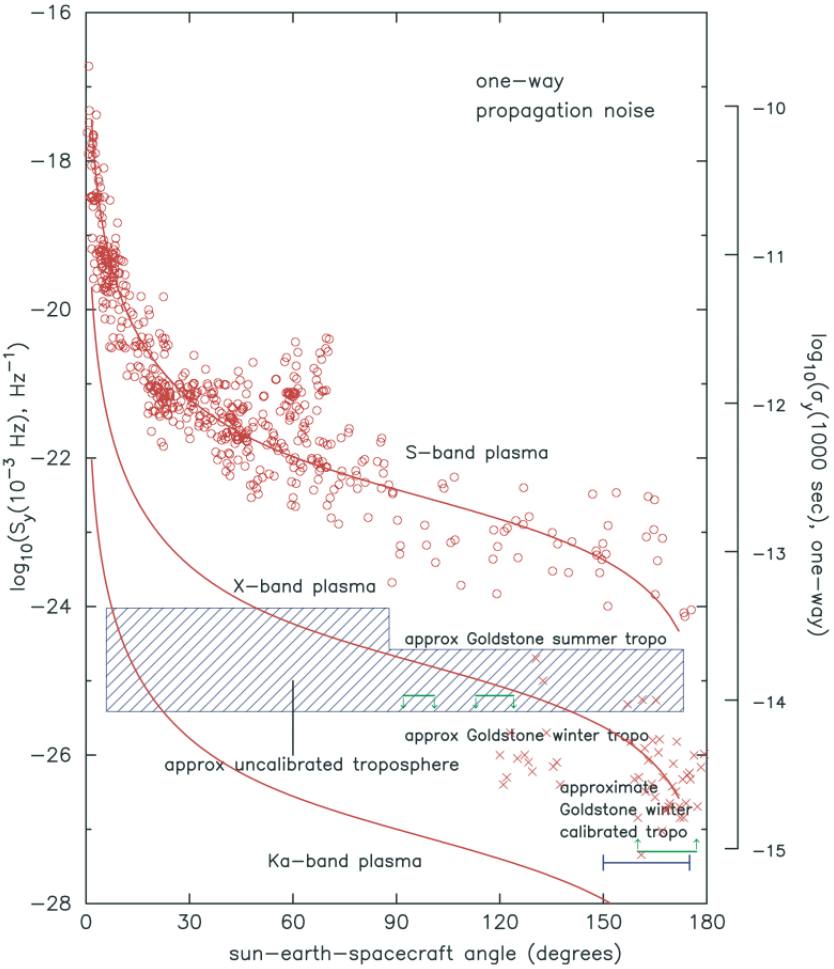

Figure 4.9: Power spectral density of one-way plasma fluctuations. Image credit: Asmar *et. al*, 2005.

June 2002 before (red solid line) and after (green dashed line) the calibration of tropospheric noise. The improvement reaches in some points, almost the 1 order of magnitude level.

The effects of the ionosphere can easily be calibrated by using multi-frequency configurations (*e.g.* simultaneous use of X and Ka bands). In fact, differential phase measurements allows the isolation of plasma noise from other non-dispersive effects such as tropospheric delay.

As for interplanetary plasma noise, it is possible to completely remove plasma noise on both legs of the link by using a multi-frequency configuration as well. For example, the Cassini spacecraft could exploit, before

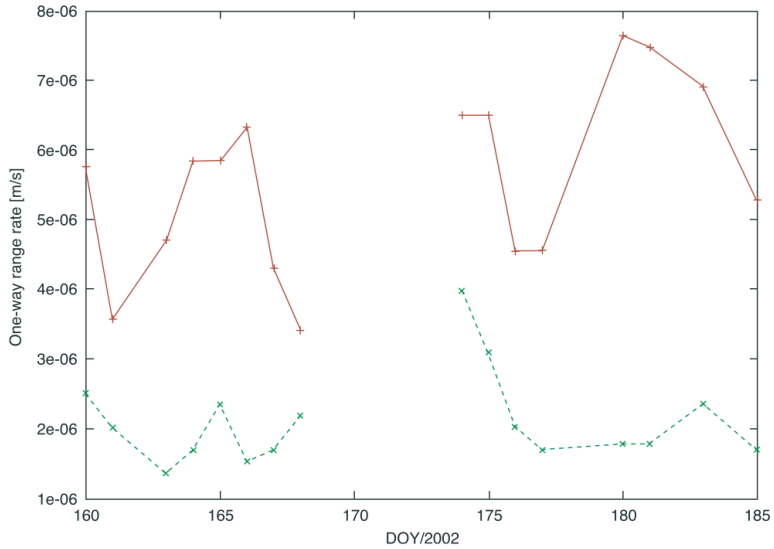

Figure 4.10: Doppler residuals of the Cassini solar conjunction experiment in 2002 at 300s integration time. Image credit: Asmar *et. al*, 2005.

the KaT failure in 2003, 5 links simultaneously (see Chapter 1, Figure 1.17), making the Doppler accuracy at conjunction almost the same as that attainable in opposition (Asmar *et. al*, 2005).

A summary of the main (calibrated and un-calibrated) sources of noise on Doppler measurements is shown in Table 4.11 (Asmar *et. al*, 2005).

4.4 Data Simulation

4.4.1 Juno

The gravity experiment onboard the Juno mission has been simulated using Doppler measurements only, within $\pm 3h$ from every pericenter. The data have been produced with a sampling time of 60 seconds. The only configuration of the KaT available for science observations will be the Ka-Ka link, for which the instrument requirement is an error on the Doppler observable not larger than $5 \times 10^{-3} mm/s$ equivalent to asking for an Allan deviation of $\sigma_y\,(1000s) = 1.67 \times 10^{-14}$. In the simulations it has been assumed that the only station tracking the Juno spacecraft during gravity measurements is the DSS 25 in Goldstone.

In order to account for the lack of a multi-frequency configuration and

Source	**Two-way Allan Deviation at 1000 seconds.**
Ground FTS	$< 10^{-15}$
USO	$\sim 10^{-13}$ (only for one-way data)
Antenna mechanical noise	$< 4 \times 10^{-15}$ (favorable conditions)
Ground electronics	2.3×10^{-16}
Plasma noise at Ka-band	$< 10^{-15}$ (for SEP $> 160°$)
Plasma noise at Ka-band	$\sim 5 \times 10^{-15}$ (for SEP $\sim 30°$)
Spacecraft motion	2.6×10^{-16}
Thermal noise	$\sim 10^{-16}$
Ka-band translator noise	$< 1.7 \times 10^{-15}$
Raw tropospheric noise	$3 - 30 \times 10^{-15}$
Tropospheric noise after calibration	$< 1.5 \times 10^{-15}$
Best Case	9.0×10^{-15}
Worst Case	1.5×10^{-14}

Table 4.11: Allan deviations for the main noise sources on range-rate measurements (Asmar *et. al*, 2005).

all the uncertainties in the description of the dynamical model, the Allan deviation corresponding to the worst case in Table 4.11 has been assumed to obtain the noise level over Juno range-rate measurements. Firstly, it is necessary to report the value to the proper sampling time:

$$\sigma_y\left(60s\right) = \sqrt{\frac{1000}{60}}\sigma_y\left(1000s\right) = 6.1 \times 10^{-14} \tag{4.21}$$

that can be converted into frequency fluctuations:

$$\Delta f\left(60s\right) = \sigma_y\left(60s\right) f_0 \sim 2.10 mHz \tag{4.22}$$

where $f_0 = 34.3 GHz$ is the reference carrier frequency. The noise RMS expressed in mHz characterizes the white Gaussian noise superposed on Juno Doppler measurements.

4.4.2 JUICE

For the JUICE mission, the simulated tracking period depends on the specific science phase: during the Ganymede orbits, Doppler measurements are collected for $6-8h$ a day, while for the Callisto flybys the tracking period is centered $\pm 4h$ around closest approach.

In any case, Doppler data are simulated with a sampling time of 60 seconds, with the involved tracking stations being: ESA DSA1 (New Norcia), ESA DSA2 (Cebreros) and NASA DSS 25 (Goldstone).

For the JUICE mission, although the Ka-Ka link represents the baseline for science observations, the exploitation of a dual- or multi-frequency configuration is possible. For this reason, to account for the Doppler noise on the simulated observable, the following scenarios, depending on the Sun elongation angle, have been considered:

$$\begin{cases} \Delta f\,(60s)_{Ka-Ka} \sim 1.20mHz & SEP > 15^\circ \\ \Delta f\,(60s)_{Ka-Ka} \sim 1.80mHz & SEP \leq 15^\circ \\ \Delta f\,(60s)_{dual} \sim 1.20mHz & \forall \quad SEP \\ \Delta f\,(60s)_{multi} \sim 1.00mHz & \forall \quad SEP \end{cases} \tag{4.23}$$

with the noise RMS varying from pass to pass.

4.5 Estimation process

The estimation process, whose mathematical principles have been discussed in Chapter 3, can be divided into the following steps:

- choice of a first-guess dynamical model, with a description of gravitational and non-gravitational forces;
- selection of nominal initial conditions for the state vector, comprising position and velocity of the spacecraft and other estimated parameters. This initialization could be different or not to the one given in simulation;
- generation of computed observables at the same epochs as for the simulated observed observables, using the reference trajectory integrated starting from the nominal initial conditions;
- computation of the partial derivatives along the reference trajectory;
- data processing through a weighted least square filter: computation of the Doppler residuals for the determination of the best estimate of the solve-for vector, along with the formal uncertainty, based on the data;

- update of the dynamical model and state vector.

The process described above is an iterative technique to be repeated until the solution meets a certain convergence criterion (see section 3.3.2). The following flow diagram is explicative of the process:

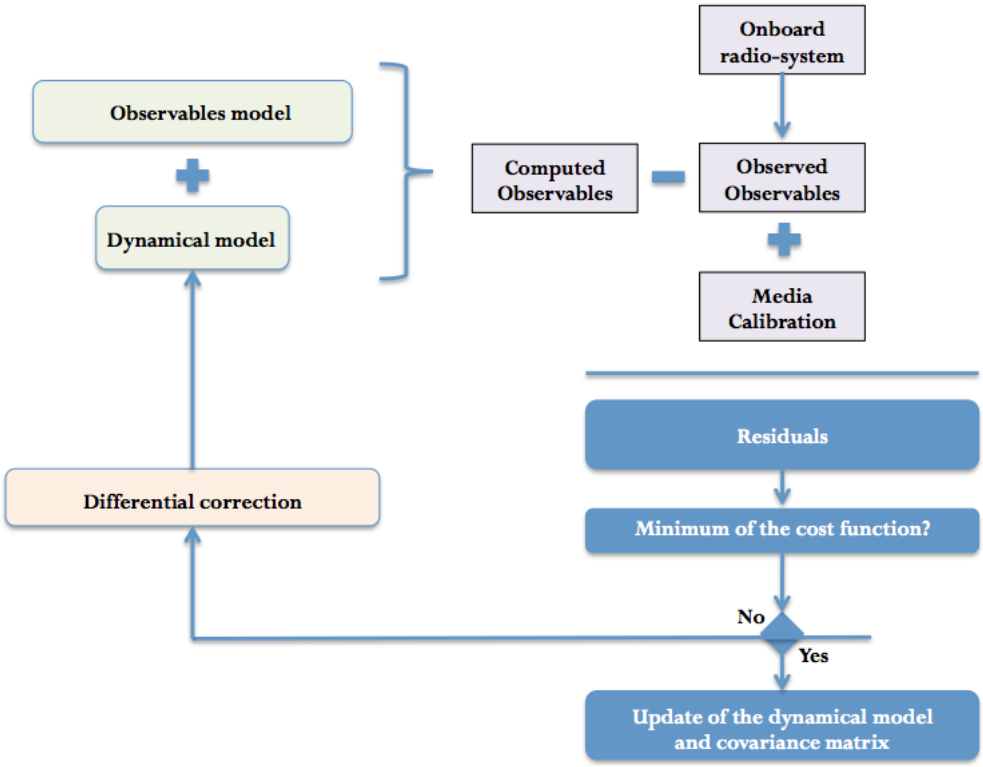

Figure 4.11: Orbit determination: flow diagram of the estimation process.

The filter, used in the frame of Juno and JUICE gravity experiment simulations, minimizes, in the least square sense, the Doppler residuals for the purpose of estimating the physical parameters of interest. The filter is capable of operating in batch mode, and uses the square root formulation in order to minimize the bad-conditioned information matrix (Racioppa, 2012). The estimation process performed by the filter provides central values for the solve-for parameters along with a full covariance matrix.

Chapter 5

Juno: the gravitational signature of Jupiter's winds

One of the cardinal scientific objectives of the Juno gravity experiment is the retrieval of Jupiter's wind depth as a function of the Jovian latitude, by means of precise Doppler measurements of the planet's gravitational signal.

In parallel, the addition of information on the structure and dynamics of the winds, has the potential of conspicuously improving the determination of the gravity field itself. An iterative method for the estimate of Jupiter's gravity harmonic coefficients using an adjoint based inverse thermal wind model has been proposed by Galanti *et al*. (2013). In this method, the recovery of the gravity field is improved thanks to the adoption of a geophysical model for Jupiter's jets, with consequent constraints on the wind morphology.

In this chapter, I will address two main tasks: the formulation of a three-dimensional model for Jupiter's density anomalies due to the presence of atmospheric dynamics, based on thermal wind balance principles; and assessing the possibility of detecting the gravitational signature coming from the winds, with particular regard for the Great Red Spot, by using radio science Doppler measurements. I will discuss the methods and implications of such developments from the point of view of the radio science experiment onboard the Juno mission.

5.1 From Cassini data to a model for Jupiter's wind speed

The penetration depth of the winds of Jupiter is still an open question among the planetary science community (Kaspi *et al.*, 2010). Precise Doppler measurements of Jupiter's gravity field from the Juno mission will be extremely sensitive to such parameter. In fact, the deeper the jet streams, the more the mass involved in the wind motion and the larger the gravity anomalies, detectable by the radio science instrument. If the wind speed profile is available, assuming that thermal wind theory reasonably describes the dynamics of Jupiter's atmosphere to a certain degree of approximation, the resulting density anomalies can be determined.

Fortunately, observations of the cloud-level winds are largely available. The main feature of Jupiter's atmosphere is the alternation of zones and belts, vast counter rotating zonal jets, almost symmetric about the equator (Choi and Showman, 2011). Current theories suggest that Jupiter's atmospheric structure can be considered slow-changing and that the winds are deep-rooted, with the main driving-mechanism being convection (Vasavada and Showman, 2005).

The model for Jupiter's wind velocity field, adopted in my work, is based upon observations of the planet's atmosphere made by the Cassini spacecraft (Choi and Showman, 2011). In the cited work, the authors provide a full 2-D longitudinal profile of Jupiter's wind surface velocity and tropospheric kinetic energy, by means of spherical harmonic analysis, although the analysis does not provide information on the underlying dynamics. The utilized data set contains observations made during Cassini Jupiter flyby in December 2000, by the Imaging Science Subsystem (ISS), including extensive multi-spectral analysis of Jupiter's atmosphere. The instrument carried out observations in both hemispheres, using 4 different filters for its narrow angle camera. The wind vector maps were then generated using an automated cloud feature tracker (Choi *et al.*, 2007), resulting in a final resolution of 0.05 deg/pixel. Unfortunately, due to low contrast and resolution at high latitudes caused by the flyby geometry, wind vectors for latitudes polewards of 50° latitude are not reported in the study. For details on the measurement and data analysis setup see Choi and Showman

(2011), Section 2.

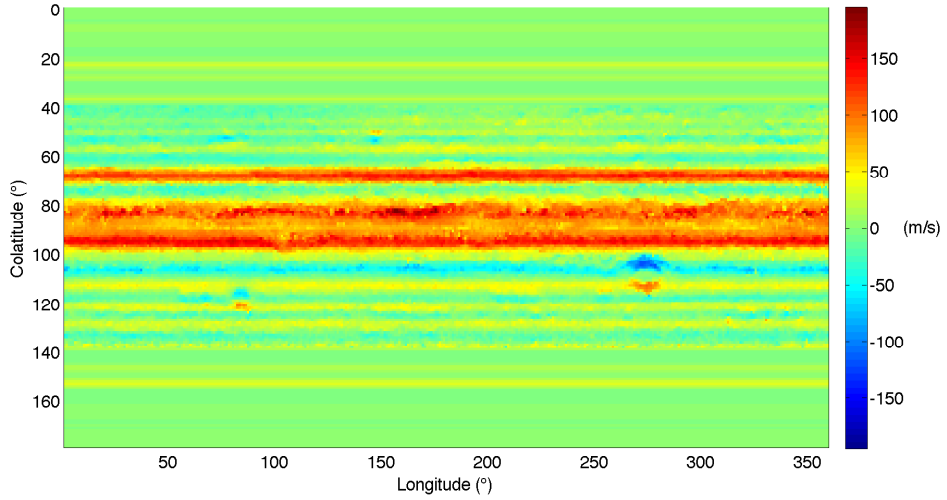

(a)

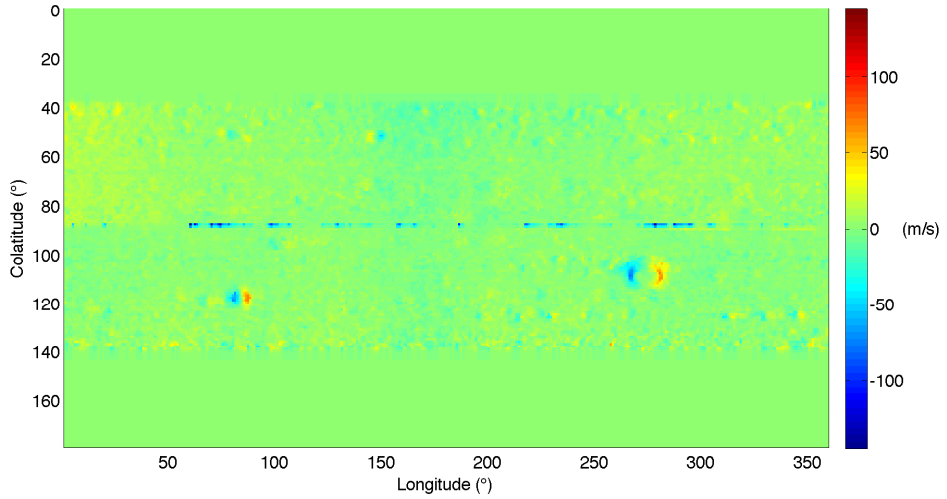

(b)

Figure 5.1: Horizontal components of the wind velocity **a)** $u(\theta, \phi)$ component, along parallels. **b)** $v(\theta, \phi)$ component, along meridians. The velocity map is derived from Choi and Showman (2011).

The results of the cloud tracker in terms of wind velocity maps (Choi and Showman, 2011) are shown in Figure 5.1. The plots were referenced using Jupiter System III convention and the typical uncertainty on the speed measurements is about $5 - 10m/s$. Each graph (*(a)* and *(b)*) represents one

horizontal component of Jupiter's wind velocity: u along parallels and v along meridians.

The winds are mostly zonal, going from west to east (positive values) and east to west (negative values), creating evident horizontal bands. The contribution of the v component to the total kinetic energy is limited, although the velocity anomalies identifying the Great Red Spot (up to 30 m/s) and the Oval BA are clearly visible in both maps (at around 110° co-latitude, 275° longitude and 120° colatitude, 85° longitude, respectively, in the chosen reference frame). As a matter of fact, the equatorial region, comprised between 80° and 100° colatitude, contributes the most to the overall energy, with a typical variance in the wind velocity of about 20-30 m/s between adjacent zonal bands, and somewhere even higher. As anticipated, data at high latitudes have been rejected, while, where available, maps of the wind vectors are affected by measurement noise, leading to typical uncertainties of 5 m/s, with peaks between 10 and 20 m/s. For a more detailed description of the effects of data processing techniques over the velocity measurements see Choi and Showman (2011), Section 5.

Starting from Choi and Showman's analysis, a complete 2-D map of Jupiter surface wind velocity has been produced. For the purposes of this dissertation, among which the generation of a 3-D model for the planet's density anomalies, it is necessary to make some assumptions on the penetration of such jets at depth. In particular, I assumed that the discussed horizontal profile, $u(\theta, \phi)$ and $v(\theta, \phi)$, penetrates in the direction parallel to the axis of rotation as a vertical decay function (Kaspi *et al.*, 2010), with the penetration depth depending on the height scale H:

$$\begin{aligned} u(r, \theta, \phi) &= u(\theta, \phi)\, e^{-\frac{R-r}{H}} \\ v(r, \theta, \phi) &= v(\theta, \phi)\, e^{-\frac{R-r}{H}} \end{aligned} \tag{5.1}$$

where R is Jupiter's mean radius. Note that for $r = R$, the surface profile corresponds to the original velocity maps. The velocity field has now assumed a three-dimensional connotation over the sphere.

Due to instrumental and measurement noise on Choi and Showman's data, a smoothing step had to be introduced. If the resolution of the map is $\delta = n \times 0.5^\circ$ (with n integer) in both longitude and latitude (*e.g.* 1°, the maximum resolution is 0.5°), then the velocity profile is stored as a matrix

of $\left(\frac{360^\circ}{\delta}\right) \times \left(\frac{180^\circ}{\delta} + 1\right)$ elements. The applied smoothing process is a linear transformation of the observed values, involving an averaging procedure between each pixel and the adjacent ones (Figure 5.2):

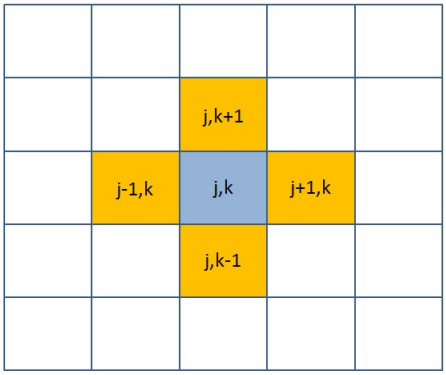

Figure 5.2: Visualization of a 2-D smoothing (*e.g.* over latitude and longitude).

The 2-D smoothing function for a scalar field ϕ is:

$$\phi(j,k) = \frac{1}{2}\phi(j,k) + \frac{1}{8}\left[\phi(j-1,k) + \phi(j+1,k) + \phi(j,k-1) + \phi(j,k+1)\right] \tag{5.2}$$

which can easily be extended to the 3-D case, as the wind velocity in (5.1).

Throughout this chapter, three different scenarios characterized by different height scales H will be considered and thoroughly analyzed:

- a shallow wind case with H = 300 km, where the location of wind dynamics is supposed to extend within 1% of Jupiter's atmosphere;
- a mid-penetrating wind case with H = 3000 km, here the winds are deeper, penetrating up to 10% of Jupiter's gaseous surface;
- a very-deep wind case, with H = 1000000 km, this represent the other extreme case where the wind dynamics involve a great portion of Jupiter's mass.

The following plots (Figure 5.3) are visual displays of the wind profile over meridional sections, at a given longitude.

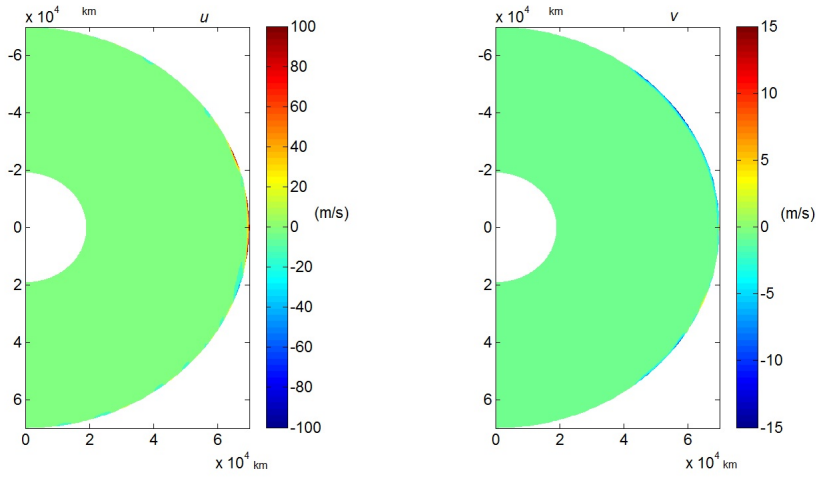

(a)

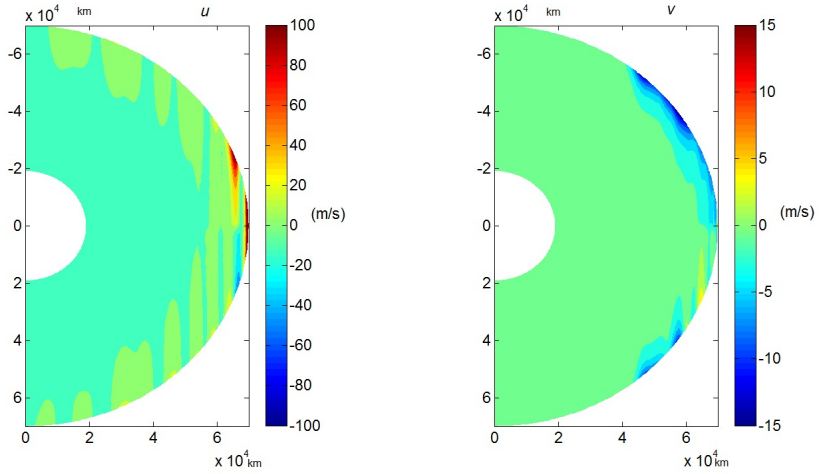

(b)

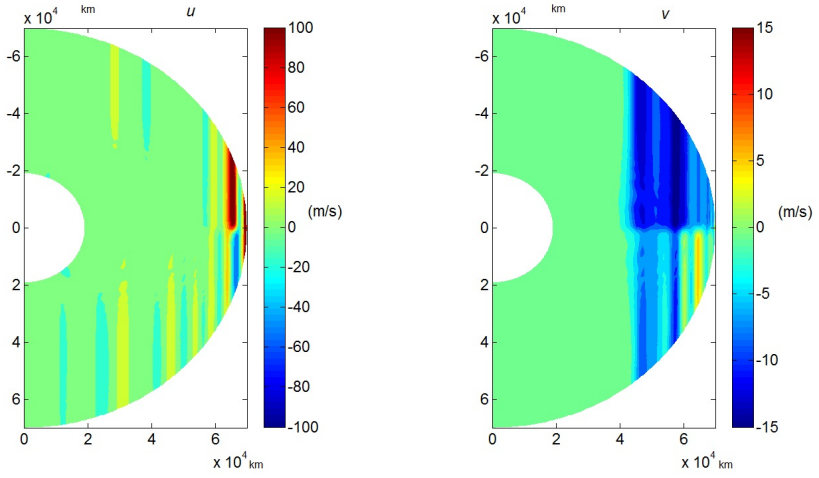

(c)

Figure 5.3: Velocity profile over a longitudinal section ($\phi = \pi$). **a)** for $H = 300km$; **b)** for $H = 3000km$; **c)** for $H = 1000000km$.

In case **a**) the penetration is very marginal, the mass involved in the wind motion is limited and the expected density anomalies are negligible; in case **b**) the penetration depth is about 1/20 of Jupiter's mean radius, the infiltration of the jets at deeper layers is evident, with peaks in the proximity of the equatorial belt; in case **c**) the height scale is much larger than Jupiter's mean radius, resulting in the complete penetration of the winds parallel to Jupiter's spin axis, with evident discontinuities in the equatorial plane.

5.2 A model of Jupiter's density anomalies

Jupiter is an extremely fast rotator and characterized by very large scales, therefore the planet's atmospheric dynamics is governed by geostrophic balance (and thus thermal wind balance in three dimensions), at least to the first order (Kaspi *et al.*, 2010).

Thermal wind balance equations have been deduced in Chapter 2, Section 2.3.6. In this formulation the density anomalies are expressed as functions of the wind velocity profile, considered as known from observations. In this paragraph, I will show how, starting from a known 3-D model of the winds speed $\boldsymbol{v}$, one can deduce the resulting distribution of the density anomalies.

Thermal wind fundamental equation is:

$$2\boldsymbol{\Omega} \cdot \nabla \left(\tilde{\rho} \boldsymbol{v} \right) = \nabla \rho' \times \boldsymbol{g_0} \tag{5.3}$$

where $\boldsymbol{\Omega}$ is the planetary rotation rate, $\tilde{\rho}\left(\boldsymbol{r}\right)$ is the hydrostatic state density, $\boldsymbol{g_0}$ is the mean gravity vector and $\rho'\left(\boldsymbol{r}\right)$ is the density anomaly.

When dealing with planetary bodies, it is convenient to adopt a set of spherical coordinates (ρ, θ, ϕ), centered at Jupiter's barycenter and related to Cartesian coordinates by:

$$\begin{cases} x = r sin\theta cos\phi \\ y = r sin\theta sin\phi \\ z = r cos\theta \end{cases} \tag{5.4}$$

where θ is the colatitude and ϕ is the longitude. In this reference frame, the gradient of the density anomaly can be expressed as:

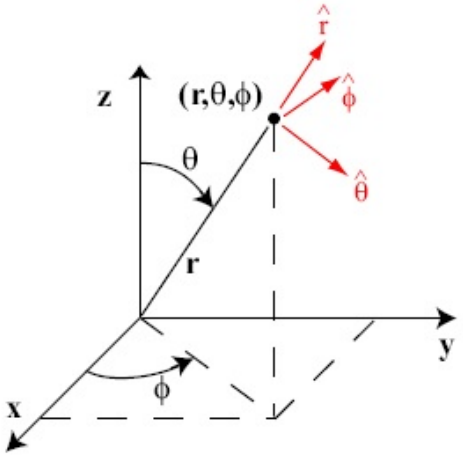

Figure 5.4: Spherical coordinates in the 3-D space (math.stackexchange.com).

$$\nabla\rho' = \frac{\partial\rho'}{\partial r}\hat{\boldsymbol{r}} + \frac{1}{r}\frac{\partial\rho'}{\partial\theta}\hat{\boldsymbol{\theta}} + \frac{1}{rsin\theta}\frac{\partial\rho'}{\partial\phi}\hat{\boldsymbol{\phi}} \tag{5.5}$$

while the gravitational acceleration has only one non-null component, along the radial direction:

$$\boldsymbol{g_0} = -g_0\hat{\boldsymbol{r}} \tag{5.6}$$

the cross-product between the gradient of the density anomaly and the gravitational acceleration is then easily computed:

$$\nabla\rho' \times \boldsymbol{g_0} = det\begin{bmatrix} \hat{\boldsymbol{r}} & \hat{\boldsymbol{\theta}} & \hat{\boldsymbol{\phi}} \\ \frac{\partial\rho'}{\partial r} & \frac{1}{r}\frac{\partial\rho'}{\partial\theta} & \frac{1}{rsin\theta}\frac{\partial\rho'}{\partial\phi} \\ -g_0 & 0 & 0 \end{bmatrix} = -\frac{1}{rsin\theta}\frac{\partial\rho'}{\partial\phi}g_0\hat{\boldsymbol{\theta}} + \frac{1}{r}\frac{\partial\rho'}{\partial\theta}g_0\hat{\boldsymbol{\phi}} \tag{5.7}$$

The left hand of the thermal balance equation can also be expanded to become:

$$\begin{aligned} 2\boldsymbol{\Omega}\cdot\nabla\left(\tilde{\rho}\boldsymbol{v}\right) &= 2\left(\Omega_x\frac{\partial}{\partial x} + \Omega_y\frac{\partial}{\partial y} + \Omega_z\frac{\partial}{\partial z}\right)\left(\tilde{\rho}\boldsymbol{v}\right) \\ &= \left(2\Omega_z\frac{\partial}{\partial z}\right)\left[\tilde{\rho}\left(w\hat{\boldsymbol{r}} + v\hat{\boldsymbol{\theta}} + u\hat{\boldsymbol{\phi}}\right)\right] \end{aligned} \tag{5.8}$$

since, by definition of a body-fixed reference frame, $\Omega_z = \mid \mathbf{\Omega} \mid$. Projecting along the $\hat{\phi}$ direction one gets:

$$2\Omega \frac{\partial \tilde{\rho} u}{\partial z} = \frac{1}{r} \frac{\partial \rho'}{\partial \theta} g_0 \tag{5.9}$$

Projecting along the $\hat{\boldsymbol{\theta}}$ direction:

$$2\Omega \frac{\partial \tilde{\rho} v}{\partial z} = -\frac{1}{r sin\theta} \frac{\partial \rho'}{\partial \phi} g_0 \tag{5.10}$$

Thus, thermal wind balance can be expressed as a system of two partial differential equations:

$$\begin{cases} \frac{\partial \rho'}{\partial \theta} = \frac{2\Omega}{g_0} r \frac{\partial \bar{\rho} u}{\partial z} \\ \frac{\partial \rho'}{\partial \phi} = -\frac{2\Omega}{g_0} r sin\theta \frac{\partial \bar{\rho} v}{\partial z} \end{cases} \tag{5.11}$$

where $\rho'(r, \theta, \phi)$ is the unknown variable to solve for.

In the next paragraphs different solutions for (5.11), depending on the structure of the winds, will be considered, analyzed and thoroughly discussed.

5.2.1 2-D model: purely zonal winds

It has already been pointed out that Jupiter's wind structure is mostly zonal, with the main jets moving parallel to the equator (see Figure 5.1). That being so, it is interesting to understand what happens to the density anomalies in the case where the v component of the wind velocity is neglected:

$$\begin{cases} u = u(r, \theta, \phi) & r \in [0, \infty), \theta \in [0, \pi], \phi \in [0, 2\pi] \\ v \equiv 0 & r \in [0, \infty), \theta \in [0, \pi], \phi \in [0, 2\pi] \end{cases} \tag{5.12}$$

To build such peculiar profile, Choi and Showman's velocity map for the u component has been averaged out over the longitudinal direction, providing a purely zonal wind structure (Figure 5.5). The field has been then propagated in the vertical direction as in Section 5.1, for different values of the height scale H.

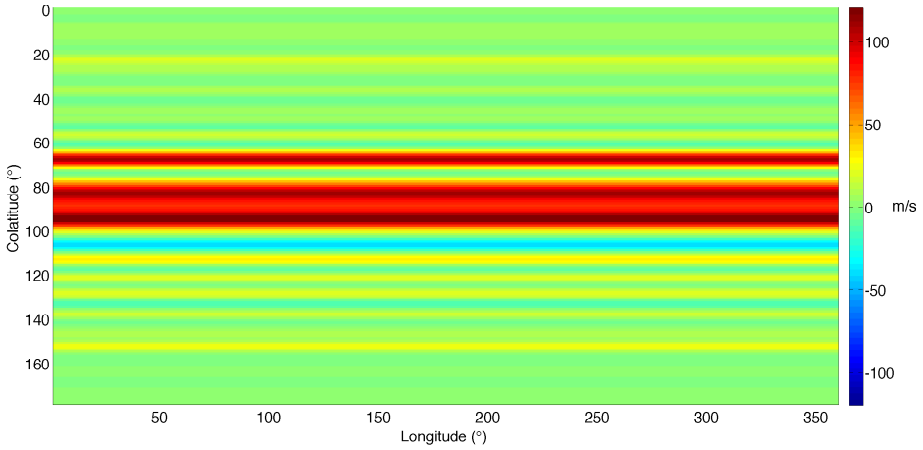

Figure 5.5: Surface velocity map for the zonal case. Display of the v component.

As a consequence, from the second equation of system (5.11), the variations of the density anomalies along the longitudinal direction ($\hat{\phi}$) are also null:

$$\frac{\partial \rho'}{\partial \phi} = 0 \tag{5.13}$$

In Section 2.3.6 of Chapter 2, it has been shown that, for a flow in geostrophic balance, the projection of the velocity divergence onto the tangent plane defined by $\hat{\boldsymbol{\theta}}\hat{\boldsymbol{\phi}}$ is null:

$$\boldsymbol{\nabla}_r \cdot \boldsymbol{v} = 0 \tag{5.14}$$

because of the mass conservation equation. Expanding the divergence operator in spherical coordinates one gets:

$$\frac{1}{rsin\theta}\frac{\partial\left(vsin\theta\right)}{\partial\theta} + \frac{1}{rsin\theta}\frac{\partial u}{\partial\phi} = 0 \tag{5.15}$$

but $v \equiv 0$, then:

$$\frac{\partial u}{\partial \phi} = 0 \tag{5.16}$$

meaning that the longitudinal component of the wind velocity cannot depend on longitude in the zonal case, which is consistent with the previous assumption. The thermal wind equations become:

$$\begin{cases} \frac{\partial \rho'}{\partial \theta} = \frac{2\Omega}{g_0} r \frac{\partial \bar{\rho} u}{\partial z} \\ \frac{\partial \rho'}{\partial \phi} = 0 \end{cases} \tag{5.17}$$

One can solve the first differential equation for $\rho'(r, \theta)$:

$$\rho'(r, \theta) = \int \left(\frac{2\Omega}{g_0} r \frac{\partial \bar{\rho} u(r, \theta)}{\partial z} \right) d\theta + \rho'_1(r) \tag{5.18}$$

where $\rho'_1(r)$ represents the constant of integration. This expression also fulfills the second equation, being the integrand entirely not dependent on ϕ. To find a unique solution for the density anomaly in equation (5.18), a boundary condition must be imposed. For example, one can impose that the density anomaly along the $\hat{\boldsymbol{\theta}}$ direction is zero-average, to maintain Jupiter's total mass:

$$\int_\theta \rho'(r, \theta)\, d\theta = 0 \tag{5.19}$$

whence:

$$\rho'_1(r) = -\int_\theta \left[\int \left(\frac{2\Omega}{g_0} r \frac{\partial \bar{\rho} u(r, \theta)}{\partial z} \right) d\theta \right] d\theta \tag{5.20}$$

Starting from the velocity map in Figure 5.5, equation (5.18) can be numerically integrated using the rectangle rule. A finite difference method is used to calculate the derivatives.

Figures 5.6-5.8 show the results in terms of density maps at the surface of the planet and over a longitudinal slice at a fixed longitude, for different values of H. From the plots it is evident that, although the main features of Jupiter's winds are captured in a 2-D model in which the density profile depends only upon the colatitude, longitudinal features such as the Great Red Spot and the Oval BA are not represented by this model.

Another option is to consider the actual velocity map for the u component (Figure 5.1 *a*), thus with longitudinal fluctuations, and integrate equation (5.18) for each longitudinal slice of Jupiter. In this case the model is quasi 2-D, meaning that the second equation of system (5.11) is still approximately satisfied, given the much less pronounced variations of the wind speed along parallels, but the latitudinal velocity profile varies, *de facto*, for each slice. However, in my dissertation I will focus directly on the complete 3-D model.

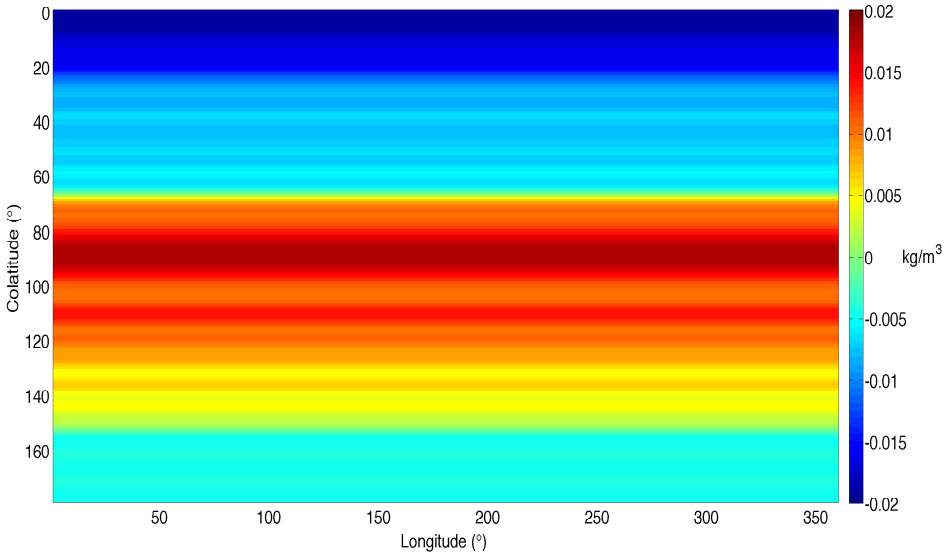

(a)

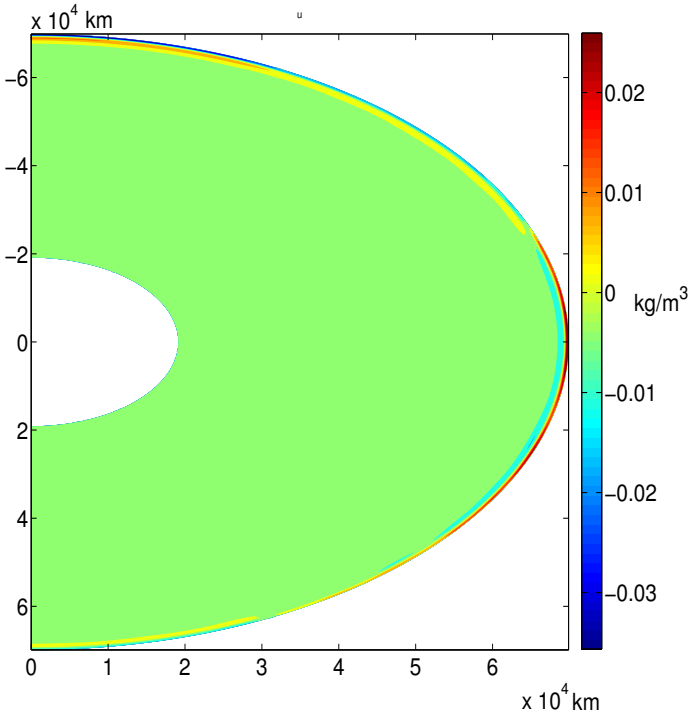

(b)

Figure 5.6: Integrated density profile for $H = 300km$. **a)** Surface density anomalies; **b)** Density anomalies over a longitudinal section, at $\phi = \pi$.

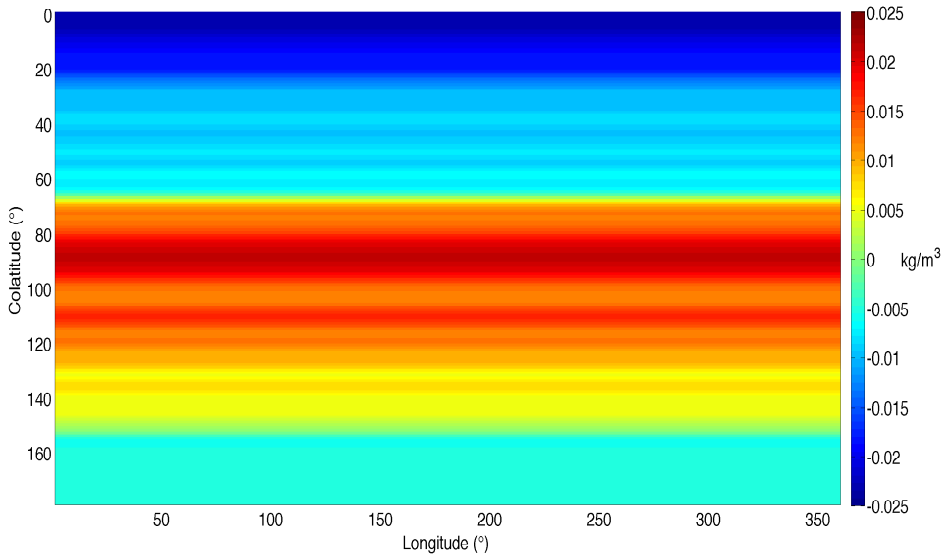

(a)

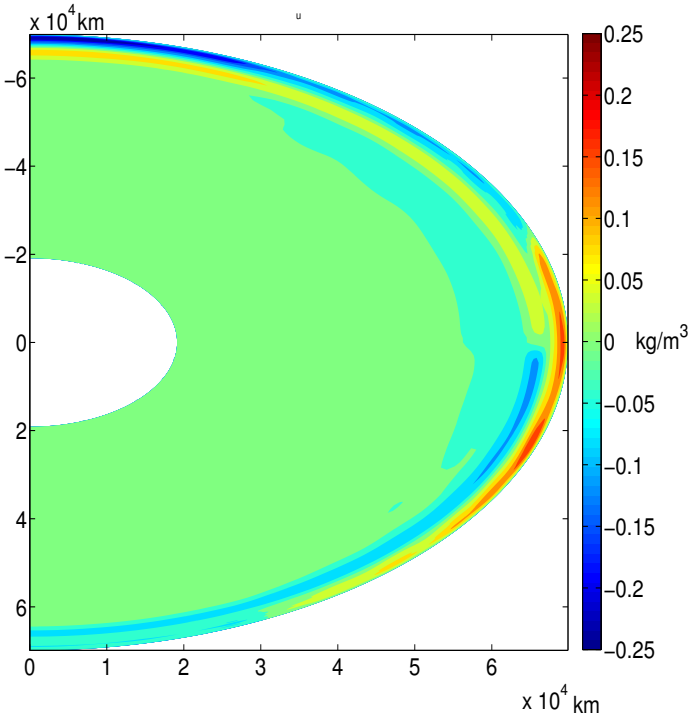

(b)

Figure 5.7: Integrated density profile for $H = 3000km$. **a)** Surface density anomalies; **b)** Density anomalies over a longitudinal section, at $\phi = \pi$.

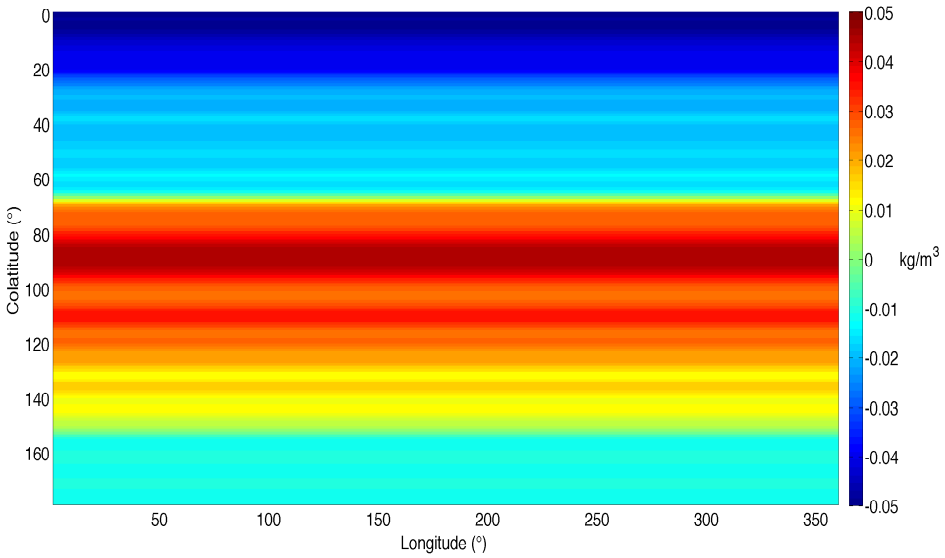

(a)

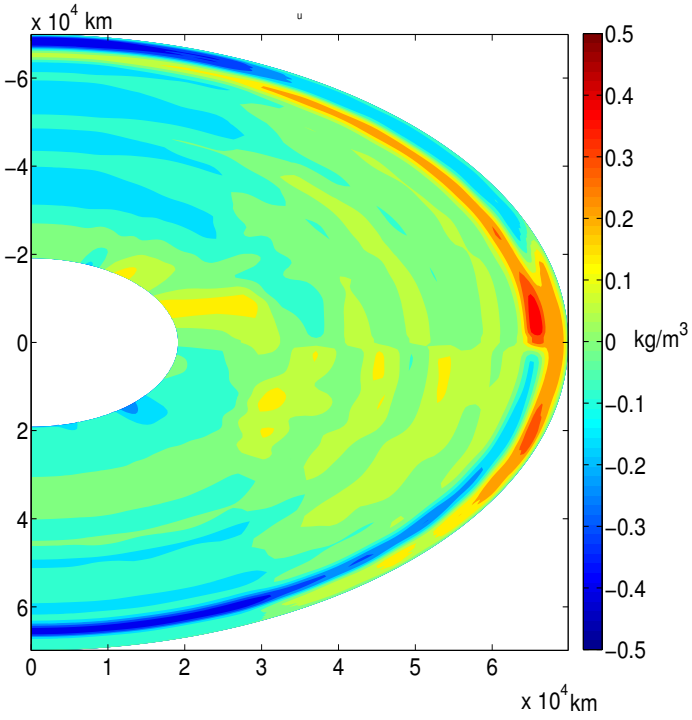

(b)

Figure 5.8: Integrated density profile for $H = 1000000km$. **a)** Surface density anomalies; **b)** Density anomalies over a longitudinal section, at $\phi = \pi$.

One could argue that, starting the integration from the south pole of Jupiter, as in this case, the density disturbances at the north pole are not zero, as evident from Figure 5.6-5.8. This happens because of the integration constant, which, in order to average out the anomalies in the latitudinal direction, assigns a negative values to the northern region. The objection itself is relevant but one must consider that in the frame of this work, the interesting outcome of this modelization is an estimate of the effect of the winds of Jupiter on the overall gravity field of the planet. Being so, this inconsistency in the density model can be neglected, since the fluctuations of the gravity harmonics ΔJ_n depend exclusively on the changes of the density anomalies along θ and ϕ (Kaspi *et al.*, 2010), while the constant of integration is a function of only r.

5.2.2 3-D model

In this subsection I will consider the general case where both components of the velocity u and v are non-negligible. Starting from system (5.11) the cross-derivative of each equation is taken:

$$\begin{cases} \frac{\partial}{\partial\phi}\left(\frac{\partial\rho'}{\partial\theta}\right) = \frac{\partial}{\partial\phi}\left(\frac{2\Omega}{g_0} r \frac{\partial\bar{\rho}u}{\partial z}\right) \\ \frac{\partial}{\partial\theta}\left(\frac{\partial\rho'}{\partial\phi}\right) = \frac{\partial}{\partial\theta}\left(-\frac{2\Omega}{g_0} r sin\theta \frac{\partial\bar{\rho}v}{\partial z}\right) \end{cases} \tag{5.21}$$

If the density anomaly function is C^2 (with second derivatives existing and continuous), then its cross derivatives are equivalent and the two equations can be summed up:

$$2\frac{\partial^2\rho'}{\partial\phi\partial\theta} = \frac{\partial}{\partial\phi}\left(\frac{2\Omega}{g_0} r \frac{\partial\bar{\rho}u}{\partial z}\right) - \frac{\partial}{\partial\theta}\left(\frac{2\Omega}{g_0} r sin\theta \frac{\partial\bar{\rho}v}{\partial z}\right) \tag{5.22}$$

Always assuming that ρ' is C^2, equation (5.22) can be integrated a first time with respect to θ:

$$\begin{aligned} \frac{\partial\rho'}{\partial\phi} &= \frac{1}{2}\int\left[\frac{\partial}{\partial\phi}\left(\frac{2\Omega}{g_0} r \frac{\partial\bar{\rho}u}{\partial z}\right) - \frac{\partial}{\partial\theta}\left(\frac{2\Omega}{g_0} r sin\theta \frac{\partial\bar{\rho}v}{\partial z}\right)\right] d\theta + f_0'(r,\phi) \\ &= \frac{1}{2}\int\frac{\partial}{\partial\phi}\left(\frac{2\Omega}{g_0} r \frac{\partial\bar{\rho}u}{\partial z}\right) d\theta - \frac{1}{2}\int\frac{\partial}{\partial\theta}\left(\frac{2\Omega}{g_0} r sin\theta \frac{\partial\bar{\rho}v}{\partial z}\right) d\theta + f_0'(r,\phi) \\ &= \frac{1}{2}\int\frac{\partial}{\partial\phi}\left(\frac{2\Omega}{g_0} r \frac{\partial\bar{\rho}u}{\partial z}\right) d\theta - \frac{1}{2}\left(\frac{2\Omega}{g_0} r sin\theta \frac{\partial\bar{\rho}v}{\partial z}\right) + f_0'(r,\phi) \end{aligned} \tag{5.23}$$

and a second time with respect to ϕ :

$$\begin{aligned}\rho' &= \tfrac{1}{2}\iint \tfrac{\partial}{\partial\phi}\left(\tfrac{2\Omega}{g_0} r \tfrac{\partial\bar{\rho}u}{\partial z}\right) d\theta d\phi - \tfrac{1}{2}\int\left(\tfrac{2\Omega}{g_0} r sin\theta \tfrac{\partial\bar{\rho}v}{\partial z}\right) d\phi + \int f_0'(r,\phi)\, d\phi + \rho_1'(r,\theta) \\ &= \tfrac{1}{2}\int\left(\tfrac{2\Omega}{g_0} r \tfrac{\partial\bar{\rho}u}{\partial z}\right) d\theta - \tfrac{1}{2}\int\left(\tfrac{2\Omega}{g_0} r sin\theta \tfrac{\partial\bar{\rho}v}{\partial z}\right) d\phi + \int f_0'(r,\phi)\, d\phi + \rho_1'(r,\theta)\end{aligned} \tag{5.24}$$

but $\int f_0'(r,\phi)\, d\phi$ is still only a function of r and ϕ, hence:

$$\rho'(r,\theta,\phi) = \frac{1}{2}\int\left(\frac{2\Omega}{g_0} r \frac{\partial\bar{\rho}u}{\partial z}\right) d\theta - \frac{1}{2}\int\left(\frac{2\Omega}{g_0} r sin\theta \frac{\partial\bar{\rho}v}{\partial z}\right) d\phi + \rho_2'(r,\phi) + \rho_1'(r,\theta) \tag{5.25}$$

Analogously to the 2-D model it is necessary to select a physical solution for the density anomalies by calculating the constants of integration $\rho_1'(r,\theta)$ and $\rho_2'(r,\phi)$. To do so, one must impose two boundary conditions.

The first constraint is that, for $v \to 0$ the expression for the density perturbation must converge to its expression for the 2-D model, hence comparing equation (5.25) with equation (5.18):

$$\lim_{v\to 0}\rho'(r,\theta,\phi) = \int\left(\frac{2\Omega}{g_0} r \frac{\partial\bar{\rho}\tilde{u}(r,\theta)}{\partial z}\right) d\theta + \rho_3'(r) \tag{5.26}$$

Suppose the *u* component of the velocity can be expressed as the sum of two different contributions: one that depends only on depth and colatitude: $\tilde{u}(r,\theta)$; and one that depends only on the longitude: $u'(\phi)$. When $v \to 0$, u tends to $\tilde{u}$ which cannot be a function of the longitude for the previously discussed reasons, then:

$$\lim_{v\to 0} u(r,\theta,\phi) = \tilde{u}(r,\theta) \tag{5.27}$$

Also, the following expressions:

$$\begin{aligned} &v \to 0, \\ &u(r,\theta,\phi) \to \tilde{u}(r,\theta) \\ &u'(\phi) \to 0 \end{aligned} \tag{5.28}$$

are equivalent. Using the general formula for the density perturbation (5.25), equation (5.26) becomes:

$$\begin{aligned}\lim_{v\to 0}\left[\tfrac{1}{2}\int\left(\tfrac{2\Omega}{g_0} r \tfrac{\partial\bar{\rho}u}{\partial z}\right) d\theta - \tfrac{1}{2}\int\left(\tfrac{2\Omega}{g_0} r sin\theta \tfrac{\partial\bar{\rho}v}{\partial z}\right) d\phi + \rho_2'(r,\phi) + \rho_1'(r,\theta)\right] \\ = \int\left(\tfrac{2\Omega}{g_0} r \tfrac{\partial\bar{\rho}\tilde{u}(r,\theta)}{\partial z}\right) d\theta + \rho_3'(r)\end{aligned} \tag{5.29}$$

whence:

$$\begin{array}{ll} \frac{1}{2} & \int \left(\frac{2\Omega}{g_0} r \frac{\partial \bar{\rho} \tilde{u}}{\partial z} \right) d\theta + \lim_{v \to 0} \left(\rho_2' \left(r, \phi \right) + \rho_1' \left(r, \theta \right) \right) \\ = & \int \left(\frac{2\Omega}{g_0} r \frac{\partial \bar{\rho} \tilde{u}}{\partial z} \right) d\theta + \rho_3' \left(r \right) \end{array} \tag{5.30}$$

and consequently:

$$\lim_{v \to 0} \left(\rho_2' \left(r, \phi \right) + \rho_1' \left(r, \theta \right) \right) = \frac{1}{2} \int \left(\frac{2\Omega}{g_0} r \frac{\partial \bar{\rho} \tilde{u}}{\partial z} \right) d\theta + \rho_3' \left(r \right) \tag{5.31}$$

At this point a few considerations about the limits on the left side of equation (5.31) are in order. Since ρ_1' is only a function of r and θ, this constant of integration can only depend on the components of u and v that don't depend on the longitude, namely $\tilde{u}$ and $\tilde{v}$. However $\tilde{v} = 0$, because the v component of the velocity must be zero-average over the longitude, otherwise we would have a net flux in the latitudinal direction (south-north or north-south), and this cannot be the case. Hence $\rho_1' = \rho_1' \left(r, \theta, \tilde{u} \right)$, and:

$$\lim_{v \to 0} \rho_1' \left(r, \theta, \tilde{u} \right) = \rho_1' \left(r, \theta, \tilde{u} \right) \tag{5.32}$$

cannot be affected by v approaching the zero value. As a consequence, from (5.31) an expression for ρ_1' is now available:

$$\rho_1' \left(r, \theta \right) = \frac{1}{2} \int \left(\frac{2\Omega}{g_0} r \frac{\partial \bar{\rho} \tilde{u} \left(r, \theta \right)}{\partial z} \right) d\theta + \rho_3' \left(r \right) - \lim_{v \to 0} \rho_2' \left(r, \phi \right) \tag{5.33}$$

Furthermore one must consider that for the second equation of system (5.11), when $v \to 0$, the density perturbation can only be a function of θ, thus:

$$\lim_{v \to 0} \rho_2' \left(r, \phi \right) = \rho_4' \left(r \right) \tag{5.34}$$

Applying the first boundary condition, one of the constants has been determined and put into the general expression for ρ_1':

$$\begin{array}{ll} \rho' \left(r, \theta, \phi \right) = & \frac{1}{2} \int \left(\frac{2\Omega}{g_0} r \frac{\partial \bar{\rho} u(r,\theta,\phi)}{\partial z} \right) d\theta - \frac{1}{2} \int \left(\frac{2\Omega}{g_0} r sin\theta \frac{\partial \bar{\rho} v(r,\theta,\phi)}{\partial z} \right) d\phi + \\ & \frac{1}{2} \int \left(\frac{2\Omega}{g_0} r \frac{\partial \bar{\rho} \tilde{u}(r,\theta)}{\partial z} \right) d\theta + \rho_2' \left(r, \phi \right) + \rho_3' \left(r \right) - \rho_4' \left(r \right) \end{array} \tag{5.35}$$

Now, indicating with $\rho'_5(r,\phi) = \rho'_2(r,\phi) + \rho'_3(r) - \rho'_4(r)$, the second boundary condition has to be imposed. In particular the constant of integration can be computed as in the 2-D case assuming that the density perturbation is zero-mean, this time over the whole 3-D domain:

$$\frac{1}{2\pi^2}\int_\theta\int_\phi \rho'(r,\theta,\phi)\,d\theta = 0 \tag{5.36}$$

meaning:

$$\begin{array}{l}\frac{1}{2\pi^2}\int_\theta\int_\phi\left[\frac{1}{2}\int\left(\frac{2\Omega}{g_0}r\frac{\partial\bar{\rho}u(r,\theta,\phi)}{\partial z}\right)d\theta - \frac{1}{2}\int\left(\frac{2\Omega}{g_0}rsin\theta\frac{\partial\bar{\rho}v(r,\theta,\phi)}{\partial z}\right)d\phi\right]d\theta + \\ \frac{1}{2\pi^2}\int_\theta\int_\phi\left[\frac{1}{2}\int\left(\frac{2\Omega}{g_0}r\frac{\partial\bar{\rho}\tilde{u}(r,\theta)}{\partial z}\right)d\theta + \rho'_5(r,\phi)\right]d\theta = 0\end{array} \tag{5.37}$$

or else:

$$\begin{array}{rl}\rho'_5(r,\phi) = \rho'_5(r) = & -\int_\theta\int_\phi\left[\frac{1}{2}\int\left(\frac{2\Omega}{g_0}r\frac{\partial\bar{\rho}u(r,\theta,\phi)}{\partial z}\right)d\theta\right]d\theta \\ & -\int_\theta\int_\phi\left[-\frac{1}{2}\int\left(\frac{2\Omega}{g_0}rsin\theta\frac{\partial\bar{\rho}v(r,\theta,\phi)}{\partial z}\right)d\phi\right]d\theta - \\ & -\int_\theta\int_\phi\left[\frac{1}{2}\int\left(\frac{2\Omega}{g_0}r\frac{\partial\bar{\rho}\tilde{u}(r,\theta)}{\partial z}\right)d\theta\right]d\theta\end{array} \tag{5.38}$$

Otherwise, we can impose that the density anomalies are null at the poles:

$$\rho'(r,\theta,\phi)_{\theta=0,\pi} = 0 \tag{5.39}$$

in any case, as stated in Section 5.2.1, the constant of integration has no effect on the resulting gravity field due to the winds.

As reported in Choi and Showman (2011), the velocity maps have been produced substituting data at high latitudes (higher than $50°$) with zonally symmetric winds, because of measurement noise and flyby geometry. For this reason, the mass anomalies calculated starting from the observed wind speed profile, can be considered reliable only for $40° < \theta < 140°$ (Choi and Showman, 2011).

Figure 5.9 reports the results of the numerical integration of the complete thermal wind equations, showing the surface density anomalies for a typical height scale of H = 3000 km. The levels of penetration in the vertical direction of the mass perturbations at different height scale are not shown but are all in all equivalent to those in Figure 5.6*b* - 5.8*b*.

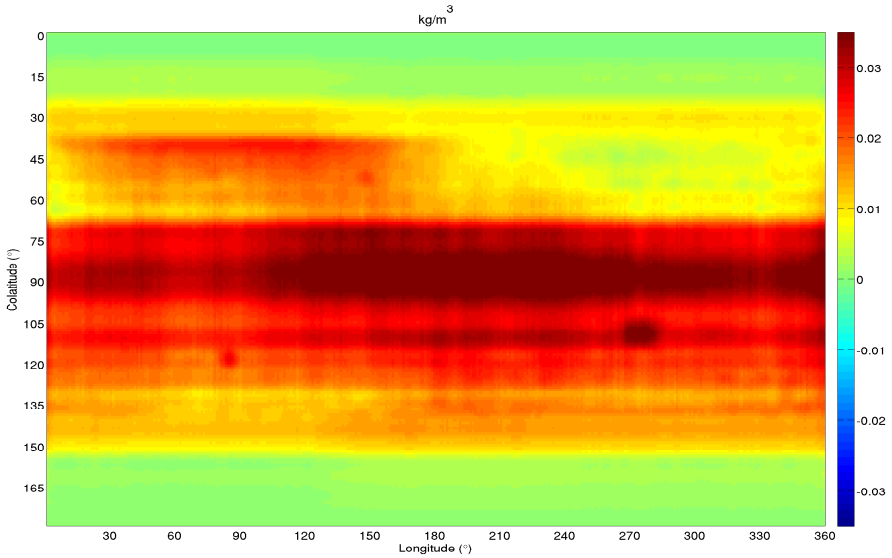

Figure 5.9: Integrated 3-D density profile for H = 3000 km at the surface of Jupiter.

When comparing Figure 5.7*a* with 5.9, a number of considerations can be made. The new density profile is not purely zonal anymore but longitudinal features appear in the surface anomalies, reflecting the actual velocity map. In particular, smaller-scale perturbations such as the Great Red Spot and the Oval BA are now evident in the plot, characterized by positive density disturbances. However, the main horizontal structure of the jets is still clear, with the equatorial band responsible for most of the mass perturbations due to Jupiter's winds.

5.3 From density anomalies to gravity

The main result of the previous section is that a 3-D map of the atmospheric density anomalies $\rho'(r, \theta, \phi)$ for Jupiter has been produced starting from the wind velocity profile. Such disturbances in the mass distribution obviously affect the gravity field of the planet up to high-degree harmonics, depending on the penetration depth of the winds. For the zonally symmetric gravity, the changes in the zonal harmonics due to the wind dynamics can be expressed as:

$$\Delta J_l = -\frac{1}{MR^l}\int_0^R r^{2+l}dr\int_0^{2\pi}d\phi\int_{-1}^{1}P_l\left(\cos\theta\right)\rho'\left(r,\cos\theta,\phi\right)d\cos\theta \quad (5.40)$$

where l is the harmonic degree, M and R are the mass and mean radius of Jupiter, r is the distance from the center of the planet and P_l is the Legendre Polynomial of degree l. Equation (5.40), expanded for the computation of tesseral harmonics as well, can be numerically integrated to produce the contributions of the winds to the gravity field of Jupiter.

In the frame of the simulations of the gravity experiment onboard the Juno mission, a 30x30 gravity field of Jupiter has been generated for three different values of the height scale. Tables 5.1reports the first 10 un-normalized zonal harmonics, due to the presence of jets, for different values of H.

Degree (n)	Central value
J_2	8.606e-09
J_4	-3.931e-09
J_6	2.549e-09
J_8	-9.298e-10
J_{10}	5.660e-10

Degree (n)	Central value
J_2	1.103e-06
J_4	-2.026e-07
J_6	1.967e-07
J_8	-2.147e-08
J_{10}	-5.585e-08

degree (n)	Central value
J_2	1.174e-05
J_4	6.916e-07
J_6	8.553e-07
J_8	-3.167e-07
J_{10}	-2.263e-07

Table 5.1: Contributions to the zonal harmonics due to the winds of Jupiter, up to degree 10. The coefficients are unnormalized. **Top left**: for H = 300 km; **Top right**: for H = 3000 km; **Bottom**: for H = 1000000 km.

Obviously, the deeper the wind penetration, the stronger the gravitational signature of the jets, in fact for H = 300 km the harmonic coefficients are at least three orders of magnitude smaller than the case for H = 3000 km and H = 1000000 km, because much more planetary mass is involved

in the wind dynamics. Figure 5.10 shows the overall 30x30 Jupiter's gravity field in terms of the real component of the tesseral harmonics (C_{lm}) for different values of H. As H grows larger, the first columns of the spectrum (zonal harmonics) acquire a darker shade, from yellow to light red, index of a stronger gravity field. The gravity coefficients decrease with the second power of the degree l.

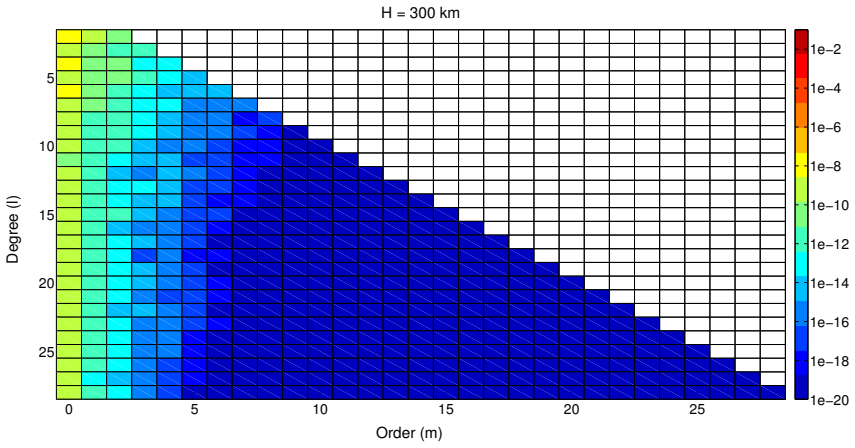

(a)

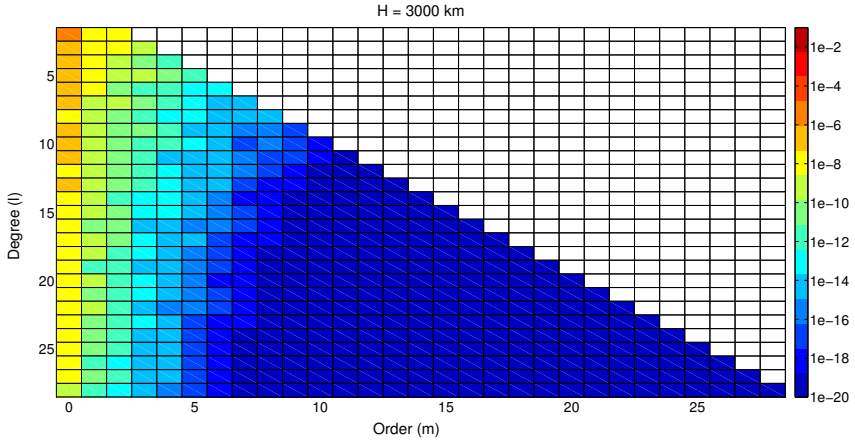

(b)

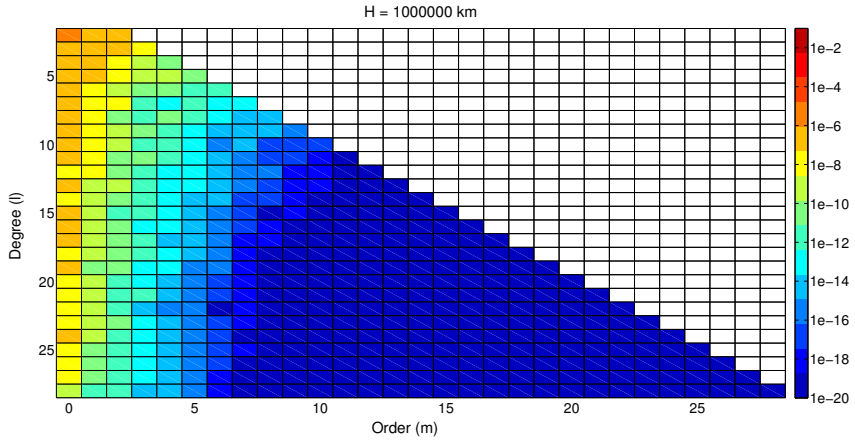

(c)

Figure 5.10: 30x30 gravity field of Jupiter. Each box indicates a specific tesseral harmonic of degree l and order m. **a)** for H = 300 km; **b)** for H = 3000 km; **c)** for H = 1000000 km.

Recalling the expression for the gravitational potential of a planetary body (Chapter 2, Section 2.1), dependent on the spherical harmonics, the surface gravity can be easily calculated as:

$$g = -\nabla U\left(R, \theta, \phi\right) \tag{5.41}$$

Figure 5.11 shows the resulting surface gravity for the three typical cases at different H. Note that the longitude scale is the same as before, with longitudes between 181° and 360° being substituted by negative angles.

In case **a)**, the gravity anomalies due to the winds are of order of tenths of mGal (1 Gal = 0.01 $\frac{m}{s^2}$), the horizontal belts and zones are clearly visible with alternate signs, and a positive gravity disturbance is placed at the location of the GRS. Also the Oval BA is visible as a localized yellow circle at 120° colatitude, 95° longitude. In case **b)** the gravity surface reaches a maximum value of 6 mGal in the equatorial belt, while the Great Red Spot contributes with an anomaly of around 3 mGal. The signature of the Oval BA is more blurred than the previous case. In the last case **c)**, the mass involved in the wind dynamics is so large that it is difficult to recognize any small-scale features, the GRS is barely visible, though the horizontal regions are still distinguishable.

5.4 Estimation setup for the Juno gravity experiment

Gravity measurements have been simulated throughout the duration of the Juno mission (2016 - 2017), using three different gravity fields for Jupiter, corresponding to as many penetration depths of the winds (see Section 5.3, Table 5.1 and Figure 5.10).

As described in Chapter 4, the first step for the estimation of physical parameters of interest by means of Doppler tracking of the spacecraft is the definition of a first-guess model for the environment surrounding the probe. Indeed, the main goal of integrating the trajectory of the spacecraft during the estimation phase is to generate the computed observables to be compared to the (synthetic) observed ones.

The gravity field of Jupiter used for initializing such process comprises only the effect of the solid body rotation up to degree 6, as intended by

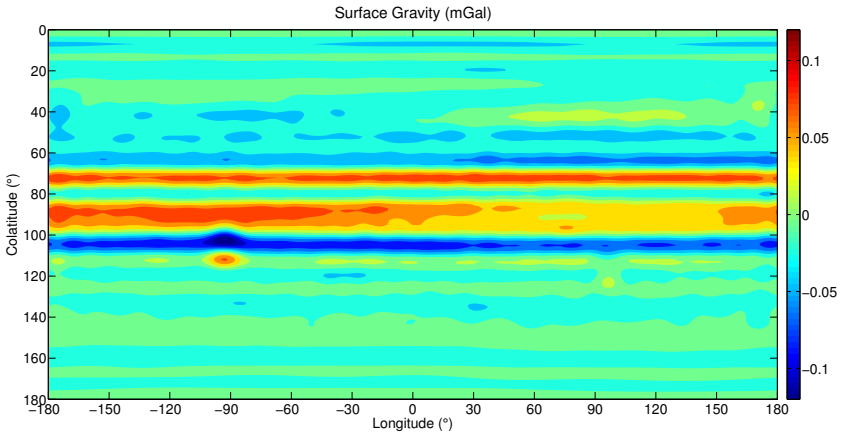

(a)

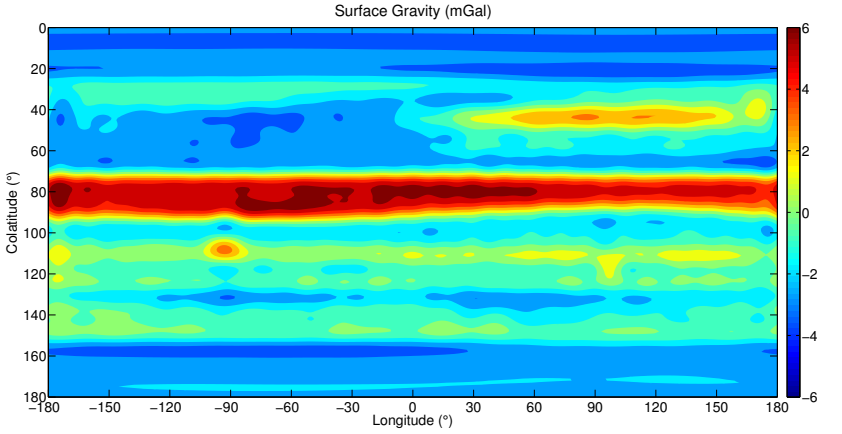

(b)

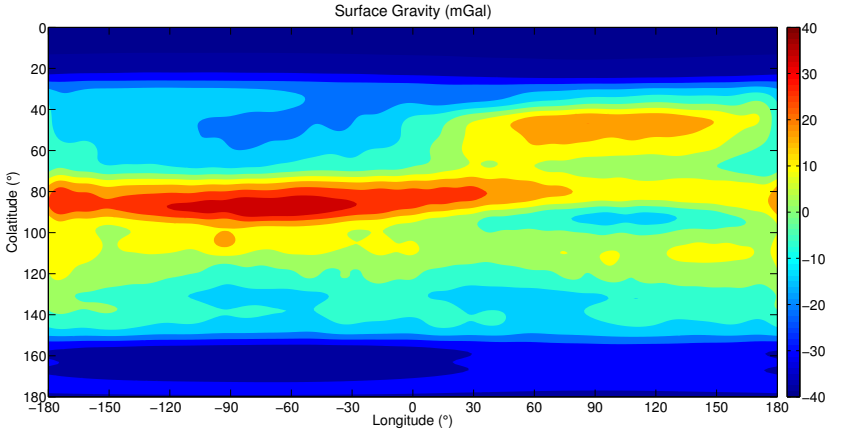

(c)

Figure 5.11: Gravitational signature of the thermal winds. **a)** for H = 300 km; **b)** for H = 3000 km; **c)** for H = 1000000 km.

Hubbard (2012) and reported in Table 4.1. All other harmonics, zonal and tesserals are initialized to null. One of the objectives of this analysis is, in fact, assessing the possibility of recovering the actual simulated gravity field, which includes the effects of the winds, starting from values that are considerably off. The first-guess tidal Love numbers' are equal to the ones used in simulations, since the estimate of such parameters is not a goal of this study.

The initial condition used to integrate the trajectory during the estimation process, are the same as the ones used for the simulated orbit, not considering any errors on the spacecraft initial position and velocity. Nevertheless, due to the differences between the gravity fields used in simulation and estimation, the two trajectories will differ at times different from the initial epoch.

All non-gravitational effects (solar radiation pressure, albedo, thermal emission, etc.), including the model of the Juno spacecraft, have been reproduced for the estimation process, starting from the simulation setup. Therefore a strong assumption is made: that forces other than gravity are perfectly calibrated by the instrument, which is in most cases untrue, however this mismodeling can be easily compensated by, for example, introducing a slightly higher noise on Doppler measurements.

In this regard, Tapley *et al*. (2004) give a tool for properly weighing the simulated observations. In particular, for Doppler data, each range-rate measurement is weighed as follows:

$$w = \frac{1}{\sigma^2} \tag{5.42}$$

where:

$$\sigma = RMS \left[1 + \frac{18}{(E+1)^2} \right] \tag{5.43}$$

RMS is the noise *standard deviation* (the same as used in the simulation step) and E is the station elevation angle characterizing the datum. Obviously, the smaller the elevation, the smaller the data weight (see Chapter 4, Section 4.3.2).

The vector of estimated parameters represents the set of physical quantities which system (3.41) is solved for. This comprises: the position and velocity of the spacecraft (6 parameters) in *Jupiter System Barycenter Earth*

Mean Equator J2000 at the beginning of each one of the 25 arcs (corresponding to the 25 flybys of Jupiter). This set represents the local parameters (totally $25 \times 6 = 150$), known with *a priori* uncertainties of 10 km for the position components and 10^{-5} km/s for the velocity components.

The vector of global parameters varies according to the minimum order of the gravity field necessary to obtain an un-biased fit of the data. This minimum set of harmonics depends, in turn, on the strength of the simulated gravity field, in particular the deeper the penetration depth, the larger the asymmetries in the gravity field of Jupiter and the higher the required harmonic order. In general, the estimated gravity field can vary between a 20x5 and a 30x30 expansion in spherical harmonics.

Figure 5.12 shows the simulated zonal harmonics due to the winds of Jupiter (not considering the solid body rotation) and the associated *a priori* uncertainties (see legend).

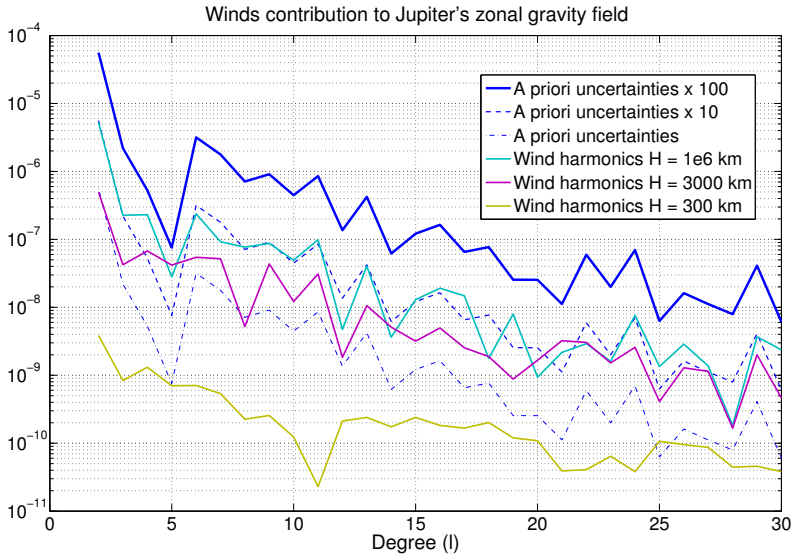

Figure 5.12: Zonal gravity field of Jupiter in terms of harmonic coefficients (degree 2 to 30) and associated *a priori* uncertainties.

As expected when the depth of the winds increases, the magnitude of the harmonics increases as well, but all lines lie below the highest uncertainty curve (blue solid line), even for very deep winds (turquoise line). This degree of freedom was adopted to make the gravity field coefficients free to vary and recover the correct wind depth. The *a priori* uncertainties

have been selected by multiplying the wind harmonics corresponding to H=10^6 km by a factor of 1, 10 and 100. Different levels of initial uncertainties are selected depending on the case.

Jupiter's GM, k_2 and k_3 are included in the solve-for vector as well, with *a priori* uncertainties of 2 km^3/s^2, 0.5 and 0.5, respectively. The masses of the Galilean satellites are taken into account in the process by including them as consider parameters, meaning that their values are not estimated and updated yet their uncertainties affect the estimate of other parameters.

5.5 Estimate of Jupiter's gravity field: detection of mass anomalies produced by winds

The estimation results in term of assessment of the accuracies attainable in the estimation of the gravity harmonic coefficients of Jupiter has already been discussed by Finocchiaro (2013). In this dissertation, I follow up on his work and try to understand whether or not solving the thermal wind balance equations in a 3-D domain is advantageous to the detection of Jupiter's wind gravitational signatures, especially that coming from small-scale features such as the Great Red Spot. In particular I will explore the prospect of recovering the actual simulated surface gravity (Figure 5.11) for different values of H, starting from a plain solid body gravity field.

5.5.1 Shallow-wind case

In this case the winds fold with a height scale of H = 300 km, indicating very shallow perturbations that influence the motion of Jupiter's atmosphere just close to the planetary surface. That being so, the gravity field deviates mildly from that of a solid rotator and one can expect very small tesseral harmonics due to winds if compared to the rotational zonal contributions. For this reason, the *a priori* uncertainties can be set tighter (x1 factor, dashed blue thin line in Figure 5.12) than for stronger field cases.

The minimum set of spherical harmonics necessary to fit the data is a degree-20 zonal gravity field, this is because the tesseral and higher zonal harmonics corresponding to this wind depth are too small to be detectable by the Juno gravity experiment. In other words the accelerations sensed by the spacecraft and due to high-frequency harmonics are so small for the

shallow wind case, that they appear to lie below the noise level. Nevertheless, since I'm interested, among other things, in detecting the gravitational signal of the GRS, I have considered a 20x5 gravity field, to maintain a certain longitudinal variations of the anomalies.

Figure 5.13 shows the estimation results, for H = 300 km, in terms of reconstruction of the gravity anomaly map. The top plot (a) shows the estimated gravity anomalies as output of the data filtering, over a *Hammer* projection of Jupiter's surface. The estimated disturbances are of the same order of magnitude of the simulated ones, ranging between $\pm$ 0.1 mGal. Between 5° and 35° Jupiter latitude, where Juno closest approaches will take place, the reconstruction of the anomaly map is rather accurate (compare with Figure 5.11a), with quite distinct boundaries between different zonal bands. As one moves poleward from this central belt, the estimated anomalies are less and less consistent with the simulated ones, because of the orbit geometry. From the graph it is not really possible to spot the longitudinal variations of the disturbances, because of the rather low-order expansion (m=5) of the gravitational potential in spherical harmonics. In particular the small gravity anomaly produced by the GRS, visible in the top plot, cannot be resolved in the estimation process for the shallow wind case.

The bottom graph (b) represents the formal uncertainties on the gravity anomalies over the reference ellipsoid, using a logarithmic scale. The same considerations are valid, the central sector ($5^\circ < LAT < 35^\circ$) is characterized by higher accuracies (around 0.01 mGal, at the 1σ level), with the uncertainties gradually growing toward the poles, reaching a maximum of about 5 mGal at the south pole.

Theoretically, in order to increase the resolution of the map and reduce the length scale of the detected features, it could be possible to expand the gravity field up to higher orders (*e.g.* m=10), expecting the gravitational signature of the GRS and other vortices to appear. In practice, this is never convenient, because of the concurrent degradation of the uncertainty map, that would jeopardize the accuracies outside the central region even more.

Generally speaking, when analyzing radio science data, this is the kind of pursued trade-off: on one hand, from a purely scientific point of view, one would want to estimate the largest number of physical parameters, on

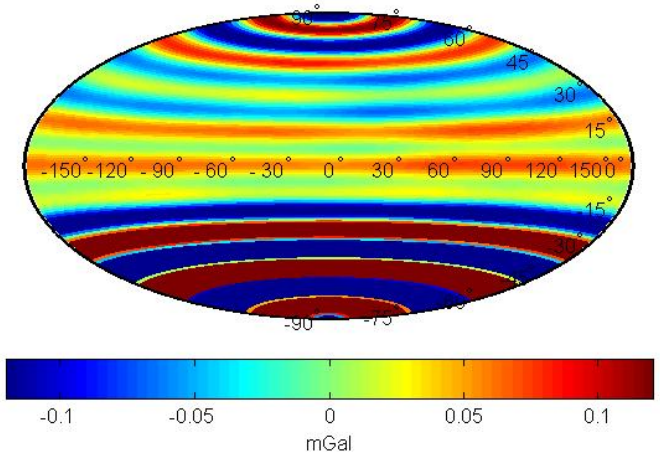

(a)

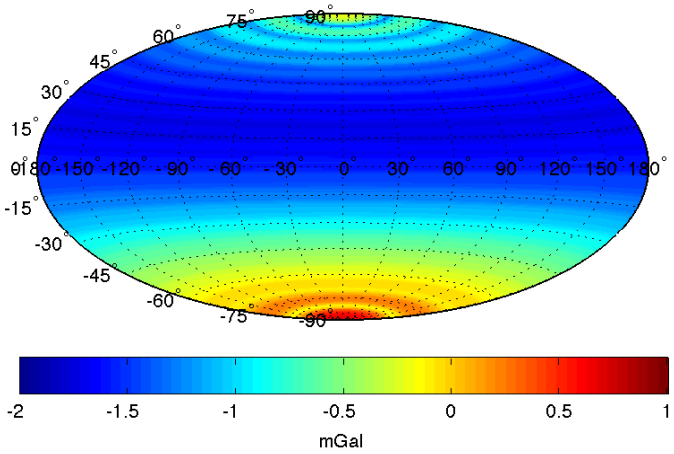

(b)

Figure 5.13: Gravity anomalies due to thermal winds, for H = 300 km. **a)** estimated anomalies; **b)** formal uncertainties (1σ, logarithmic scale).

the other hand the formal uncertainties tend to increase with this number. The sought compromise consists in balancing these two effects.

Figure 5.14 shows the quality of the data fit in terms of proper reconstruction of the gravity disturbance map. A possible performance index is the ratio of the differences between the simulated and estimated anomalies (estimation errors) to the correspondent formal uncertainties at 1σ. Consequently, the index is an adimensional quantity. The smallest relative errors are localized either at low-north latitudes, where the sensitivity to the gravity field is the highest, or at the poles, where the uncertainties are very large. In any case, everywhere on the map the magnitude of the errors is contained within 3σ.

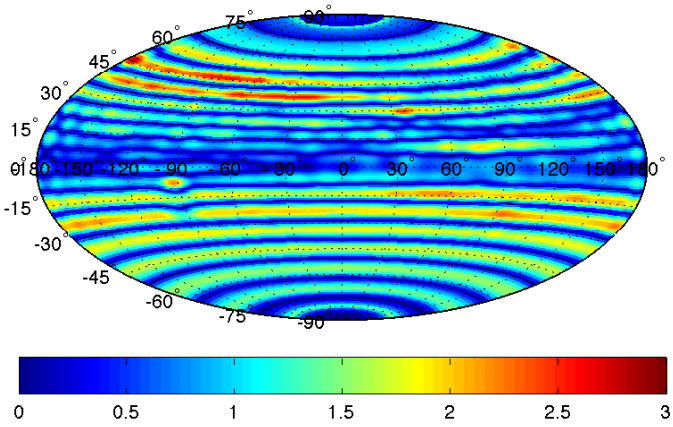

Figure 5.14: Estimation errors versus formal uncertainty (1σ).

At this point, one might be interested in comparing the gravitational signature of the gravity anomalies due to Jupiter's shallow winds to the mapped formal uncertainties, in other words the signal to noise ratio (SNR). To this end, the adimensional ratio of the two quantities, at the 1σ level, is produced and plotted using a *Hammer* projection (Figure 5.15). If the ratio is smaller than the unit the signal of the gravity anomaly is weaker than the uncertainty characterizing the measure, thus it's not detectable. Hence, for clarity, only absolute values in the range 1-4 have been plotted, while the extended dark blue region represents the areas in which gravity measurements are not sensitive to mass anomalies produced by shallow winds. All

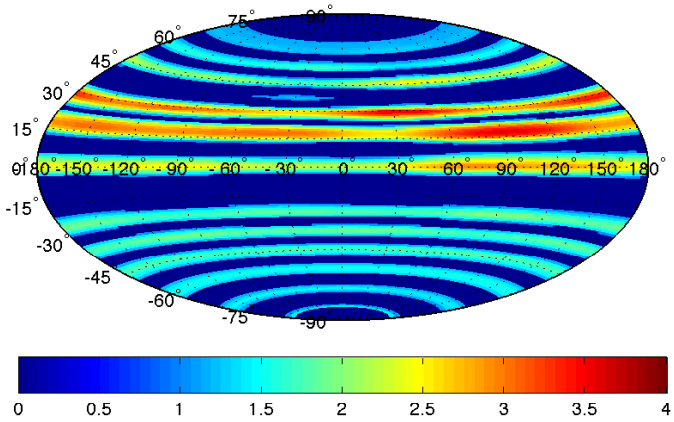

Figure 5.15: Ratio of the gravitational signal of the anomalies and associated formal uncertainties (1σ).

over the map, the strength of the gravity anomaly signal does not exceed 4σ, meaning that the detection of the density disturbances due to winds characterized by a small height scale (300 km) is highly challenging, if not improbable, except maybe for the equatorial and northern low-latitude regions.

In particular, in the shallow wind case, there are no premises for inferring any properties characterizing the Great Red Spot, besides the fact that it does not extend in depth below 300 km under the surface of Jupiter, since the anomaly is not visible by gravity observations, the SNR being only 2.5 times bigger than the local uncertainty in that region.

5.5.2 Mid-deep wind case

Winds characterized by a folding scale of H=3000 km represent the intermediate case where the penetration extends to 5% of Jupiter's mean radius. In this case a much stronger atmospheric gravitational signal is expected, involving also evident large and small scale longitudinal variations. The *a priori* uncertainties are set 10 times larger than the shallow wind case, in order to allow the estimated gravity field to deviate from Hubbard's (2012) solution and better adjust to the actual simulated surface gravity. At least a 30x20 gravity field expansion is needed to properly fit the synthetic

Doppler data, giving the gravitational map a higher resolution then before.

Figure 5.16 top plot (a) shows the estimated gravity anomalies. The gravitational disturbances range, in general, between $\pm$ 6 mGal and, at the GRS location, a signature of order 3 mGal is visible, meaning that, at this penetration depth, there is some prospect of perceiving the presence of Jupiter's vortices from gravity measurements.

The estimation process suffers from the same limitation as before: one can trust the reconstructed gravity map only in the usual north-equatorial band where gravity measurements are more precise (compare to Figure 5.11b). In this case, given the high-degree and high-order gravity field expansion, the longitudinal dependence of the anomalies is evident, although the profile seems quite indented with a frequency that resembles the spacing between two consecutive ground tracks, rather than the actual simulated map. Indeed, the ground tracks are evident in the bottom plot (b) showing the formal uncertainties. The 25 gravity flybys ground tracks basically follow the meridians, with a span of 12°, and are represented by darker blue stripes. Again the central region is better resolved, while the determination of the gravity field at the poles is much less accurate. The uncertainties are about one order of magnitude larger than the shallow-wind case, going from 0.1 mGal at the equator to 30 mGal at the poles, due to the growth of the number of estimated parameters.

Also in this case the estimation errors are contained within 3σ all over the map, except for a few points that slightly exceed this margin, located where the uncertainties are the smallest (Figure 5.17). The plotted parameter is adimensional, being the ratio of the error to the associated formal uncertainty.

In order to find out whether the gravitational signature of the GRS is detectable or not, two distinct concurring factors must be taken into account: on one hand the gravity anomaly is stronger simply because the winds are deeper, on the other hand the uncertainties have increased because of the higher-degree and order gravity field necessary to fit the simulated Doppler data. The adimensional parameter used to quantify the proportion between these two effects is again the ratio between the gravity anomalies to the formal uncertainties (SNR, see Figure 5.18).

For $5^\circ < LAT < 35^\circ$, the ratio is very large where the central belt

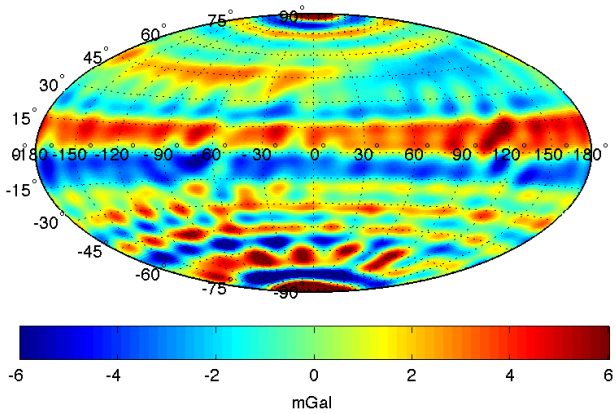

(a)

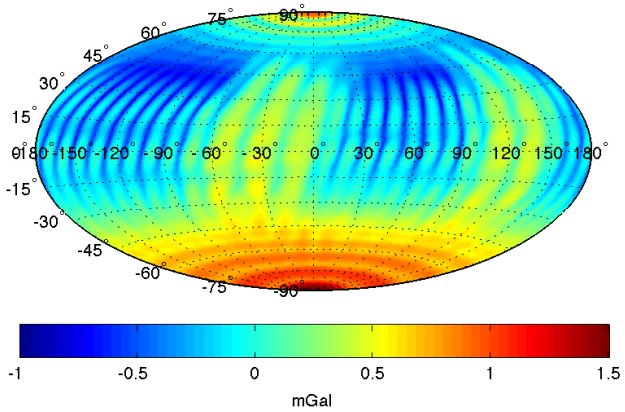

(b)

Figure 5.16: Gravity anomalies due to thermal winds, for H = 3000 km. **a)** estimated anomalies; **b)** formal uncertainties (1σ, logarithmic scale).

intersects the ground tracks, with the gravity signal being even 10 times larger than the noise standard deviation. In particular the signatures of the equatorial and northern jets are expected to be clearly observable by means of radiometric measurements. Regarding the vortices, the expected disturbance in correspondence to the GRS location is clearly visible in Figure 5.18

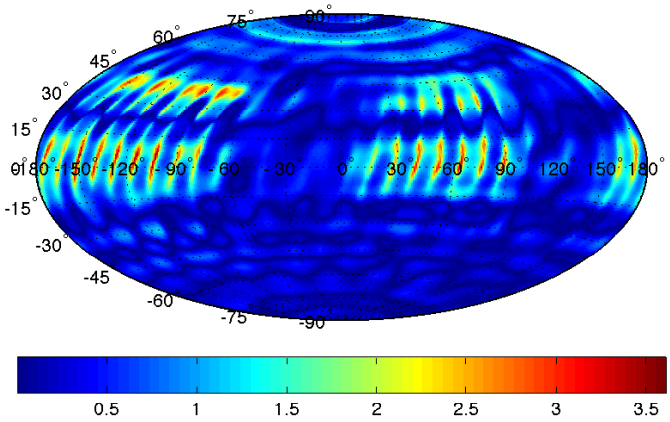

Figure 5.17: Estimation errors versus formal uncertainty (1σ).

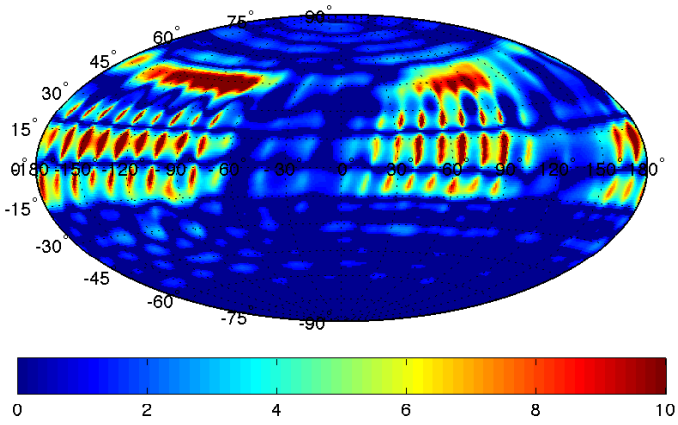

Figure 5.18: Ratio of the gravitational signal of the simulated anomalies to associated formal uncertainties (1σ).

as a bright point isolated at a very specific latitude ($-15°$). Thus, in principle one can detect the signature of this major vortex, although the high altitude of the Juno spacecraft when flying over this particular location and the longitudinal spacing between two adjacent flybys can make the discrimination between this particular anomaly and the background mean field very disturbed, pointing out the inadequacy of a normal basis as the spherical harmonics in describing localized regional phenomena such as vortices.

In support to this, it is useful to plot the estimated gravity anomalies, once the mean longitudinal field has been removed (Figure 5.19).

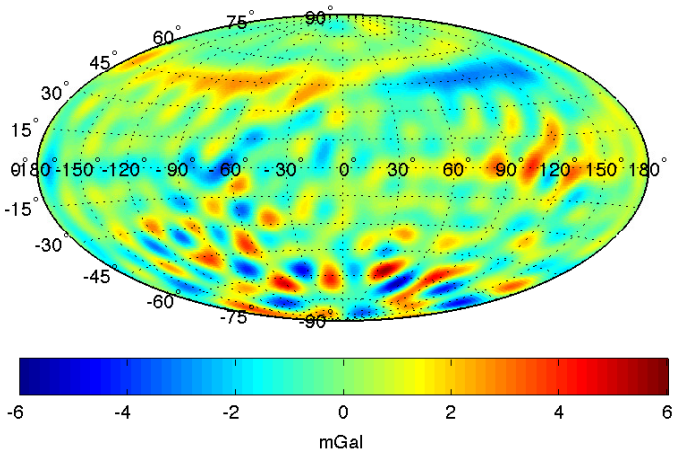

Figure 5.19: Estimated gravity anomalies after the removal of the mean field along the longitude direction.

At the GRS location ($LAT = -15°, LONG = -90°$) there is, indeed, evidence for a localized gravity anomaly of order 3 mGal, however the poor quality of the gravity resolution in the southern hemisphere makes it difficult to distinguish between the GRS signature and other disturbances of the same order of magnitude that could be a result of the natural oscillation of the central value within 3σ.

Nevertheless, looking at Figure 5.18 it is evident that the GRS-like anomalies in Figure 5.19 only appear where the ratio of the gravity disturbances to the uncertainties is very small, if not undetectable. In the clear-signal region below the equator, the GRS is the only visible anomaly, as underlined by Figure 5.20, that shows the ratio of the gravity anomalies minus the longitudinal mean to the formal uncertainties (SNR).

Looking at the enlargement in Figure (5.20), one can conclude that, for a wind penetration depth of about 3000 km, the signature of the Great Red Spot is detectable by the radio science instrument, although with very small margins.

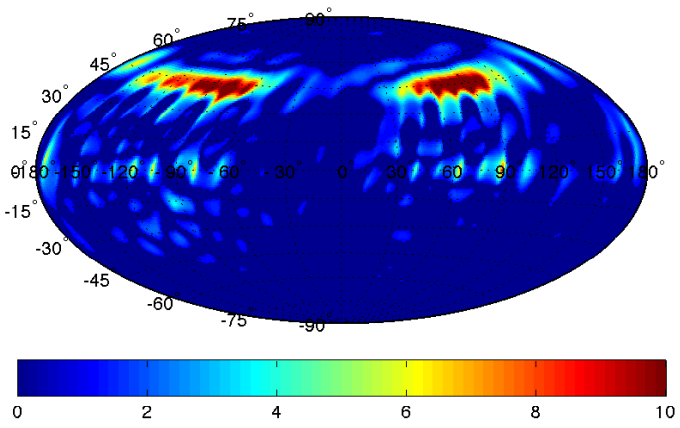

(a)

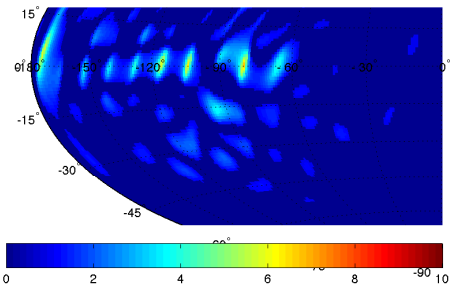

(b)

Figure 5.20: Ratio of the gravitational longitudinal oscillations of the estimated anomalies and associated formal uncertainties (1σ).

5.5.3 Very-deep wind case

The last case analyzed is that of very deep winds greatly affecting Jupiter's interior dynamics. The height scale (H=10^6 km) is much larger than Jupiter's radius, meaning that the winds penetrate all the way in a direction parallel to the spin axis, creating discontinuities at the equator.

The simulated and estimated anomalies (Figure 5.11 *c* and Figure 5.21a) are one order of magnitude larger than the mid-deep wind case. The most visible effect is the resulting oblateness due to the predominant equatorial jets, appearing as a 40 mGal zonal anomaly at the equator and counter-balancing anomalies at the poles. The vector of solve-for parameters com-

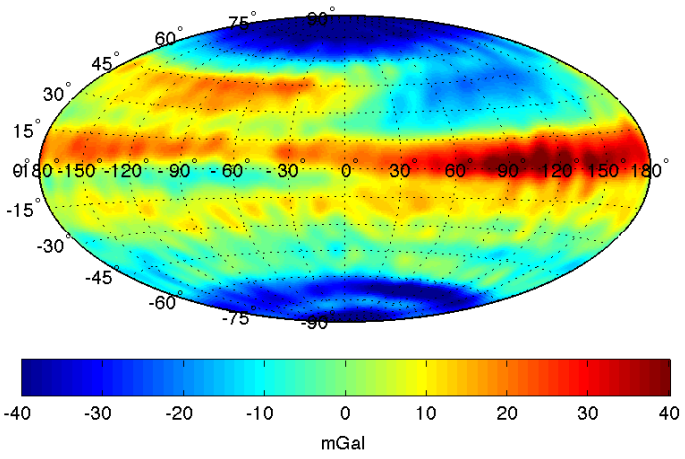

(a)

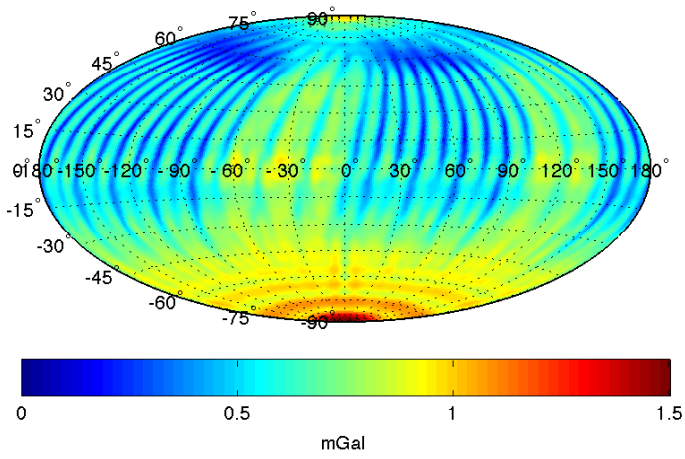

(b)

Figure 5.21: Gravity anomalies due to thermal winds for H = 1000000 km. **a)** estimated anomalies; **b)** formal uncertainties (1σ, logarithmic scale).

prises a full 30x30 gravity field, while the *a priori* uncertainties are set so as to be non-constrictive at all (x 100 multiplying factor in Figure 5.12).

Being the disturbances due to the winds so large, they can be retrieved much better in the estimation process, even outside the usual central region. On the other hand, the gravity anomaly due to the GRS is always of order of a few mGal, thus not really visible on the map. The uncertainty plot (b) still presents the same characteristics, with better accuracies where the spacecraft trajectory outlines the ground tracks. In the case of very deep winds, the uncertainties on the gravity anomalies range between 1 and 30 mGal.

Regarding the estimation errors, their ratio to the formal uncertainties is decisively below the 3σ level all over the map (Figure 5.22).

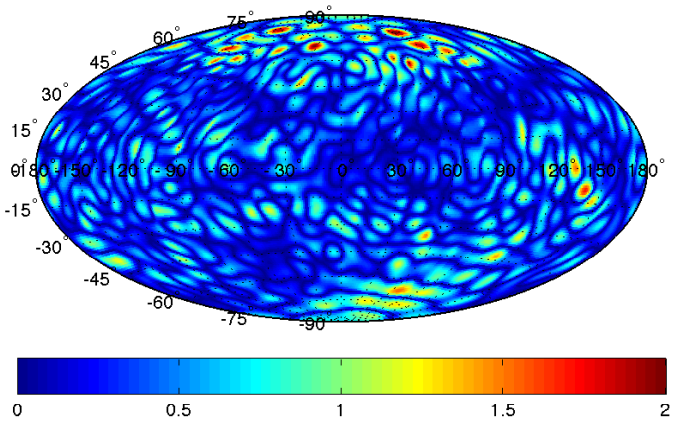

Figure 5.22: Estimation errors over formal uncertainty (1σ).

It is interesting to analyze what happens in this case to the signal to noise ratio (Figure 5.23). Again, on one hand, the gravity disturbances are evidently larger, on the other hand, the uncertainties have significantly increased. The result is that, at the poles and at the equator, where the anomalies are the largest, the first contribution is prevalent and the signal is stronger than in the former cases; on the contrary, for $-60° < LAT < 0°$, the uncertainties are so large that the map looks more blurry than before. Particularly at the GRS location, the signal is not even twice as large as 1σ.

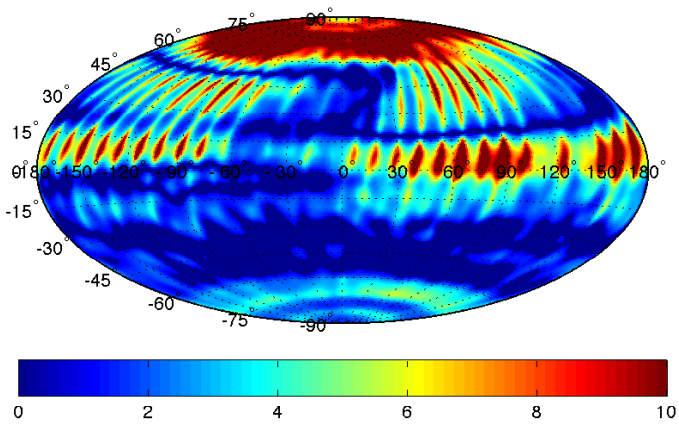

Figure 5.23: Ratio of the gravitational signal of the estimated anomalies to associated formal uncertainties (1σ).

Subtracting the mean zonal field as done in the previous subsection, the results do not change, the longitudinal fluctuation due to GRS still does not exceed the 3σ level. Looking at Figure 5.24 and at its enlargement (Figure 5.25), one can conclude that, in the deep wind case, the increase in the formal uncertainties due to the required higher degree and order expansion of the gravity field has a stronger effect on the detection of the GRS gravitational signature than the increase in the gravity anomalies itself, at least at the GRS particular location.

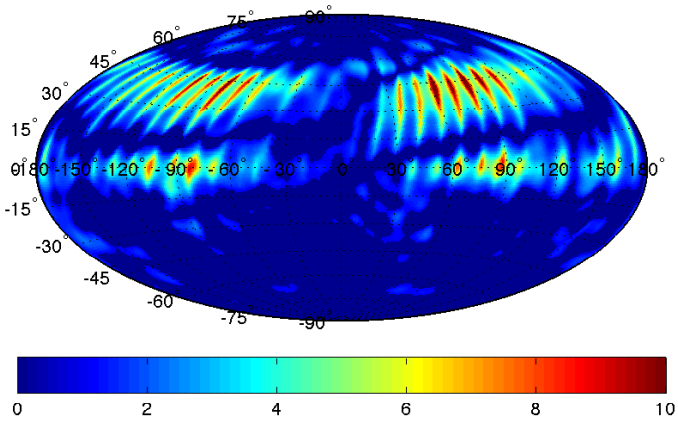

Figure 5.24: Ratio of the gravitational longitudinal oscillations of the estimated anomalies and associated formal uncertainties (1σ).

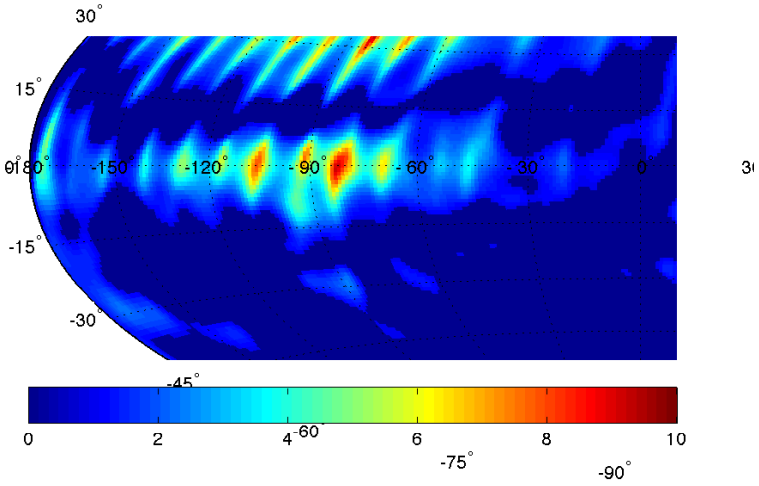

Figure 5.25: Enlargement of Figure 5.24 near the GRS location.

Chapter 6

Numerical simulations of the JUICE gravity experiment

Gravity measurements are essential to fully characterize the interior structure and investigate the formation of Ganymede and Callisto, throughout JUICE different science phases. If the bodies are found in hydrostatic equilibrium, the radial density distribution may be constrained from their moment of inertia factor and low-degree gravity field coefficients (Asmar *et al.*, 2009). Furthermore, the Love number k_2 provides the magnitude of the icy satellites' response to tidal forces exerted by Jupiter. Since tidal deformations would be much larger in case of presence of a liquid layer within the body, the determination of this parameter represents potential evidence for sub-surface oceans on the Galilean satellites.

The main goal of performing numerical simulations of radio science experiments is assessing the accuracies in the estimation of planetary gravity fields and tidal distortions and the capability of the orbit determination process of reconstructing the spacecraft trajectory. In the first sections of this chapter I introduce a number of techniques used to improve the estimation process, while the latter ones present the results of the analysis of synthetic radiometric data using Ka-band, as scheduled for the JUICE mission, with as many dedicated sections as the mission targets.

6.1 Satellite ephemeris update

Jupiter satellite ephemerides are provided by NASA/JPL and are composed of sets of Chebyshev polynomial coefficients given at specific epochs, called nodes, usually 4-18 days apart. At any other time instant, the polynomials are interpolated between two adjacent nodes in order to provide the state of Jupiter's satellites. The position and velocity of the bodies are obtained by numerically integrating the equations of motion starting from a reference epoch. The adopted special perturbation technique is the Cowell method (Peters, 1981).

Since observations of the Jupiter system are fewer than, for example, those collected for Saturn's satellites, the state of the Galilean satellites are known with larger uncertainties. For this reason, during radio science data analysis, it is necessary to update the position and velocity of the central body, otherwise either the data cannot be fit or the estimated parameters suffer from biases. For the JUICE mission, the set of adopted and updated satellite ephemerides is JUP230.

6.2 Satellite tides

Satellite Love numbers are auxiliary parameters introduced in the orbit determination process for the purpose of estimating the variability of the body gravity field along its orbit. A necessary step to estimate such coefficients is to compute the partial derivatives of the observable ν with respect to the Love numbers. In case only degree-2 distortions are considered, this can be done by using the chain rule:

$$\begin{aligned} \frac{\partial \nu}{\partial k_2^{\Re}} &= \sum_m \frac{\partial \nu}{\partial C_{2m}} \frac{\partial C_{2m}}{\partial k_2^{\Re}} \\ \frac{\partial \nu}{\partial k_2^{\Im}} &= \sum_m \frac{\partial \nu}{\partial C_{2m}} \frac{\partial C_{2m}}{\partial k_2^{\Im}} \end{aligned} \tag{6.1}$$

and considering that the first term on the right hand is a direct output of the OD code, being nothing other than the partial derivatives of the observable with respect to the degree-2 gravity field coefficients. The second term represents the fluctuation in the dynamical gravity field of the satellite with respect to the Love numbers. In particular, from equation (2.44) it is evident that the dependence of the dynamical part of C_{2m} on k_2 is linear

and consequently the derivative depends linearly on the orbit eccentricity and on trigonometric functions of the mean anomaly (for details see Iess *et al.*, 2012, Supplementary Material).

Furthermore, it is necessary to account for the resulting accelerations caused by a non-null value of k_2 while integrating the spacecraft trajectory. Therefore, at each iteration, the quadrupole gravity field must be corrected introducing tidal variations in the definition of the dynamical model, depending on the previously estimated k_2. However, although k_2 is constant, the fluctuations in the degree-2 coefficients are continuously varying along the trajectory, due to their dependence on the mean anomaly. A good approximation is to consider ΔC_{2m} constant within the 1-day single arc integration and adjust the values from pass to pass. This assumption is not compromising considering that the average tracking pass lasts 8 hours which represents a small fraction of Ganymede and, even more, Callisto orbital periods.

6.3 Ganymede

JUICE orbits around Ganymede represent the most extended and final stage of the mission. As the satellite is the main target, the covariance analysis of the gravity experiment at Ganymede is discussed first.

The requirements on the gravity field determination are very ambitious but supported by a great number of available observations, for which the satellite coverage will be uniform ($i = 90°$). The angle between the orbital cross direction and the Earth-spacecraft direction is such that the spacecraft is never occulted by Ganymede and is always illuminated for solar power charging, although this is not ideal for Doppler tracking. Doppler and range measurements are collected each day for 132 days, the tracking schedule is shown in Table 6.1.

Obs	Sample time	Tracking (h)	Min E (deg)	Noise RMS
Range-rate	60 s	8	20	0.30-0.45 mHz
Range	50 points/pass	8	20	1 RU

Table 6.1: Observation schedule for the Ganymede orbital phase.

Occultations by Jupiter and other Galilean satellites are taken into account as well as data removal due to small station elevation angles.

6.3.1 Estimation setup

Gravity measurements at Ganymede have been simulated using the dynamical model described in Chapter 4. For the estimation process, the dynamical environment, in term of gravitational effects, is the same as the simulated one, except for the gravity field and Love numbers of Ganymede itself. In particular, the former has been initialized to the 2x2 expansion in Table 4.2, setting all higher-frequency harmonics to null, although the simulated gravity field is a full 30x30 expansion. The Love numbers are initialized to null as well (both components).

Parameter	Initial value
GM	9887.83 km^3/s^2
J_2	1.27 $\times 10^{-4}$
C_{22}	3.83 $\times 10^{-5}$
$k_2^{\Re}$	0.0
$k_2^{\Im}$	0.0

Table 6.2: Initial values for the mass and quadrupole gravity field of Ganymede. Spherical harmonic coefficients whose initial conditions are not shown are initialized to null.

As for non-gravitational accelerations, in the frame of these simulations I assumed perfect calibration of the disturbances by means of the orbit determination code, although this condition is far for being true. For instance, the presence of a thin oxygen atmosphere of Ganymede is expected to provide the largest disturbances and to prove the most difficult to calibrate. However, given the geometry and duration of the orbital phase, estimates of the atmospheric density or drag coefficient of the spacecraft can be attempted in order to absorb the acceleration without jeopardizing the determination of the gravity field coefficients, as has been done for Enceladus (Iess *et al.*, 2014).

For the integration of the trajectory arcs, no errors on the initial conditions of the spacecraft state are considered, nevertheless the simulated and

estimated trajectories are necessarily different due to in-congruence in the adopted dynamical models.

The data weighting method is the same as described in Section 5.4, with weights inversely proportional to the square of the expected RMS of the residuals and considerably decreasing with low station elevation.

The vector of estimated parameters is composed of:

- Locals:
  - the JUICE spacecraft position and velocity at every initial epoch for each arc (total of 132×6) with *a priori* uncertainties of $1km$ on the position components and $5mm/s$ on the velocity.
- Globals:
  - Ganymede's GM (1 parameter) with *a priori* uncertainty of 3.00 km^3/s^2.
  - Ganymede's spherical harmonic coefficients up to degree and order 30 (957 parameters).
  - Ganymede's Love number k_2, real and imaginary components, *a priori* uncertainties of $\sigma_{k_2}^{AP} = 1.0$.
  - Ganymede's position and velocity with respect to Saturn barycenter (6 parameter) with uncertainties of $10km$ on the position components and $10mm/s$ on the velocity components.

The *a priori* uncertainties on the coefficients of the gravity field have been selected in the following way: a strong full 30x30 gravity field has been generated using a large Kaula coefficient of $A_k = 50$. Then, the unnormalized coefficients have been set up to be the initial uncertainties on the first-guess gravity field.

6.3.2 Estimation results

In this subsection the estimation results in regard to the Ganymede phase are shown and thoroughly discussed. The data simulated for the JUICE orbital phase are processed in a multiarc filter where a unique solution for the global parameters is obtained by combining the information matrix from each of the 132 passes (of 1-day duration).

Gravity field estimation

The information contained in Ganymede's gravity field 30x30 expansion can be synthesized by calculating the correspondent Kaula coefficients C_l, using the normalized estimated spherical harmonics characterized by the same degree (see equation 2.14). The formal uncertainties on these parameters are computed using the chain rule:

$$\sigma_{C_l}^2 = \sum_m \left(\frac{\partial C_l}{\partial C_{lm}} \right)^2 \sigma_{C_{lm}}^2 + \left(\frac{\partial C_l}{\partial S_{lm}} \right)^2 \sigma_{S_{lm}}^2 \tag{6.2}$$

where $\frac{\partial C_l}{\partial C_{lm}}$ and $\frac{\partial C_l}{\partial S_{lm}}$ are analytically derived from (2.14) while $\sigma_{C_{lm}}$ and $\sigma_{S_{lm}}$ are outputs of the filtering process. In turn, both central values and uncertainties must be compared to the true errors, defined as the differences between simulated and estimated Kaula coefficients.

Figure 6.1 shows the estimation results for Ganymede's gravity field, from degree 2 to degree 30. The curve of the estimated Kaula coefficients for a very weak field ($A_k = 2$, solid blue line) shows how, around degree 15 of the spectrum, the relative uncertainty, obtained by comparing the 3σ curve (dashed black line) with the central values, becomes larger than 10%. This means that gravity measurements at Ganymede, as intended for the JUICE mission, are sensitive at least to the satellite degree-15 gravitational potential, but could actually go much further, if the gravity field were stronger ($A_k > 2$). For example, for $A_k = 20, 200$ (solid orange and green lines) the 10% relative uncertainty level moves further, around degree 25 and 30, respectively. However, as discussed in the previous chapter, when dealing with gravity experiments one has to find the minimum set of harmonic coefficients capable of fitting the data, in order not to jeopardize the accuracies in the estimation of the gravity field. The true errors (red line), which represent the capability of the filter to recover the simulated gravity field by estimating the harmonic coefficients, are small and well below the 3σ level.

Table 6.3 is a summary of such results in terms of un-normalized zonal harmonics up to degree 30, plus degree-2 real sectorial. Both degree-2 coefficients J_2 and C_{22} can be estimated with a relative accuracy smaller than 2 part in 10000 (absolute un-normalized uncertainty of about 3×10^{-10} and 2×10^{-11} respectively), without imposing any constraints on the hydrostacy of the satellite.

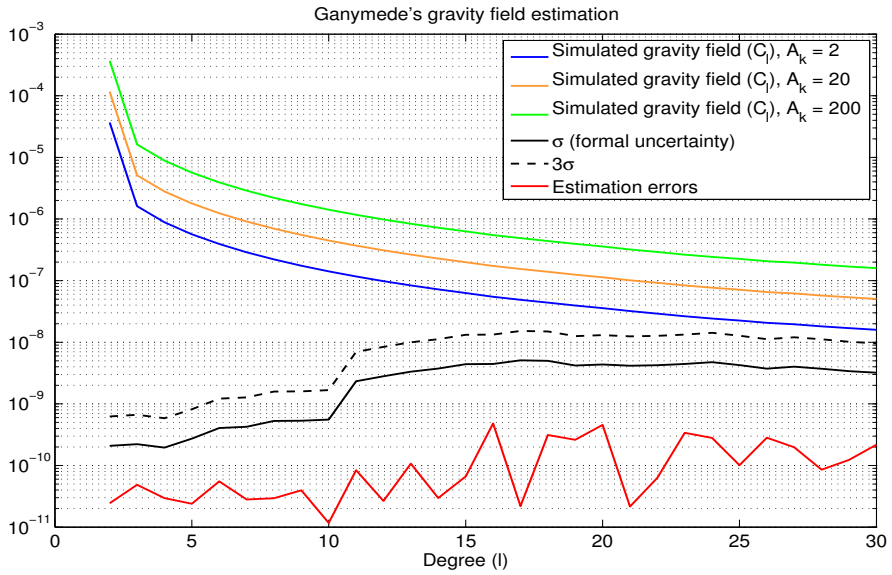

Figure 6.1: Visual display of Kaula's rule for Ganymede's gravity field. Estimated coefficients for $A_k = 2, 20, 200$ (blue, orange, green line), formal uncertainties (black solid/dashed line, $\sigma/3\sigma$ level) and estimation errors (red line).

Gravity coefficient	Formal uncertainty	Relative uncertainty (%)
J_2	$2.9 \cdot 10^{-10}$	$2.2 \cdot 10^{-4}$
C_{22}	$1.8 \cdot 10^{-11}$	$3.7 \cdot 10^{-5}$
J_3	$3.5 \cdot 10^{-10}$	$1.6 \cdot 10^{-2}$
J_4	$5.0 \cdot 10^{-10}$	$2.7 \cdot 10^{-2}$
J_5	$6.2 \cdot 10^{-10}$	$2.4 \cdot 10^{-2}$
J_6	$7.9 \cdot 10^{-10}$	$4.4 \cdot 10^{-2}$
J_7	$9.9 \cdot 10^{-10}$	$1.0 \cdot 10^{-1}$
J_8	$1.2 \cdot 10^{-9}$	$7.5 \cdot 10^{-2}$
J_9	$1.5 \cdot 10^{-9}$	$7.9 \cdot 10^{-2}$
J_{10}	$1.9 \cdot 10^{-9}$	$2.5 \cdot 10^{-2}$
J_{20}	$5.0 \cdot 10^{-9}$	$3.5 \cdot 10^{-1}$
J_{30}	$2.5 \cdot 10^{-9}$	$2.6 \cdot 10^{-1}$

Table 6.3: Estimation results for unnormalized Ganymede's zonal harmonic coefficients, plus degree-2 sectorial (real component).

This condition is decisive for the determination of the satellite moments of inertia. One has to consider that, being the simulated gravity field a very weak one, the relative uncertainties are actually overestimated and

could be even smaller, since the covariance matrix does not depend on the nominal values but only on the observation conditions and the geometry of the spacecraft trajectory.

Figure 6.2 shows the correlation matrix, output of the filter, for the global parameters. As expected, the elements of the principal diagonal are unitary (blue elements). There seems to exist rather high correlations ($\mu = 0.5$) between the coefficients of degree l and degree $l + 2$ of the gravity field (*e.g* degree-2 coefficients and degree-4 coefficients). This peculiarity can be explained considering the trajectory geometry: the orbit presents a rather evident symmetry about the equator, being polar and circular. This leads to high correlations between even zonals of different degrees, and the same between odd zonals. All other combinations of parameters seem to be characterized by low mutual correlations ($\mu < 0.3$).

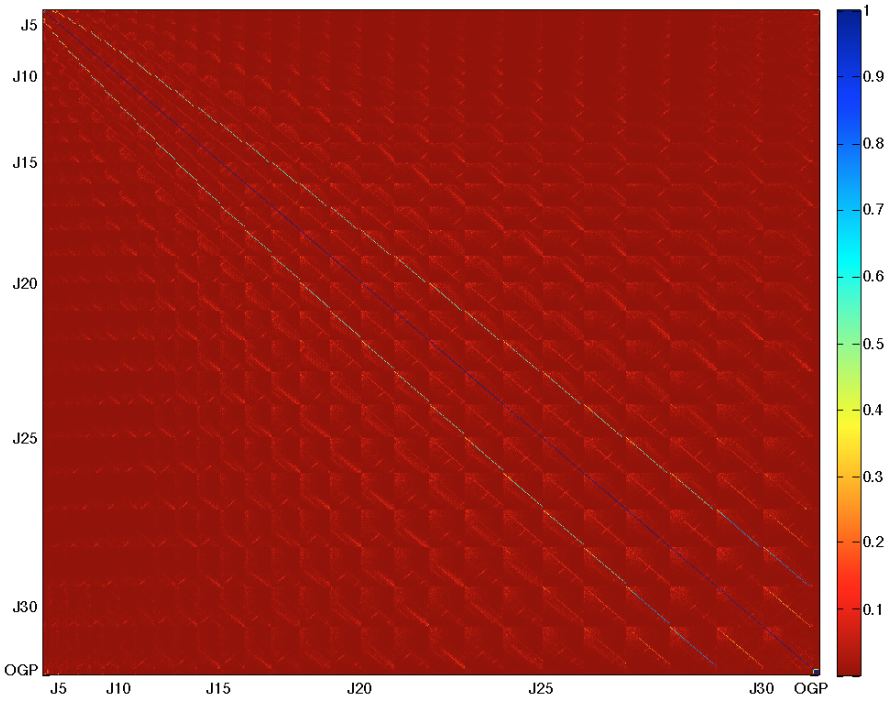

Figure 6.2: Correlation matrix for global parameters.

Gravity anomalies

The same results can be presented in terms of gravity anomalies Δg over the reference ellipsoid of Ganymede. The map includes contributions from all gravity coefficients except for the degree-2 zonal J_2 and sectorial C_{22}, which are used to define the ellipsoid itself. Figure 6.3 shows the simulated gravity anomalies of Ganymede in terms of central value (a), formal uncertainties (b) and estimation errors (c). For a very weak gravity field, maximum gravity disturbances of about $\pm$ 10 mGal are expected (a).

The uncertainty plot (b) shows how JUICE polar orbit allows a rather uniform coverage of the satellite, with uncertainties of the order of 10^{-2} mGal if defined as:

$$\sigma^2_{\Delta g} = \left(\frac{\partial \Delta g}{\Delta x}\right) P \left(\frac{\partial \Delta g}{\Delta x}\right)^T \tag{6.3}$$

where x is the vector of solve-for parameters and P is the covariance matrix. The accuracies are slightly better at the poles, due to the orbit geometry. The gravity experiment at the icy satellite will allow the reconstruction of the surface gravity with very high precision and small relative uncertainties (0.01 % - 0.10 % for the 10-mGal anomalies).

The bottom plot shows the estimation errors in the gravity anomalies of Ganymede. As evident, the errors are contained into a 3σ level which is an indicator of the OD process ability to recover the actual surface gravity of the satellite.

Geoid heights

Likewise one can show the estimation results in terms of geoid heights Δr (Figure 6.4): central values (a) and formal uncertainties (b). The latter defined as:

$$\sigma^2_{\Delta r} = \left(\frac{\partial \Delta r}{\Delta x}\right) P \left(\frac{\partial \Delta r}{\Delta x}\right)^T \tag{6.4}$$

The maximum reliefs and depressions expected for a weak gravity field are of order 40 m and characterized by very small formal uncertainties that range between 0.5 cm (poles) and 3.0 cm (low-mid latitudes). The uncertainty distribution is very similar to that of the gravity anomaly, with a global and uniform coverage of the satellite surface.

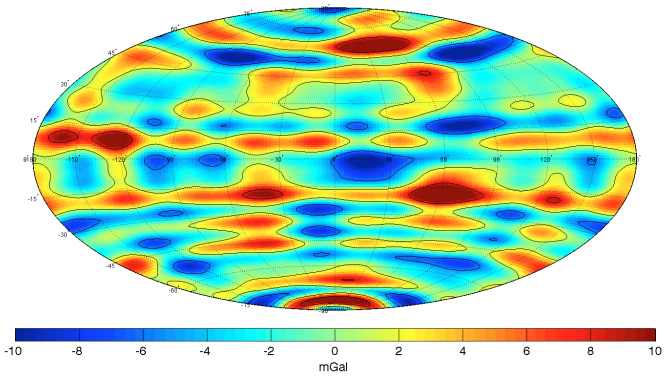

(a)

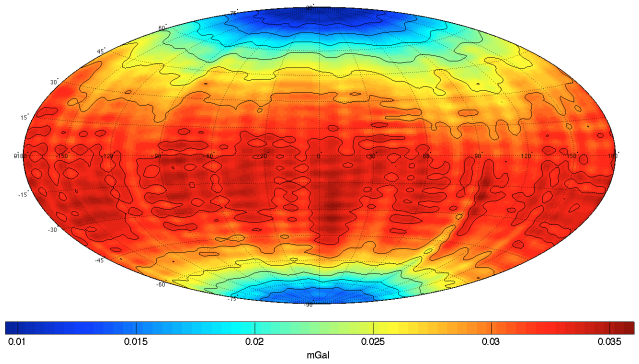

(b)

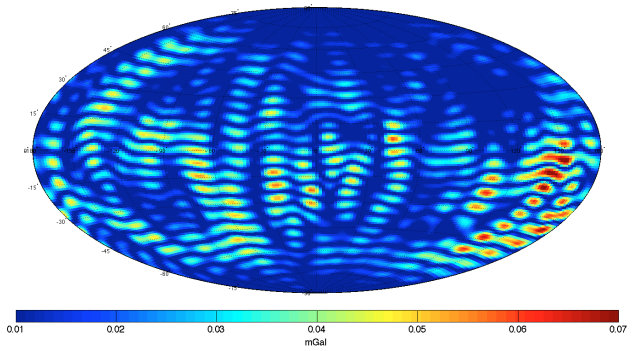

(c)

Figure 6.3: Gravity disturbances over the reference ellipsoid of Ganymede. Central values (a); formal uncertainties (b); estimation errors (c).

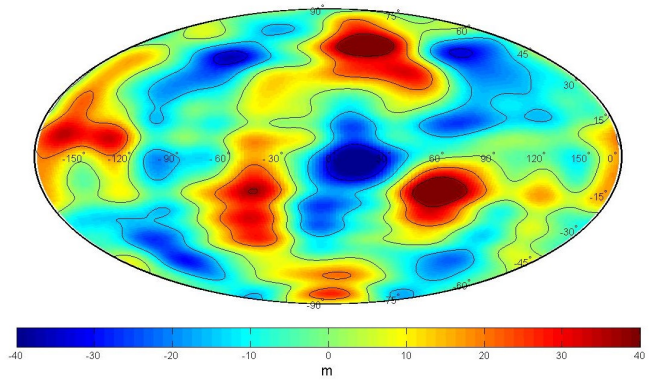

(a)

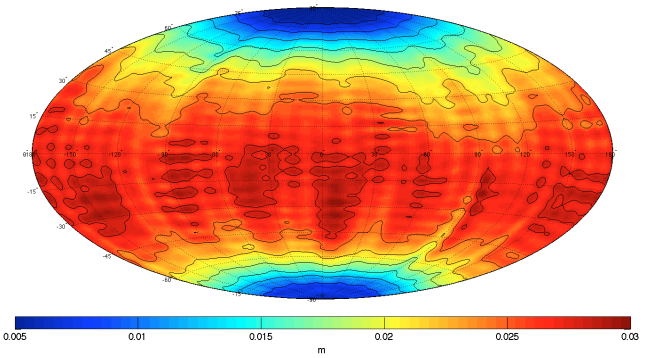

(b)

Figure 6.4: Geoid heights over the reference ellipsoid of Ganymede. Central values (a); formal uncertainties (b); estimation errors (c).

Residuals

The quality of the fit can be verified by plotting the post-fit Doppler residuals (Figure 6.5), in addition to comparing the estimation errors to the formal uncertainties.

Throughout the Ganymede 132-day orbital phase, the Doppler residuals are characterized by a mean which is very close to zero ($\approx 3 \cdot 10^{-6}$) and show no evident signatures, present in case of mis-calibrated accelerations. What appears on the plot is basically white noise, with an overall RMS of 0.4 mHz, very close to that of the AWGN used in the simulation process. To reach the convergence of the solution and un-biased Doppler residuals, a number of 3 iterations was needed.

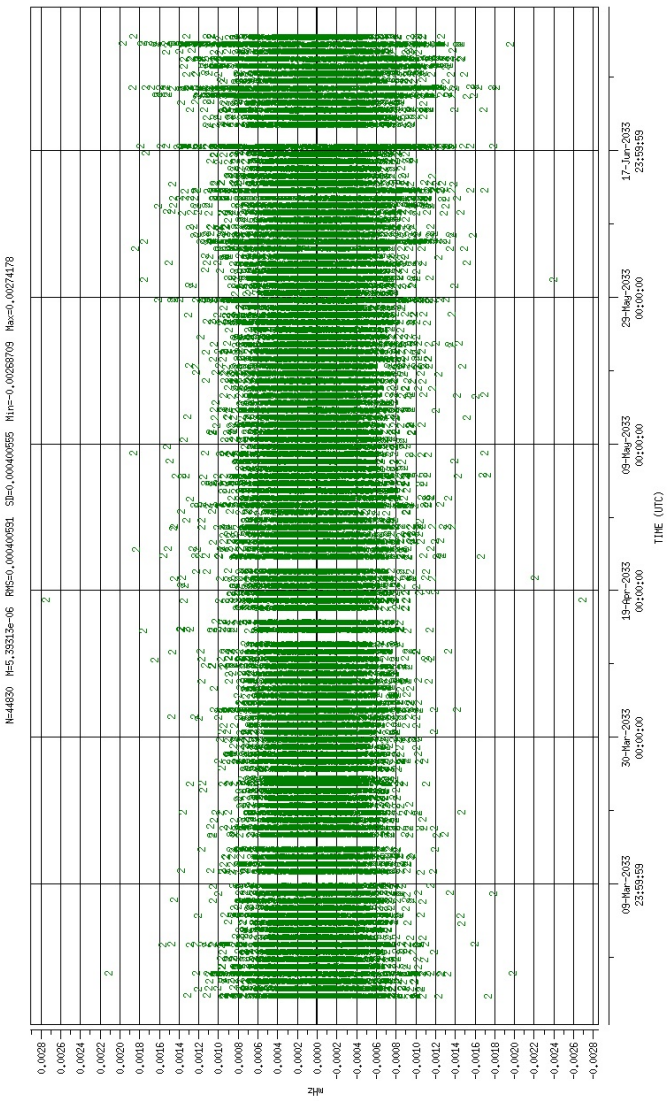

Figure 6.5: Doppler residuals of range-rate measurements at Ganymede, from February 22, 2033 to July 4, 2033.

Love number estimate

One of the major objectives of the JUICE gravity experiment is the determination of Ganymede's degree-2 Love number, both real and imaginary components. The more precise the measurement of such parameters, in terms of formal uncertainties attainable with a state-of-the-art microwave tracking system, the more reliable the detection of existing liquid water oceans underneath the satellite's icy crust. Given the relevance of the

estimate of these coefficients, a subsection is dedicated to the convergence of the parameter estimation process and the assessment of the accuracies output of the data filtering.

Table 6.4 summarizes the convergence steps of the least mean square solution, after 4 iterations of the process. In order to test the capability of the filter of recovering the simulated values, the initial values for both components of k_2 were set to null, although the simulated real component was chosen so as to be Earth-like ($k_{2_{sim}}^{\Re} = 0.3$, see Section 4.2.1).

Iter	$\mid k_2^{\Re}(e) - k_2^{\Re}(s) \mid$	$\sigma k_2^{\Re}$	$\mid k_2^{\Im}(e) - k_2^{\Im}(s) \mid$	$\sigma k_2^{\Im}$
0	$4.97 \cdot 10^{-3}$		$1.95 \cdot 10^{-2}$	
1	$9.12 \cdot 10^{-4}$		$9.87 \cdot 10^{-4}$	
2	$8.71 \cdot 10^{-5}$	$1.27 \cdot 10^{-4}$	$5.25 \cdot 10^{-5}$	$1.13 \cdot 10^{-4}$
3	$1.03 \cdot 10^{-5}$		$1.55 \cdot 10^{-5}$	
4	$2.67 \cdot 10^{-5}$		$1.70 \cdot 10^{-5}$	

Table 6.4: Convergence of Ganymede's tidal Love number, real and imaginary components, to the simulated value, after 4 iterations.

The table shows how the estimation errors (2^{nd} and 4^{th} columns) tend to approach values that are contained in the error bars (3^{rd} and 5^{th}), which suggests that the estimated parameters have converged to the simulated ones.

In Figure 6.6 the same results are graphically displayed. As the number of iterations increases, the estimation lines (blue dots) ease down on the simulated value (green lines) in such a way that their differences do not exceed the error bars (red lines).

Convergence criteria are evidently satisfied and it has been pointed out how the filter is capable of recovering the simulated tidal Love number, which controls the time-variable part of the gravity field. As a matter of fact, convergence has been reached after only 3 iterations, the latter functioning as a further test of the solution stability.

As a result of this analysis, not only has it been demonstrated that the real and imaginary components of k_2 are detectable by the 3GM experiment onboard JUICE, but also the uncertainties with which the estimate will be possible have been determined: about 2 parts in 10^4 for both components,

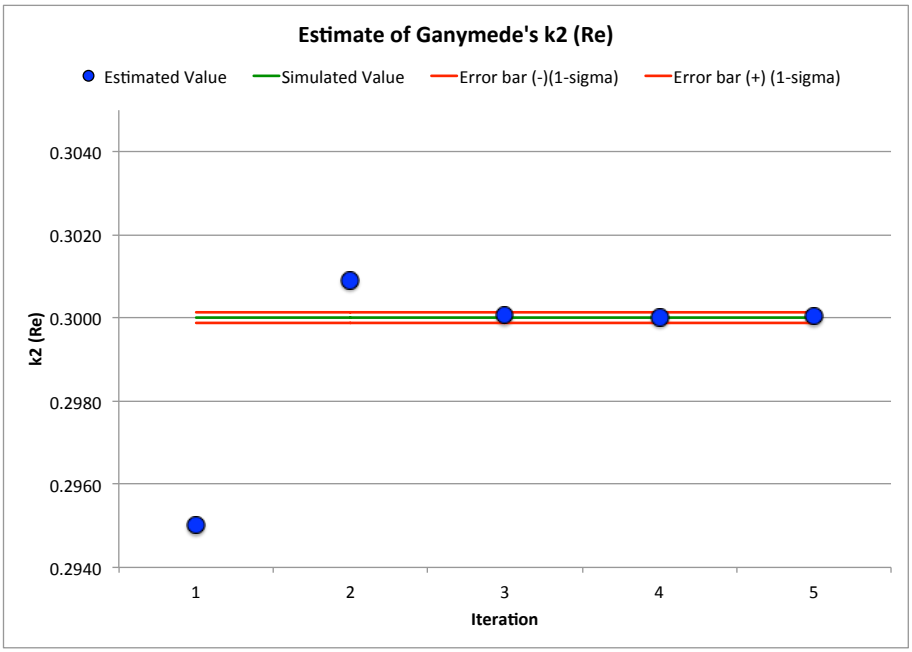

(a)

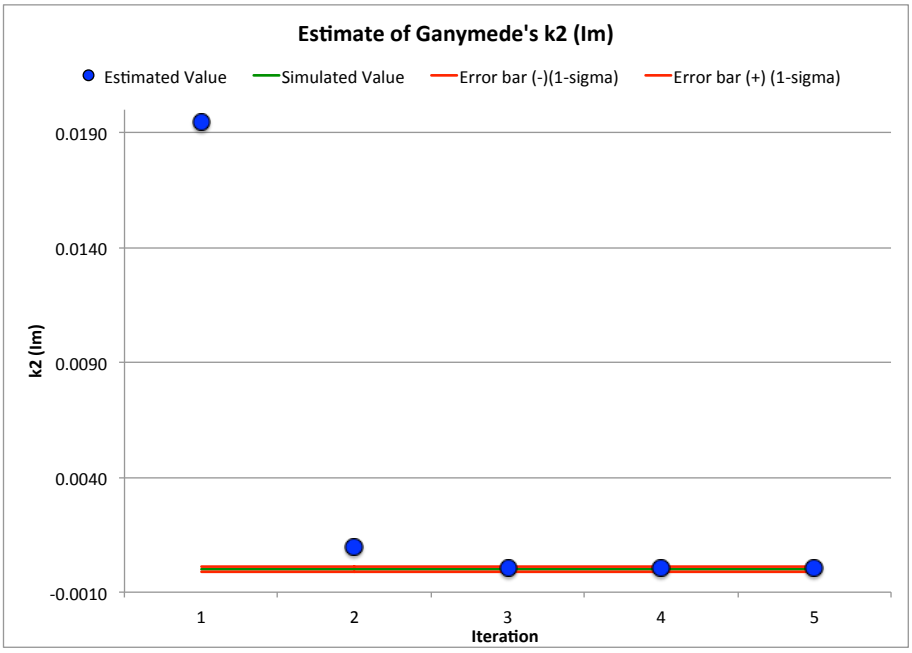

(b)

Figure 6.6: Convergence of the estimation process of Ganymede's tidal Love number, real and imaginary components, to the simulated value, after 4 iterations. (a) $k_2^{\Re}$; (b) $k_2^{\Im}$.

on a parameter whose order of magnitude is 10^0 and bears crucial information on Ganymede's interior. Here follows another evidence to support the visibility of the tidal coefficients. If, indeed, an Earth-like $k_2^{\Re}$ for Ganymede can be assumed in the frame of the simulations, then the maximum expected dynamical variations of Ganymede's un-normalized degree-2 zonal harmonic, during JUICE orbital phase, are (see Section 2.2.3):

$$\mid \Delta J_2 \mid = 2 \cdot \frac{1}{2} k_2^{\Re} \left(\frac{\mu_J}{\mu_G} \right) \left(\frac{R_G}{a} \right)^3 3e \sim 2 \cdot 10^{-7} \tag{6.5}$$

which can be compared to the formal uncertainty on the estimation of the static coefficient, which yields:

$$\mid \Delta J_2 \mid \sim 2 \cdot 10^{-7} \gg \sigma_{J_2} \sim 3 \cdot 10^{-10} \tag{6.6}$$

result that clearly supports the prospect of observing tidal variations in the gravity field of Ganymede with the JUICE mission. If the actual Love number proved to be larger, then the situation would be even more favorable, while a much smaller value of $k_2^{\Re}$ is not expected for other observational motivations (Kivelson *et al.*, 2002). These excellent results are made possible by the optimal geometry of Ganymede orbits (circular and polar) and by the extended duration of the orbital phase: more than 4 months, during which Ganymede will complete about 18 complete revolutions, and thus double the tidal cycles, around Jupiter.

GM estimate

The monopole term of the gravity field of Ganymede determines the bulk of the gravitational accelerations which the JUICE spacecraft will be subject to during the orbital phase. The current best estimate of Ganymede's gravitational parameter GM is heritage to the Galileo mission (Jacobson, 2002), and is characterized by an accuracy of 0.03 km^3/s^2. However, JUICE will have the opportunity of estimating and updating both the value and the uncertainty on this parameter.

Figure 6.7 shows the multiarc estimation results for the satellite's GM. The gravity experiment at Ganymede will provide an improvement in the knowledge of the moon's monopole term by a factor of about 600 with respect to the Galileo measurement, with an absolute post-fit formal uncertianty of $4.9 \cdot 10^{-5} km^3/s^2$. Also, the estimation error after 4 iterations (red

bar) is smaller than the formal uncertainty (blue bar), pointing to a certain stability of the solution.

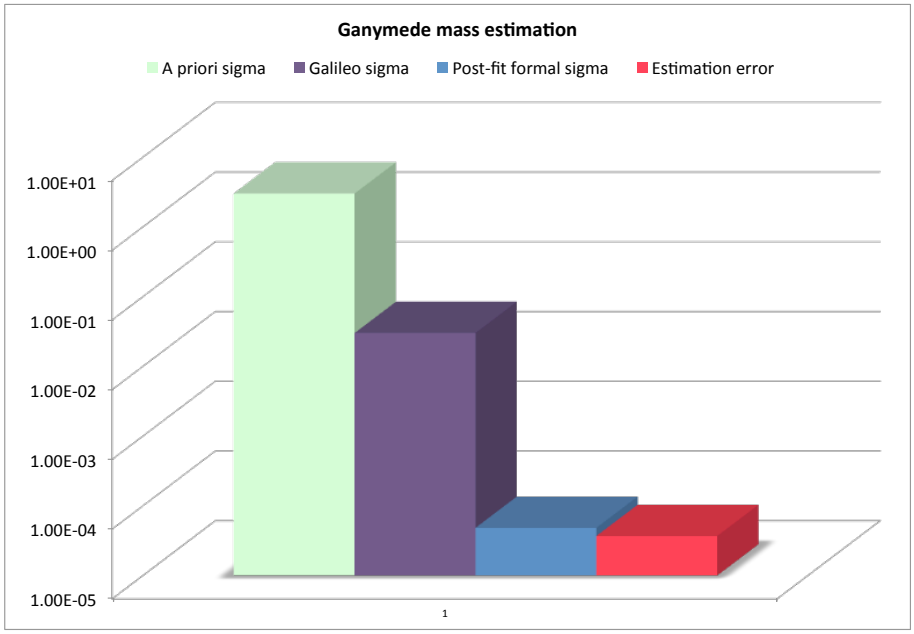

Figure 6.7: Ganymede's GM estimate: output of the multi-arc filter.

Precise spacecraft positioning

In the previous sections it has been shown how the gravity field of Ganymede can be determined with very high accuracies. This updated knowledge can be exploited for the precise reconstruction of JUICE trajectory by using the output of the multiarc filter. The relevance of this procedure lies in its applications in the field of laser altimetry, the reconstruction of the satellite's topography and in general for precise geo-referencing of optical images.

After the multiarc step a further single arc estimation is performed. In this last stage of the data filtering, the 30×30 gravity field coefficients and Ganymede's mass are treated as consider parameters, whose *a priori* uncertainties are taken into account in the determination of the single-arc covariance matrix, but are not estimated. Only, this time, the *a priori* uncertainties on the considers are not large but set to the post-fit uncertainties output of the multiarc filter.

The components of JUICE position and velocity vectors are estimated again with large *a priori* uncertainties. However, given the improved knowl-

edge of the gravity field of the satellite, the position of the spacecraft can be determined with higher accuracies through this step.

Figure 6.8 shows the results of this process in terms of uncertainties in the determination of JUICE position components in the 3 fundamental directions (radial, across-track and along-track), with respect to Ganymede's barycenter and as a function of time. The whole duration of the orbital phase (132 days) has been considered.

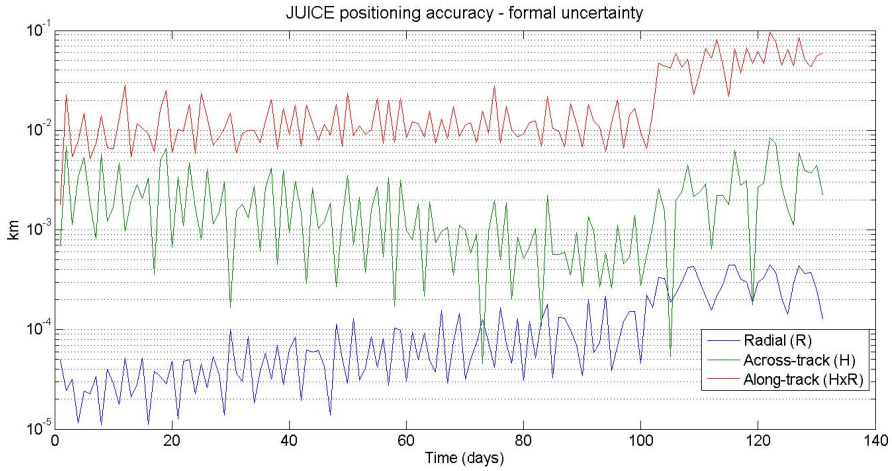

Figure 6.8: Accuracies in the determination of the spacecraft position. Radial component (blue line); across-track component (red line); along-track component.

The radial position of the spacecraft, referenced to Ganymede's barycenter, is characterized by increasing uncertainties between 1 cm (beginning of the orbital phase) and 10 cm (end). This worsening in the accuracies is due to changes in the angle between the normal to JUICE orbital plane and the line of sight, which, at the end of the 132 arcs, is dangerously close to 0°, affecting the effectiveness of Doppler measurements. However, the results meet the scientific goal of radial orbital referencing to better than 1 m. The component along the spacecraft angular momentum (H, red line) presents higher uncertainties (as expected), of order a few meters. The accuracies attained in the determination of this component are favorable to a good detection of Ganymede's librations. As for the along-track component (green line), which is usually the worst determined in spaceflight dynamics, the uncertainties oscillate around 10 m.

These results can be obtained if tracking from ground is available. The elements of the state covariance matrix for the spacecraft increase considerably when radiometric measurements are not accessible. A possible operational configuration is to operate the Medium Gain Antenna simultaneously with the laser altimeter, which would guarantee the Doppler tracking of the spacecraft.

6.4 Callisto

The JUICE mission will provide the opportunity of extensively observe and explore Callisto as well. With 20 flybys of the moon, the Callisto high latitude phase is the second most extended, and the second in order of scientific objectives.

The gravity field determination requirements for this phase are: the estimation of Callisto's full degree-3 gravity field and the determination of the real component of its degree-2 Love number k_2. The encounters with this satellite will be used mostly to increase the spacecraft inclination with respect to Jupiter's equatorial plane and to provide the necessary gravity assist. That being so, the flybys do not present an optimal and ideal distribution in terms of Callisto orbital mean anomaly and ground tracks on the surface of the satellite. Nevertheless, the mission will achieve major results in the study of the icy moon.

Simulations of the observation campaign are carried out within $\pm$ 12 h from each closest approach, which guarantees at least 3 h and up to 9.5 h of spacecraft tracking centered at C/A. Table 6.5 contains crucial information about the closest approaches of the spacecraft with the satellite.

Within the observation pass, Doppler data are sampled at 60 seconds, while the total number of range points is 50 per tracking pass. White Gaussian noise has been added to both Doppler (RMS = 0.30-0.45 mHz) and ranging (RMS = 1RU) measurements. Occultations by Jupiter and other Galilean satellites are taken into account as well as data removal due to small station elevation angles (minimum elevation is set to 20°).

It is worth underlining that the flyby tracking schedule is relative to potential tracking periods, in terms of visibility from ground stations, not considering the real availability of the flybys to gravity investigations. To

Flyby	Epoch (UTC)	H (km)	M (deg)	Track-sched (h)
C6	2030/11/16	1107	327.8	4.5(25)
C7	2031/01/16	1725	202.9	4.0(25) + 8.5(34)
C8	2031/02/02	743	203.4	3.5(55)
C11	2031/03/12	837	300.7	4.0(55) + 4.0(25)
C13	2031/04/14	200	299.1	4.0(25) + 9.5(34)
C14	2031/05/01	200	297.6	4.0(55) + 4.0(25)
C15	2031/05/17	367	298.1	4.0(55)
C16	2031/06/03	713	298.3	10.0(34)
C17	2031/06/20	200	298.3	4.0(25) + 9.0(34)
C18	2031/07/07	200	297.4	4.0(55)
C19	2031/07/15	200	117.6	4.0(25) + 9.0(34)
C20	2031/07/31	200	116.4	4.0(55)
C21	2031/08/17	1305	115.7	9.0(34)
C22	2031/09/03	200	116.8	9.5(34)
C23	2031/09/19	200	115.6	4.0(25)
C24	2031/10/06	589	115.6	4.0(55)
C26	2031/11/22	382	48.8	2.5(55)
C27	2031/12/17	1704	224.7	2.5(55)
C28	2032/01/16	528	142.2	9.0(34)
C29	2032/02/01	4936	142.4	4.0(25)

Table 6.5: Relevant information on Callisto flybys. The flyby nomenclature is consistent with the one set by ESA.

address this issue, the result section will be divided into two scenarios: a gravity experiment using both the HGA and the MGA; and a gravity experiment using the HGA only.

6.4.1 Estimation setup

Similarly to what has been done for the main phase, the only differences between the simulated and estimated dynamical models concern the gravity field of Callisto. Although a full degree-3 gravity field has been used for producing the simulated trajectory, for the estimation process all spherical harmonic coefficients have been set to null, except for J_2 and C_{22},

for which I used the values in Table 4.2 (Bagenal, 2004).

Parameter	Initial value
GM	7179.29 km^3/s^2
J_2	3.27 $\times 10^{-5}$
C_{22}	1.02 $\times 10^{-5}$
$k_2^{\Re}$	0.0

Table 6.6: Initial values for the mass and quadrupole gravity field of Callisto. All other gravity coefficients whose initial conditions are not shown are initialized to null.

The real component of the Love number was initialized to zero as well, although the simulated value is Earth-like. The initial conditions for the state vector components are set to the nominal values, for all 20 flybys.

The components of the solve-for vector are:

- Locals:
  - the JUICE spacecraft position and velocity at every initial epoch for each flyby (total of 20×6) with *a priori* uncertainties of 1 km on the position components and 5 mm/s on the velocity components.
- Globals:
  - Callisto's GM (1 parameter) with *a priori* uncertainty of 1.00 km^3/s^2 (uncertainty from Galileo multiplied by a factor 100).
  - Callisto's spherical harmonic coefficients up to degree and order 3 (12 parameters).
  - Callisto's Love number k_2, real component (1 parameter), *a priori* uncertainties of $\sigma_{k_2}^{AP} = 1.0$.
  - Callisto position and velocity with respect to Saturn barycenter (6 parameter) with uncertainties of 1 km on the position components and 5 mm/s on the velocity components.

The *a priori* uncertainties on the gravity field coefficients have been chosen in the following way: multiplying by a factor 10^3 the formal uncertainties on the quadrupole coefficients reported in Table 4.2 (Bagenal, 2004);

adjusting the pre-fit uncertainties for the degree-3 gravity field by scaling the degree-2 terms using the normalization factors.

6.4.2 Estimation results

In a space mission, the transmission of science data is performed, nominally, with the spacecraft HGA, whose pointing tolerance is less than 0.1°. The tight requirements on the spacecraft attitude during radio science measurements make simultaneous observation campaign by other instruments not realistic. Therefore it is unreasonable to think that all 20 flybys of Callisto will be allocated for gravity science. In this section I explore two possible different scenarios: one in which the spacecraft is endowed with a Medium Gain Antenna, whose pointing requirements are much more loose and thus can transmit radio signals while other instruments are operative; the other where the radio science experiment relies only on JUICE HGA.

In the former case, the lower antenna gain will cause an increase in thermal noise. However, since this contribution is very small if compared to predominant contributions by propagation noise, the overall SNR is not quite affected. As a result, the RMS of the Additive White Gaussian noise is still determined by tropospheric and ionospheric delays, and the same simulation setup can be used for both cases.

Scenario 1: Gravity Science with HGA + MGA

In this frame the radio link is still established with the HGA when a flyby of Callisto is allocated to gravity measurements. In addition, when other instruments are the leading experiment, radio science can still be performed by means of the MGA. As a result, I performed numerical simulations of the gravity experiment at Callisto by collecting radio science measurements during all 20 flybys and processing all data in a multiarc filter, whose output is a global solution for the gravity field of the satellite.

Estimate of gravity spherical harmonics

Figure 6.9 shows the estimation results in terms of unnormalized spherical harmonic coefficients, representing Callisto's full degree-3 gravity field. As usual I compared the current knowledge of the gravity coefficients as

measured by the Galileo mission whit the prospective improvement attainable with JUICE, and the post-fit formal uncertainties with the estimation errors.

The plots underline an increase in the accuracies with respect to the Galileo measurements: for J_2 by a factor of about 30, with an absolute and relative uncertainty of $2.5{\cdot}10^{-8}$ and 0.08%, respectively; for C_{22} by a factor of about 65, with an absolute and relative uncertainty of about $5{\cdot}10^{-9}$ and 0.05%, respectively; for J_3 there's no comparison with Galileo but the absolute pot-fit uncertainty is about $2.3{\cdot}10^{-8}$, which is about a thousand times better of what has been done by Cassini with Enceladus (Iess *et al.*, 2014). However, one has to consider that, differently from what has been done for the Galileo data analysis, in the simulations of JUICE Callisto flybys the hypothesis of hydrostatic equilibrium has not been used to constrain the estimation of the quadrupole gravity field, making future observations even more crucial.

Once again, the estimation errors, coming from the comparison between estimated and simulated coefficients, are all contained within a 3σ level (fuchsia bars in Figure 6.9).

The correlation matrix (Figure 6.10) shows high correlations between the components of Callisto state vector with respect to Saturn barycenter and between some degree-2 and degree-3 coefficients (*e.g.* S_{22} and S_{33}). Otherwise the elements of the matrix are all below 0.5.

Gravity anomalies

Using the output of the multiarc filter it is possible to display the uncertainties on Callisto gravity anomalies over the satellite map. Figure 6.11 shows such accuracies in the estimation of the disturbances over the reference ellipsoid as a function of Callisto latitude and longitude.

The uncertainties (b) range between 10^{-3} and 10^{-2} mGal and are smaller in correspondence to JUICE ground tracks during the Callisto science phase (black curves). Wherever the spacecraft flies above, the accuracies are better, especially in presence of cross-overs and multiple passes. In general one can conclude that the gravity anomaly map of Callisto will be better determined in the southern hemisphere and near 0° (facing Jupiter) and

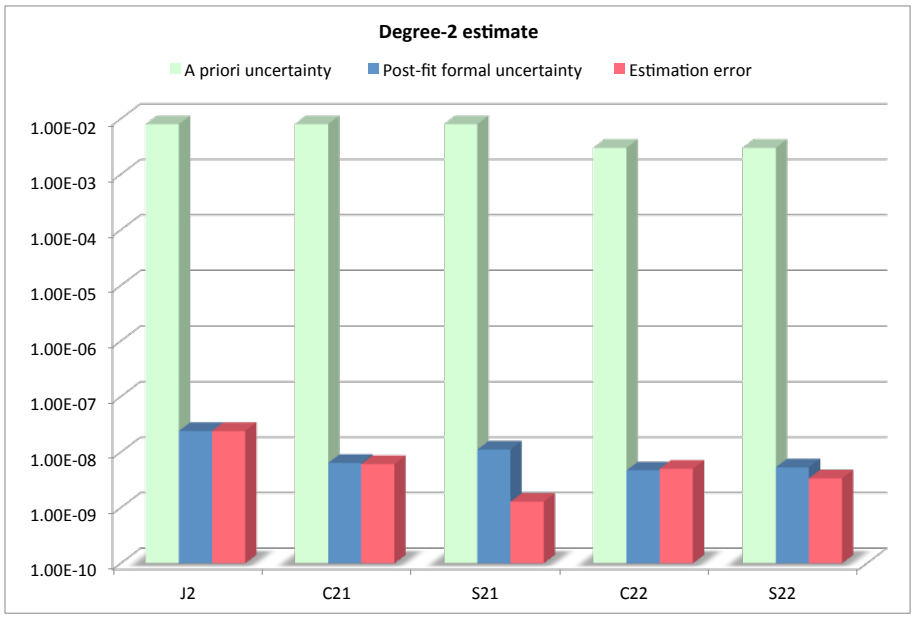

(a)

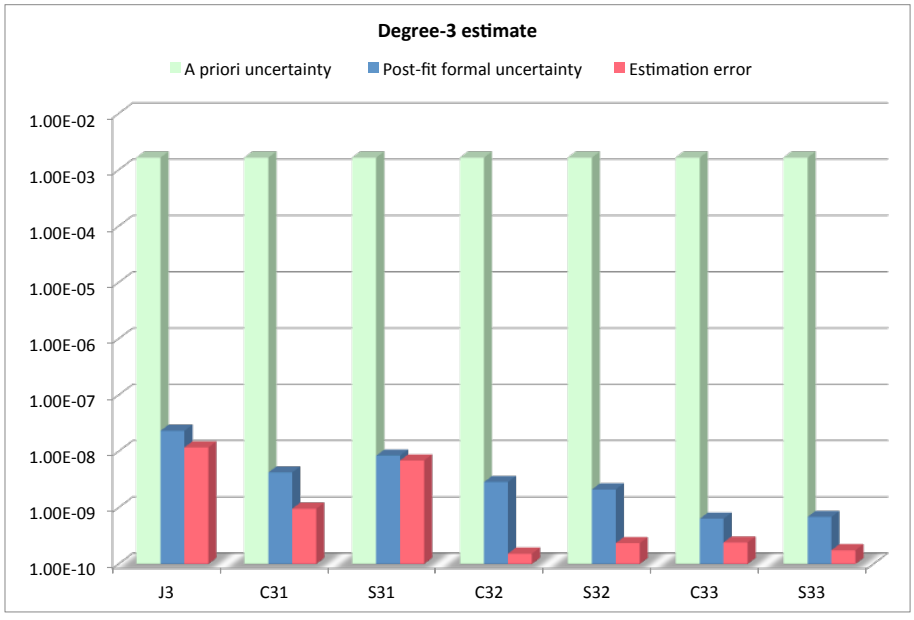

(b)

Figure 6.9: Estimation results for the gravity field of Callisto. (a) unnormalized degree-2; (b) unnormalized degree-3.

$180°$ longitude.

By comparison, the multiarc estimation errors (b) are everywhere smaller than 3σ, ranging between 1-7 $\cdot 10^{-3}$ mGal.

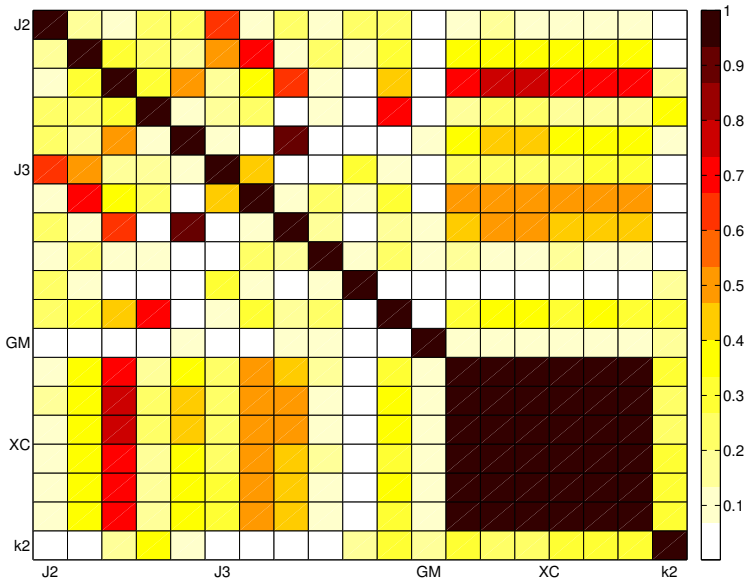

Figure 6.10: Callisto science phase: numerical simulations. Correlation matrix for the global parameters.

Geoid heights

The results in terms of geoid heights over the reference ellipsoid of Callisto are analogous: the uncertainties are very small (about 0.01 m) in the region overflown by the spacecraft during the gravity flybys, and worsen (up to 0.10 m) as the relative distance grows.

Residuals

The post-fit Doppler residuals for the multiarc analysis of Callisto flybys are shown in Figure 6.13. The distribution, after 4 iterations, is zero-mean and shows no evident signatures. The residual RMS, about 0.34 mHz, is compatible with the one superposed in the simulations. The color map refers to different tracking complexes: Goldstone (green dots), New Norcia (purple dots) and Cebreros (blue dots), the time scale is spread over more than one year with tracking passes of variable duration.

Love number estimate

Despite a non-ideal distribution of JUICE Callisto flybys along the satel-

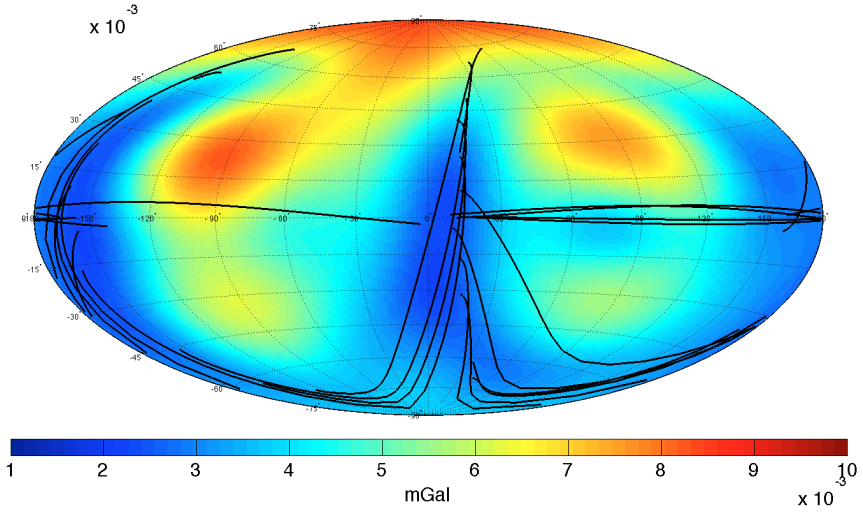

(a)

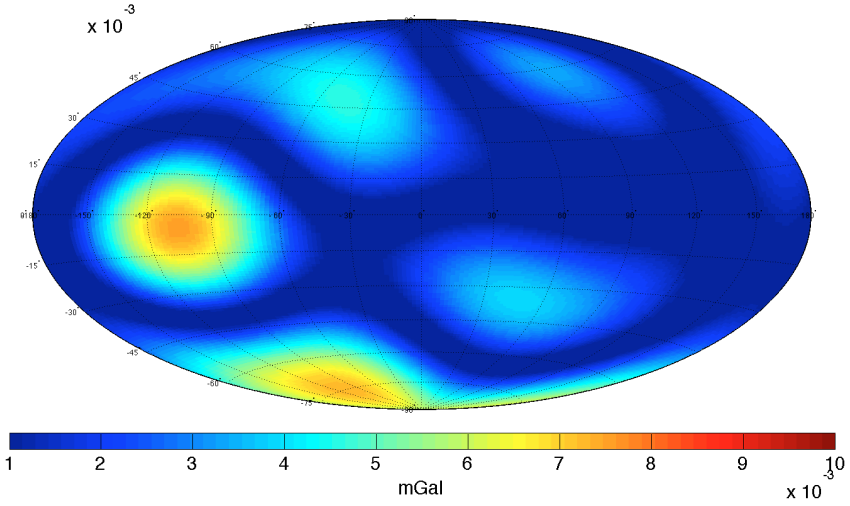

(b)

Figure 6.11: Gravity disturbances over the reference ellipsoid of Callisto. Formal uncertainties (a), the black lines represent JUICE ground tracks over the satellite surface; estimation errors (b).

lite orbit around Jupiter, the determination of the real component of its degree-2 Love number is still possible with a rather good accuracy.

Unfortunately, the spacecraft will encounter the satellite many time at intervals of 16 days, or at integer multiples. This time lapse corresponds roughly to Callisto mean orbital period, which governs the tidal distortions of the satellite, causing overlapping of many flybys in terms of mean

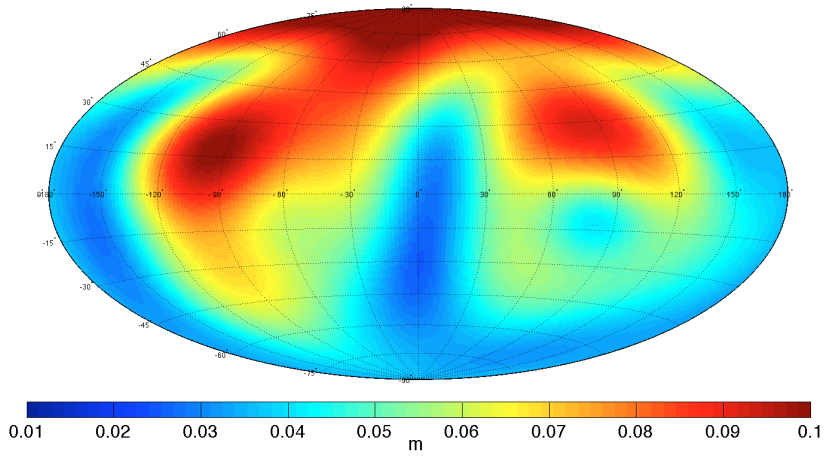

Figure 6.12: Geoid heights over the reference ellipsoid of Callisto, in terms of formal uncertainties.

anomaly, as it is shown in Figure 6.14. Intuitively, the more different mean anomalies are sampled by the gravity experiment, the better the accuracy in the estimation of the tidal k_2.

Two main agglomerations composed of about 6 encounters characterized by the same mean anomaly (of which at least 4 at 200 km altitude) can be spotted in the plot, around 120° and 300° from periapsis, respectively. In addition to the poor sample diversification, 13 out of 20 flybys occur at mean anomalies that are very close to quadrature, where tidal distortions are null. Indeed, 7 other flybys will occur at 5 different mean anomalies but almost every remaining encounter will be characterized by high altitudes on the satellite surface.

Figure 6.15 shows the estimation results in the determination of Callisto's Love number. Starting from $k_2^I = 0.0$, the ability of the filter to recover the simulated value $k_2^S = 0.3$ has been tested, performing 4 iterations. Despite all the limitations that have been pointed out, JUICE gravity experiment at Callisto will still be able to determine the tidal number with an accuracy of $\sigma_{k_2} = 2.7 \cdot 10^{-2}$, value that determines the error bars in the plot (red lines). As evident, after 3 or 4 iterations, the estimation errors are contained within 1σ.

GM estimate

Callisto science phase gives also the opportunity of updating the knowl-

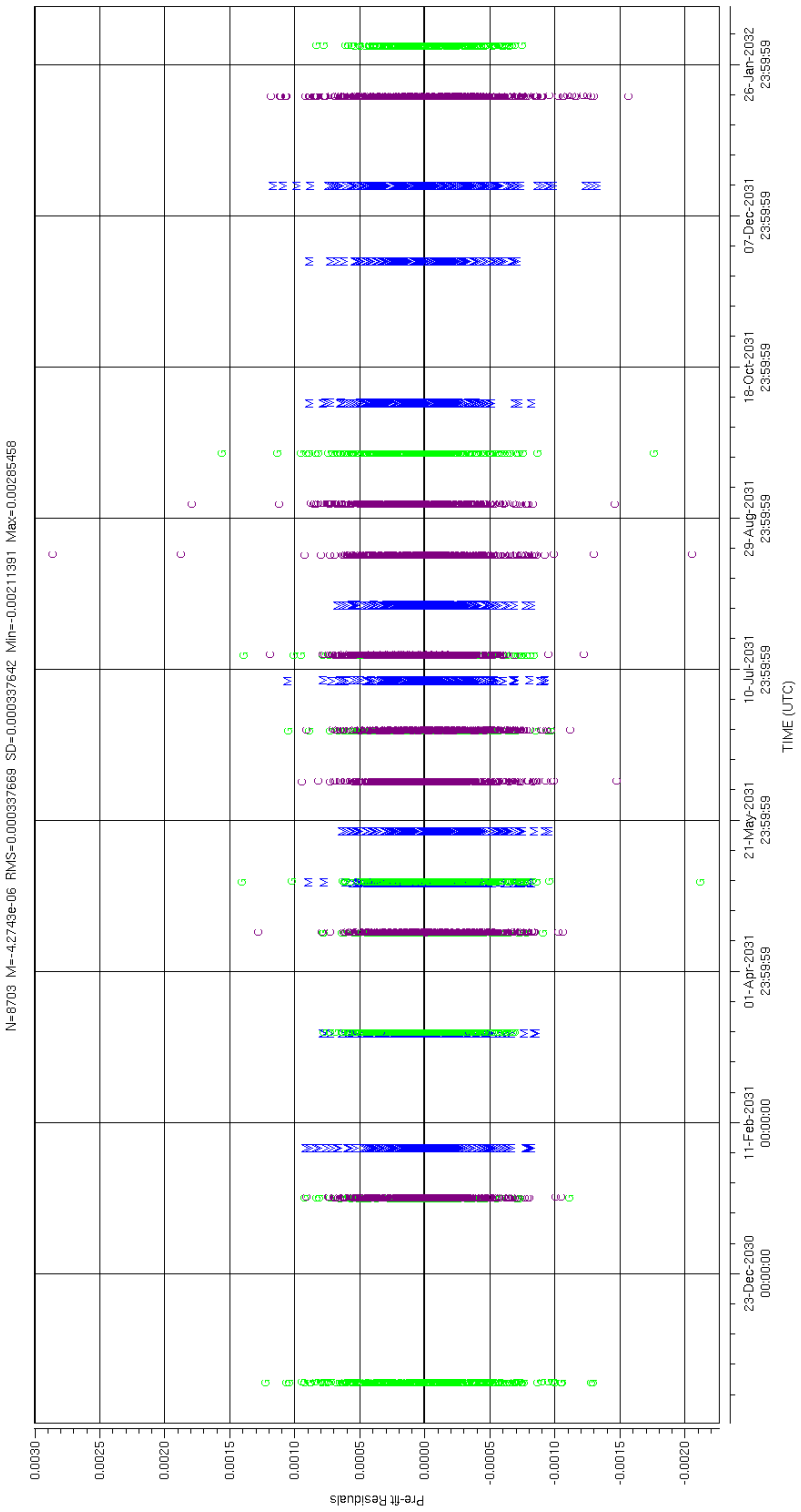

Figure 6.13: Doppler residuals of range-rate measurements at Callisto, for all 20 flybys. Spacecraft tracking from: Goldstone (green dots); New Norcia (purple dots); Cebreros (blue dots).

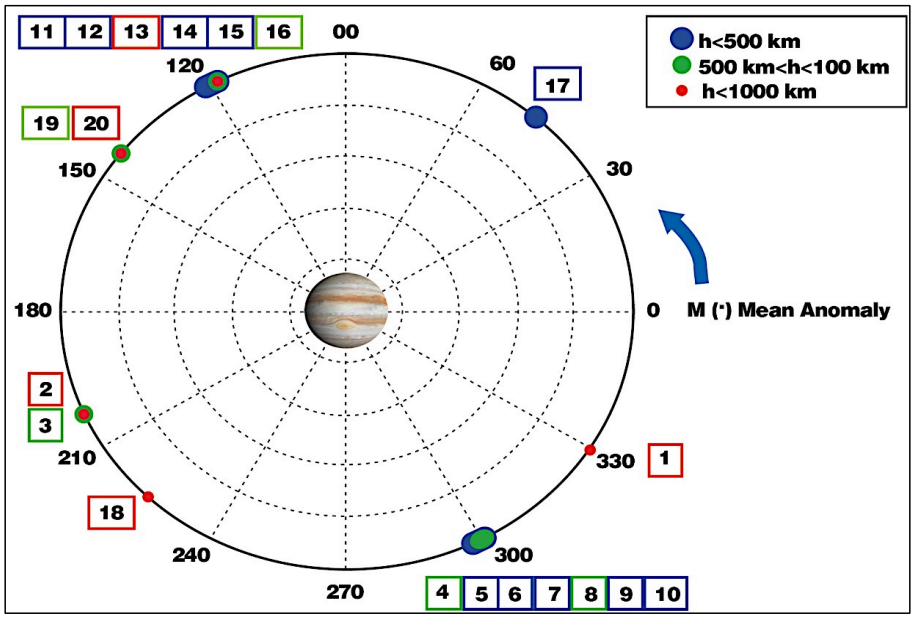

Figure 6.14: Distribution of Callisto flybys in terms of satellite mean anomaly (M).

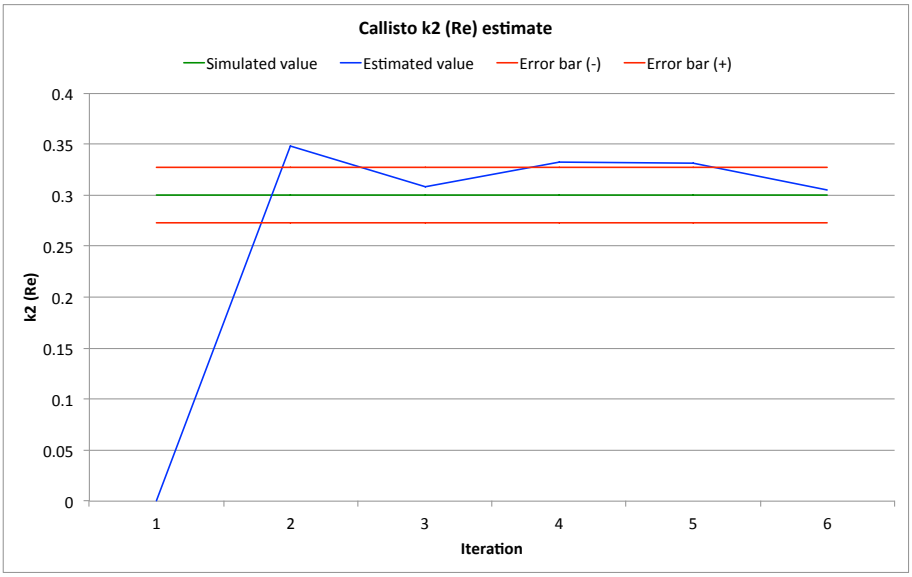

Figure 6.15: Convergence of the estimation process of Callisto's tidal Love number, real component, to the simulated value, after 4 iterations.

edge of the satellite mass, in terms of central value and formal uncertainty. The results of the simulations are shown in Figure 6.16.

The graph clearly shows that, by means of 20 flybys of Callisto, it is possible to improve the accuracy in the estimate of Callisto mass, with re-

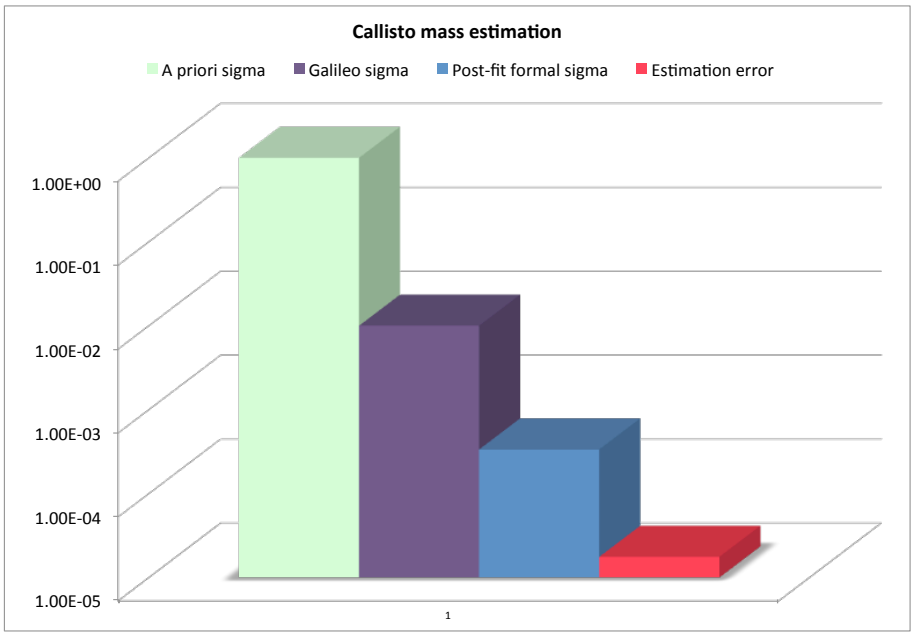

Figure 6.16: Callisto's GM estimate: output of the multiarc filter.

spect to the Galileo measurements, by 2 orders of magnitude, from $1.00 \cdot 10^{-2} km^3/s^2$ (1σ) to $3.35 \cdot 10^{-4} km^3/s^2$ (1σ).

Scenario 2: Gravity science with HGA only

In this case only a limited number of flybys will be devoted to gravity investigations, due to the unfeasibility of carrying out gravity measurements simultaneously with other instruments. With these premises, a parametric study had to be performed, where different aspects of the experiment were discussed in terms of descoping and potential losses due to the reduced amount of collected data.

In particular, in the frame of this work, I chose the determination of Callisto's tidal Love number as the discriminating parameter, since this physical constant is crucial for detecting hidden subsurface ocean on the satellite. I've been searching for the best combination of encounters in terms of attainable accuracy in k_2 estimates, as the number of allocated gravity flybys changes. The parameters that influence the choice of the best combination are of varying nature: Callisto mean anomaly at the time of the flyby; the SEP angle at the time of the flyby; the altitude of the flyby and so on.

Within this scenario two sub-cases are discussed: one where a baseline Ka-Ka link is considered for the radio tracking of the spacecraft; the other where a (at least partial) multi-frequency configuration is adopted, making Doppler link performance virtually independent of the solar elongation angle, or Sun-Earth-probe angle (SEP). Obviously different circumstances yield different results in the search for the best combination and the minimum requirement on the number of flybys.

Search for the best combination

The study has been carried out by producing and analyzing every possible combination of Callisto flybys, for a total of $\binom{20}{n}$ sequences, where n is the number of encounters allocated to gravity science. However only the results relative to feasible values of n are presented in this work: I will neglect the outcome of the analysis when less than 4 flybys are devoted to radio science; on the same note, it is not realistic to think that more than 7 flybys out of a total of 20 could be reserved for gravity investigations. Results for $4 \leq n \leq 7$ and for different link configurations, follow.

- Number of gravity flybys: 4

  Best combination:

  C8, C13, C26, C27

  Best $\sigma_{k_2} = 9.5 \cdot 10^{-2}$

  Link: Ka-Ka

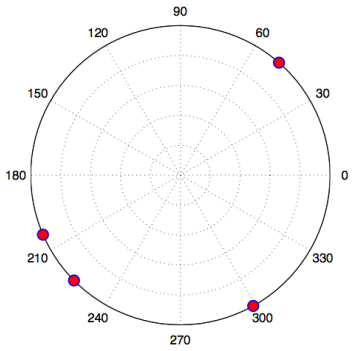

- Number of gravity flybys: 5

  Best combination:

  C8, C16, C26, C27, C28

  Best $\sigma_{k_2} = 6.2 \cdot 10^{-2}$

  Link: Ka-Ka

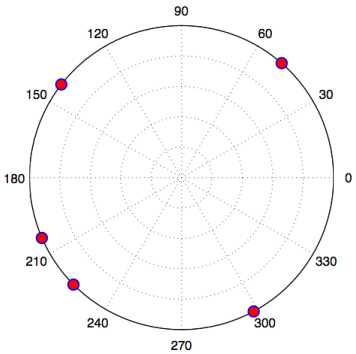

- Number of gravity flybys: 6

  Best combination:

  C8, C16, C19, C26, C27, C28

  Best $\sigma_{k_2} = 5.3 \cdot 10^{-2}$

  Link: Ka-Ka

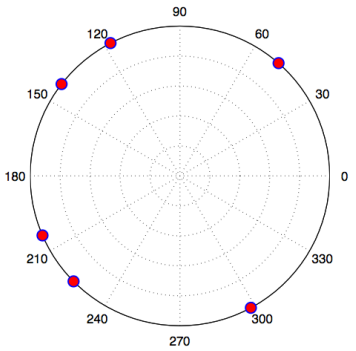

- Number of gravity flybys: 7

  Best combination:

  C8, C13, C16, C19, C26, C27, C28

  Best $\sigma_{k_2} = 4.2 \cdot 10^{-2}$

  Link: Ka-Ka

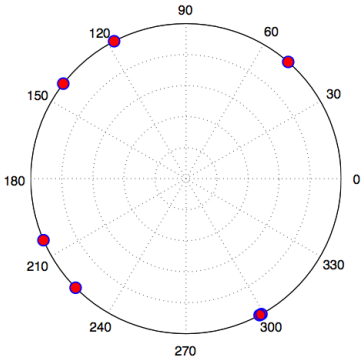

- Number of gravity flybys: 4

  Best combination:

  C8, C26, C27, C28

  Best $\sigma_{k_2} = 7.6 \cdot 10^{-2}$

  Link: Ka-Ka + X/X

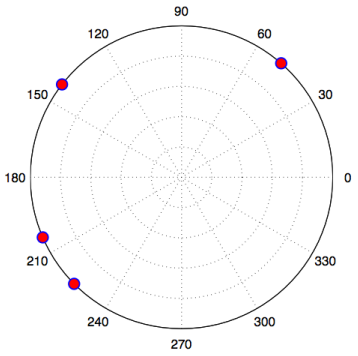

- Number of gravity flybys: 5

  Best combination:

  C8, C16, C26, C27, C28

  Best $\sigma_{k_2} = 5.0 \cdot 10^{-2}$

  Link: Ka-Ka + X/X

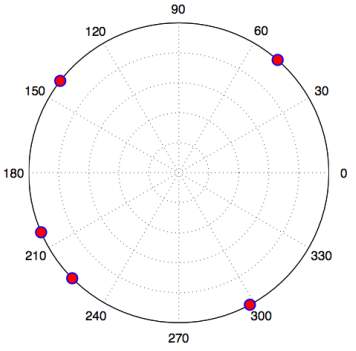

- Number of gravity flybys: 6

  Best combination:

  C8, C13, C16, C26, C27, C28

  Best $\sigma_{k_2} = 4.4 \cdot 10^{-2}$

  Link: Ka-Ka + X/X

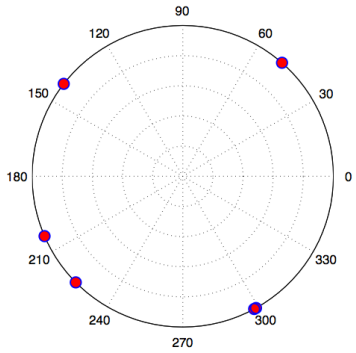

- Number of gravity flybys: 7

  Best combination:

  C8, C13, C16, C19, C26, C27, C28

  Best $\sigma_{k_2} = 3.3 \cdot 10^{-2}$

  Link: Ka-Ka + X/X

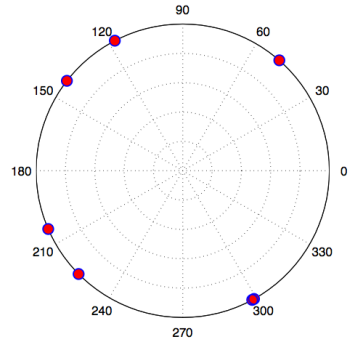

As expected, the results for the case exploiting only a Ka-Ka link and the case with both Ka-Ka and X-X links are different, since in the latter situation the SEP at the times of the flybys does not play a significant role, changing the selection criteria.

In the Ka-Ka case, if 7 flybys are selected for gravity, the uncertainty on the determination of the tidal Love number is still 50% worse than what could be achieved by using an MGA to collect data during all 20 flybys. On the other hans, in the Ka-Ka+X-X case, 7 gravity flybys correspond to a formal uncertainty on k_2 only 20% worse than before.

In general, one can appoint a minimum requirement on the estimation of Callisto's tidal number, for example, I set this upper bound to the level of accuracy achieved by Iess *et al.* (2012) on the determination of Titan's k_2, which translates in $\sigma_{k_2} \leq 0.06$. Selecting all best combinations, as the number of flybys changes, one can build a plot of the best attainable accuracy as a function of n, for both link configurations (Figure 6.17.

I can conclude that, in order to fulfill the minimum requirement on the estimation of Callisto's k_2, at least 6 flybys of the satellite must be devoted to gravity measurements when using the baseline Ka-Ka link (blue line), although the choice of this minimum number would not leave much mar-

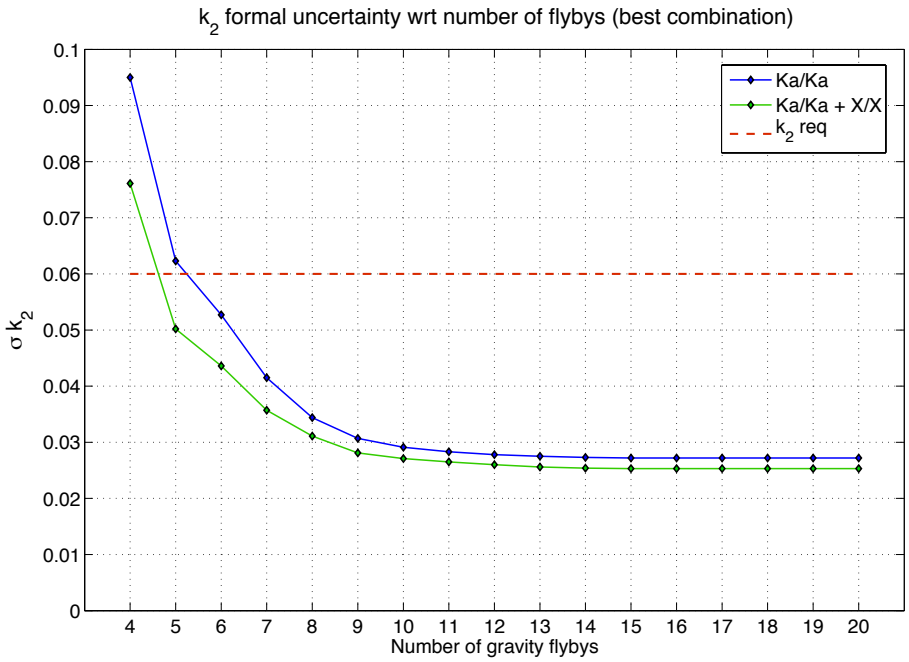

Figure 6.17: Estimation accuracy of Callisto tidal Love number attainable with a different number of flyby (at the best combination).

gin for possible eventualities that could jeopardize the observations (noisy tracking passages).

Using a double Ka-Ka+X-X link configuration (green line), the situation is slightly more relaxed and choosing 6 flybys anyway would, most likely, guarantee the fulfillment of the experiment requirement.

Chapter 7

Conclusions and Discussion

This thesis demonstrates how the knowledge of the geodesy of the Jovian system bodies will greatly benefit from the gravity investigations to be carried out with the Juno and JUICE missions in the next few decades. In this last chapter, the main results of the analyses are highlighted and discussed, and potential future research perspectives are proposed.

The issue of the determination of the penetration depth of Jupiter's winds can be tackled in different ways, the one proposed in this frame entails the detection of the gravity anomalies due to Jupiter's atmospheric dynamics, including small-scale disturbances, by using very precise Doppler measurements of the spacecraft velocity.

It has been pointed out how two complementary factors concur in the successful determination of Jupiter's wind anomaly map, with particular regard for the Great Red Spot: on one hand there's the increase in the wind gravitational signal due to the increase in the wind penetration depth, on the other hand, the larger H , the more parameters are needed to fit the simulated Doppler data with consequent degradation of the estimation accuaracies. The evolution of these two contributions has been studied by performing several simulations of the Juno gravity experiment for different values of H, starting from very shallow winds up to height scales larger than Jupiter's radius, indicating total penetration.

The result of this parametric study is that there is a range of values of H for which the gravity anomaly related to the GRS is clearly visible with a quite good signal to noise ratio. Figure 7.1 shows the ratio of the

gravitational signal to the formal uncertainty output of the filter, at the GRS location.

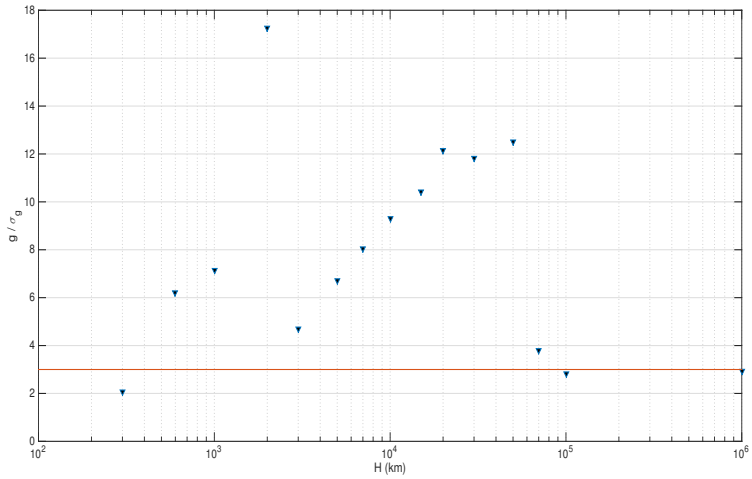

Figure 7.1: Ratio of the gravitational signal to the formal uncertainty at the Great Red Spot location, for different values of H. The black triangles represent the analysis results. The red line represents the lower bound on the SNR.

From the plot one can conclude that approximately for 1000 km $< H <$ 5000 km, where SNR > 3 (considering the proper error bars), the Juno gravity experiment should be able to detect the GRS anomaly, provided that the minimum set of estimated parameters, capable of fitting the Doppler data, is chosen.

On a different note, the analysis has shown that the spherical harmonic basis is not the most appropriate tool to describe punctual or localized phenomena such as vortices, because of the periodic nature of the harmonic functions. Consequently a discrete disturbance in the gravitational potential of an isolated body, if described by spherical harmonics, would require a very broad and articulate frequency spectrum. The cure for this limitation could lie in the introduction of a different model capable of taking into account the presence of localized masses: the mascons. These elements consist of concentrated masses that can assume different geometries: points; cylinders, disks and so on. This way, vortices and other small-scale localized anomalies can be described as concentrated masses while the background global gravity field is still represented by spherical harmonics. The

mass, the location and the geometry of each mascon can be put in the vector of solve-for parameters, providing also an estimate of the vortex extension. Nevertheless, the possibility of adopting such method has to be implemented and tested.

The results of the numerical simulations of the JUICE radio science experiment have pointed out the potentiality of the mission of unraveling the interior structure of two of the Galilean satellites: Ganymede and Callisto. Above all, the results concerning the accuracies obtained in the estimation of the satellites' tidal Love numbers for the detection of liquid layers underneath the icy crust. For Ganymede, the determination of this parameter will be possible with uncertainties about 1000 times better than what has been done with Titan using Cassini gravity data (Iess *et al.*, 2012).

However, the JUICE mission is currently in the early-definition phase, meaning that both the trajectory and the observation schedule of the mission are subject to variations due to technical constraints and optimization issues. For example, in order to reduce the total ΔV, the cancellation of the 200-km orbital phase at Ganymede has been proposed, with the prospect of eventually recovering the science phase if the remainder ΔV allows it.

The cancellation of the last 30 days of mission will certainly have an impact on the scientific return of the gravity experiment, however the entity of the losses has not yet been evaluated, making this issue the most compelling subject of the near-future developments of the numerical simulations of the experiment.

An extensive covariance analysis of the estimation uncertainties in the determination of the gravity fields of the satellites with the JUICE mission has been carried out in the past three years. The results are quite solid and very few and little changes are expected in the results, provided that the nominal trajectory remains the same. However a thorough analysis of the trajectory stability is needed, with the possibility of implementing a sequential batch filter in which the trajectory of the spacecraft is propagated and improved for the whole duration of the mission, instead of being initialized at the beginning of each arc.

The main goal of the numerical simulations of the JUICE gravity experiment is certainly that of arriving in 2030 with a solid tool for the de-

termination of the satellites' gravity, but also to provide, in this early definition phase, a tool for the bargaining of observation windows, given that radio science investigations have proven, during the past few decades to be very reliable and consistent means for the understanding of the interior structure of celestial bodies, holding with the highest regard the search for liquid water oceans.

Bibliography

[Anderson 1996] Anderson, J.D., Lau, E.L., Sjogren, W.L., Schubert, G. and Moore, W.B. 1996. *Gravitational constraints on the internal structure of Ganymede* Nature, Vol. 384, pp. 541-543.

[Anderson, 1997] Anderson, J. D., Lau, E. L., Sjogren, W. L., Schubert, G. and Moore, W. B. 1997. *Europa's differentiated internal structure: Inferences from two* Galileo *encounters* Science, Vol. 276, pp. 1236-1239.

[Anderson, 1998] Anderson, J. D., Schubert, G., Jacobson, R. A., Lau, E. L., Moore, W. B. and Sjogren, W. L., 1998. *Distribution of rock, metals and ices in Callisto* Science, Vol. 280, pp. 1573-1576.

[Anderson, 2001] Anderson, J. D., Jacobson, R. A., McElrath, T. P., Moore, W. B., Schubert, G. and Thomas, P. C., 2001. *Shape, mean radius, gravity field and interior structure of Callisto* Icarus, Vol. 153, pp. 157-161.

[Archinal, 2010] Archinal, B.A., A'Hearn, M.F., Bowell, E., Conrad, A., Consolmagno, G.J., Courtin, R., Fukushima, T., Hestroffer, D:, Hilton, J.,L., Krasinsky, G.A., Neumann, G., Oberst, J., Seidelmann, P.K., Stooke, P., Tholen, D.J., Thomas, P.C. and Williams I.P., 2010. *Report of the IAU Working Group on cartographic coordinates and rotational elements: 2009*, Celest. Mech. Dyn. Astr., doi:10.1007/s10569-010-9320-4.

[Armstrong, 2008] Armstrong, J. W., 2008. *Low-Frequency Gravitational Wave Searches Using Spacecraft Doppler Tracking* Living Rev. Relativity, Vol. 9 (2006), 1.

[Asmar, 2005] Asmar, S. W., Armstrong, J. W., Iess, L., Tortora, P., 2005. *Spacecraft Doppler tracking: Noise budget and accuracy achievable in precision radio science observations*. Radio Science, Vol. 40, Issue 2, RS2001, doi:10.1029/2004RS003101.

[Asmar, 2009] Asmar, S. W., Folkner, W. M., Iess, L. and Tortora, P., 2009. *Galilean Satellites Gravity Investigations and Interior Structure with Future Missions*. American Geophysical Union, Fall Meeting 2009, abstract # P51E-1172.

[Bagenal, 2004] Bagenal, F., Downling, T. E., McKinnon, W. B., 2004. *Introduction*, *Chapters 3* and *13* in *Jupiter: the planet, satellites and magnetosphere*, F. Bagenal, T. E. Dowling and W. B. McKinnon Editors 2004, Cambridge University Press: Cambridge, U.K.; New York, pp. 1-18, 35-58, 281-306.

[Bernardini, 2008] Bernardini A., 2008. *Sistemi di Comunicazione Satellitare*, Edizioni Ingegneria 2000, ISBN: 888665846X, 9788886658461.

[Bertotti, 2003] Bertotti B., Farinella P., Vokrouhlicky D., *Physics of the Solar System Dynamics and Evolution, Space Physics and Spacetime Structure*, Astrophysics and Space Science Library, Kluwer Academic Publishers, P.O. Box 322, 3300 AH Dordrecht, The Netherlands.

[Bolton, 2010] Bolton, S. J., 2010. *The Juno mission* in Proceedings of the International Astronomical Union Symposoum No. 269, Padua, Italy, 2010, vol. 6, pp. 92-100.

[Burgdorf, 2000] Burgdorf, M.J., Encrenaz, T., Brucato, J.R., Feuchtgruber, H., Davis, G.R., Lellouch, E., Swinyard, B.M., MÃ$\frac{1}{4}$ller, T.G., Sidher, S.D., Morris, P., Griffin, M.J., Colangeli, L., Mennella, V., 2000. *The Emissivity of Mars and Callisto in the Far Infrared*. ISO beyond the peaks: The 2nd ISO workshop on analytical spectroscopy. Eds. A. Salama, M.F. Kessler, K. Leech and B. Schulz. ESA-SP 456. pp. 9.

[Choi, 2007] Choi, D.S, Banfield, D., Gierasch, P., Showman, A.P., 2007. *Velocity and vorticity measurements of Jupiter's Great Red Spot using automated cloud feature tracking.*, Icarus, Vol. 188, pp. 35-46.

[Choi, 2011] Choi, D.S, Showman, A.P., 2011. *Power spectral analysis of Jupiter's clouds and kinetic energy from Cassini*, Icarus, Vol. 216, pp. 597-609.

[Cornell Education] Lectures of the course: Astronomy 6570, *Physics of the Planets, Tidal Evolution*.

[ESA, 2009] ESA/SRE(2008)2, *Jupiter Ganymede Orbiter: ESA contribution to the Europa Jupiter system mission. Assessment study Report*. 12 February 2009.

[ESA, 2011] ESA/SRE(2011)18, The JUICE Science Study Team *JUICE. Exploring the emergence of habitable worlds around gas giants. Assessment Study Report*. December 2011.

[ESA, 2012] ESA PR 13 2012, *Juice is Europe's next large science mission*. 02 May 2012. ESA Media Relations Office Communication Department.

[ESA, 2013a] *http://sci.esa.int/jump.cfm?oid=50073*.

[ESA, 2013b] *ESA ESTRACK brochure* from ESA/ESOC - Darmstadt, Germany. Last update: 22 January 2013.

[Finocchiaro, 2013] Finocchiaro, S., 2013. *Numerical Simulations of the Juno Gravity Experiment*. Doctoral Dissertation. Retrieved from Pubblicazioni Aperte Digitali della Sapienza, code 1889.

[Geerts, University of Wyoming] B. Geerts, E. Linacre and L. Oolman. *Notes of Resources in Atmospheric Sciences*. Chapter 12, Thermal Wind, University of Wyoming.

[Galanti, 2013] Galanti, E., Finocchiaro, S., Kaspi, Y., Iess, L., 2013. *An improved method for estimation of Jupiter's gravity field using the Juno expected measurements, a trajectory estimation model, and an adjoint based thermal wind model*. American Geophysical Union, Fall Meeting 2013, abstract n. P21C-1746.

[Gauss, 1809] Gauss, K.F., 1809. *Theoria Motus Corporum Coelestium*. Translated into English: Davis, C.H., Theory of the Motion of Heavenly Bodies Moving about the Sun in Conic Sections, Dover, New York, 1963.

[Grammier, 2009] Grammier, R. S., 2009. *A look inside the Juno Mission to Jupiter*. Aerospace Conference. IEEE, Big Sky, MT, 2009, pp 1-10, paper #1582.

[Hall, 1998] Hall, D. T., Feldman, P. D., McGrath, M. A. and Strobel, D. F., 1998. *The Far-Ultraviolet Oxygen Airglow of Europa and Ganymede*. The Astrophysical Journal, Vol. 499, pp. 475-481.

[Hide 1976] Hide, R. and Stannard, D., 1976. *Jupiter's magnetism: Observations and theory* in *Jupiter*, T. Gehrels (ed), University of Arizona Press, pp. 767-787.

[Hubbard 2012] Hubbard, W.B., 2012. *High-precision Maclaurin-based models of rotating liquid planets*, The Astrophysical Journal Letters, 756, L15, doi:10.1088/2041-8205/756/1/L15.

[Iess, 2010] Iess L., Rappaport, N.J., Jacobson, R.A., Racioppa, P., Stevenson, D.J., Tortora, P., Armstrong, J.W., Asmar, S.W., 2010. *Gravity Field, Shape, and Moment of Inertia of Titan*, Science, Vol. 327 (5971).

[Iess, 2012] Iess L., Jacobson, R.A., Ducci, M., Stevenson, D.J., Lunine J.I., Armstrong, J.W., Asmar, S.W., Racioppa, P., Rappaport, N.J., Tortora, P., 2012. *The Tides of Titan*, Science, Vol. 337 (6093), pp. 457-459.

[Iess, 2014] Iess L., Stevenson, D.J., Parisi M., Hemingway D., Jacobson, R.A., Lunine J.I., Nimmo F., Armstrong, J.W., Asmar, S.W., Ducci M, Tortora, P., 2010. *The Gravity Field and Interior Structure of Enceladus*, Science, Vol. 344 (6179) pp. 78-80.

[Jacobson, 2002] R.A. Jacobson, 2002. *Pioneer and Voyager Jupiter Encounter Orbit Reconstruction in the ICRF system*, AAS/AIAA Space Flight Mechanics Meeting, 2002, Paper 02-157.

[Jacobson, 2003] R.A. Jacobson, 2003. *JUP230 Orbit Solution*, JPL Solar System Dynamics Web Site.

[Jacobson, 2011] R.A. Jacobson, 2011. *On the Titan Tide Model*, Internal technical note, Jet Propulsion Laboratory, California Institue of Technology, 4800 Oak Grove Drive, Pasadena, California 91109-8099, January 5, 2011.

[Juno Press Kit] NASA Press Kit, August 2011 *Juno Launch*.

[Kaula, 1966] Kaula, W. M., 1966. *Theory of Satellite Geodesy*. 1966 by Blaisdell Publishing Company, A Division of Ginn and Company,

Waltham, Massachussetes. Library of Congress Catalog Card Number: 65-14571.

[Kaspi, 2009] Kaspi, Y., Flierl, G. R., Showman, A. P., 2009. *The deep wind structure of the giant planets: Results from an anelastic general circulation model*. Icarus, Vol. 202, pp 525-542.

[Kaspi, 2010] Kaspi, Y., Hubbard, W. B., Showman, A. P., Flierl, G. R., 2010. *Gravitational signature of Jupiter's internal dynamics*. Geophysical Research Letters, Vol. 37, Issue 1, doi: 10.1029/2009GL041385.

[Khurana, 1998] Khurana, K.K., Kivelson, M. G., Stevenson, D. J., Schubert, G., Russell, C. T., Walker, R. J., Joy, S., Polanskey., C., 1998. *Induced magnetic fields as evidence for subsurface oceans in Europa and Callisto*. Nature, Vol. 395, pp 777-780. doi 10.1038/27394.

[Kivelson, 2002] Kivelson, M.G., Khurana, K.K. and Volwerk, M., 2002. *The permanent and inductive magnetic moments of Ganymede*. Icarus, Vol. 157, pp 507-522.

[Kliore, 2004] Kliore, A.J., Anderson, J.D., Armstrong, J.W., Asmar, S.W., Hamilton, C.L., Rappaport, N.J., Wahlquist, H.D., Ambrosini, R., Flasar, F.M., French, R.G., Iess, L., Marouf, E.A., Nagy, A.F., 2004. *Cassini Radio Science*. Space Science Reviews 115 (1-4): pp. 1-70.

[Marconi, 2007] Marconi M.L., 2007. *A kinetic model of Ganymede's atmosphere*. Icarus, Vol. 190, pp. 155-174.

[Marshall, 2011] Marshall, D.A., Hands, T.O., Griffiths, I., Douglas ., 2011. *A22 Thawing of Europa by a stellar Jupiter*. Journal of Physics Special Topics, vol. 10, No 1.

[McKinnon, 1986] McKinnon, W.B. and Parmentier, E.M., *Ganymede and Callisto* in *Satellites*. J. A. Burns, M. S. Matthews (eds), University of Arizona Press, pp 718-763, 1986.

[Milani and Gronchi, 2010] Milani A. and Gronchi G.F., *Multi Arc Strategy, The theory of orbit determination*, Chapter 15, Cambridge University Press, 2010, pp. 311-314.

[Morabito, 1979] Morabito, L. A., Synnott, S. P., Kupferman P. N., Collins, S. A., 1979. *Discovery of Currently Active Extraterrestrial Volcanism*. Science 1 June 1979: Vol. 204 no.4396 pp. 972. doi: 10.1126/science.204.4396.972.

[Mueller, 1988] Mueller, S. and McKinnon, W. B., 1988. *Three-layered models of Ganymede and Callisto: Compositions, structures, and aspects of evolution*. Icarus, Vol. 76, pp 437-464.

[Galileo Press Kit] NASA Press Kit. *Galileo End of Mission*. September 2003.

[NASA, 2009] NASA/Jet Propulsion Laboratory. *NASA Facts: Galileo Mission to Jupiter*. Retrieved 2009-07-09.

[NASA, 2011] NASA/Jet Propulsion Laboratory. *NASA Facts: Juno Mission to Jupiter*. JPL 400-1382 4/09. Retrieved 2011-04-05.

[Nybakken, 2009] Nybakken, R., 2009. *The Juno mission to Jupiter - A prelaunch update*. Aerospace Conference. IEEE, Big Sky, MT, 2011, pp 1-8, paper #1179.

[Parisi, 2012] Parisi, M., Iess, L., Finocchiaro, S., 2012. *Gravity Science with the JUICE Mission*. EGU General Assembly 2012, held 22-27 April, 2012 in Vienna, Austria, p. 11912.

[Racioppa, 2012] Racioppa, P., 2012. *ORACLE Documentation*. Html, Department of Mechanical and Aerospace Engineering, Sapienza Universitá di Roma.

[Schilling, 2004] Schilling, N., Khurana, K. K. and Kivelson, M.G., 2003. *Limits on the instrinisc dipole moment in Europa* Journal of Geophysical Research, Vol. 109, Issue E5.

[Schubert, 1981] Schubert, G., Stevenson, D. J. and Ellsworth, K., 1981. *Internal structures of the Galilean satellites* Icarus, Vol. 47, pp. 46-59.

[Schubert, 1986] Schubert, G., Spohn, G. T. and Reynolds, R. T., 1986. *Thermal histories, composition and internal structures of the moons f the solar system* in *Satellites*. J. A. Burns, M. S. Matthews (eds), University of Arizona Press, pp 224-292, 1986.

[Schubert, 1996] Schubert, G., Zhang, K., Kivelson, M. G. and Anderson, J. D., 1996. *The magnetic field and internal structure of Ganymede*. Nature, Vol. 384, pp. 544-545.

[Seiff, 1998] Seiff, A. *et al.*, 1998. *Thermal structure of Jupiter's armosphere near the edge of a 5-μm hot spot in the north equatorial belt*. Journal of Geophysical research, Vol. 104(E10) pp. 22857.

[Simone, 2009] Simone, L. *et al*, 2009. *A Ka-band translator for radio-science applications*. Advanced RF Sensors and Remote Sensing Instruments. ESA-ESTEC, 2009.

[Slobin, 2010] Slobin, S.D., 2010. *34-m BWG Stations Telecommunications Interfaces*. DSN Telecommunications Link Design Handbook, 104, Rev.F, NASA-DSN.

[Smith, 1979] Smith, B. A., Soderblom, L. A., Johnson, T. V., et al., 1979. *The Jupiter System Through the Eyes of Voyager*. Science, Vol. 204 no.4396 pp. 951-972. doi: 10.1126/science.204.4396.951.

[Spencer, 1983] Spencer, J. R., 1983. *Ganymede in the Thermal Infrared: Preliminary Analysis of Voyager IRIS Data*. Lunar and Planetary Science XIV, pp. 731-732. Abstract.

[Stevenson, 1977] Stevenson, D.J. and Salpeter, E.E., 1977. *The phase diagram and transport properties for hydrogen-helium fluid planets*. ApJS, Vol. 35, pp. 221-237.

[Tapley, 2004] B.D. Tapley, B.E. Schutz, G.H. Born, 2004. *Statistical Orbit Determination*. Elsevier Academic Press. ISBN: 0-12-683630-2.

[Thales, 2012] Thales Alenia Space, 2012. *Deep Space and Secure Transponders, Ka Band Transponder for Radio-Science*. Updated : June 2012.

[UCI Edu ESS124] Prof.Jin-Yi Yu, Course of Earth Sciences, Lecture 8, University California Irvine.

[Vallis, 2006] Geoffrey K. Vallis, 2006. *Atmospheric and Oceanic Fluid Dynamics: Fundamentals and Large-scale Circulation*. Princeton University, New Jersey, Cambridge University Press.

[Vasavada, 2005] Vasavada, A.R., Showman, A.P., 2005. *Jovian atmospheric dynamics: An update after Galileo and Cassini*. Rep. Prog. Phys. 68, 1935-1996.

[Yeomans, 2006] Yeomans, D.K., 2006. *Planetary Satellite Physical Parameters*. JPL Solar System Dynamics. Retrieved 2007-11-05.

[Zimmer, 2000] Zimmer, C. and Khurana, K. K., 2000. *Subsurface Oceans on Europa and Callisto: Constraints from Galileo Magnetometer Observations*. Icarus, Vol. 147, pp 329-347. doi:10.1006/icar.2000.6456.